QUARKONIUM TRANSPORT THEORY IN ULTRA-RELATIVISTIC HEAVY-ION COLLISIONS

A Dissertation

by

XIAOJIAN DU

Submitted to the Office of Graduate and Professional Studies of
Texas A&M University
in partial fulfillment of the requirements for the degree of

DOCTOR OF PHILOSOPHY

Chair of Committee,	Ralf Rapp
Committee Members,	Siu Ah Chin
	Che-Ming Ko
	Saskia Mioduszewski
	Frank Sottile
Head of Department,	Grigory Rogachev

August 2019

Major Subject: Physics

ABSTRACT

The study of the fundamental strong interaction is an important vehicle for advancing our understanding of nuclear physics. Quarkonia, bound states of heavy quark-antiquark pairs, are promising probes for studying the strong force, in particular its confining property which constrains quarks and gluons to hadrons. Ultrarelativistic heavy-ion collisions (URHICs) are the only experimental method that can screen the strong force by creating a hot and dense medium. The suppression of quarkonia observed in URHICs is believed to be due to the formation of a deconfined quark-gluon plasma (QGP), a medium with unbound quarks and gluons. In order to study this phenomenon, we utilize a transport model to describe the evolution of quarkonium states in URHICs. This model calculates the suppression of heavy quarkonia, as well as recombination of heavy quark-antiquark pairs, in the medium. For charmonium, in particular, the recombination is essential for describing the momentum and energy dependencies of their spectra. Based on the fact that different binding energies lead to different dissociation temperatures, a "sequential regeneration" of excited and ground-state charmonia is proposed and implemented to compare to experimental data in nuclear collisions. Charmonium production in proton/deuteron-ion (p/d-A) collisions is also calculated with an extension of the transport model. The extension has a new background medium for p/d-A and more complete hadronic dissociation rates including many more mesons interacting with charmonia. This is particularly important at the Relativistic Heavy-Ion Collider (RHIC) energy because of the dominance of the hadronic contribution. The calculation suggests a QGP formation even in a small collision system such as p-Pb collisions at the Large Hadron Collider (LHC). The same transport model is deployed to study bottomonium kinetics, providing a comprehensive framework for both charm and bottom bound states. A stronger suppression for excited bottomonium states is found compared to the ground state. Furthermore, bottomonium is particularly sensitive to the in-medium strong force, as recombination is found to be at a much smaller level than for charmonium. This enables us to implement the transport model into a statistical analysis to constrain, for the first time, the in-medium properties of the underlying potential via transport parameters in χ^2 fits to experimental data. A rather strong in-medium heavy quark-antiquark potential is extracted, indicating the quark-gluon plasma to be a strongly coupled medium.

Dedicated to my parents

ACKNOWLEDGEMENTS

First and foremost, I would thank my Ph.D. advisor, Prof. Ralf Rapp, for his enthusiasm, dedication and guidance during research through the past years. Without his help, the dissertation can not be accomplished.

I am grateful to Prof. Che-Ming Ko, for his suggestions and discussions on physics.

Special thanks go to Prof. Siu Ah Chin, Prof. Che-Ming Ko, Prof. Saskia Mioduszewski and Prof. Frank Sottile for their kind serving in my committee.

Further special thanks go to Prof. Valery Pokrovsky for attending my preliminary exam and to Prof. Rainer Fries for attending my final exam.

I would thank Prof. Pengfei Zhuang for his hospitality during my visit to Tsinghua University.

Many thanks go to the colleagues who stayed before or during my years at the Cyclotron Institute: Prof. Xingbo Zhao, Prof. Min He, Prof. Nathan Holt, Prof. Yunpeng Liu, Prof. Baoyi Chen, Prof. Zhen Zhang, Dr. Shuai Liu, Dr. Paul Hohler, Dr. Feng Li, Dr. Yifeng Sun, Dr. Zilong Chang, Dr. Zhidong Yang, Dr. Kaijia Sun, Joseph Atchison, Isaac Sarver, Yanfang Liu. I had fruitful discussions with them.

I would also thank several experimental colleagues who helped me during my service work in the community: Prof. Enrico Scomparin, Prof. Roberta Arnaldi, Prof. Zhenyu Ye, Prof. Anton Andronic, Dr. Rongrong Ma, Dr. Zaochen Ye.

Finally, the most heartful dedication should be given to my dear parents, for raising me up and supporting me, and never complaining about my rare visit.

CONTRIBUTORS AND FUNDING SOURCES

Contributors

This work was supported by a dissertation committee consisting of Prof. Ralf Rapp, Prof. Siu Ah Chin, Prof. Che-Ming Ko, Prof. Saskia Mioduszewski of the Department of Physics & Astronomy and Prof. Frank Sottile of the Department of Mathematics.

The original transport machinery for J/ψ in A-A collisions was provided by Prof. Xingbo Zhao. The Langevin simulated bottom quark spectra in Chapter 5 was provided by Prof. Min He. The parameterization of the trial potential in Chapter 6 was provided by Dr. Shuai Liu. All the other work conducted for the dissertation was completed by the student under the supervision of Prof. Ralf Rapp of the Department of Physics & Astronomy.

Funding Sources

This work is supported by the U.S. NSF through grant no. PHY-1306359 and PHY-1614484.

NOMENCLATURE

3D/4D	3 or 4 dimension
CNM	Cold Nuclear Matter
EoS	Equation of State
HF	Heavy Flavor
HICs	Heavy Ion Collisions
HQ	Heavy Quark
HRG	Hadron Resonance Gas
LHC	Large Hadron Collider
LO	Leading Order
lQCD	Lattice QCD
NLO	Next Leading Order
nPDF	nuclear Parton Distribution Function
PDF	Parton Distribution Function
pQCD	Perturbative QCD
QCD	Quantum Chromodynamics
QED	Quantum Electrodynamics
QGP	Quark-Gluon Plasma
RHIC	Relativistic Heavy Ion Collider
SPS	Super Proton Synchrotron
URHICs	Ultra Relativistic Heavy Ion Collisions

TABLE OF CONTENTS

Page

LIST OF FIGURES

LIST OF TABLES

TABLE Page

1. INTRODUCTION

The strong nuclear force is an intriguing component of the four fundamental forces in nature: the electromagnetic interaction, the weak interaction, the strong interaction and the gravitational interaction. It "glues" the fundamental quarks together and makes atomic nuclei, most of the visible mass in the universe. This motivates us to pursue the path of understanding how the strong interaction binds quarks together.

In this section, we first present a brief overview of the Quantum Chromodynamics (QCD) serving as a modern theory of the strong interaction, and its properties: asymptotic freedom, confinement and chiral symmetry breaking. Next, we give a review of Ultrarelativistic Heavy-Ion Collisions (URHICs), which serves as the only experimental method that can screen the strong force and liberate the quarks bound inside nuclei. We then discuss the significance of utilizing quarkonium as a probe of deconfinement in URHICs. At the end of the section, we will provide an outline of the dissertation, and start our journey into the investigation of the strong force with quarkonia as probes.

1.1 Quantum Chromodynamics

Quantum Chromodynamics (QCD), as a non-abelian gauge theory [1] with local color symmetry [2], is very successful in describing the phenomena of strong interaction. The QCD Lagrangian density reads:

$$\mathcal{L} = -\frac{1}{2}\mathrm{tr}F_{\mu\nu}F^{\mu\nu} + \sum_{f=1}^{N_f} \bar{\Psi}^f \left(i\gamma^\mu D_\mu - m^f\right) \Psi^f, \tag{1.1}$$

where $F_{\mu\nu}$ is the field strength tensor representing the term of gluon fields and their self interactions. Ψ^f are the 4-component Dirac spinors, 3-vectors in color space with the flavor index f representing the quark fields and their interaction coupled to gluons; γ^μ

are the 4×4 gamma matrices; and m^f the bare masses of quarks. Furthermore, $D_\mu = \partial_\mu - igA^a_\mu t^a$ is the covariant derivative in a tensor form, with A^a_μ the gauge fields, t^a the SU(3) group generators and g the strong coupling. Here, a=1,..,N_c^2-1 is the color index, with N_c=3 the number of colors in the SU(3) gauge group. The generators t^a are 3×3 matrices in color space following

$$\left[t^a, t^b\right] = -\left[t^b, t^a\right] \;=\; if^{abc}t^c, \tag{1.2}$$

with f^{abc} the structure constant. The field strength tensor is

$$F_{\mu\nu} = \partial_\mu A^c_\nu t^c - \partial_\nu A^c_\mu t^c - ig\left[A^a_\mu t^a, A^b_\nu t^b\right] \tag{1.3}$$

In summary, QCD has two species of fields: (1) 8 gluons A^a with a=1,...,8, which carry the strong force, (2) 18 quarks Ψ and 18 anti-quarks $\bar{\Psi}$ with 3 colors N_c=3 and 6 flavors N_f=6, which build the visible matter, and three kinds of interactions: (1) order g gluon-quark interaction, (2) order g three-gluon self interaction, and (3) order g^2 four-gluon self interaction.

1.1.1 Properties of QCD

1.1.1.1 Asymptotic Freedom

One important feature of QCD as a non-abelian theory is its asymptotic freedom. In contrary to the QED, the QCD running coupling decreases at large energy scale, represented by a negative β function, which in 1-loop approximation reads [3, 4][1]

$$\beta(\alpha_s) = \frac{\partial \alpha_s}{\partial \ln\mu} = \frac{\alpha_s^2}{2\pi}\left(-\frac{11}{3}N_c + \frac{2}{3}N_f\right) = -\alpha_s^2\beta_0, \tag{1.4}$$

---

[1] The β function was originally calculated as $\beta(g) = \frac{\partial g}{\partial \ln\mu}$ in the very first papers [3, 4]. It can be easily reformulated as $\beta(\alpha_s) = \frac{g}{2\pi}\beta(g)$ with $\alpha_s = \frac{g^2}{4\pi}$.

where N_f is the number of quark flavors active at the energy scale μ. The gluon self interaction, which only arises in a non-abelian theory, generates the negative sign of the β function and causes anti-screening. The fermion-gluon interaction leads to the usual screening effect as one can also see in an abelian theory like QED. So the QCD running coupling as function of momentum transfer Q to 1-loop reads

$$\alpha_s(Q) = \frac{\alpha_s(\mu_0)}{1+\frac{1}{2\pi}\left(\frac{11}{3}N_c - \frac{2}{3}N_f\right)\alpha_s(\mu_0)\ln\left(\frac{Q}{\mu_0}\right)} = \frac{1}{\beta_0 \ln\left(\frac{Q}{\Lambda_{\mathrm{QCD}}}\right)} \tag{1.5}$$

where $\Lambda_{\mathrm{QCD}} = \mu_0 \exp\left(-\frac{1}{\alpha_s(\mu_0)\beta_0}\right)$ is the QCD scale. Clearly, the value of the QCD scale defines the divergence of the running coupling. It can be well defined only in 1-loop order and determined experimentally, roughly indicating the range where perturbative QCD (pQCD) is applicable ($Q \gg \Lambda_{\mathrm{QCD}}$) or fails. A common way is to quote the running coupling value at a certain large mass, $e.g.$, $\alpha_s(m_Z)$. In Fig. 1.1 we plot the running coupling $\alpha_s(Q)$. The asymptotic freedom qualitatively represents the fact that quarks are free at large momentum transfer or small distance, which is observed in deep inelastic scattering (DIS) experiments of electron-proton scatterings [6, 7]. The small distance physics in QCD with weak coupling is viable for pQCD calculations. The transition amplitudes of two-quark scattering from pQCD leads to a color Coulomb potential in the static limit, similar to the electric Coulomb potential in QED. The very strong coupling at small momentum transfer indicates a failure of pQCD and implies the onset of nonperturbative effects.

1.1.1.2 Confinement

One important non-perturbative effect in QCD is the absence of free quarks and gluons in nature, called confinement: the quarks and gluons are confined in color neutral hadrons. The separation of two color charges generates a long-range constant force between them, leading to an additional linear behavior confining term in the potential between them.

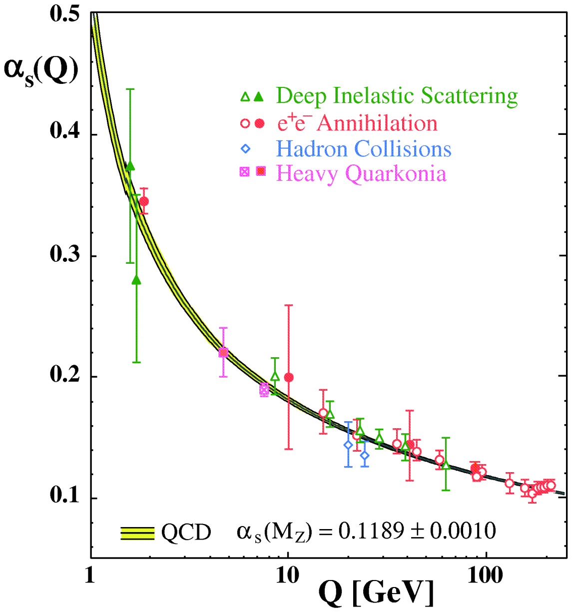

Figure 1.1: Running coupling $\alpha_s(Q)$ of QCD as a function of momentum transfer. The figure is reprinted from [5].

However, it is more favorable for producing a new quark-antiquark pair when the two color charges are separated at long enough distance. This process is called fragmentation.

One successful parametrization of the QCD potential between a static quark-antiquark pair is the Cornell potential [8, 9]

$$V_{q\bar{q}}(r) = -\left(\frac{N_c^2 - 1}{2N_c}\right)\frac{\alpha_s}{r} + \sigma r, \tag{1.6}$$

where $N_c = 3$ is the color charge number, α_s is the strong QCD coupling (see Eq. (1.5)), and σ is the strength of the confining force since $F = -\frac{\mathrm{d}V(r)}{\mathrm{d}r}$. See Fig. 1.2 for an illustration. The originally phenomenological Cornell potential is now accurately confirmed by lattice QCD [10, 11].

Similar to the separation of the parameterized QCD potential into two parts at short and long distances, many QCD processes can be factorized into two components" infrared-

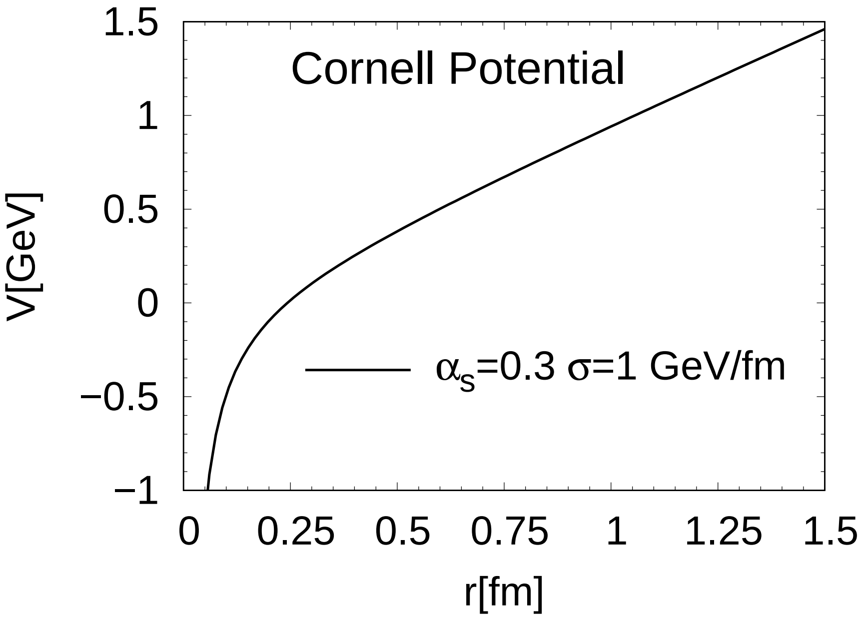

Figure 1.2: Cornell potential with α=0.3, σ=1 GeV/fm

.

safe processes at short distance, which are calculable by pQCD, and nonperturbative parts which are more difficult to calculate.

1.1.1.3 Chiral Symmetry Breaking

Another important feature of QCD is the chiral symmetry breaking [12]. The masses of quarks differ significantly. Quarks can be categorized into the light sector which includes the up quark (u), the down quark (d), sometimes also the strange quark (s), and the heavy sector which includes the charm quark (c), the bottom quark (b), and the top quark (t). Considering the light quarks only, the QCD Lagrangian in the massless limit reads

$$\mathcal{L} = -\frac{1}{2}\mathrm{t}rF_{\mu\nu}F^{\mu\nu} + \sum_{f=u,d}\left(\bar{\Psi}_L^f i\gamma^\mu D_\mu \Psi_L^f + \bar{\Psi}_R^f i\gamma^\mu D_\mu \Psi_R^f\right), \tag{1.7}$$

with left handed $\Psi_L = \frac{1}{2}(1-\gamma_5)\Psi$ and right handed $\Psi_R = \frac{1}{2}(1+\gamma_5)\Psi$ components of the quark field. The Lagrangian is invariant under chiral transformation, leading to a chiral symmetry. The chiral symmetry is spontaneously broken by the condensate of quarks in the QCD vacuum

$$\left\langle \bar{\Psi}\Psi \right\rangle = \left\langle 0|\bar{\Psi}_R\Psi_L + \bar{\Psi}_L\Psi_R|0 \right\rangle \neq 0, \tag{1.8}$$

which includes a mass difference of hadrons with their chiral partners (hadrons transform into each other under chiral transformation). In addition, there is also a gluon condensate in the QCD vacuum. Around 98 % of the quark masses inside hadrons are from the QCD condensation, and only a small portion of the masses originate from the Higgs mechanism.

1.1.2 QCD Phase Diagram

There are no free quark or free gluon observed in nature, which is the phenomenon of confinement. An important question to ask is if there is way to melt the hadrons at high temperature, $T \gtrsim \Lambda_{QCD} \simeq$200 MeV. It is intuitively expected that highly compressed hadrons may overlap and the absence of their boundaries may allow the quarks and gluons to move freely.

Before the existence of QCD, Hagedron conjectured that the hadronic density grows exponentially [13] with hadron mass,

$$\rho(m) \propto m^{-\frac{5}{2}}\mathrm{exp}\left(\frac{m}{T_H}\right), \tag{1.9}$$

and predicted a “highest possible temperature”, T_H=158 MeV by fitting to the known hadron spectroscopy.

Besides the phenomenological estimates, there is an ab-initio method based on the study of the QCD Lagrangian on the discretized space-time, called Lattice QCD (lQCD),

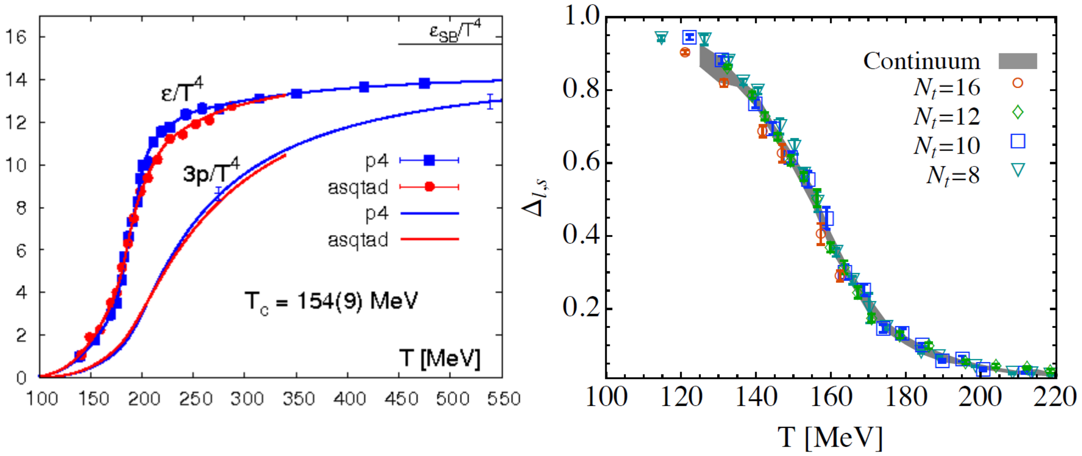

Figure 1.3: Left panel: energy density and pressure as function of temperature from lQCD (The figure is reprinted from [16]). Right panel: chiral condensation as function of temperature (The figure is reprinted from [14]).

evaluating observables with a path integral form,

$$\langle \mathcal{O}(A,\bar{\psi},\psi)\rangle = \frac{1}{\mathcal{Z}}\int [\mathrm{d}A][\mathrm{d}\bar{\psi}][\mathrm{d}\psi]e^{-\int \mathcal{L}\mathrm{d}^4x}\mathcal{O}(A,\bar{\psi},\psi), \tag{1.10}$$

with $\mathcal{Z}$ the partition function of QCD. The lQCD calculations show a quickly increasing energy density and a vastly dropping quark condensate around the critical temperature $T_c{\sim}155\,\mathrm{MeV}$ [14, 15] (see Fig. 1.3), indicating a new phase of matter at extremely high temperature, namely the quark-gluon plasma (QGP). However, the sign problem limits the methods of lQCD to be mostly effective at vanishing density. Theoretical studies at large baryon density [17, 18] suggest another new phase of matter, namely the color superconductor, where quark-quark pairs form a condensate (in contrast to quark-antiquark pairs binding in the hadronic phase). See the QCD phase diagram in Fig. 1.4.

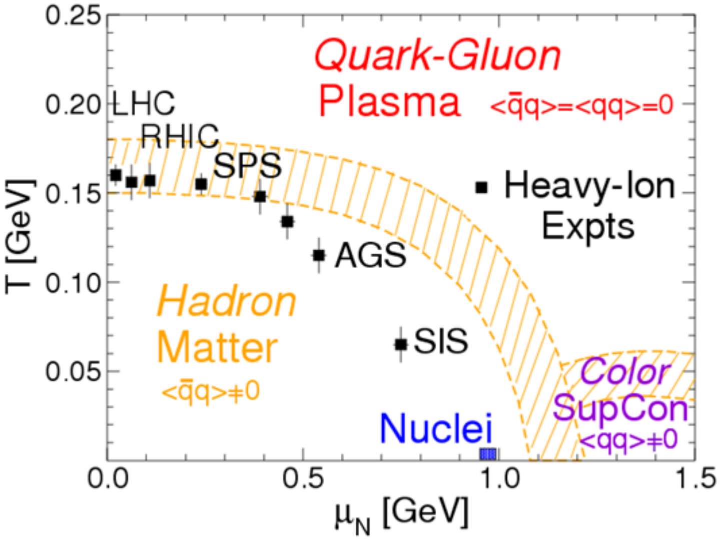

Figure 1.4: Schematic view of QCD phase diagram as function of temperature T and baryon chemical potential μ_N. The points are matter produced at several heavy-ion experiments. The figure is reprinted from [19].

1.2 Quark-Gluon Plasma and Ultrarelativistic Heavy-Ion Collisions

It is believed that during the first few microseconds of the universe evolution, before hadronization, free quarks and gluons existed in an evolving high-temperature QGP. There are experiments called Ultrarelativistic Heavy-Ion Collisions (URHICs) to reproduce and give access to the QGP phase in the laboratory.

1.2.1 Overview of Ultrarelativistic Heavy-Ion Collisions

In the experiments of Ultrarelativistic Heavy-Ion Collisions, physicists accelerate two heavy ions to extremely high speed (close to the speed of light), then collide them, and detect the particles produced in the collisions. The high-speed collisions by the energetic nucleons in the heavy ions make large energy transfer between the produced particles available, for converting it into thermal energy possibly, producing high temperature QGP. This enables us to study the properties of the QGP. The heavy ions have enough nucleons

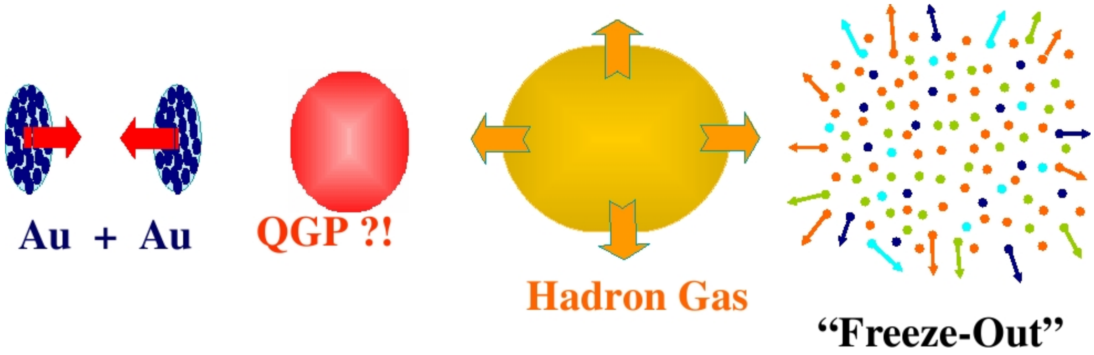

Figure 1.5: Schematic view of different stages of heavy-ion collision. The figure is reprinted from [19].

(and thus partons: quarks and gluons inside the nucleon) so that the collisions produce a large number of particles in approximately local thermal equilibrium, gaining access to the study of the QCD phase diagram, through experiments at different collision energies and with different colliding nuclei, see Fig. 1.4.

There are so far several heavy-ion experimental facilities with different beams at various collision energies, including: the Super-Proton-Synchrotron (SPS) at the European Organization for Nuclear Research (CERN), targeting heavy/light ions, into heavy/light ions; the Relativistic Heavy-Ion Collider (RHIC) at Brookhaven National Laboratory (BNL), with p-Al, p-Au, d-Au, ^{3}He-Au, Au-Au, Cu-Au, Cu-Cu, U-U, Zr+Zr, Ru+Ru collisions up to 200 GeV; the Large Hadron Collider (LHC) at CERN, with p-Pb, Pb-Pb, Xe-Xe collisions from 2.76Tev TeV to 8.16 TeV; and the Facility for Antiproton and Ion Research (FAIR) under construction at GSI Helmholtz Centre for Heavy Ion Research (GSI). The fixed target experiment at FAIR with lower energy will be able to probe QCD matter at high baryon density.

There are several stages of a URHIC (see the schematic view in Fig. 1.5), similar to the cooling of the universe after the big bang. The initial energetic head-on collisions from two nuclei transfer large momentum between partons inside, liberating the quarks and gluons. The collision creates a pre-equilibrium partonic stage. Subsequently, the partons tend to thermalize and form the QGP in a fireball above the critical temperature T_c within a formation time of τ_0=0.2-1.5 fm/c [20]. The partons are concentrated within the fireball, and the gradients of the produced parton density drive the fireball to expand. The partons in the QGP are strongly coupled, with a small viscosity over entropy density ratio, making the QGP evolving as a nearly perfect liquid [21, 22]. Once the fireball cools down to the critical temperature T_c after a duration τ_{QGP}=3-6 fm/c, the hadronization begins. There is not only a recovery of the confinement but also a breaking of the chiral symmetry and the condensation of gluons and condensation of quarks. The hadronization process is followed by a chemical freezeout [23] of different hadron species, resulting in a hadronic phase. Finally, the fireball expands to a large enough size and the medium is so dilute, that the hadrons stop colliding with each other. This is called the kinetic freezeout. Finally, the freezeout particles free stream to the detectors.

1.2.2 Observables in Ultrarelativistic Heavy-Ion Collisions

Physicists analyze the freezeout particles to deduce the information about the medium evolution and particle properties during the evolution, similar to the flame test in chemistry that people analyze the elements in the flame by its color. There are many observables in URHICs for us to understand the properties of the QGP. The “probes” of the matter created in URHICs originate from the medium (either the QGP or the hadronic matter) itself and provide the observables.

The probes can be categorized into soft and hard according to their typical energies. The bulk of light hadrons serves as the soft sector. The soft probes encode the collective phenomena of the medium. For semi-central or peripheral heavy-ion collisions, the initial shape of the fireball forms an ellipse in the transverse plane. In the reaction plane (plane determined by two center points of the two colliding nuclei and the longitudinal axis), called “in-plane”, it has larger gradient in the density which results in a larger pressure than in the perpendicular direction “out-of-plane”. It turns out that the medium expansion in-plane accelerates faster due to the larger pressure, resulting in a larger flow velocity (and particle momentum). One observable commonly measured in URHICs to characterize the anisotropies of the momentum spectra is the elliptic flow. The elliptic flow v_2 is the second-order azimuthal-angle expansion coefficient in the produced particle spectra.

$$\frac{\mathrm{d}^2N(b,p_T,\phi)}{p_T\mathrm{d}p_T\mathrm{d}\phi} = \frac{1}{2\pi}\frac{\mathrm{d}N(b,p_T)}{p_T\mathrm{d}p_T}[1+2v_2(b,p_T)\cos(2\phi)+\ldots], \tag{1.11}$$

where $\frac{\mathrm{d}^2N(b,p_T,\phi)}{p_T\mathrm{d}p_T\mathrm{d}\phi}$ is the spectrum as function of transverse momentum p_T and azimuthal-angle ϕ at a certain impact parameter b which is related to the “centrality” of the collision. The impact parameter b is the distance of the centers of the two colliding nuclei in the transverse plane, ranging from zero (most central collision) to twice the nuclear radius (peripheral collision). Larger impact parameters lead to larger anisotropies and larger v_2. The larger light hadron v_2 measured at higher energies (RHIC and the LHC) than previous measurements indicates the existence of the strongly medium, see Fig 1.6, based on hydrodynamic modeling of the QGP bulk evolution [24]:

Hard probes with large energy $\gg T_c$ can be either high transverse-momentum light particles or heavy particles with large masses. One observable representing the medium modification to the hard probes in URHICs is the nuclear modification factor

$$R_{\mathrm{AA}}(b,p_T) = \frac{\mathrm{d}N^{AA}(b,p_T)/p_T\mathrm{d}p_T}{N_{\mathrm{coll}}(b)\mathrm{d}N^{pp}(p_T)/p_T\mathrm{d}p_T}. \tag{1.12}$$

Here, $\mathrm{d}p_TN^{AA}(b,p_T)/p_T\mathrm{d}p_T$ is the spectrum of a specific particle produced in URHICs, and A specifies the heavy ion used in URHICs, $e.g.$, gold (Au), lead (Pb), $etc.$ $\mathrm{d}N^{pp}(p_T)/p_T\mathrm{d}p_T$ is the spectrum of a specific particle produced in proton-proton colli-

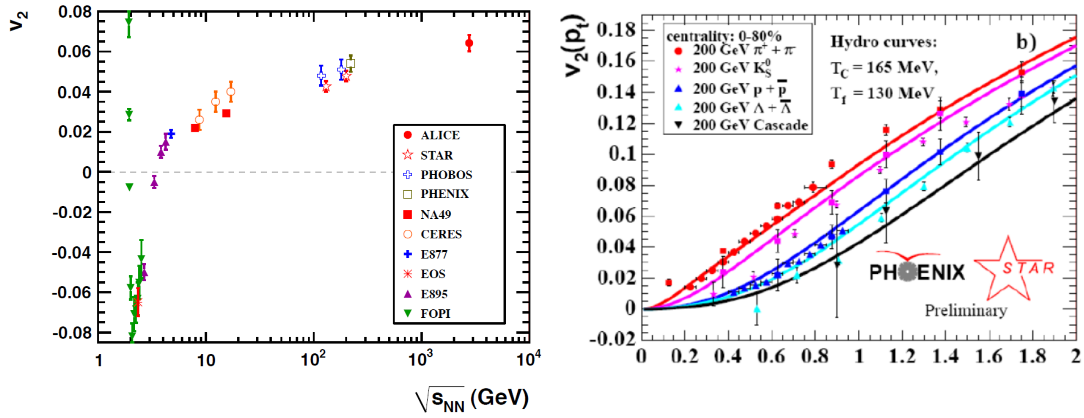

Figure 1.6: Left panel: p_T-integrated v_2 of charged particles in semi-central collisions at various energies [25]. Right panel: light hadron v_2 from STAR [26] and PHENIX [27], compared with hydrodynamic calculations [24]. The figures are reprinted from [25, 27].

sions (pp collisions). $N_{\text{coll}}(b)$ is the collision number of all nucleons within the two nuclei in URHICs used as a scaling factor. The nuclear modification factor $R_{\text{AA}}(b, p_T)$ will be simply equal to 1 if there is no medium effects in the URHICs. The parton produced in the heavy-ion collisions with high energy tends to undergo energy loss traveling through the QGP medium via radiation process, resulting in a substantial suppression at high p_T. This phenomenon is called “jet quenching” [28, 29]. The strongly interacting QGP with high density is expected to provide larger energy loss compared to the hadronic matter. The larger jet quenching observed in more central collision suggests the formation of a QGP medium. Heavy quarks, also hard probes, have an additional softer scale $p{\sim}m_Q v{\simeq}2$-5 GeV, which renders collisional energy loss through the evolution of the medium to be dominant. The initially hard-produced heavy quarks are far off-equilibrium and tend to thermalize through the medium evolution. It is noticeable that the thermal relaxation for charm quarks has a time scale comparable with the QGP lifetime, carrying a memory of the whole QGP evolution. See more in a review [19].

One promising hard probe with two additional softer scales is heavy quarkonium. Be-

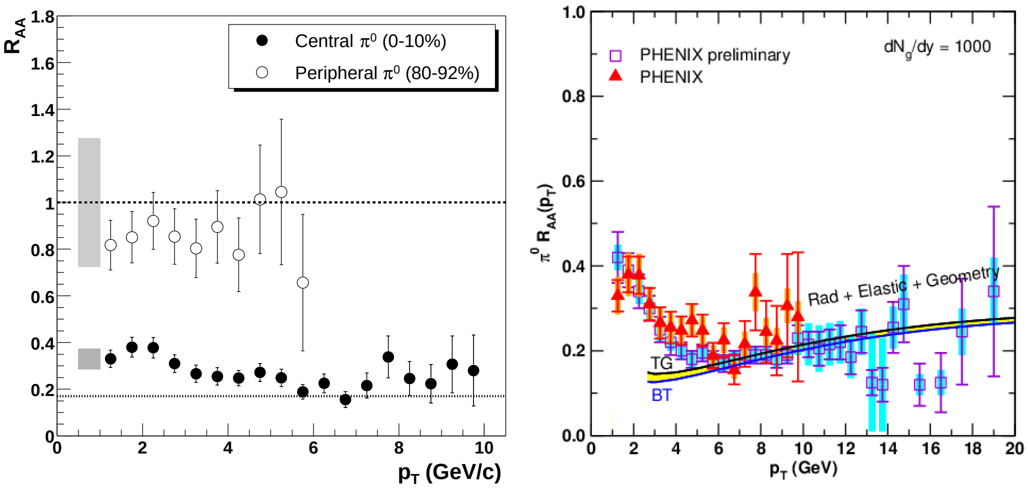

Figure 1.7: Left panel: neutral pion R_{AA} at central and peripheral collisions from PHENIX [30]. Right panel: neutral pion $R_{\mathrm{AA}}(p_T)$ from PHENIX [30] compared with jet-quenching calculations [31]. The figures are reprinted from [30, 31].

sides its hard scale of mass m, it also has a soft scale of momentum $p{\sim}m_Q v$ and an ultrasoft scale of binding energy $E_b{\sim}m_Q v^2$.

1.2.3 Quarkonia as Probes in Ultrarelativistic Heavy-Ion Collisions

The very first discovered quarkonium state is the ground state charmonium J/ψ, independently at Brookhaven National Laboratory (BNL) [33] and the Stanford Linear Accelerator Center (SLAC) [34].

Quarkonium consists of a heavy quark-antiquark pair, $e.g.$: charmonium is a charm quark and an anti-charm quark ($c\bar{c}$); bottomonium is a bottom quark and anti-bottom quark ($b\bar{b}$). The "toponium" ($t\bar{t}$) state does not exist because it will decay through the electroweak interaction before its bound-state formation. The quarkonium spectra are shown in Fig. 1.8.

We shall focus on the vector states, which can couple to photons, and thus the dilepton measurements are viable. However, the non-vector species also contribute to the ground-state particle yield via feeddowns and will be included in our studies. The most relevant

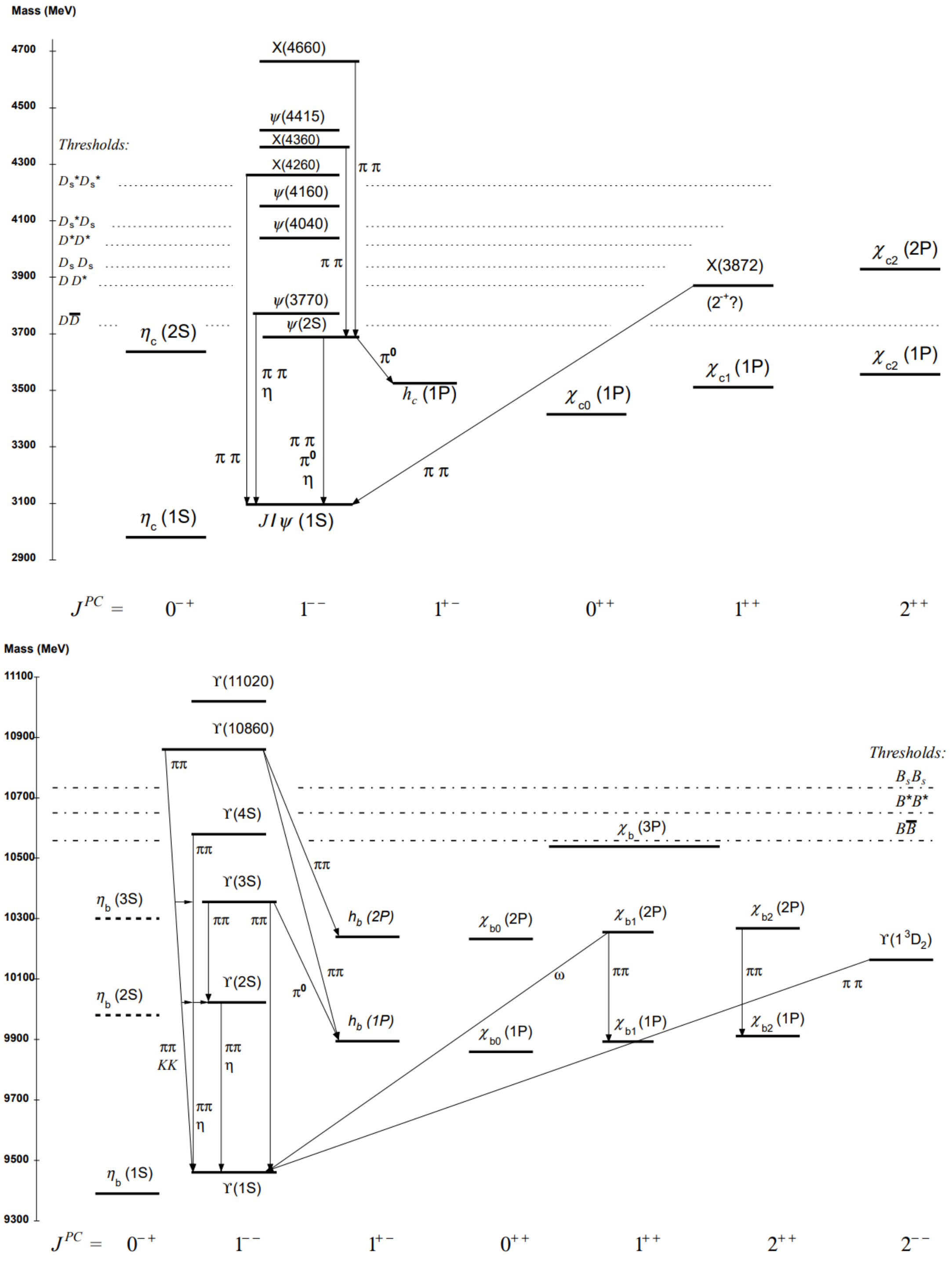

Figure 1.8: Spectrum of charmonium states (upper panel) and spectrum of bottomonium states (lower panel). The figures are reprinted from [32].

charmonia for this dissertation have the following vacuum masses:

$$\begin{aligned} m_{J/\psi(1S)} &= 3096.900 \pm 0.006 \mathrm{MeV} \\ m_{\psi(2S)} &= 3686.097 \pm 0.025 \mathrm{MeV} \end{aligned}$$

and the most relevant bottomonia for this dissertation have vacuum masses:

$$\begin{aligned} m_{\Upsilon(1S)} &= 9460.30 \pm 0.26 \mathrm{MeV} \\ m_{\Upsilon(2S)} &= 10023.26 \pm 0.31 \mathrm{MeV} \\ m_{\Upsilon(3S)} &= 10355.2 \pm 0.5 \mathrm{MeV} \end{aligned} \tag{1.13}$$

There are also many species with a mass larger than the threshold ($D\bar{D}$ masses, $B\bar{B}$ masses), inevitably having quick decays before their formation in the medium.

The large mass m_Q as a hard scale makes the $Q\bar{Q}$ production be strongly restricted to the initial hard collisions of the two nuclei, providing a pQCD calculable baseline before the QGP formation. This leads to a clear separation of the primordial hard process and the following soft process in medium.

The small momentum $m_Q v$ as the soft scale of quarkonium enables the nonrelativistic reduction (NRQCD), and consequently an ultrasoft scale $m_Q v^2$ validates the potential picture (pNRQCD), where the quarkonium is bound by static quark-antiquark potential, Eq. (1.6).

Furthermore, the ultrasoft scale of binding energy $E_b{\sim}m_Q v^2$, is comparable with the typical fireball temperature $E_b{\simeq}T_{QGP}{>}T_c$ in URHICs. This allows the quarkonia to survive under rather high temperature conditions, capable of gaining access to the QGP. The quarkonia are bound by the quark-antiquark potential, and the color force between the quark and anti-quark is screened in the QGP medium. Therefore, quarkonia are ideal for

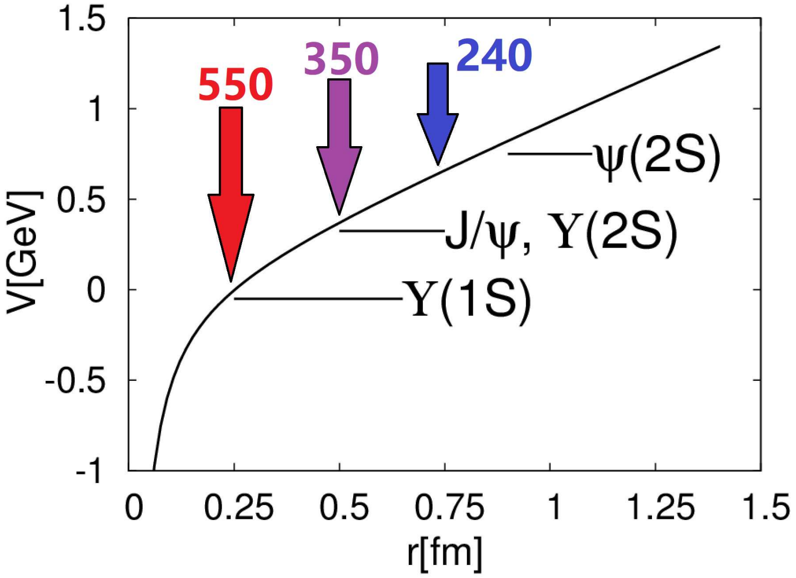

Figure 1.9: Different quarkonia have different melting temperature probing different part of the quark-antiquark potential. The figure is reprinted from [35]

.

investigating the medium modification to the heavy quark-antiquark potential (Eq. (1.6)) and the underlying fundamental QCD force. The different quarkonium species (as we see in Fig. 1.8, J/$\psi(1S)$, $\chi_c(1P)$, $\psi(2S)$, ..., $\Upsilon(1S)$, $\chi_b(1P)$, $\Upsilon(2S)$, $\Upsilon(3S)$, ...) with various binding energies, are proficient in probing different parts of the quark-antiquark potential, see Fig. 1.9. The exact form of the in-medium quark-antiquark potential is still unknown. lQCD studies compute the free energy [36, 11] of a static quark-antiquark pair $F_{Q\bar{Q}}(r,T)$, which however, is not identical to the potential but a lower limit. The corresponding internal energy

$$U_{Q\bar{Q}}(r,T) = F_{Q\bar{Q}}(r,T) - T\frac{\partial F_{Q\bar{Q}}(r,T)}{\partial T} \tag{1.14}$$

provides an upper limit to the "true" potential. The free energy corresponds to a weak potential, while the internal energy to a strong potential. A realistic in-medium potential will be somewhere between these two cases.

Matsui and Satz [37] first suggested the measurement of J/ψ suppression as a signature of QGP formation. The excited states with weaker binding energies survive only at lower temperature. Thus the melting of excited and ground charmonium states follow a sequence when the temperature increases. This is called the "sequential suppression" or "sequential melting" [38]. Following these ideas, quarkonium and its medium modification have been intensively studied for over 30 years both experimentally and theoretically.

Right after the Matsui and Satz paper, the NA38 Collaboration at the SPS found the signal of J/ψ suppression in a fixed target experiment using O projectiles on a U target at 200GeV [39]. However, this result and the results from similar light-ion experiments at the SPS can be described by an initial-state effect called nuclear absorption (we will have a brief introduction of nuclear absorption based on Glauber model in Sec. 2.2.9.3), revealing the fact that there is not enough evidence for the existence of the QGP in the light-ion collision system at the SPS energy. Later measurements at the SPS with heavier ion (Pb-Pb) collisions at $\sqrt{s}$=17 GeV (158 GeV fixed-target) energy suggest stronger suppression [40], which can not be explained by an extrapolation of the nuclear absorption mechanism, revealing a signal of the QGP [41]. Many models based on the final-state interaction can well describe this "anomalous" suppression ($e.g.$ see review [42]).

A similar suppression of J/ψ to what was found at the SPS was further confirmed in Au-Au collisions at $\sqrt{s}$=200 GeV at RHIC [43]. Considering the higher collision energies at RHIC, the similar suppressions at RHIC and the SPS indicate an additional charm quark coalescence or recombination contribution to charmonium [44, 45, 46, 47], which compensates the in-medium suppression of J/ψ. The recombination effect was also predicted and explicitly elaborated with transport models including both direct suppression and regeneration for LHC due to larger charm production [48, 49], and confirmed by experimental data [50, 51].

The measurements of bottomonium suppression in URHICs are available in recent years at RHIC [52, 53] and LHC energies [50, 54]. Here, a sequential suppression for different bottomonium species is reported [55]. The bottomonium suppression can be described with models without regeneration, indicating that bottomonia are possibly cleaner probes of heavy quark-antiquark potential than charmonia.

The complexity of J/ψ production at RHIC and LHC energies reveals many more interesting questions and stimulates more efforts of study. They include (but not limited to): What are the production yields for the excited charmonium states, for example $\psi(2S)$ [56, 57]? Is there any signal of the QGP in small system (p/d-A) collisions [58]? How large is the bottomonium regeneration [59]? What is the difference between charmonium production and bottomonium production [35]? And an even deeper question, what can we learn about the fundamental QCD force from quarkonium phenomenology in the URHICs [60]? This dissertation is trying to address the above questions and to enhance our understanding of quarkonium production in the QGP medium.

1.3 Outline of the Dissertation

In this dissertation, we will investigate the medium modification of quarkonium production in URHICs with various species (mainly J/$\psi(1S)$, $\psi(2S)$, $\Upsilon(1S)$, $\Upsilon(2S)$, $\Upsilon(3S)$), via a transport model.

In Sec. 2, we first provide a brief overview of kinetic theory and derive our main quarkonium transport equation, namely the Boltzmann equation. The exact detailed balance relation between the dissociation rate and the regeneration rate is given from the microscopic derivation, followed by a kinetic rate equation which validates the detailed balance relation. The exact detailed balance relation holds only in a thermal medium. Thus, for an off-thermal medium, a thermal relaxation time correction to the rate equation and its derivation from a relaxation time equation is provided. We then discuss the key ingredients to the transport equations, starting from a discussion of the "quasifree" approximation of the parton-induced dissociation in the QGP and a gluo-dissociation based on a color singlet-octet transition mechanism in the QGP. Dissociation in hadronic matter based on an SU(4) meson-exchange model is also briefly discussed. The equilibrium limit in the transport equation and its calculation is based on a statistical model and heavy-quark conservation. There are also corrections due to a "correlation volume" caused by a finite spatial diffusion of heavy quarks which is absent in the original statistical model. The background temperature evolution for the transport equation is discussed based on a fireball model assuming a conservation of total entropy due to the fact that the QGP is a nearly perfect liquid. We then turn to the initial condition of the transport equation, its coordinate and momentum distributions, and their nuclear modifications. A brief introduction of Langevin and Fokker-Planck equations used in the heavy-quark simulation is also given, with a discussion of the close relation between heavy quarks (open heavy flavor) and heavy quarkonium (hidden heavy flavor).

In Sec. 3, we first give a brief introduction to the features of J/ψ production in URHICs, especially at LHC energies. Next, we turn to a discussion of $\psi(2S)$ production in URHICs. The J/ψ and $\psi(2S)$ production in small system d-Au collisions at RHIC energy is calculated within an extension of the transport approach to d-A collisions. We extend the hadronic reaction rates in the study of d-A collisions which produce a medium mostly in the hadronic phase at RHIC energy. Furthermore, in the study of $\psi(2S)$ production in A-A collisions, based on the same argument of "sequential suppression", we propose a so called "sequential regeneration" mechanism, revealing a regeneration that is earlier for the J/ψ than for the $\psi(2S)$.

In Sec. 4, we systematically study charmonium production in small system p/d-A collisions at both RHIC and LHC energies. Fluctuations are important for such a small size system, generating an elliptic shape of the initially produced parton density. In order to capture the fluctuation effect, we construct an elliptic fireball with initial boundary from a Monte-Carlo Glauber model generator and implement it into the transport model. The fireball parameters are adjusted to reproduce the measured light-hadron spectra and elliptic flow. We discuss J/ψ and $\psi(2S)$ suppression in both the Pb-going direction and the p-going direction, which have different fireball sizes. We also present the calculated elliptic flow of J/ψ and $\psi(2S)$.

In Sec. 5, we develop a transport model for bottomonium production based on the Boltzmann equation. The in-medium binding energies are implemented in the calculation, instead of vacuum binding energies. These developments bring the bottomonium transport model to the same level as it is for the charmonia. Due to the large mass of the bottom quark, the bottom quarks are far from thermalization and the thermal blastwave description of charmonium spectra is not reliable in the bottomonium sector. Instead, we implement non-thermal bottomonium regeneration spectra with the Langevin equation simulated bottom-quark spectra, via an instantaneous coalescence model. We further investigate the sensitivities of the R_{AA} observables to several inputs. The p_T-dependent R_{AA} and v_2 for both $\Upsilon(1S)$ and $\Upsilon(2S)$ are worked out. We find the $\Upsilon(1S)$ to be a very promising probe of the in-medium QCD force, since the observable is sensitive to its binding energy.

In Sec. 6, following the inspiring findings from Sec. 5 that bottomonium is well-suited for probing the in-medium QCD force, we develop a statistically integrated transport model, to quantitatively extract the in-medium QCD potential directly from the experimental data. This is carried out for the first time in this context. The bottomonium in-medium binding energies from a parameterized color-screened quark-antiquark potential are translated to R_{AA} observables via the transport model. Within the transport model, a scaling factor accounting for nonperturbative effects in the direct heavy-quark coupling to the medium is implemented in the quarkonium reaction width in the QGP suggested by heavy-quark diffusion studies. Then we perform a chi-square test with the R_{AA} calculated from the transport model to constrain the parameters of the potential in fits to the experimental data. Best fits with corresponding confidence levels are extracted. The implications of our findings for the strongly-coupled properties of the QGP are discussed.

In Sec. 7, we summarize, conclude, and provide several remarks on future directions for improving the transport model and our understanding of quarkonium production in the study of the QGP.

2. REVIEW OF TRANSPORT THEORY

Transport theories are powerful tools to describe the kinetics and non-equilibrium dynamics of many-particle systems. Quarkonium production in URHICs has several dynamical contributions through dissociation and regeneration, and has a strong relation to the dynamics of individual heavy quarks.

This section is organized as follows: In Sec. 2.1, we give a brief review of the kinetic theory based on a general Markov process to derive the kinetic equations describing the quarkonium transport, and also a stochastic Langevin equation simulating the closely related heavy-quark transport. Then we focus on quarkonium transport in Sec. 2.2, introducing the transport equation in Sec. 2.2.1. The detailed balance in Sec. 2.2.2 leads to a rate equation in Sec. 2.2.3. In the quarkonium transport equation, the reaction widths as the first main transport coefficients, are discussed in Sec. 2.2.4, Sec. 2.2.5, and Sec. 2.2.6. The second main transport coefficient, the equilibrium limit, is discussed in Sec. 2.2.7. Other ingredients, the fireball medium background, the initial conditions, feeddown fractions and formation time effects are presented in Sec. 2.2.8, Sec. 2.2.9,Sec. 2.2.10, Sec. 2.2.11. Finally we discuss the connection between quarkonium and heavy quarks in Sec. 2.2.12.

2.1 Stochastic Process and Kinetic Theory

In this section, we present a general discussion of kinetic theory and provide a brief derivation of the main transport equations we use in our research.

2.1.1 Markov Process and Chapman-Kolmogorov Equation

Consider a particle with a stochastic motion among different states (in our context of charmonium production, a "$c\bar{c}$ pair" among its different forms of states, open charm: $D\bar{D}$ and hidden charm: J/ψ, $\psi(2S)$, *etc.*) in a sequence: $\{s_1, t_1\}$, $\{s_2, t_2\}$, $\{s_3, t_3\}$,...,$\{s_n, t_n\}$, with $t_1<t_2<...<t_i<...<t_n$. Note that the time index i is not a notation of different states. We may define a conditional probability representing the particle to arrive at state $\{s_n, t_n\}$ with a previous track of time series $\{s_1, s_2, s_3..., s_{n-1}\}$. A stochastic process is called a Markov process when the particle does not have any memory, in other words, the conditional probability is only depending on the most recent step:

$$P(s_n, t_n | s_1, t_1; s_2, t_3; ...; s_{n-1}, t_{n-1}) = P(s_n, t_n | s_{n-1}, t_{n-1}). \tag{2.1}$$

The probability density $P(s_n, t_n | s_{n-1}, t_{n-1})$ is called the transition probability density of a Markov process between states $\{s_{n-1}, t_{n-1}\}$ and $\{s_n, t_n\}$. A Markov process is called a Markov chain [61] if the number of states is countable $\forall s_i \in \mathbb{S} = \{S_{\bar{1}}, S_{\bar{2}}, S_{\bar{3}}, ..., S_{\bar{N}}\}$ (In the context of charmonium production, $\mathbb{S} = \{D\bar{D}, \mathrm{J}/\psi, \psi(2S), ...\}$. The index under s is a time index, while the index with a bar under S is the species index. For example, s_6=J/ψ means at time index=6, the $c\bar{c}$ pair is in a form of hidden J/ψ). The properties of the conditional probability and Bayes's theorem easily lead us to the equation of the transition probabilities (Chapman-Kolmogorov equation) [62]:

$$P(s_3, t_3 | s_1, t_1) = \sum_{s_2 \in \mathbb{S}} P(s_3, t_3 | s_2, t_2) P(s_2, t_2 | s_1, t_1). \tag{2.2}$$

2.1.2 Master Equation

A summation or an integration of Eq. (2.2) over an initial probability $P(s_1, t_1)$ gives the form

$$P(s_3, t_3) = \sum_{s_2 \in \mathbb{S}} P(s_3, t_3 | s_2, t_2) P(s_2, t_2). \tag{2.3}$$

The summation over s_2 is in the whole state space $\mathbb{S}$, so it also includes the current state of s_3. Thus the transition probability has two contributions:

(1) $\sum P(s_3, t_3|s_2, t_2)|_{s_2 \neq s_3}$, particle transits from all possible states but not from s_3.

(2) $P(s_3, t_3|s_2, t_2)|_{s_2 = s_3}$, particle stays in the current state s_3.

In case (2), the probability of staying locally equals to "1 minus the the probability of a transition to other states". That is

$$P(s_3, t_3|s_2, t_2)|_{s_2=s_3} = P(s_3, t_3|s_3, t_2)|_{s_2=s_3} = 1 - \sum_{s_2 \in \mathbb{S}} P(s_2, t_3|s_3, t_2)|_{s_2 \neq s_3}. \tag{2.4}$$

With further derivations pluging the above relation into Eq. (2.3), we have

$$P(s_3, t_3) - P(s_3, t_2) = \sum_{s_2 \in \mathbb{S} \setminus \{s_3\}} \left(P(s_3, t_3|s_2, t_2)P(s_2, t_2) - P(s_2, t_3|s_3, t_2)P(s_3, t_2)\right) \tag{2.5}$$

We define the transition rate $W(s_j|s_i)$ representing the transition from state s_i to state s_j, so that $P(s_j, t_3|s_i, t_2) = W(s_j|s_i)\,(t_3 - t_2)$. Reorganize the Eq. (2.5) and simplify the notations $\mathrm{d}t = t_3 - t_2 \to 0$, $t = t_2$, $r = s_2$, $s = s_3$, we arrive at the master equation:

$$\frac{\mathrm{d}P(s,t)}{\mathrm{d}t} = \sum_{r \in \mathbb{S} \setminus \{s\}} \left(W(s|r)P(r,t) - W(r|s)P(s,t)\right). \tag{2.6}$$

The differentiation is only on the time since the "state" is not differentiable. The physics meaning of the master equation is that the change of a probability (particle density in state space) is from two components, the gain term representing the state transition of $r \to s$ and a loss term representing the state transition of $s \to r$.

2.1.3 Rate Equation and Boltzmann Equation

We can derive a general rate equation of quarkonium evolution with loss and gain terms from the master equation, assuming the state s we are evaluating in Eq. (2.6) to be the quarkonium state we want to observe, and the summation states r to be sources (open heavy quark-antiquark pairs, different species of quarkonia, *etc.*). Notice that the summation over the transition rate of the second term in Eq. (2.6) can be performed, we may change the notation:

$$\alpha(s,t) = \sum_{r\in\mathbb{S}\setminus\{s\}} W(r|s) \tag{2.7}$$

$$\beta(s,t) = \sum_{r\in\mathbb{S}\setminus\{s\}} W(s|r)P(r,t). \tag{2.8}$$

The master equation can be reformulated as a rate equation for state “s”:

$$\frac{\mathrm{d}P(t)}{\mathrm{d}t} = \beta(t) - \alpha(t)P(t), \tag{2.9}$$

where we have suppressed the state notation “s”. So far in the derivation, we have not considered the transition in coordinate-momentum phase space ($\vec{x}$,$\vec{p}$). Thus the rates are inelastic rates representing chemical reactions of quarkonium. Assuming the probability density and rates of the quarkonium to be dependent on the coordinate-momentum phase space, we arrive at a Boltzmann equation of quarkonium:

$$\frac{\mathrm{d}P(\vec{x},\vec{p},t)}{\mathrm{d}t} = \beta(\vec{x},\vec{p},t) - \alpha(\vec{x},\vec{p},t)P(\vec{x},\vec{p},t). \tag{2.10}$$

We will present the detailed discussion of the above Boltzmann equation and its application to quarkonium states in Sec. 2.2.1.

2.1.4 Stochastic Differential Equation and its Corresponding Partial Differential Equation

We have derived a Chapman-Kolmogorov equation and master equation of stochastic one-particle motion. In many-body physics, the probabilities represent the distribution of all particles on average. Another way of looking at a stochastic process is to study the particle motion via a random walk.

Generally, a stochastic process of a particle with random variable $X(t)$, can be affected by two types of contributions, a drift part and a random (diffusion) part. The change of the random variable $\mathrm{d}X(t)$ can be described by a stochastic differential equation [63]

$$\mathrm{d}X(t) = \mu(X,t)\mathrm{d}t + \sigma(X,t)\mathrm{d}W(t), \tag{2.11}$$

where $\mu(X,t)\mathrm{d}t$ is the drift term and $\sigma(X,t)\mathrm{d}W(t)$ is the diffusion term. The $W(t)$ is a Wiener process that satisfies the following:
(1) For time t, the increment $\Delta W(t) = W(t+\Delta t) - W(t)$ for any Δt, are independent of past values $W(s)$, $s<t$.
(2) The increment $\Delta W(t)$ follows a Gaussian distribution that $\Delta W(t) = W(t+\Delta t) - W(t) \sim \mathcal{N}(0, \Delta t)$.
Note that (1) also means that $W(t)$ represents a Markov process. The condition (2) of a Gaussian distribution is a special case satisfying condition (1). A weaker version of (2) with another stationary distribution is usually called a Levy process. We see that without the random term, the stochastic equation $\mathrm{d}X(t) = \mu(X,t)\mathrm{d}t$ is deterministic. Without the drift term, the stochastic equation $\mathrm{d}X(t) = \sigma(X,t)\mathrm{d}W(t)$ always has an expectation value of 0 and $X(t)$ becomes a Martingale.

It is convenient to derive the corresponding partial differential equation of the stochastic equation using Itô's calculus. Suppose we define another random variable which relates to X and t by $g(X,t)$, Itô's lemma [64] tells us that the increment of the variable follows a stochastic differential equation

$$\mathrm{d}g = \left(\frac{\partial g}{\partial t} + \mu(X,t)\frac{\partial g}{\partial X} + \frac{1}{2}\sigma^2(X,t)\frac{\partial^2 g}{\partial^2 X}\right)\mathrm{d}t + \sigma(X,t)\frac{\partial g}{\partial X}\mathrm{d}W(X,t). \tag{2.12}$$

Suppose $g(X,t)$ is the distribution function of all particles we collect, then the total number of particles is conserved. That means the expectation value of the distribution which is the total number, is conserved, and its total increment $\langle \mathrm{d}g \rangle = 0$. Therefore the mean of the random part $\left\langle \sigma(X,t)\frac{\partial g}{\partial X}\mathrm{d}W(X,t)\right\rangle = 0$, and we arrive at a partial differential equation for the particle distribution (Kolmogorov backward equation) [65],

$$\frac{\partial}{\partial t}g(X,t) = -\mu(X,t)\frac{\partial}{\partial X}g(X,t) - \frac{1}{2}\sigma^2(X,t)\frac{\partial^2}{\partial^2 X}g(X,t). \tag{2.13}$$

Suppose $g(X,t)$ is not the distribution function but an arbitrary function with a Martingale property. Then Eq. (2.13) still holds. Instead, we can assume $f(X,t)$ to be the distribution function of all particles we collect. Next we multiply Eq. (2.13) with $f(X,t)$, integrate over X and t, and perform an integration by parts. With suitable choices of initial and final values of $g(X,t)$, and using the fact that the distribution $f(X,t)$ and its gradient vanish at the boundaries (or infinity), the boundary terms vanish. We arrive at the following equation:

$$\iint g(X,t)\left(-\frac{\partial}{\partial t}f(X,t) - \frac{\partial}{\partial X}\left(\mu(X,t)f(X,t)\right) + \frac{1}{2}\frac{\partial^2}{\partial^2 X}\left(\sigma^2(X,t)f(X,t)\right)\right)\mathrm{d}X\mathrm{d}t = 0. \tag{2.14}$$

Because the $g(X,t)$ is arbitrary, we have the Kolmogorov forward equation [65],

$$\frac{\partial}{\partial t}f(X,t) = -\frac{\partial}{\partial X}\left(\mu(X,t)f(X,t)\right) + \frac{1}{2}\frac{\partial^2}{\partial^2 X}\left(\sigma^2(X,t)f(X,t)\right). \tag{2.15}$$

2.1.5 Langevin Equation and Fokker-Planck Equation

In Eq. (2.11), the random variables and coefficients can be generalized to higher-dimensional phase spaces like 3D momentum and coordinates $X(t) = (\vec{x},\vec{p})$, $\mu(X,t) = \vec{\mu}(\vec{x},\vec{p},t)$, $W(X,t) = \vec{W}(\vec{x},\vec{p},t)$. A Langevin equation [66] which describes a particle moving in phase space is governed by two differential equations

$$\begin{aligned} \mathrm{d}x_i &= \frac{p_i}{E}\mathrm{d}t & (2.16) \\ \mathrm{d}p_i &= -A(\vec{x},\vec{p},t)p_i\mathrm{d}t + \sqrt{2D(\vec{x},\vec{p},t)}\mathrm{d}W_i(\vec{x},\vec{p},t), & (2.17) \end{aligned}$$

with $i = 1, 2, 3$ the index in dimensions. $A(\vec{x},\vec{p},t)$ is the relaxation rate and $D(\vec{x},\vec{p},t)$ is the diffusion coefficient. The momentum increment follows a stochastic equation and the corresponding Kolmogorov forward equation of the Langevin equation via Ito's lemma is the Fokker-Planck equation [67]

$$\frac{\partial}{\partial t}f(\vec{x},\vec{p},t) = \frac{\partial}{\partial p_i}\left(A(\vec{x},\vec{p},t)p_i f(\vec{x},\vec{p},t)\right) + \frac{\partial^2}{\partial p_i \partial p_i}\left(D(\vec{x},\vec{p},t)f(\vec{x},\vec{p},t)\right) \tag{2.18}$$

where the index i follows the Einstein summation convention.

In the stationary limit, the Fokker-Planck equation is solvable and the solution is determined by the Einstein relation. Note that the stationary distribution $f^{\mathrm{eq}}(\vec{x},\vec{p})$ only depends on $\vec{x}$ and $\vec{p}$, so that $\frac{\partial}{\partial t}f^{\mathrm{eq}}(\vec{x},\vec{p}) = 0$. It can be easily verified that an Einstein relation [68]

$$A(\vec{x},\vec{p},t)p_i = D(\vec{x},\vec{p},t)\frac{\partial\Omega(\vec{x},\vec{p})}{\partial p_i} - \frac{\partial D(\vec{x},\vec{p},t)}{\partial p_i} \tag{2.19}$$

leads to a stationary distribution [69]

$$f^{\mathrm{eq}}(\vec{x},\vec{p}) \simeq \exp(-\Omega(\vec{x},\vec{p})). \tag{2.20}$$

2.2 Quarkonium Transport Theory

The full transport equations of different quarkonia can be expressed as a set of master equations. The in-medium dynamics of heavy quarkonium (hidden heavy flavor) is mainly from inelastic collisions, and the one of a heavy quark (open heavy flavor) is mainly from elastic scattering, allowing the Boltzmann equation and the Langevin equation to describe their transport, respectively.

In this section, we will discuss more details of the Boltzmann equation of the quarkonium transport and its ingredients, and the connections between the open and hidden heavy-flavor sector.

2.2.1 Boltzmann Equation Description of Quarkonium Transport

The master equation describes the transition between different quarkonium (or open $Q\bar{Q}$ pair) states. It encodes a detailed balance assuming the transition matrices to be symmetric under time reversal. In URHICs, the initially produced heavy-quark number is much larger than the quarkonium number, and the total heavy-quark number is approximately conserved afterwards because the thermal medium is not energetic enough to produce heavy-quark pairs $T_{QGP} \ll 2m_Q$ during the evolution. Thus the heavy quarks in the system can be treated as a source term for the quarkonium. One may integrate out the states of heavy quarks leaving only the master equation of quarkonium, see Sec. 2.1.3. Assuming a quarkonium distribution in coordinate and momentum space as a function of time, $f(\vec{x},\vec{p},t)$, this equation can be expressed as a Boltzmann equation (see Eq. (2.10)):

$$\begin{aligned}\frac{\mathrm{d}f(\vec{x},\vec{p},t)}{\mathrm{d}t} &= \frac{\partial f(\vec{x},\vec{p},t)}{\partial t} + \dot{\vec{x}}\cdot\nabla f(\vec{x},\vec{p},t) + \dot{\vec{p}}\cdot\nabla_p f(\vec{x},\vec{p},t) \\ &= \frac{\partial f(\vec{x},\vec{p},t)}{\partial t} + \frac{\vec{p}}{E(\vec{p})}\cdot\nabla f(\vec{x},\vec{p},t) + \vec{F}\cdot\nabla_p f(\vec{x},\vec{p},t) \\ &= -\alpha(\vec{x},\vec{p},t) f(\vec{x},\vec{p},t) + \beta(\vec{x},\vec{p},t),\end{aligned} \tag{2.21}$$

with $\nabla = (\frac{\partial}{\partial x}, \frac{\partial}{\partial y}, \frac{\partial}{\partial z})$ and $\nabla_p = (\frac{\partial}{\partial p_x}, \frac{\partial}{\partial p_y}, \frac{\partial}{\partial p_z})$. Besides the time derivative term $\frac{\partial f(\vec{x},\vec{p},t)}{\partial t}$, the $\frac{\vec{p}}{E(\vec{p})}\cdot\nabla f(\vec{x},\vec{p},t)$ term and $\vec{F}\cdot\nabla_p f(\vec{x},\vec{p},t)$ term are representing the diffusion and external drag force. The $\alpha(\vec{x},\vec{p},t)$ is the dissociation rate representing the loss of quarkonium states in the system. The $\beta(\vec{x},\vec{p},t)$ is the regeneration rate representing the gain of quarkonium during the medium evolution. The coordinate and time dependence in the rates are due to the fact that the rates are affected by the temperature distribution $T(\vec{x},t)$ of the background medium evolving with time. So the rates can also be expressed as $\alpha(\vec{p},T(\vec{x},t))$ and $\beta(\vec{p},T(\vec{x},t))$. We will revisit the details of α and β, and their relation in the upcoming sections. Due to the large masses of quarkonia, $m_\Psi \gg T_{QGP}$, the mean-field forces applied to quarkonia from medium are small, and we assume $\vec{F}=0$ for approximation. The equation can be simplified as

$$\frac{\partial f(\vec{x},\vec{p},t)}{\partial t}+\vec{v}\cdot\nabla f(\vec{x},\vec{p},t)=-\alpha(\vec{p},T(t))f(\vec{x},\vec{p},t)+\beta((\vec{p},T(t)), \tag{2.22}$$

with $\vec{v}=\frac{\vec{p}}{E(\vec{p})}$. The solution reads [70]:

$$\begin{aligned} f(\vec{x},\vec{p},t) &= f(\vec{x}-\vec{v}(t-t_0),\vec{p},t_0)e^{-\int_{t_0}^{t}\mathrm{d}t'\alpha(\vec{x}-\vec{v}(t-t'),\vec{p},t')} \\ &+ \int_{t_0}^{t}\mathrm{d}t'\beta(\vec{x}-\vec{v}(t-t'),\vec{p},t')e^{-\int_{t'}^{t}\mathrm{d}t''\alpha(\vec{x}-\vec{v}(t-t''),\vec{p},t'')}, \end{aligned} \tag{2.23}$$

where the $f(\vec{x}-\vec{v}(t-t_0),\vec{p},t_0)$ is the initial quarkonium distribution at initial time t_0. The shift terms "$\vec{v}(t_2-t_1)$" in coordinates space are due to the diffusion feature of the transport equation. The interpretation of the solution is that the primordial component (first term in Eq. (2.23)) receives a direct dissociation during the evolution, and the regenerated quarkonium (second term in Eq. (2.23)) has further dissociation from the time, t', of formation to the current time, t.

2.2.2 Relation between the α and β: Detailed Balance

The α and β are representing the rates of two opposite components in the Boltzmann equation: α the dissociation of quarkonium and β the regeneration of quarkonium. They are related via detailed balance of the two processes. There are two main mechanisms (taking charmonium as example, and we use Ψ=J/ψ, $\psi(2S)$,... to represent the different charmonium states here, see Sec. 2.2.4 and Sec. 2.2.5 for details), for the α [71, 72, 73, 47]:

(1) LO, gluo-dissociation: $g + \Psi \to c + \bar{c}$

(2) NLO, quasi-free: $i + \Psi \to i + c + \bar{c}$

where i is parton (gluon or light quark in medium). The detailed balance requires β to have two inverse processes:

(1) LO, gluo-dissociation: $c + \bar{c} \to g + \Psi$

(2) NLO, quasi-free: $i + c + \bar{c} \to i + \Psi$

In the following, we will start from a general expression of reaction rates, subsequently constructing the α and β, and prove the exact detailed balance relation between them. Generally, a reaction rate of the Ψ in vacuum can be expressed as:

$$\Gamma_0(\vec{p}) = \frac{1}{2E_\Psi} \sum_i \int \mathrm{d}\Pi_{\text{out}} \overline{|M_{\text{in}\to\text{out}}|^2}, \tag{2.24}$$

where we have a summation over all partons involved in the interaction, denoted by i. The phase space of out-states is

$$\mathrm{d}\Pi_{\text{out}} = (2\pi)^4 \delta^{(4)} \left(\sum_{\text{int}} p_{\text{int}} - \sum_{\text{out}} p_{\text{out}} \right) \prod_{\text{out}} \frac{\mathrm{d}^3 p_{\text{out}}}{(2\pi)^3 2E_{\text{out}}}. \tag{2.25}$$

The product of Lorentz invariant measure $\prod \frac{\mathrm{d}^3 p}{(2\pi)^3 2E}$ does not include the Ψ itself. In the medium, we have to take an average over all the incoming particles except for Ψ itself, so we have

$$\Gamma(\vec{p}, T) = \frac{1}{2E_\Psi} \sum_i \int \mathrm{d}\Pi_{\text{in}} \mathrm{d}\Pi_{\text{out}} \overline{|M_{\text{in}\to\text{out}}|^2} \prod_{\text{in}} f_{\text{in}}(p_{\text{in}}), \tag{2.26}$$

where the phase space of in-states is

$$\mathrm{d}\Pi_{\text{in}} = \prod_{\text{in}} \frac{\mathrm{d}^3 p_{\text{in}}}{(2\pi)^3 2E_{\text{in}}}. \tag{2.27}$$

The quantum statistical corrections to the rate need Bose enhancement/Fermi blocking factors which modify the rate further as:

$$\Gamma(\vec{p},T) = \frac{1}{2E_\Psi}\sum_i \int \mathrm{d}\Pi_{\text{in}}\mathrm{d}\Pi_{\text{out}}\overline{|M_{\text{in}\to\text{out}}|^2}\prod_{\text{in}} d_{\text{in}} f_{\text{in}}(p_{\text{in}})\prod_{\text{out}}(1\pm f_{\text{out}}(p_{\text{out}})), \tag{2.28}$$

with "+" for bosons and "−" for fermions. The out-state distribution f_{out} is either a Bose-Einstein distribution for bosons or Fermi-Dirac distribution for fermions to ensure the enhancement/blocking feature of the quantum correction. d_{in} is the degeneracy of the incoming particles. Since the charm quarks as in-states are from the bath of all charms in the medium, and production of charm is difficult through the medium evolution due to lack of energy from thermal medium ($2m_c \gg T_{QGP}$), their numbers are conserved. That said, if charm quarks are in-states (regeneration of Ψ, β rate), they need to have an overall normalization factor γ_c (called fugacity factor) to be determined by the charm number conservation. Since charm and anti-charm are produced in pairs, their fugacity factors are the same in QGP.

Following the general expression of rates in a quantum statistical medium, we can easily construct the rates α and β for NL and NLO.

(1) The LO α for the gluo-dissociation $g + \Psi \to c + \bar{c}$:

$$\begin{aligned}\alpha_{\text{LO}}(\vec{p},T) = {} & \frac{1}{2E_\Psi}\int \frac{\mathrm{d}^3 p_g}{(2\pi)^3 2E_g}\frac{\mathrm{d}^3 p_c}{(2\pi)^3 2E_c}\frac{\mathrm{d}^3 p_{\bar{c}}}{(2\pi)^3 2E_{\bar{c}}}\overline{|M_{g\Psi\to c\bar{c}}|^2} \\ & \times (2\pi)^4\delta^{(4)}(p + p_g - p_c - p_{\bar{c}})(1 - f_c(p_c))(1 - f_{\bar{c}}(p_{\bar{c}}))d_g f_g(p_g),\end{aligned} \tag{2.29}$$

where f_c, $f_{\bar{c}}$ follow Fermi-Dirac distribution and f_g follows Bose-Einstein distribution.

(2) The LO β for the inverse gluo-dissociation $c + \bar{c} \to g + \Psi$:

$$\beta_{\mathrm{LO}}(\vec{p}, T) = \frac{1}{2E_\Psi} \int \frac{\mathrm{d}^3 p_g}{(2\pi)^3 2E_g} \frac{\mathrm{d}^3 p_c}{(2\pi)^3 2E_c} \frac{\mathrm{d}^3 p_{\bar{c}}}{(2\pi)^3 2E_{\bar{c}}} \overline{|M_{c\bar{c}\to g\Psi}|^2}$$
$$\times (2\pi)^4 \delta^{(4)} \left(p_c + p_{\bar{c}} - p - p_g\right) (1 + f_g(p_i)) d_c \gamma_c f_c(p_c) d_{\bar{c}} \gamma_c f_{\bar{c}}(p_{\bar{c}}). \tag{2.30}$$

(3) The NLO α for the quasi-free $i + \Psi \to i + c + \bar{c}$:

$$\alpha_{\mathrm{NLO}}(\vec{p}, T) = \frac{1}{2E_\Psi} \sum_i \int \frac{\mathrm{d}^3 p_i}{(2\pi)^3 2E_i} \frac{\mathrm{d}^3 \tilde{p}_i}{(2\pi)^3 2\tilde{E}_i} \frac{\mathrm{d}^3 p_c}{(2\pi)^3 2E_c} \frac{\mathrm{d}^3 p_{\bar{c}}}{(2\pi)^3 2E_{\bar{c}}} \overline{|M_{i\Psi\to\tilde{i}c\bar{c}}|^2}$$
$$\times (2\pi)^4 \delta^{(4)} \left(p + p_i - \tilde{p}_i - p_c - p_{\bar{c}}\right) (1 \pm f_i(\tilde{p}_i))(1 - f_c(p_c))(1 - f_{\bar{c}}(p_{\bar{c}})) d_i f_i(p_i), \tag{2.31}$$

where $\tilde{i}$ represents the out-going parton, d_i is the parton degeneracy. f_c, $f_{\bar{c}}$ and f_i are in-medium charm and parton distributions. The $1 \pm f$ is a Bose enhancement/Pauli blocking factor.

(4) The NLO β for the inverse quasi-free $i + c + \bar{c} \to i + \Psi$:

$$\beta_{\mathrm{NLO}}(\vec{p}, T) = \frac{1}{2E_\Psi} \sum_i \int \frac{\mathrm{d}^3 p_i}{(2\pi)^3 2E_i} \frac{\mathrm{d}^3 \tilde{p}_i}{(2\pi)^3 2\tilde{E}_i} \frac{\mathrm{d}^3 p_c}{(2\pi)^3 2E_c} \frac{\mathrm{d}^3 p_{\bar{c}}}{(2\pi)^3 2E_{\bar{c}}} \overline{|M_{\tilde{i}c\bar{c}\to i\Psi}|^2}$$
$$\times (2\pi)^4 \delta^{(4)} \left(\tilde{p}_i + p_c + p_{\bar{c}} - p - p_i\right) (1 \pm f_i(p_i)) d_{\tilde{i}} f_i(\tilde{p}_i) d_c \gamma_c f_c(p_c) d_{\bar{c}} \gamma_c f_{\bar{c}}(p_{\bar{c}}). \tag{2.32}$$

We will show that for both LO and NLO, in the limit of thermal distribution, the simple relation

$$\beta = \gamma_c^2 d_\Psi e^{-E_\Psi} \alpha \tag{2.33}$$

holds.

The detailed balance of the amplitudes implies

$$\sum |M_{g\Psi\to c\bar{c}}|^2 \;=\; \sum |M_{c\bar{c}\to g\Psi}|^2 \tag{2.34}$$

$$\sum |M_{i\Psi\to\tilde{i}c\bar{c}}|^2, \;=\; \sum |M_{\tilde{i}c\bar{c}\to i\Psi}|^2, \tag{2.35}$$

where we have summation over all in and out-states. The average amplitude which appears in the rate formulas, involves an average over the initial states so that

$$\overline{|M_{\text{in}}\to \text{out}|^2} = \frac{\sum |M_{\text{in}}\to \text{out}|^2}{\prod d_{\text{in}}}, \tag{2.36}$$

and we thus have

$$d_g d_\Psi \overline{|M_{g\Psi\to c\bar{c}}|^2} \;=\; d_c d_{\bar{c}} \overline{|M_{c\bar{c}\to g\Psi}|^2} \tag{2.37}$$

$$d_i d_\Psi \overline{|M_{i\Psi\to\tilde{i}c\bar{c}}|^2}, \;=\; d_{\tilde{i}} d_c d_{\bar{c}} \overline{|M_{\tilde{i}c\bar{c}\to i\Psi}|^2}. \tag{2.38}$$

Comparing the α_{LO} and β_{LO} (α_{NLO} and β_{NLO}), we find that their measure and four-momentum conservation are of the same form. Absorbing the degeneracy factors into the amplitude square, we only need to prove the relations between thermal distributions and the Bose/Fermi factors. In other words, we have

$$\alpha_{\text{LO}}(\vec{p},T) = \int \mathrm{d}\Pi_1 d_g \overline{|M_{g\Psi\to c\bar{c}}|^2}(1-f_c(p_c))(1-f_{\bar{c}}(p_{\bar{c}}))f_g(p_g), \tag{2.39}$$

$$\beta_{\text{LO}}(\vec{p},T) = \int \mathrm{d}\Pi_1 d_c d_{\bar{c}} \overline{|M_{c\bar{c}\to g\Psi}|^2}(1+f_g(p_i))\gamma_c f_c(p_c)\gamma_c f_{\bar{c}}(p_{\bar{c}}), \tag{2.40}$$

$$\alpha_{\text{NLO}}(\vec{p},T) = \sum_i \int \mathrm{d}\Pi_2 d_i \overline{|M_{i\Psi\to\tilde{i}c\bar{c}}|^2}(1\pm f_i(\tilde{p}_i))(1-f_c(p_c))(1-f_{\bar{c}}(p_{\bar{c}}))f_i(p_i), \tag{2.41}$$

$$\beta_{\text{NLO}}(\vec{p},T) = \sum_i \int \mathrm{d}\Pi_2 d_{\tilde{i}} d_c d_{\bar{c}} \overline{|M_{\tilde{i}c\bar{c}\to i\Psi}|^2}(1\pm f_i(p_i))f_i(\tilde{p}_i)\gamma_c f_c(p_c)\gamma_c f_{\bar{c}}(p_{\bar{c}}), \tag{2.42}$$

with

$$\mathrm{d}\Pi_1 = \frac{1}{2E_\Psi}\frac{\mathrm{d}^3p_g}{(2\pi)^3 2E_g}\frac{\mathrm{d}^3p_c}{(2\pi)^3 2E_c}\frac{\mathrm{d}^3p_{\bar{c}}}{(2\pi)^3 2E_{\bar{c}}} \times (2\pi)^4\delta^{(4)}\left(p+p_g-p_c-p_{\bar{c}}\right), \tag{2.43}$$

$$\mathrm{d}\Pi_2 = \frac{1}{2E_\Psi}\frac{\mathrm{d}^3p_i}{(2\pi)^3 2E_i}\frac{\mathrm{d}^3\tilde{p}_i}{(2\pi)^3 2\tilde{E}_i}\frac{\mathrm{d}^3p_c}{(2\pi)^3 2E_c}\frac{\mathrm{d}^3p_{\bar{c}}}{(2\pi)^3 2E_{\bar{c}}}(2\pi)^4\delta^{(4)}\left(p+p_i-\tilde{p}_i-p_c-p_{\bar{c}}\right). \tag{2.44}$$

Simplify the notation by defining $\mathrm{d}X_1$ and $\mathrm{d}X_2$, so that $\mathrm{d}X_1 d_\Psi = \mathrm{d}\Pi_1 d_c d_{\bar{c}}\overline{|M_{c\bar{c}\to g\Psi}|^2}$ and $\mathrm{d}X_2 d_\Psi = \mathrm{d}\Pi_2 d_{\tilde{i}} d_c d_{\bar{c}}\overline{|M_{\tilde{i}c\bar{c}\to i\Psi}|^2}$. Denoting $x_i = e^{\frac{E_i}{T}}$ for particle i, we have a Bose distribution for a gluon, as $f^B = \frac{1}{x_g-1}$ and a Fermi distribution for a quark, as $f^F = \frac{1}{x_q+1}$. We thus have for LO:

$$\begin{aligned}
\alpha_{\mathrm{LO}} &= \int \mathrm{d}X_1\left(1-\frac{1}{x_c+1}\right)\left(1-\frac{1}{x_{\bar{c}}+1}\right)\frac{1}{x_g-1} \\
&= \int \mathrm{d}X_1\frac{x_c x_{\bar{c}}}{(x_c+1)(x_{\bar{c}}+1)(x_g-1)}, \qquad (2.45)\\
\beta_{\mathrm{LO}} &= \int \mathrm{d}X_1 d_\Psi\left(1+\frac{1}{x_g-1}\right)\frac{\gamma_c}{x_c+1}\frac{\gamma_c}{x_{\bar{c}}+1} \\
&= \int \mathrm{d}X_1\frac{\gamma_c^2 d_\Psi x_g}{(x_c+1)(x_{\bar{c}}+1)(x_g-1)}. \qquad (2.46)
\end{aligned}$$

Using the energy conservation $E_\Psi + E_g = E_c + E_{\bar{c}}$, we immediately have $x_\Psi x_g = x_c x_{\bar{c}}$, so that $\beta = \gamma_c^2 d_\Psi / x_\Psi \alpha = \gamma_c^2 d_\Psi e^{-\frac{E_\Psi}{T}}\alpha$. Similarly, for NLO:

$$\begin{aligned}
\alpha_{\mathrm{NLO}} &= \sum_i \int \mathrm{d}X_2\left(1\pm\frac{1}{x_{\tilde{i}}\mp 1}\right)\left(1-\frac{1}{x_c+1}\right)\left(1-\frac{1}{x_{\bar{c}}+1}\right)\frac{1}{x_i\mp 1} \\
&= \sum_i \int \mathrm{d}X_2\frac{x_{\tilde{i}} x_c x_{\bar{c}}}{(x_c+1)(x_{\bar{c}}+1)(x_i\mp 1)(x_{\tilde{i}}\mp 1)}, \qquad (2.47)\\
\beta_{\mathrm{NLO}} &= \sum_i \int \mathrm{d}X_2 d_\Psi\left(1\pm\frac{1}{x_i\mp 1}\right)\frac{1}{x_{\tilde{i}}\mp 1}\frac{\gamma_c}{x_c+1}\frac{\gamma_c}{x_{\bar{c}}+1} \\
&= \sum_i \int \mathrm{d}X_2\frac{\gamma_c^2 d_\Psi x_i}{(x_c+1)(x_{\bar{c}}+1)(x_i\mp 1)(x_{\tilde{i}}\mp 1)}. \qquad (2.48)
\end{aligned}$$

Using the energy conservation $E_\Psi + E_i = E_c + E_{\bar{c}} + E_{\tilde{i}}$, we have $x_\Psi x_i = x_c x_{\bar{c}} x_{\tilde{i}}$, so that $\beta = \gamma_c^2 d_\Psi / x_\Psi \alpha = \gamma_c^2 d_\Psi e^{-\frac{E_\Psi}{T}} \alpha$.

This relation is more general than the current level of approximation, and it can be extended to higher order contributions. The relation can be understood as follows: once the Ψ state reaches thermal equilibrium, the collisional term in the Boltzmann equation vanishes and there will be no more time evolution. The equilibrium limit of the Boltzmann equation is

$$f^{\mathrm{eq}}(\vec{p}, T) = \frac{\beta(\vec{p}, T)}{\alpha(\vec{p}, T)} = \gamma_c^2 d_\Psi e^{-\frac{E_\Psi}{T}}. \tag{2.49}$$

In a medium with non-thermalized partons, or heavy quarks, the equilibrium limit will be modified. However, this relation is very useful when conducting numerical calculations since the β_{NLO} is numerically intensive. The number of integrals look the same for α and β, but once we neglect the Bose enhancement/Fermi blocking factors, some integrals with the amplitude square can be simplified to a cross section, except for the integrals with distributions f. For α_{NLO}, there is only one with parton f_i, and for β_{NLO}, there are three: f_i, f_c and $f_{\bar{c}}$.

2.2.3 Kinetic Rate Equation

Utilizing detailed balance relation Eq. (2.49), the Boltzmann equation can be simplified to

$$\frac{\partial f(\vec{x}, \vec{p}, t)}{\partial t} + \vec{v} \cdot \nabla f(\vec{x}, \vec{p}, t) = -\alpha(\vec{p}, T(t)) \left(f(\vec{x}, \vec{p}, t) - f^{\mathrm{eq}}(\vec{p}, T(t)) \right). \tag{2.50}$$

With the differential form of the quarkonium distribution $f(\vec{x},\vec{p},t)=\frac{\mathrm{d}^6N}{\mathrm{d}^3x\mathrm{d}^3p}$, an integration over the phase space gives the left hand side of Eq. (2.50)

$$\begin{aligned}
& \int \mathrm{d}^3p \int_V \mathrm{d}^3x \left(\frac{\partial f(\vec{x},\vec{p},t)}{\partial t} + \vec{v}\cdot\nabla f(\vec{x},\vec{p},t)\right) \\
= \ & \frac{\partial N}{\partial t} + \int \mathrm{d}^3p \oint_S \left(\vec{v}\cdot \mathrm{d}\vec{S} f(\vec{x},\vec{p},t)\right) = \frac{\mathrm{d}N}{\mathrm{d}t}. \qquad (2.51)
\end{aligned}$$

Using an approximation for the right hand side,

$$\int \mathrm{d}^3p \int_V \mathrm{d}^3x\alpha(\vec{p},T(t))f(\vec{x},\vec{p},t) \approx \Gamma(T(t))N(t), \qquad (2.52)$$

$$\int \mathrm{d}^3p \int_V \mathrm{d}^3x\alpha(\vec{p},T(t))f^{\mathrm{eq}}(\vec{x},\vec{p},t) \approx \Gamma(T(t))N^{eq}(T(t)), \qquad (2.53)$$

these two terms give us a kinetic rate equation

$$\frac{\mathrm{d}N(t)}{\mathrm{d}t} = -\Gamma(T(t))\left(N(t) - N^{\mathrm{eq}}(T(t))\right), \qquad (2.54)$$

where the product of the reaction rate and the equilibrium limit $\Gamma(T(t))N^{\mathrm{eq}}(T(t))$ gives the "regeneration rate" (β) , representing how fast the recombination processes are. Notice that Eq. (2.10) is a more general form of rate equation than the current Eq. (2.54).

As we discussed, the detailed balance relation and the rate equation Eq. (2.54) are valid when we have thermalized charm quarks in the gain term. At the early stage of the fireball evolution, the charm quarks from hard production do not easily form quarkonium through regeneration processes since they are far from thermal with generally harder momentum distributions. However, we can apply a correction to the gain term of the rate equation by employing a relaxation time factor [74] to account for non-thermalized charm quarks. In order to do it, we can estimate how charm quarks evolve with a simple relaxation time approach

$$\frac{\mathrm{d}N^{\mathrm{limit}}(t)}{\mathrm{d}t} = -\frac{1}{\tau_c(T(t))}\left(N^{\mathrm{limit}}(t) - N^{\mathrm{eq}}(T(t))\right), \tag{2.55}$$

where $N^{\mathrm{limit}}(t)$ is a "realistic limit" of the rate equation, which is not in equilibrium. Notice the difference between the rate equation Eq. (2.54) and the relaxation time equation Eq. (2.55) that τ_c is the relaxation time for charm quarks in the medium. According to T-matrix calculation and Langevin simulation, the relaxation time for charm quarks is $\tau_c \simeq$3-6 fm, and a factor of m_b/m_c longer for heavier bottom quarks, $\tau_b \simeq$10-15 fm [75]. The relaxation time equation can be understood as following: at the very beginning of the fireball evolution, all charm quarks are directly from the hard production and no diffusion is applied to them. The high speed charm quarks are not able to recombine with high speed anti-charm quarks. This non-thermalization of charm quarks weakens the recombination, reduces the "regeneration rate" close to zero at the beginning, so that $\Gamma(T(t))N^{\mathrm{limit}}(0) = 0$. This requires us to set the initial condition to be $N^{\mathrm{limit}}(0) \to 0$. The solution of the relaxation time equation can be factorized into two parts

$$N^{\mathrm{limit}}(T(t)) = N^{\mathrm{eq}}(T(t))\mathcal{R}(t) = N^{\mathrm{eq}}(T(t))\left[1 - \exp\left(-\int_0^t \frac{\mathrm{d}t'}{\tau_c(T(t'))}\right)\right]. \tag{2.56}$$

We can rewrite the modified rate equation as

$$\frac{\mathrm{d}N(t)}{\mathrm{d}t} = -\Gamma(T(t))\left(N(t) - N^{\mathrm{eq}}(T(t))\mathcal{R}(t)\right), \tag{2.57}$$

where

$$\mathcal{R}(t) = 1 - \exp\left(-\int_0^t \frac{\mathrm{d}t'}{\tau_c(T(t'))}\right), \tag{2.58}$$

is the relaxation time factor. The $\mathcal{R}(t)$ curve in Fig. 2.1 shows that the relaxation time factor is $\mathcal{R}(0) = 0$ at the beginning, and gradually increases to $\mathcal{R}(t) = 1$ for a large t, due

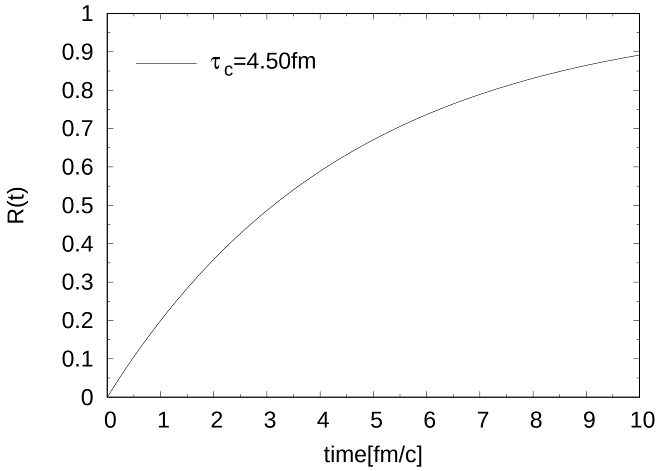

Figure 2.1: Schematic view of $\mathcal{R}(t)$ for charm quark with constant τ_c=4.5 fm.

to the fact that charm-quark spectra keep softening during the thermal diffusion, and keep enhancing the regeneration rate $\Gamma(T(t))N^{\mathrm{eq}}(T(t))\mathcal{R}(t)$.

A more realistic treatment of the relaxation time modification requires a Langevin simulation of charm quarks in the fireball.

2.2.4 Quasi-Free Process

The NLO process is a $2 \to 3$ process and can be complicated to calculate exactly. We employ a $2 \to 2$ reduction, namely the “quasi-free approximation", using a pQCD calculated amplitude $\overline{|M_{ic\to\tilde{i}c}|^2}$ to simplify the calculation of the amplitude $\overline{|M_{i\Psi\to\tilde{i}c\bar{c}}|^2}$. The idea is to treat either the charm quark or the anti-charm quark in Ψ as a “free state", while the other one scatters off the incoming parton from the medium. See Fig. 2.2 for an illustration.

In the $2 \to 3$ process $i + \Psi \to \tilde{i} + c + \bar{c}$, we have five 4-momenta $p_i, p_\Psi, p_{\tilde{i}}, p_c, p_{\bar{c}}$. The quasi-free process exposes the single quarks in Ψ and we should have six 4-momenta $p_i, p_{c'}, p_{\bar{c}'}, p_{\tilde{i}}, p_c, p_{\bar{c}}$ instead, where the c' and $\bar{c}'$ with prime sign are the charm and anti-charm quarks in the incoming states. Suppose the anti-charm is the “free quark”, we thus

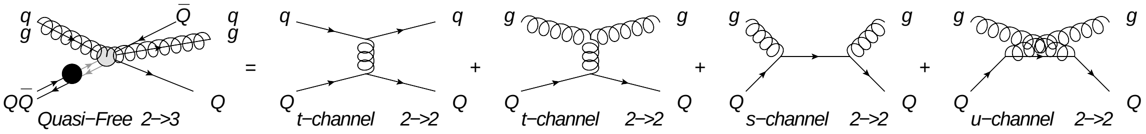

Figure 2.2: Illustration of the $2 \to 3$ processes to $2 \to 2$ reduction via the quasifree approach. The quasifree process includes 4 diagrams.

have $p_{\bar{c}} = p_{\bar{c}'}$ and also $m_{\bar{c}} = m_{\bar{c}'} = m_c$, since the out-going anti-charm is also a free state. The binding of Ψ state requires

$$m_{c'} + m_{\bar{c}'} = m_\Psi = m_c + m_{\bar{c}} - E_b, \tag{2.59}$$

thus

$$m_{c'} = m_c - E_b = m_\Psi - m_c. \tag{2.60}$$

Furthermore, the charm c' and anti-charm $\bar{c}'$ in the Ψ must have the same velocity, thus

$$\frac{\vec{p}_{c'}}{\sqrt{\vec{p}_{c'}^{\,2} + (m_\Psi - m_c)^2}} = \vec{v}_{c'} = \vec{v}_{\bar{c}'} = \frac{\vec{p}_{\bar{c}'}}{\sqrt{\vec{p}_{\bar{c}'}^{\,2} + m_c^2}}, \tag{2.61}$$

together with the fact that $\vec{p}_{c'} + \vec{p}_{\bar{c}'} = \vec{p}_\Psi$, gives the expression of 3-momentum:

$$\vec{p}_{c'} = \frac{m_\Psi - m_c}{m_\Psi} \vec{p}_\Psi, \tag{2.62}$$

$$\vec{p}_{\bar{c}'} = \frac{m_c}{m_\Psi} \vec{p}_\Psi. \tag{2.63}$$

It can be easily verified that the 4-momentum case also holds for the above relation:

$$p_{c'} = \frac{m_\Psi - m_c}{m_\Psi} p_\Psi, \tag{2.64}$$

$$p_{\bar{c}'} = \frac{m_c}{m_\Psi} p_\Psi. \tag{2.65}$$

The momentum conservation gives

$$\begin{aligned}
&\delta^{(4)}(p_\Psi + p_i - \tilde{p}_i - p_c - p_{\bar{c}}) \\
&= \delta^{(4)}\left(\frac{m_\Psi - m_c}{m_\Psi} p_\Psi + \frac{m_c}{m_\Psi} p_\Psi + p_i - \tilde{p}_i - p_c - p_{\bar{c}}\right) \\
&= \delta^{(4)}(p_{c'} + p_{\bar{c}'} + p_i - \tilde{p}_i - p_c - p_{\bar{c}}) \\
&= \delta^{(4)}(p_{c'} + p_i - \tilde{p}_i - p_c) \\
&= \delta^{(4)}\left(\frac{m_\Psi - m_c}{m_\Psi} p_\Psi + p_i - \tilde{p}_i - p_c\right).
\end{aligned} \tag{2.66}$$

If we reduce the $2 \to 3$ process to the $2 \to 2$ process, the calculation should eliminate one momentum integral over the "free quark" $\bar{c}$. We actually have

$$\int \frac{d^3 p_{\bar{c}}}{(2\pi)^3 2E_{\bar{c}}} (2\pi)^3 2E_{\bar{c}} \delta^{(3)}\left(\vec{p}_{\bar{c}} - \frac{m_c}{m_\Psi} \vec{p}_\Psi\right) = 1, \tag{2.67}$$

and thus we need to employ an over all factor $(2\pi)^3 2E_{\bar{c}} \delta^{(3)}\left(\vec{p}_{\bar{c}} - \frac{m_c}{m_\Psi}\vec{p}_\Psi\right)$ to reduce the "free quark" integral without changing the final results. In this sense, the $2 \to 3$ amplitude square should be replaced by

$$\begin{aligned}
&\overline{|M_{i\Psi \to \tilde{i}c\bar{c}}(p_i, p_\Psi, \tilde{p}_i, p_c, p_{\bar{c}})|^2} \\
&= 2\overline{\left|M_{ic \to \tilde{i}c}\left(p_i, \frac{m_\Psi - m_c}{m_\Psi} p_\Psi, \tilde{p}_i, p_c\right)\right|^2} (2\pi)^3 2E_{\bar{c}} \delta^{(3)}\left(\vec{p}_{\bar{c}} - \frac{m_c}{m_\Psi}\vec{p}_\Psi\right).
\end{aligned} \tag{2.68}$$

In principle there is no difference between choosing the charm or anti-charm quark to be the "free quark", thus it requires an overall factor of 2 to account for the dissociation of Ψ.

The quasifree α rate expressed with the effective 2→2 amplitude is

$$\begin{aligned}\alpha_{\mathrm{NLO}}(\vec{p},T) = &\frac{1}{E_\Psi}\sum_i \int \frac{\mathrm{d}^3 p_i}{(2\pi)^3 2E_i}\frac{\mathrm{d}^3 \tilde{p}_i}{(2\pi)^3 2\tilde{E}_i}\frac{\mathrm{d}^3 p_c}{(2\pi)^3 2E_c} \\ &\times \overline{\left| M_{ic\to\tilde{i}c}\left(p_i, \frac{m_\Psi - m_c}{m_\Psi}p, \tilde{p}_i, p_c\right)\right|^2} \\ &\times (2\pi)^4 \delta^{(4)}\left(\frac{m_\Psi - m_c}{m_\Psi}p + p_i - \tilde{p}_i - p_c\right) d_i f_i(p_i), \end{aligned} \tag{2.69}$$

where we neglect the quantum correction due to Bose-enhancement and Fermi-block factors since their effects are quite small[*]. Notice that the out-states' momenta $\tilde{p}_i$ and p_c are only involved in the scattering amplitude and energy-momentum conservation, therefore we can define a Lorentz invariant cross section

$$\begin{aligned}\sigma_{\mathrm{i}}(\vec{p},\vec{p}_i) &= \frac{1}{4\sqrt{(p\cdot p_i)^2 - m_\Psi^2 m_i^2}}\int \mathrm{d}\Pi_{\mathrm{out}}\overline{|M|^2} \\ &= \frac{1}{4E_\Psi E_i v_{\mathrm{rel}}}\sum_i \int \frac{\mathrm{d}^3 \tilde{p}_i}{(2\pi)^3 2\tilde{E}_i}\frac{\mathrm{d}^3 p_c}{(2\pi)^3 2E_c} \\ &\quad\times \overline{\left| M_{ic\to\tilde{i}c}\left(p_i, \frac{m_\Psi - m_c}{m_\Psi}p, \tilde{p}_i, p_c\right)\right|^2} \\ &\quad\times (2\pi)^4 \delta^{(4)}\left(\frac{m_\Psi - m_c}{m_\Psi}p + p_i - \tilde{p}_i - p_c\right), \end{aligned} \tag{2.70}$$

where

$$v_{\mathrm{rel}} = \frac{\sqrt{(p\cdot p_i)^2 - m_\Psi^2 m_i^2}}{E_\Psi E_i} \tag{2.71}$$

is the relative velocity between Ψ and parton i. The cross section in NLO can be calculated

---

[*] It nearly cancels between Bose-enhancement for g and Fermi-block for q, $\bar{q}$

analytically to reduce the numerical efforts. We can rewrite the α rate as

$$\alpha_{\mathrm{NLO}}(\vec{p},T) = 2\sum_i \int \frac{\mathrm{d}^3p_i}{(2\pi)^3}\sigma(\vec{p},\vec{p_i})v_{\mathrm{rel}}d_i f_i(p_i). \tag{2.72}$$

Notice that for non-thermalized charm quark distributions, the simple and general relation between α and β does not hold and we need to calculate β explicitly. The quasifree β rate with 2→2 amplitude is

$$\begin{aligned}
\beta_{\mathrm{NLO}}(\vec{p},T) &= \frac{1}{E_\Psi}\sum_i \int \frac{\mathrm{d}^3p_i}{(2\pi)^3 2E_i}\frac{\mathrm{d}^3\tilde{p}_i}{(2\pi)^3 2\tilde{E}_i}\frac{\mathrm{d}^3p_c}{(2\pi)^3 2E_c} \\
&\times \overline{\left|M_{\tilde{i}c\to ic}\left(p_i, \frac{m_\Psi - m_c}{m_\Psi}p, \tilde{p}_i, p_c\right)\right|^2} \\
&\times (2\pi)^4\delta^{(4)}\left(\frac{m_\Psi - m_c}{m_\Psi}p + p_i - \tilde{p}_i - p_c\right) d_{\tilde{i}} f_i(\tilde{p}_i) d_c\gamma_c f_c(p_c) d_{\bar{c}}\gamma_c f_{\bar{c}}\left(\frac{m_c}{m_\Psi}p\right). \\
&= \frac{1}{E_\Psi}\sum_i \int \frac{d^3p_i}{(2\pi)^3 2E_i}\frac{d^3p_c}{(2\pi)^3 2E_c}\frac{2\pi}{2\tilde{E}_i}\overline{\left|M_{\tilde{i}c\to ic}\left(p_i, \frac{m_\Psi - m_c}{m_\Psi}p, \tilde{p}_i, p_c\right)\right|^2} \\
&\times \delta\left(\frac{m_\Psi - m_c}{m_\Psi}E_\Psi + E_i - \tilde{E}_i - E_c\right) d_{\tilde{i}} f_i(\tilde{p}_i) d_c\gamma_c f_c(p_c) d_{\bar{c}}\gamma_c f_{\bar{c}}\left(\frac{m_c}{m_\Psi}p\right),
\end{aligned} \tag{2.73}$$

where $\tilde{\vec{p}_i} = \frac{m_\Psi - m_c}{m_\Psi}\vec{p}_\Psi + \vec{p}_i - \vec{p}_c$. Considering that the cross section σ can be analytically calculated, we see that the β rate is numerically more intensive than the α rate in two aspects: (1) β has more integrals. (2) β requires the solution to a complicated algebraic equation of the energy conservation, which has two roots. Both roots need to be included to correctly calculate β.

2.2.5 Gluo-Dissociation Process

The gluo-dissociation process g+Ψ→c+$\bar{c}$ is another important inelastic scattering of charmonium in the QGP. Considering a color-singlet charmonium state dissociated by a thermal in-medium gluon into a color-octet state, the gluo-dissociation can be realized by a color singlet-octet transition. It was initially derived by Bhanot and Peskin [71, 72]

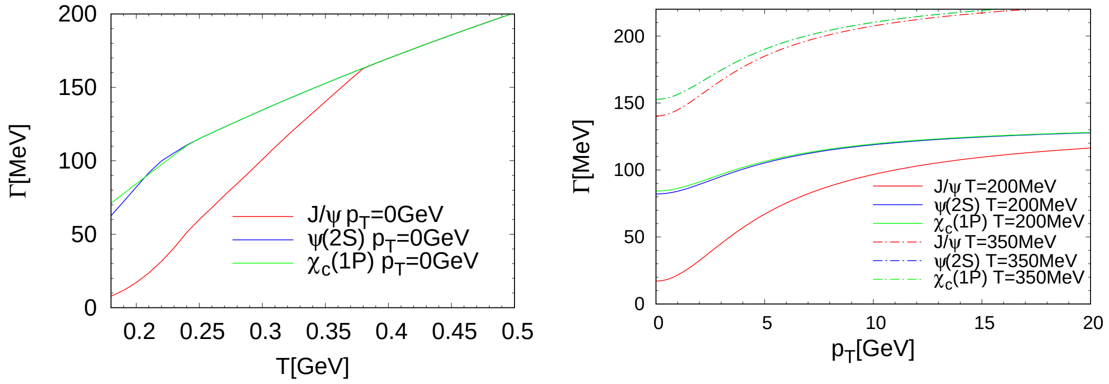

Figure 2.3: Left (right) panel: The temperature (momentum) dependent quasifree rate Γ=$\alpha(\vec{p},T)$ for Jψ, $\psi(2S)$ and $\chi_c(1P)$.

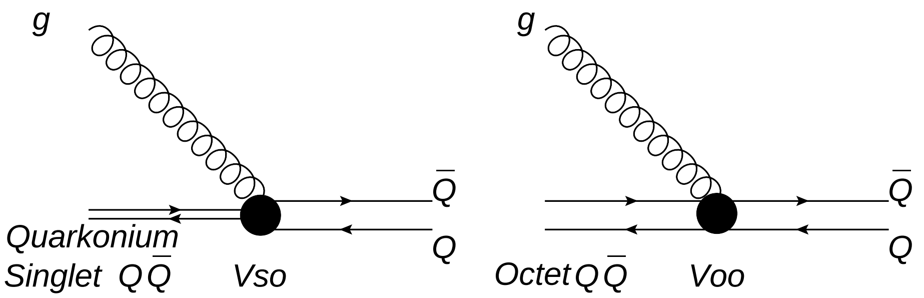

Figure 2.4: Effective vertices of singlet-octet transition (left) and octet-octet transition (right). The singlet-octet transition is responsible for the leading order gluo-dissociation process. The Q and $\bar{Q}$ represents heavy quark c,b and anti-heavy quark $\bar{c}$, $\bar{b}$ respectively.

with an operator-product expansion technique, and later developed in pNRQCD effective theory [76].

A multi-pole expansion of the nonrelativistic effective QCD Hamiltonian enables effective vertices of singlet-octet transition and octet-octet transition of a quark-antiquark pair. The leading order (LO) gluo-dissociation only involves the singlet-octet transition, see Fig. 2.4.

The original LO gluo-dissociation cross section was derived assuming a Coulombic wave function of quarkonium and is later widely used in the literature. The LO gluo-dissociation width with wave function generated by realistic Cornell type potential was investigated in [77] and later extended to NLO [78].

Due to lack of phase space, it turns out that the LO gluo-dissociation is much less efficient than the quasifree process [47] in high temperature QGP medium. The NLO gluo-dissociation suggests an increase of the width [78] with temperature.

Indeed, there is a feature of the gluo-dissociation which fails at high-temperature when quarkonium state becomes loosely bound and gluon becomes more energetic, due to the fact the dipole approximation in the effective QCD Hamiltonian fails when gluon energy E_g is larger than the quarkonium binding energy E_b.

The gluo-dissociation might play a role in the bottomonium dissociation due to its large binding energies.

2.2.6 Hadronic Dissociation Process

2.2.6.1 SU(4) Meson-Exchange Model

The hadronic dissociation for the charmonium can be modeled by a flavor-SU(4) meson-exchange model [79, 80] which includes the relevant light mesons (π, η, ρ, ω, ...), strange mesons (K family) coupled to J/ψ and charmed mesons (D family), with a smallest possible symmetry group. The model has an effective Lagrangian at the hadronic level

$$\mathcal{L} = \mathrm{Tr}\left(\partial_\mu P^\dagger \partial^\mu P\right) - \frac{1}{2}\mathrm{Tr}\left(\partial_{\mu\nu} F^\dagger \partial^{\mu\nu} F\right) \tag{2.74}$$

$$+i\frac{g}{2}\mathrm{Tr}\left(\partial^\mu P[P^\dagger, V_\mu^\dagger] + \partial^\mu P^\dagger [P, V_\mu]\right) - \frac{g^2}{4}\mathrm{Tr}\left([P^\dagger, V_\mu^\dagger][P, V^\mu]\right) \tag{2.75}$$

$$+i\frac{g}{2}\mathrm{Tr}\left(\partial^\mu V^\nu [V_\mu^\dagger, V_\nu^\dagger] + \partial_\mu V_\nu^\dagger [V^\mu, V^\mu])\right) + \frac{g^2}{8}\mathrm{Tr}\left([V^\mu, V^\nu][V_\mu^\dagger, V_\nu^\dagger]\right), \tag{2.76}$$

with $F_{\mu\nu} = \partial_\mu V_\nu - \partial_\nu V_\mu$. The pseudo-scalar meson matrix reads

$$P = \frac{1}{\sqrt{2}} \begin{pmatrix} \frac{\pi^0}{\sqrt{2}} + \frac{\eta}{\sqrt{6}} + \frac{\eta_c}{\sqrt{12}} & \pi^+ & K^+ & \bar{D}^0 \\ \pi^- & -\frac{\pi^0}{\sqrt{2}} + \frac{\eta}{\sqrt{6}} + \frac{\eta_c}{\sqrt{12}} & K^0 & D^- \\ K^- & \bar{K}^0 & -\sqrt{\frac{2}{3}}\eta + \frac{\eta_c}{\sqrt{12}} & D_s^- \\ D^0 & D^+ & D_s^+ & -\frac{3\eta_c}{\sqrt{12}} \end{pmatrix} \tag{2.77}$$

and the vector meson matrix reads

$$V_\mu = \frac{1}{\sqrt{2}} \begin{pmatrix} \frac{\rho^0}{\sqrt{2}} + \frac{\omega'}{\sqrt{6}} + \frac{J/\psi}{\sqrt{12}} & \rho^+ & K^{*+} & \bar{D}^{*0} \\ \rho^- & -\frac{\rho^0}{\sqrt{2}} + \frac{\omega'}{\sqrt{6}} + \frac{J/\psi}{\sqrt{12}} & K^{*0} & D^{*-} \\ K^{*-} & \bar{K}^{*0} & -\sqrt{\frac{2}{3}}\omega' + \frac{J/\psi}{\sqrt{12}} & D_s^{*-} \\ D^{*0} & D^{*+} & D_s^{*+} & -\frac{3J/\psi}{\sqrt{12}} \end{pmatrix}_\mu \tag{2.78}$$

The hadronic cross section for the excited state $\psi(2S)$ is scaled with the ratio of $\psi(2S)$ over J/ψ radius square $\sigma^{had}_{\psi(2S)}=\left(\frac{r_{\psi(2S)}}{r_{J/\psi}}\right)^2 \sigma^{had}_{J/\psi}$.

Dissociation rates of charmonia in hadronic matter are usually considered to be much smaller than in the QGP (see, $e.g.$, the discussion in Ref. [42]). However, for the $\psi(2S)$ this is not so obvious, since the proximity of its mass to the $D\bar{D}$ threshold provides a large phase space for break-up reactions. In the following, we revisit hadronic reactions rates for J/ψ and $\psi(2S)$ mesons based on effective meson Lagrangians summarized above.

2.2.6.2 Updates on Hadronic Dissociation Rates

Our starting point is the above hadronic model for the processes $J/\psi + \rho \to D + \bar{D}, D^\star + \bar{D}^\star$ (exothermic for $m_{J/\psi} + m_\rho > m_D + m_{\bar{D}}$ and endothermic for $m_{J/\psi} + m_\rho < m_{D^\star} + m_{\bar{D}^\star}$) and $J/\psi + \pi \to D^\star + \bar{D}, D + \bar{D}^\star$ (endothermic). For those reactions, the J/ψ dissociation rate at T=170 MeV amounts to 1-2 MeV, corresponding to a lifetime of 100-200 fm/c. Even with the typical uncertainties (factor ~2-3) associated with the

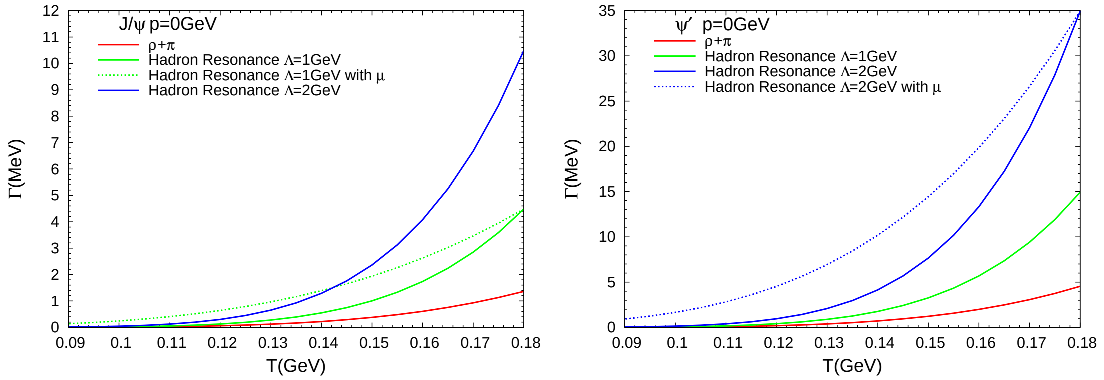

Figure 2.5: (Color online) Temperature dependence of hadronic dissociation rates for J/ψ (left panel) and $\psi(2S)$ (right panel) at rest in a thermal bath. Previous results for a $\pi\rho$ gas with Λ=1 GeV (solid red lines) are compared to our updated results for a meson resonance gas using Λ=1 GeV and 2 GeV (solid green and blue lines, respectively). The blue-dotted lines additionally account for finite meson chemical potential that build up for temperatures below the chemical freezeout in URHICs [82]. The figures are reprinted from [56].

hadronic formfactor cutoff values, this is too small to affect the J/ψ abundance during the 5-10 fm/c lifetime of the hadronic phase in URHICs. For the $\psi(2S)$, geometric scaling by the vacuum radius has been assumed, increasing its rates by a factor $\left(\frac{r_{\psi(2S)}}{r_{J/\psi}}\right)^2 \simeq 3.7$, which is approximately compatible with constituent-quark model calculations [81].

A hadron resonance gas (HRG), however, contains many more species than π and ρ. To estimate their impact on the charmonium dissociation rates, we simply adopt the existing ρ- and π-induced matrix elements and shift their kinematics according to the pertinent 2-particle threshold, $i.e.$,

$$\Gamma^{\rm diss}_{X+J/\psi}(T) = \int \frac{d^3k}{(2\pi)^3} f^X(E_X(k);T)\sigma^{\rm in}_{X+J/\psi}(s, s^X_{\rm thr})v_{\rm rel} \tag{2.79}$$

with X the meson interaction with J/ψ, $s = (p_{J/\psi} + k)^2$ and $s^X_{\rm thr} = (m_{J/\psi} + m_X)^2$ for exothermic and $s^X_{\rm thr} = (2m_D)^2$ for endothermic channels ($s^X_{\rm thr} = (m_D + m_{D_s})^2$ if X contains a strange quark). We include a total of 52 non-strange and single-strange meson species, up to a mass of $m_X = 2\,\mathrm{GeV}$. As before, we apply geometric scaling to obtain the reaction rates for the χ_c and $\psi(2S)$. Our results for a meson gas in chemical equilibrium are summarized by the solid lines in Fig. 2.5. At the highest temperature (T=180 MeV), the additional resonances enhance the J/ψ dissociation rate by a factor of ~2.5, and another factor of ~2.5 when increasing the hadronic formfactor cutoff from Λ=1 GeV to 2 GeV, reaching a maximal rate of 10.5 MeV. For the $\psi(2S)$, geometric scaling leads a maximum rate of up to 35 MeV, translating into a lifetime of ~6 fm/c which is now comparable to the duration of the hadronic phase in URHICs. This becomes even more significant if chemical freezeout is accounted for, which implies the build-up of meson chemical potentials leading to a slower decrease of the meson densities as temperature decreases, cf. dotted lines in Fig. 2.5.

2.2.7 Equilibrium Limit: Statistical Hadronization Model and Heavy-Quark Number Conservation

2.2.7.1 Fugacity Factor

We again take charmonium as example. The $c\bar{c}$ are produced in pairs from initial hard production via gluon fusion or quark annihilation. After the initial production, some pairs are bound into charmonium states and those are called hidden charm. However, most of c and $\bar{c}$ separate from each other, some may bind with a light quark to become a D meson, or a strange quark to become a D_s meson. Those are called open charm. We will construct the charm quark number conservation via discussion of the open charm sector.

Denoting a partition function for one charm quark (anti-charm quark) $Z_c(T)$ ($Z_{\bar{c}}(T)$), the partition function for the open $c\bar{c}$ pair reads

$$Z^{pair}(T) =< Z_c(T) Z_{\bar{c}}(T) >= (Z_1(T))^2 \,, \tag{2.80}$$

where the second equality means that there is no correlation between c and $\bar{c}$.

Assuming that there is only correlation within one $c\bar{c}$ pair but not between different pairs (we will see correction beyond this approximation in Sec. 2.2.7.2), we have the partition function for "n $c\bar{c}$ pairs"

$$Z_n^{pair}(T) = \frac{(< Z_c(T) Z_{\bar{c}}(T) >)^n}{n! n!} = \left(\frac{(Z_1(T))^n}{n!} \right)^2, \tag{2.81}$$

where $n!n!$ is due to the fact that charm is identical particle and anti-charm is also identical particle. The total partition function for all different numbers of pairs reads

$$Z = \sum_{n=0}^{\infty} Z_n^{pair}(T) = \sum_{n=0}^{\infty} \left(\frac{(Z_1(T))^n}{n!} \right)^2 = I_0(2Z_1(T)), \tag{2.82}$$

and thus the probability for the existence of "n $c\bar{c}$ pairs" is

$$P_n = \frac{Z_n^{pair}}{Z} = \left(\frac{(Z_1(T))^n}{n!} \right)^2 \frac{1}{I_0(2Z_1(T))}. \tag{2.83}$$

Then we can calculate the expectation number of the open-charm pair numbers

$$N_{op} =< n >= \sum_{n=0}^{\infty} n P_n = \sum_{n=0}^{\infty} n \left(\frac{(Z_1(T))^n}{n!} \right)^2 \frac{1}{I_0(2Z_1(T))} = Z_1(T) \frac{I_1(2Z_1(T))}{I_0(2Z_1(T))}. \tag{2.84}$$

There are also hidden charm bound as quarkonium states in the medium. Both open and hidden charm contribute to the total number of $c\bar{c}$ pairs. Thus the $c\bar{c}$ conservation equation reads:

$$N_{c\bar{c}} = N_{op} + N_{hid} = Z_1(T) \frac{I_1(2Z_1(T))}{I_0(2Z_1(T))} + N_{hid}, \tag{2.85}$$

where $N_{c\bar{c}}$ is the total number of $c\bar{c}$ pairs. In practice, it is determined from experimental data in heavy-ion collisions. N_{op} and N_{hid} are $c\bar{c}$ pairs in the open and hidden sectors respectively.

Next, we discuss how the partition functions in the conservation equation are constructed and how the fugacity factor γ_c is extracted. We define charm-quark distribution in momentum and coordinate space, $F_c(\vec{p}, T(\vec{x}), \vec{x}) = f_c(\vec{p}, T(\vec{x}))\rho(\vec{x})$. Here, $\rho(\vec{x})$ is the distribution of charm quark in coordinate space which gives $\int \rho(\vec{x}) d^3x = V_{\mathrm{FB}}$, equal to the volume of the produced fireball medium in URHICs. $f_c(\vec{p}, T(\vec{x}))$ is the charm quark momentum spectrum that figures in the calculation of β in previous Sec. 2.2.2 and Sec. 2.2.4. $T(\vec{x})$ is the temperature distribution. The partition function for a single c is:

$$\begin{aligned} Z_c(T) &= \gamma_c \int F_c(\vec{p}, T(\vec{x}), \vec{x}) \frac{\mathrm{d}^3p}{(2\pi)^3} \mathrm{d}^3x && (2.86) \\ &= \gamma_c \int f_c(\vec{p}, T(\vec{x})) \frac{\mathrm{d}^3p}{(2\pi)^3} \rho(\vec{x}) \mathrm{d}^3x = \gamma_c \int n_c(T(x))\rho(x) \mathrm{d}^3x. && (2.87) \end{aligned}$$

In a uniform medium $T(\vec{x}) = T$, thus

$$Z_c(T) = \gamma_c \int n_c(T)\rho(\vec{x}) \mathrm{d}^3x = \gamma_c n_c(T) V_{\mathrm{FB}}. \tag{2.88}$$

If c and $\bar{c}$ have no correlation, then we have

$$N_{c\bar{c}} = N_{op} + N_{hid} = \gamma_c n_c(T) V_{\mathrm{FB}} \frac{I_1(2\gamma_c n_c(T) V_{\mathrm{FB}})}{I_0(2\gamma_c n_c(T) V_{\mathrm{FB}})} + N_{hid}, \tag{2.89}$$

Note that we have made the assumption that $n_c = n_{\bar{c}}$. Considering that $c\bar{c}$s are produced in pairs, and using the notation $n_{\mathrm{op}} = n_c + n_{\bar{c}}$ to represent the density of a $c\bar{c}$ pair, we have

$$N_{c\bar{c}} = N_{op} + N_{hid} = \frac{1}{2} \gamma_c n_{\mathrm{op}}(T) V_{\mathrm{FB}} \frac{I_1(\gamma_c n_{\mathrm{op}}(T) V_{\mathrm{FB}})}{I_0(\gamma_c n_{\mathrm{op}}(T) V_{\mathrm{FB}})} + N_{hid}. \tag{2.90}$$

Solving this equation, we obtain the fugacity factor as a function of temperature $\gamma_c(T)$, and the equilibrium limit in the rate equation Eq. (2.54)

$$N_{\Psi}^{\mathrm{eq}}(T) = V_{\mathrm{FB}}\gamma_c^2(T)n_{\Psi}(m_{\Psi}, T). \tag{2.91}$$

There are two limits worth noticing:

(1) canonical-limit: $2Z_1(T) \ll 1$, $\frac{I_1(2Z_1(T))}{I_0(2Z_1(T))} \to Z_1(T)$, $N_{c\bar{c}} = (Z_1(T))^2 + N_{hid}$.

(2) grand-canonical limit: $2Z_1(T) \gg 1$, $\frac{I_1(2Z_1(T))}{I_0(2Z_1(T))} \to 1$, $N_{c\bar{c}} = Z_1(T) + N_{hid}$.

The canonical limit corresponds to a situation with roughly less than 1 pair of $c\bar{c}$, and the grand-canonical limit corresponds to a situation with many more than 1 pair of $c\bar{c}$. The factor $\frac{I_1(2Z_1(T))}{I_0(2Z_1(T))}$ can be interpreted as the probability of a c to find its $\bar{c}$ partner. In grand-canonical limit, the abundance of $c\bar{c}$ pairs allows the c to find its $\bar{c}$ partner much easier with probability$\simeq$1.

2.2.7.2 Correlation Volume

The $c\bar{c}$ pairs are produced locally expanding to only a finite size in the fireball during the medium evolution. This motivates the introduction of a correlation volume [83, 84] for $c\bar{c}$ pairs accounting for this effect. The finite volume for a c to find its twin $\bar{c}$ is the correlation volume, which can be parameterized as

$$V_{\mathrm{corr}} = \frac{4}{3}\pi\left(r_0 + \langle v_c\rangle t\right)^3. \tag{2.92}$$

The initial radius of the correlation volume, r_0 characterizes a typical strong interaction range, and the recoil velocity, $\langle v_c\rangle$, can be estimated from D-meson p_T spectra.

We understand that the partition function $Z_1(T) = \gamma_c n_c(T) V_{\mathrm{FB}}$ gives the probability of having a c reside in the fireball. Thus the ratio $\frac{I_1(2Z_1(T))}{I_0(2Z_1(T))}$ can be interpreted as the conditional probability of a c to find its partner $\bar{c}$. Lacking spatial information in $c\bar{c}$ production, the c has chance to explore the whole fireball volume V_{FB} to find the $\bar{c}$. Within finite correlation volume, the implementation of the finite correlation length requires the V_{FB} to be replaced by V_{co}, modifying Eq. (2.89) to

$$N_{c\bar{c}} = N_{op} + N_{hid} = \gamma_c n_c(T) V_{\mathrm{FB}} \frac{I_1(2\gamma_c n_c(T) V_{\mathrm{corr}})}{I_0(2\gamma_c n_c(T) V_{\mathrm{corr}})} + N_{hid}, \tag{2.93}$$

or

$$N_{c\bar{c}} = N_{op} + N_{hid} = \frac{1}{2}\gamma_c n_{\mathrm{op}}(T) V_{\mathrm{FB}} \frac{I_1(\gamma_c n_{\mathrm{op}}(T) V_{\mathrm{corr}})}{I_0(\gamma_c n_{\mathrm{op}}(T) V_{\mathrm{corr}})} + N_{hid}, \tag{2.94}$$

In the above derivation we have assumed the $c\bar{c}$ production and recombination in pairs. The more realistic treatment goes beyond the pair production picture that c can find a $\bar{c}$ from another pair. One may notice that when the $c\bar{c}$ pairs are abundant, there is a large chance for c to find its partner outside its own correlation volume. Then, the total correlation volume bubbles are merged and the effective volume for c to find its partner $\bar{c}$ could be as large as the whole fireball volume V_{FB}. In this limit, the Eq. (2.93) goes back to Eq. (2.89). In our calculations in this dissertation, we use the condition

$$V_{\mathrm{corr}} N_{c\bar{c}} \geq \frac{1}{2} V_{\mathrm{FB}}, \tag{2.95}$$

for the criterion of merging. A more detailed treatment of the correlation volume needs a simulation of c and $\bar{c}$ evolution spatially, with the help of the Langevin heavy-quark transport.

2.2.8 Fireball Model: Entropy Conservation and Relativistic Expansion

The solution of the transport equations requires the relation between temperature and time, namely the temperature evolution of the medium background. The temperature evolution can be approximated from a fireball model assuming a conservation of the total entropy due to the property of nearly perfect liquid of the QGP. The total entropy is the product of entropy density of the medium and the expanding volume of the fireball

$$S_{\text{tot}} = s(T) V_{\text{FB}}(t). \tag{2.96}$$

The entropy density is obtained from the equation of state of the medium (either the QGP or the hadronic matter). The fireball volume is assumed to follow a relativistic expansion form with a cylindrical shape, with a uniformly expanding longitudinal direction and an accelerated transverse expansion

$$V_{\text{FB}}(t) = (z_0 + v_z t)\, \pi R(t)^2, \tag{2.97}$$

where the initial longitudinal length is determined by the QGP formation time $z_0 = t_{\text{QGP}} \Delta y$, with rapidity overage of one fireball $\Delta y \simeq 1.8$. The value is approximately $t_{\text{QGP}} \simeq 0.6\,\text{fm}$ at RHIC energy [85] and $t_{\text{QGP}} \simeq 0.2\,\text{fm}$ at the LHC energy [20, 86].

The partons in the fireball form a gradient in the spatial transverse plane which gives positive pressure pushing the partons to diffuse and the fireball to expand. Suppose each small cell in the fireball is expanding with a constant acceleration due to the pressure, we may construct the relativistic expansion form accordingly. For each cell in the fireball, there are two frames, one in lab frame in which the cell is moving, the other one in fluid cell rest frame (denoted by prime) which defines the rest frame of the cell. The Lorentz transforms of the moving cell between the two frames are

$$\begin{aligned} \mathrm{d}x &= \gamma \left(\mathrm{d}x' + v \mathrm{d}t'\right), \qquad (2.98) \\ \mathrm{d}t &= \gamma \left(\mathrm{d}t' + v \mathrm{d}x'\right), \qquad (2.99) \end{aligned}$$

where x is the radial location of the cell, v is the fluid velocity of the cell in the lab frame and $\gamma = \frac{1}{\sqrt{1-v^2}}$. The cells are moving outward which contributes to the fireball expansion so we only need to consider the radial direction. Define the velocity of the cell in two frames $u = \frac{\mathrm{d}x}{\mathrm{d}t}$ and $u' = \frac{\mathrm{d}x'}{\mathrm{d}t'}$, we arrive at the velocity transform $u = \frac{u'+v}{1+u'v}$. A further differentiation on the cell velocity gives

$$\mathrm{d}u = \frac{\mathrm{d}u'}{\gamma^2 \left(1 + u'v\right)^2}. \tag{2.100}$$

Considering the fact that $u' = 0$ and $u = v$, we have the relation of acceleration of the moving cell between two frames.

$$a = \frac{a'}{\gamma^3 \left(1 + u'v\right)^3} = \frac{a'}{\gamma^3} = a' \left(1 - u^2\right)^{\frac{3}{2}}. \tag{2.101}$$

We assume the acceleration in the fluid rest frame to be a constant, denoted by $a' = a_T$. We thus have

$$\frac{\mathrm{d}u(t)}{(1 - (u(t))^2)^{\frac{3}{2}}} = a_T \mathrm{d}t. \tag{2.102}$$

Solving this differential equation, we arrive at the relativistic form of fireball velocity in lab frame

$$u(t) = \frac{a_T t}{\sqrt{1 + (a_T t)^2}}. \tag{2.103}$$

From this we can derive the acceleration

$$a(t) = \frac{a_T}{\left(1 + (a_T t)^2\right)^{\frac{3}{2}}}, \tag{2.104}$$

and radius

$$R(t) = R_0 + \frac{\sqrt{1 + (a_T t)^2} - 1}{a_T}. \tag{2.105}$$

For the mixed phase between the QGP and the hadronic matter, we define the QGP fraction in the mixed phase as

$$f_{\mathrm{QGP}}(t) = \frac{s(t) - s_{\mathrm{HG}}(T_c)}{s_{\mathrm{QGP}}(T_c) - s_{\mathrm{HG}}(T_c)}, \tag{2.106}$$

where $s(\tau) = S_{\mathrm{total}}/V_{\mathrm{FB}}(t)$ is the entropy density in the mixed phase; $s_{\mathrm{QGP}}(T_c)$ ($s_{\mathrm{HG}}(T_c)$) is the entropy density of the QGP (hadronic matter) at T_c; and $f_{\mathrm{HG}}(t) = 1 - f_{\mathrm{QGP}}(t)$ is the hadronic fraction.

2.2.9 Initial State Effects

The initial quarkonium distribution $f(\vec{x}, \vec{p}, t_0)$ can be calculated from models for initial state effects. We here employ the widely used optical Glauber model, constructed from Woods-Saxon distributions of the heavy ions assuming a collision density overlap of the colliding ions, to distribute primordial quarkonia spatially as $f(\vec{x})$. For our purpose of accuracy in the final state interaction transport calculations, the primordial p_T spectra of quarkonium $f(\vec{p})$ and the cross section σ_{Ψ}^{pp} can be extracted and extrapolated from experimental data in pp collisions at various collision energies, and rescaled by the number of nucleon-nucleon collisions in one nucleus-nucleus collision, N_{coll}. The product of $f(\vec{x})$ from the Glauber model and $f(\vec{p})$ from experimental data constructs the initial quarkonium distribution $f(\vec{x}, \vec{p}, t_0)$. There are also implementations to modify the initial distribution to mimic the effects of nuclear shadowing, nuclear absorption, and Cronin effect, as described below.

2.2.9.1 Quarkonium Production in pp Collision

There are several widely used models to generate the primordial quarkonium cross section σ_{Ψ}^{pp} in pp collision. The primordial quarkonium cross section can be factorized based on perturbatively hard production in nucleon nucleon collisions of quark-antiquark pairs, N+N→c+$\bar{c}$ (taking charmonium as as example), and nonperturbative long distance processes of $c\bar{c}$ to Ψ transitions,

$$\sigma_{\Psi}^{pp} = \sigma_{NN\to\Psi} = \int \mathrm{d}\Pi_{c\bar{c}} \sigma_{NN\to c\bar{c}} f_{c\bar{c}\to\Psi}, \tag{2.107}$$

where $\mathrm{d}\Pi_{c\bar{c}}$ is the $c\bar{c}$ phase space measure. To leading order, the hard production of $c\bar{c}$ pair is mainly due to gluon fusion and quark-antiquark annihilation processes in nucleon-nucleon collisions and can be calculated from pQCD. There are also higher-order contributions. The realization of the nonperturbative $c\bar{c}$ to Ψ transitions, $f_{c\bar{c}\to\Psi}$ has been studied in several models: (1) the Color-Evaporation Model (CEM) [87] fits the transition probabilities to experimental data; (2) the Color-Singlet Model (CSM) [88] implements the transition probability via a projection of the $c\bar{c}$ wave functions to Ψ wave functions of color-singlet $c\bar{c}$ pairs; (3) the Color-Octet Model (COM) [89], realized by Nonrelativistic QCD (NRQCD) approach, extends the CSM by including color singlet-octet transition by emitting a gluon, which enables color-octet $c\bar{c}$ to form Ψ states.

In the thesis, we take σ_{Ψ}^{pp} directly from experimental data.

2.2.9.2 Nuclear Shadowing and Nuclear Absorption

There are modifications of the primordial cross section in A-A collisions compared to that in pp collisions due to a nuclear modification to the parton distribution functions in the free proton defined as

$$R_i^A(x, Q^2) = \frac{f_i^A(x, Q^2)}{A f_i^p(x, Q^2)}, \tag{2.108}$$

with i=q, $\bar{q}$ or g. $f_i^A(x, Q^2)$ is called the nuclear parton distribution function (nPDF) and $f_i^p(x, Q^2)$ is the parton distribution function in a proton. There are several effects of nPDF illustrated in Fig. 2.6: (1) shadowing at small-x, relative suppression of parton distribution in nuclei; (2) anti-shadowing at intermediate-x, relative enhancement of parton distribution in nuclei; (3) EMC-effect at large-x, and (4) Fermi-motion at extremely large-$x$$\simeq$1. The

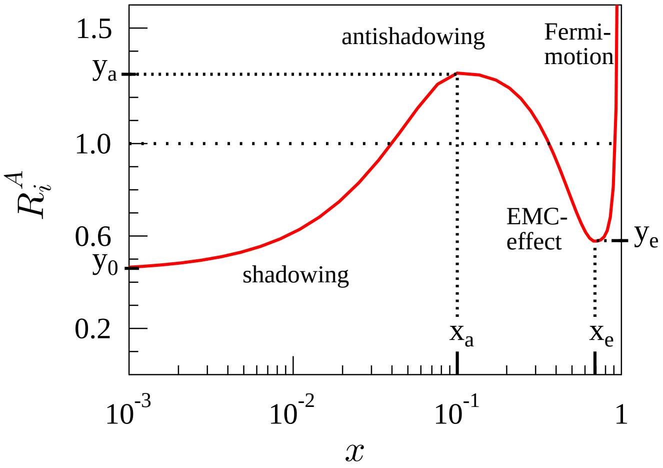

Figure 2.6: Schematic view of nuclear modification to the proton parton distribution function $R_i^A(x, Q^2)$. The Figure is reprinted from [90].

momentum fraction x, of the partons at two rapidities from the incoming nuclei can be evaluated as

$$x_{\pm} = \frac{\sqrt{p_T^2 + m_\Psi^2}}{\sqrt{s}} e^{\pm y}, \tag{2.109}$$

where

$$y = \frac{1}{2} \ln \left(\frac{E + p_z}{E - p_z} \right) \tag{2.110}$$

is the rapidity of the incoming parton. Since the primordial quarkonia are mainly originating from gluon-induced processes, the corresponding nuclear modification factor can be approximated as

$$S_{\text{nuc}} = R_g^A(x_+, Q^2) R_g^A(x_-, Q^2) \tag{2.111}$$

where the momentum transfer square Q^2 correspond to the invariant mass squared of the quarkonium.

There is also the effect that the $c\bar{c}$ pairs forming a Ψ are disrupted while traveling through the nucleus [91]. This effect is more prominent at RHIC energy where the Lorentz contraction factor is not as extreme as it is at the LHC energy and the nuclear "pancake" is thick. This effect can be simulated by the Glauber model.

2.2.9.3 Glauber Model

The Glauber Model [92] is a widely used method to calculate some basic quantities related to the primordial binary nucleon-nucleon (N-N) collisions in URHICs, such as collision number N_{coll}, participant number N_{part}, $etc.$ It is also useful to effectively generate the spatial distribution of nucleons and partons in the A-A collisions. A modification of the Glauber model with an effective absorption cross section can mimic the nuclear shadowing effect and nuclear absorption effect.

Starting from the Woods-Saxon distribution of a nucleus with A nucleons inside, at transverse radius r and longitudinal distance z

$$\rho(r,z) = \frac{\rho_0}{1 + \exp\left(\frac{\sqrt{r^2+z^2}-R}{a}\right)}, \tag{2.112}$$

we may define a normalized distribution $\hat{\rho}(r,z) = \frac{\rho(r,z)}{A}$ so that

$$\int_{-\infty}^{+\infty} \mathrm{d}^2 r \mathrm{d}z \hat{\rho}(r,z) = 1. \tag{2.113}$$

We may define its thickness function in the transverse plane

$$T_A(r) = \int_{-\infty}^{+\infty} \mathrm{d}z \hat{\rho}(r,z). \tag{2.114}$$

A semi-central or peripheral A-A collision has two nuclei colliding at a distance of b between their centers in the transverse plane, see Fig. 2.7. This b is called the impact

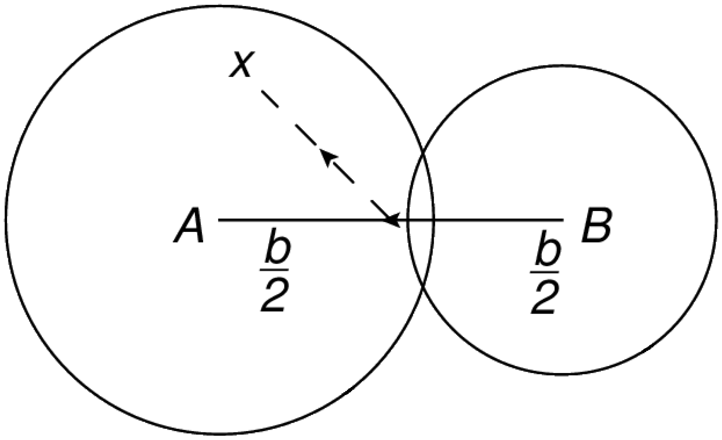

Figure 2.7: Schematic view of a non-central collision in a transverse plane.

parameter. Assuming a vector $\vec{b}$ with length of b and pointing from the center of one nucleus to the other's in the transverse plane, their overlap function reads

$$T_{AB}(b) = \int_{-\infty}^{+\infty} \mathrm{d}^2 r T_A\left(r_A\right) T_B\left(r_B\right), \tag{2.115}$$

with $r_A = |\vec{r} - \frac{\vec{b}}{2}|$ and $r_B = |\vec{r} + \frac{\vec{b}}{2}|$, see Fig. 2.7. Note that the integration over the overlap of the Woods-Saxon thickness functions is not depending on the direction of $\vec{b}$ anymore and we can simply suppress the vector sign above $\vec{b}$. For a specific rapidity range $\Delta y \simeq 1.8$, the spatial distribution in the transverse plane can be constructed from

$$f(\vec{r}, b) = \Delta y \frac{\mathrm{d}\sigma_\Psi^{pp}}{\mathrm{d}y} AB T_A\left(r_A\right) T_B\left(r_B\right) = \Delta y \frac{\mathrm{d}\sigma_\Psi^{pp}}{\mathrm{d}y} AB \int_{-\infty}^{+\infty} \mathrm{d}z_A \mathrm{d}z_B \hat{\rho}(r_A, z_A) \hat{\rho}(r_B, z_B). \tag{2.116}$$

The initial state suppression like nuclear shadowing and nuclear absorption can be mimic by implementing an effective absorption cross section σ_{abs} into the Glauber model. The distribution needs to be modified as

$$f_{\text{nuc}}(\vec{r},b)=\Delta y\frac{\mathrm{d}\sigma_{\Psi}^{pp}}{\mathrm{d}y}AB\int\limits_{-\infty}^{+\infty}\mathrm{d}z_A\mathrm{d}z_B\hat{\rho}(r_A,z_A)\hat{\rho}(r_B,z_B)$$
$$\times\quad\exp\left(-\sigma_{\text{abs}}\left[(A-1)\int\limits_{z_A}^{+\infty}\mathrm{d}z\hat{\rho}(r_A,z_A)+(B-1)\int\limits_{z_B}^{+\infty}\mathrm{d}z'\hat{\rho}(r_B,z_B)\right]\right)\tag{2.117}$$

The resulting "cold-nuclear matter" suppression factor can be defined as

$$S_{\text{nuc}}(b)=\frac{\int_{-\infty}^{+\infty}\mathrm{d}^2rf_{\text{nuc}}(\vec{r},b)}{\int_{-\infty}^{+\infty}\mathrm{d}^2rf(\vec{r},b)}.\tag{2.118}$$

The longitudinal coordinate dependence is neglected and the spatial distribution of a collision with impact parameter b is $f(\vec{x}_T)$=$f(\vec{r},\vec{b})|_{\vec{x}_T=\vec{r}}$.

The collision number of a nucleus with mass number A and an other nucleus with mass number B reads

$$N_{\text{coll}}(b)=\sigma_{\text{inel}}^{NN}ABT_{AB}(b),\tag{2.119}$$

and its participant number can be obtained as

$$N_{\text{part}}(b)\quad=\quad A\int\limits_{-\infty}^{+\infty}\mathrm{d}^2rT_A(r_A)\{1-\left[1-\sigma_{\text{inel}}^{NN}T_B(r_B)\right]^B\}\tag{2.120}$$
$$+\quad B\int\limits_{-\infty}^{+\infty}\mathrm{d}^2rT_B(r_B)\{1-\left[1-\sigma_{\text{inel}}^{NN}T_A(r_A)\right]^A\},\tag{2.121}$$

with $\sigma_{\text{inel}}^{NN}$ the inelastic scattering cross section for a nucleon-nucleon collision at collision energy $\sqrt{s}$.

2.2.9.4 *Cronin Effect*

The Cronin effect [93, 94] accounts for the multiple-scattering of partons in the target nucleus before the $c\bar{c}$ formation. Based on a random process, it is usually implemented by a Gaussian smearing of the original p_T spectra in a pp collision as

$$f(\vec{p}_T, b) = \frac{1}{\pi a_{gN} L(b)} \int_{-\infty}^{+\infty} \mathrm{d}^2 p'_T f_{pp}(|\vec{p}_T - \vec{p}'_T|) \exp(-\frac{{p'_T}^2}{a_{gN} L(b)}) \ , \tag{2.122}$$

where a_{gN} is the p_T broadening per unit path length and $L(b)$ the mean path length of the gluon in A-A collisions before fusing into a Ψ state [95]. It can be calculated as:

$$L(b) = \frac{\int_{-\infty}^{+\infty} \mathrm{d}^2 r \mathrm{d}z_A \mathrm{d}z_B \left(l^A(r_A, z_A) + l^B(r_B, z_B)\right) K(b, r, z_A, z_B)}{\int_{-\infty}^{+\infty} \mathrm{d}^2 r \mathrm{d}z_A \mathrm{d}z_B K(b, r, z_A, z_B)}, \tag{2.123}$$

for a nucleus A colliding with B. In the above expression, $l^A(r_A, z_A) = \frac{A}{\rho_0} \int_{-\infty}^{z_A} \mathrm{d}z \hat{\rho}_A(r_A, z)$, $l^B(r_B, z_B) = \frac{B}{\rho_0} \int_{z_B}^{\infty} \mathrm{d}z \hat{\rho}_B(r_B, z)$. The kernel

$$\begin{aligned} K(b, r, z_A, z_B) &= \hat{\rho}_A(r_A, z_A) \hat{\rho}_B(r_A, z_A) \\ \times \ \exp &\left(-\sigma_{\text{abs}} \left[(A-1) \int_{-\infty}^{z_A} \mathrm{d}z \hat{\rho}_A(r_A, z) + (B-1) \int_{z_B}^{\infty} \mathrm{d}z \hat{\rho}_B(r_B, z) \right] \right) \end{aligned} \tag{2.124}$$

represents the coordinate distribution of partons in the collision.

2.2.10 Feeddown in Quarkonia

As mentioned in Chap. 1, there are excited charmonium states that can decay and contribute to the lower mass charmonium states. There are about 67 % J/ψ from its direct production while 25 % from the $\chi_c(1P)$ states, and 8 % from the $\psi(2S)$ state [96]. The bottomonia have more species that are included in our transport model calculations. The bottomonium feeddown fractions are summarized in Appendix. A.2.

2.2.11 Formation Time Effect

To schematically account for the effects of quantum evolution in the early stages of the quarkonium evolution, we utilize formation times [97, 98, 99], $\tau_{\Psi}^{\rm form}$, for the different states that are assumed to have a range of 1-2 fm to reflect uncertainties associated with their binding energies. Their effect is rather small in semi-/central A-A collisions, but becomes augmented in small systems due to shorter fireball lifetimes. The formation times not only influence (suppress) the magnitude of the early charmonium dissociation but also modify its p_T dependence due to Lorentz time dilation implemented via

$$\tilde{\Gamma}_{\Psi}(\vec{p}_T, T(\tau)) = \Gamma_{\Psi}(\vec{p}_T, T(\tau)) \frac{\tau}{\tau_{\Psi}^{\rm form}} \frac{m_{\Psi}}{\sqrt{p_T^2 + m_{\Psi}^2}} \tag{2.125}$$

for $\tau < \tau_{\Psi}^{\rm form} \frac{\sqrt{p_T^2+m_{\Psi}^2}}{m_{\Psi}}$.

2.2.12 Connection to Heavy-Quark Transport

The physics of individual heavy-quark transport is a closely to quarkonium transport. The common approach for heavy-quark transport relies on the Langevin realization of stochastic process presented and summarized in Sec. 2.1.5. The quarkonium transport can be connected to heavy-quark transport in several aspects, which can ultimately help to further constrain the quarkonium production in various aspects.

First, the regeneration rate $\beta(\vec{p}, T(t))$ can be evaluated through the heavy-quark momentum spectra $f_Q(\vec{p}, T(t))$ simulated by Monte-Carlo methods via the Langevin equation, providing a dynamical time evolution of the regeneration component. Second, the Langevin simulated spatial distributions of heavy-quark enable us to rigorously calculate the effects of correlation volume and the recombination beyond the production in pair approximation. Third, the reduced 2→2 scattering amplitude within the "quasifree" approximation is essentially the same as that of the heavy-quark collisional energy loss [60], opening a window for an integrated open/hidden heavy flavor transport at a microscopic level. These connections provide guidance from heavy-quark phenomenology for an improved treatment of the quarkonium phenomenology and vice versa. This will be an important feature in quantitatively extracting the quark-antiquark potential, discussed in Chap. 6.

3. CHARMONIUM PRODUCTION IN A-A COLLISIONS*

So far we have presented the main ingredients to the transport model. The most important model component is the rate equation which catches the main physics of the quarkonium kinetics in URHICs: direct suppression of primordially produced quarkonium and regeneration of quarkonium from heavy quarks. In this and the following sections, we will utilize the transport model to simulate the evolution of quarkonia in heavy-ion collisions and solve some realistic problems in different collision systems. This includes the investigations of ground and excited state quarkonia, large (A-A) and small (p/d-A) systems, charmonium and bottomonium systems and a statistical driven rate equation based machinery for extracting the in-medium heavy quark-antiquark potential.

This section mainly discusses the charmonium production in A-A collision systems. In Sec. 3.1 we discuss the ground state J/ψ production in A-A including SPS, RHIC and LHC energies. In Sec. 3.2, we propose the so-called "sequential regeneration" mechanism for ground and excited states J/ψ and $\psi(2S)$, providing an estimation of the $\psi(2S)/J/\psi$ $R_{\rm AA}$ double ratio based on this mechanism which can help us understand the feature of $\psi(2S)$ production in URHICs. We conclude at Sec. 3.3.

3.1 J/ψ Production

Charmonium production in URHICs has been studied for over 30 years. The originally proposed J/ψ suppression signature of Quark-Gluon Plasma (QGP) formation [37] has evolved into a more complex problem where both suppression and so-called regeneration (or statistical hadronization) mechanisms need to be considered. Their interplay and

---

*Part of this section is reprinted with permission from "Sequential Regeneration of Charmonia in Heavy-Ion Collisions" by Xiaojian Du and Ralf Rapp, 2015, Nucl.Phys. A943, 147-158, Copyright 2015 by Elsevier, and "psi(2S) Production at the LHC" by Xiaojian Du and Ralf Rapp, 2017, J.Phys.Conf.Ser. 779 (2017) no.1, 012042, Copyright 2017 by IOP Publishing relevance depend on collision energy, system size and the 3-momentum of the measured charmonia, see, $e.g.$, Refs. [42, 100, 101] for recent reviews. The phenomenological modeling of these mechanisms, and their relation to the underlying in-medium properties, has progressed significantly in recent years. In particular, kinetic transport approaches, when calibrated with existing data from SPS and RHIC, have predicted the main features of the J/ψ production observed in the new energy regime at the LHC [49, 102, 103] (although significant uncertainties due to, $e.g.$, the open-charm cross section persist [104]). These include the overall increase of the nuclear modification factor, $R_{\rm AA}$, compared to RHIC energies and its enhancement at low transverse momentum, p_T [105].

3.1.1 J/ψ Production at the LHC

The J/ψ production from our transport model has been tested at SPS, RHIC, and LHC energies over the recent years. At LHC energy, increasingly precise measurements of J/ψ production in Pb-Pb and the new Xe-Xe collision systems are released. The transport model provides two main contributions, the direct suppression and the regeneration. The former increases in higher-multiplicity (more central) collisions due to the higher medium density and thus higher fireball temperature and longer lifetime. The regeneration acts in an opposite way: charm and anti-charm quarks can be more easily recombined into J/ψ in higher-multiplicity (more central) collisions due to large $c\bar{c}$ production cross sections. The larger $c\bar{c}$ cross section at LHC renders the J/ψ equilibrium limit in the grand-canonical region so that $N^{\rm eq}_{J/\psi}{\sim}\frac{N^2_{c\bar{c}}}{V_{\rm FB}}{\sim}\left(N_{\rm coll}\frac{\sigma^{pp}_{c\bar{c}}}{\sigma^{pp}_{\rm inel}}\right)^2/V_{\rm FB}$ and thus the $R^{\rm reg}_{\rm AA}$ increases with centrality,

$$R^{\rm reg}_{\rm AA} = \frac{N^{\rm reg}_{J/\psi}}{N_{\rm coll}\frac{\sigma^{pp}_{J/\psi}}{\sigma^{pp}_{\rm inel}}} \propto \frac{N^{\rm eq}_{J/\psi}}{N_{\rm coll}\frac{\sigma^{pp}_{J/\psi}}{\sigma^{pp}_{\rm inel}}} \sim \frac{\left(N_{\rm coll}\frac{\sigma^{pp}_{c\bar{c}}}{\sigma^{pp}_{\rm inel}}\right)^2}{N_{\rm coll}\frac{\sigma^{pp}_{J/\psi}}{\sigma^{pp}_{\rm inel}}V_{\rm FB}} \sim \frac{N_{\rm coll}}{V_{\rm FB}} \sim A^{\frac{1}{3}} \tag{3.1}$$

A naïve expectation from the direct-only component is a decreasing trend of $R_{\rm AA}$ from peripheral (small $N_{\rm part}$) to central (large $N_{\rm part}$) collisions. However, both data and model

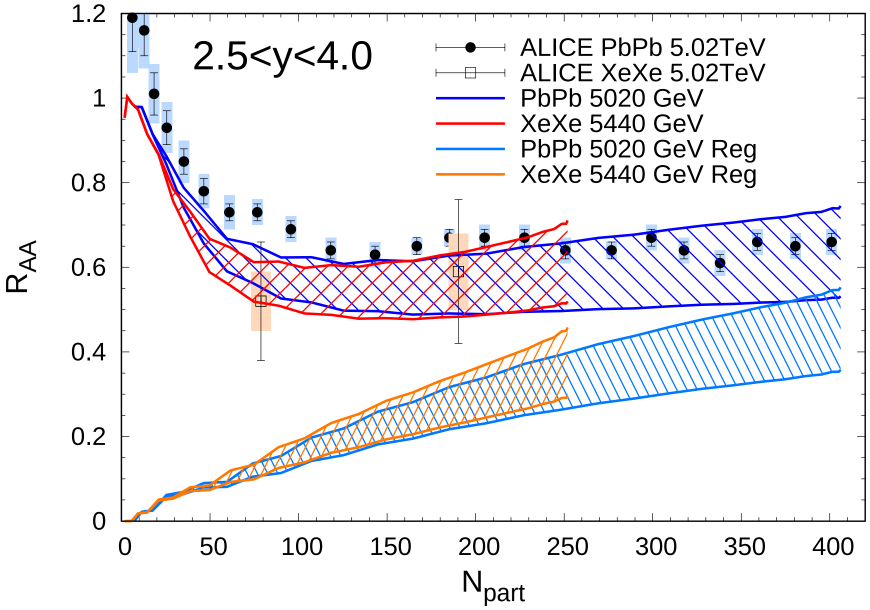

Figure 3.1: Theoretical calculations of J/ψ $R_{\rm AA}$ in Pb-Pb and Xe-Xe collisions compare with ALICE data [106, 107], as function of centrality indicator nuclear participate number $N_{\rm part}$. The light blue and orange bands are for the regeneration components of Pb-Pb and Xe-Xe collisions.

calculation show a flat trend which indicates the importance of the interplay between direct suppression and regeneration, see Fig. 3.1.

The interplay of the two components is further verified by the $R_{\rm AA}(p_T)$. The direct component is highly suppressed at all p_Ts and the regeneration component from the low momentum $c\bar{c}$ pairs is accumulated at low p_T. A peak at the low p_T with a decreasing trend and then leveling off of $R_{\rm AA}(p_T)$ is shown by both experimental data and the theoretical model calculations. Without the regeneration component, the peak at low p_T is absent while the remaining $R_{\rm AA}(p_T)$ at high p_T is impossible to describe without the direct component, see Fig. 3.2.

Furthermore, the measurements of a relatively large J/ψ v_2 also indicate a large portion of regeneration for the J/ψ, see Fig. 3.3 and reference [108].

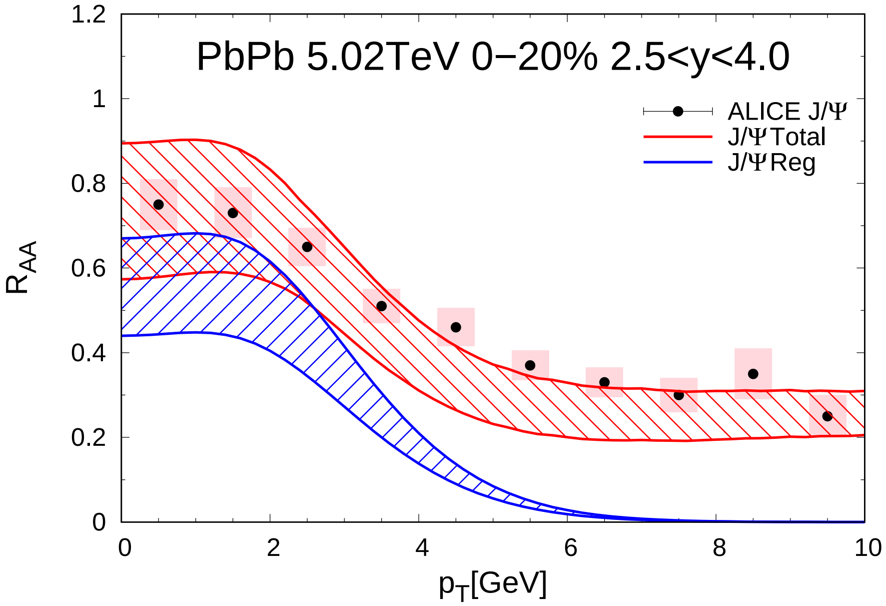

Figure 3.2: Comparison of theoretical prediction and experimental data [106] of J/ψ $R_{\rm AA}(p_T)$ in Pb-Pb collisions.

The $c\bar{c}$ cross section in pp collisions as an input to the transport calculation significantly influences the charmonium regeneration yields. The calculations presented at 5.02 TeV forward rapidity in Fig. 3.1 and Fig. 3.2 use $\frac{\mathrm{d}\sigma_{c\bar{c}}}{\mathrm{d}y}\simeq$0.57 mb, taken guidance from the first versions of ALICE [109] and LHCb [110], and extrapolated to the relevant energy and rapidity by FONLL [111, 112]. The extrapolated 5.02 TeV mid-rapidity cross section would be $\frac{\mathrm{d}\sigma_{c\bar{c}}}{\mathrm{d}y}\leq$0.85 mb correspondingly. However, the newest measurements of D mesons at 5.02 TeV mid-rapidity by ALICE [113] suggest a larger cross section $\frac{\mathrm{d}\sigma_{c\bar{c}}}{\mathrm{d}y}\simeq$0.90 mb. Taking charmed baryons into consideration, the $\frac{\mathrm{d}\sigma_{c\bar{c}}}{\mathrm{d}y}$ would be even higher. This increased $c\bar{c}$ cross section favors our transport calculations since the upper band (no shadowing) of the current results in Fig. 3.1 and Fig. 3.2 are more consistent with the experimental data. It can be expected that the increased $c\bar{c}$ cross section with full shadowing effect (lower band) would be more consistent with the experimental data.

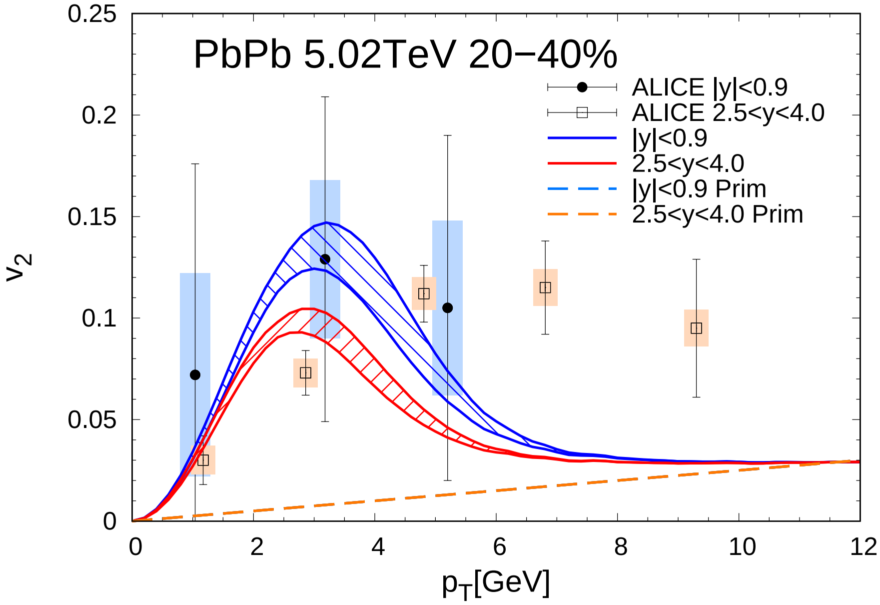

Figure 3.3: Theoretical calculations of J/ψ $v_2(p_T)$ in 5.02 TeV Pb-Pb collisions with 20-40% centrality compare with ALICE data [108]. The light blue and orange bands are for the primordial components of Pb-Pb and Xe-Xe collisions.

3.1.2 J/ψ Excitation Function From SPS via RHIC to the LHC

The importance of the regeneration component can be tested and demonstrated through the collision energy dependence of the $R_{\mathrm{AA}}(\sqrt{s})$, from SPS via RHIC to the LHC, at fixed centrality. In Fig. 3.4, we plot the excitation function (energy dependence) of J/ψ production, from collision energy per nucleon $\sqrt{s}$=17 GeV at SPS to 5.02 TeV at the LHC. The increasing trend of the excitation function is found by both experimental data and model calculations, caused by the interplay of the direct and regeneration component. The regeneration component dominates at higher energies where the $c\bar{c}$ production cross sections become large. This phenomenon was predicted in our group [47].

Four kinds of tests, $R_{\mathrm{AA}}(N_{\mathrm{part}})$, $R_{\mathrm{AA}}(p_T)$, $v_2(p_T)$, $R_{\mathrm{AA}}(\sqrt{s})$, all demonstrate the importance of the two components, especially the regeneration component, for the J/ψ.

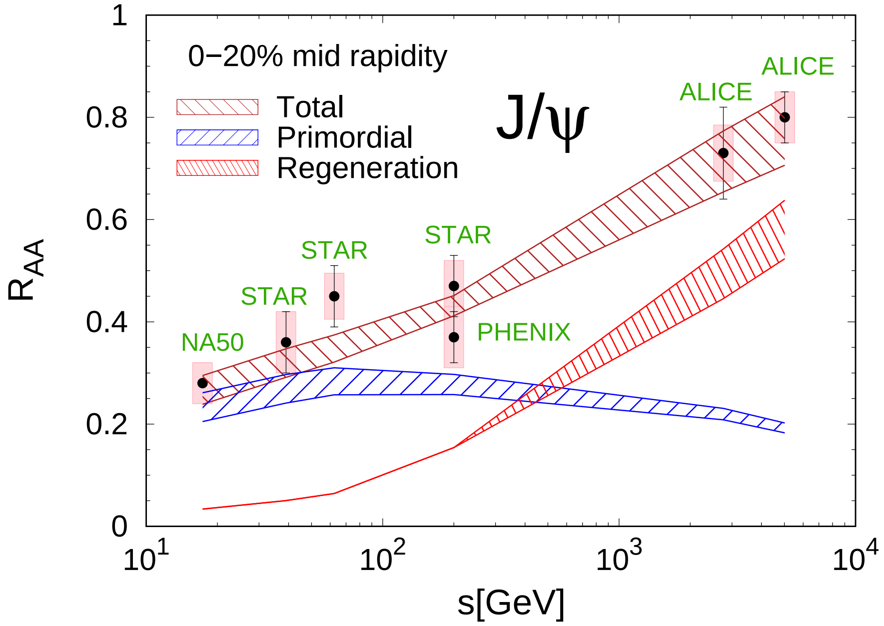

Figure 3.4: Excitation function of J/ψ $R_{\mathrm{AA}}(\sqrt{s})$ in Pb-Pb collisions from SPS, via Au-Au collisions at RHIC to the Pb-Pb collisions at the LHC. The $\sqrt{s}$ is collision energy of the system. Data are from [114, 115, 116, 117, 118, 119]. The figure is adapted from [35].

However, the importance of the regeneration component found in the charmonium sector is no longer obvious in the bottomonium sector where the $b\bar{b}$ pair production cross section is quite small. The total regeneration contribution is small for the ground state, while it may be substantial for the excited states. We will return to this issue in Sec. 5.6.

3.2 $\psi(2S)$ Production: Sequential Suppression and Sequential Regeneration

As one of the excited states in charmonium sector, $\psi(2S)$ becomes a rather hot topic since many experimental data are available in both p-A/d-A collisions [120, 121, 122, 123, 124, 125, 126, 127] and A-A collisions [128, 129, 130, 131, 132], and some theoretical models are trying to describe it [133, 134, 135, 56, 57, 136, 137, 138], in the recent years.

3.2.1 Experimental Results of $\psi(2S)$ Production in URHICs

Due to the smaller binding energy for excited state $\psi(2S)$ compared to the ground state J/ψ, the sequential suppression picture suggests a larger suppression of $\psi(2S)$ than J/ψ. This has been firstly verified in A-A collisions at SPS [128], then *p*/*d*-A collision at RHIC [120, 123, 124] and the LHC [121, 122, 127]. It became puzzling since CMS Collaboration announced their $\psi(2S)$ over J/ψ double ratio above unity with $3.0<p_T<30.0$ GeV at LHC energy [129]. Some recent data also shows larger than unity double ratio but with large uncertainty [124, 126] and for *p*/*d*-A collisions. Some models are trying to explain it with different mechanisms [133, 56, 57, 137].

We propose the idea of sequential regeneration mechanism [56] to help us understand it. The sequential regeneration mechanism suggests that due to the smaller binding energy of $\psi(2S)$ relative to J/ψ, the $\psi(2S)$ will regenerate at a later stage of the medium evolution when the medium cools down and the $\psi(2S)$ can start to form. At the later stage of medium evolution, the larger flow in medium pushes the charm quark to higher p_T. In other words, the recombined $\psi(2S)$ from charm quarks gain additional momentum from the flow. This is reflected at an intermediate p_T region $\simeq$ 3-6 GeV as many $\psi(2S)$ are being pushed to this region while most of J/ψ are accumulated at low p_T. The experimental data with a p_T cut at 3 GeV excludes most of the regenerated J/ψ but keep the $\psi(2S)$. This gives a $R_{\rm AA}(\psi(2S))$ over $R_{\rm AA}(J/\psi)$ double ratio above unity. Aside from a schematic model [56], we also did a preliminary calculation [57] with the transport approach but simply assuming the same pp spectra baseline for J/ψ and $\psi(2S)$, which is, however, not supported by experimental data [139, 140].

Later, both CMS [130] and ALICE [131] Collaborations announced their double ratio at a higher collision energy of 5.02 TeV and forward rapidity. The data suggest the double ratio to be below unity in central collisions. Upon implementing the empirical pp spectra in our calculation, we found that our double ratio will also be below unity.

3.2.2 Sequential Production and Flow Effects of Charmonia

Because of the importance of hadronic interactions for $\psi(2S)$, we first investigate the consequences of the updated hadronic reaction rates (Sec. 2.2.6.2) for Pb-Pb collisions at the LHC, followed by calculations of the $\psi(2S)$ over J/ψ R_{AA} double ratio. We consider both 2.76 TeV and 5.02 TeV Pb-Pb collisions at the LHC. Since the pertinent CMS data are for “prompt" J/ψ and $\psi(2S)$ production, we do not include contributions from B feeddown in the current calculation.

The earlier predictions within our transport approach framework for inclusive J/ψ production in these reactions [49] (see also the Sec. 3.1) resulted in a fair agreement with the centrality, transverse-momentum and rapidity dependencies observed by the ALICE and CMS collaborations, and thus serves as our framework to evaluate $\psi(2S)$ observables. In the transport model, we focus on the so-called “strong-binding scenario", where the in-medium charmonium properties are taken with guidance from a T-matrix approach [75] with the internal energy from lattice-QCD as underlying potential. This assumption gives a better agreement than using the free energy both with correlators from lattice-QCD and the overall charmonium phenomenology at SPS and RHIC [48]. For the hadronic rates, we employ the form factor with Λ=0.75(2) GeV for the J/ψ ($\psi(2S)$).

Let us first inspect the time evolution of direct J/ψ and $\psi(2S)$ mesons in 0-20% central Pb-Pb (without shadowing), as following from the solution of the kinetic rate equation

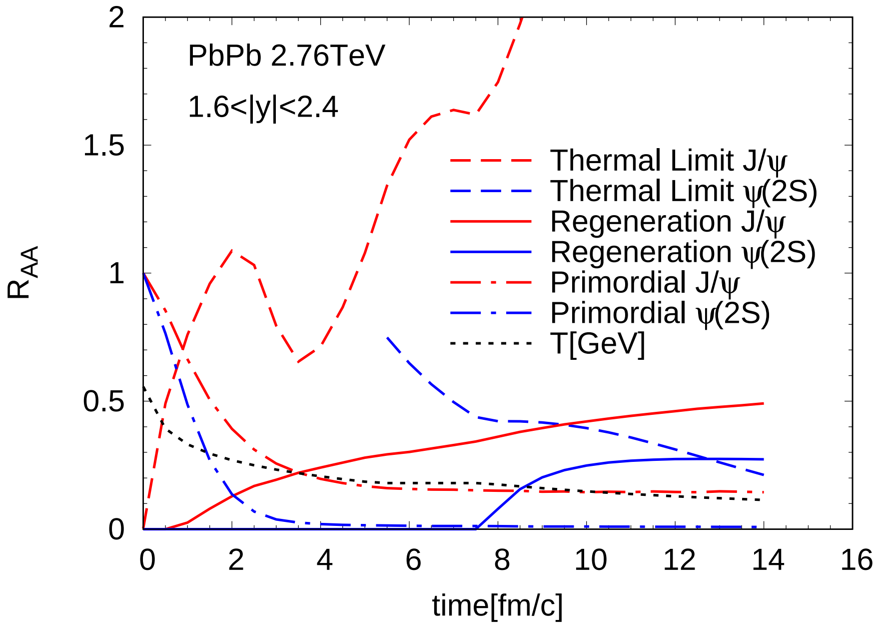

Figure 3.5: (Color online) Time dependence of prompt J/ψ and $\psi(2S)$ nuclear modification factors in central($N_{\rm part}$=324) Pb-Pb collisions at $\sqrt{s}$=2.76 TeV.The red (blue) curves are for direct J/ψ ($\psi(2S)$), with the solid (dotted) line styles representing the regeneration (primordial) contributions; the dash-dotted curves indicate the pertinent equilibrium limits (including a thermal relaxation time correction [74]), starting from the time when the fireball has cooled down to the dissociation temperature below which regeneration commences.

Eq. (2.54), see Fig. 3.5. Compared to our previous results without hadronic corrections (cf. lower panel in Fig. 2 of Ref. [49]), the J/ψ now picks up a regeneration contribution in the hadronic phase, by about 0.15 units in $R_{\rm AA}$, which, despite a small rate, is due to the large equilibrium limit. Most of the production, however, occurs prior to the onset of the mixed phase at $\tau \simeq 5.5\,{\rm fm}/c$. On the contrary, $\psi(2S)$ production only starts to set in at that point, leveling off at around τ≃9-10 fm/c, when the temperature of the fireball has dropped to about 150-160 MeV. The main qualitative and robust feature here is that the lower dissociation temperature of the $\psi(2S)$, relative to the J/ψ, implies a later production through regeneration in the time evolution of the fireball in URHICs. The large enhancement of $\psi(2S)$ regeneration from the updated hadronic rates provides a basis for raising up the $\psi(2S)$ over J/ψ R_{AA} double ratio.

The flow effects on charmonia are closely related to the p_T spectra of charmonia. We decompose the p_T spectra into two components. We use Boltzmann equation with only loss term

$$\frac{\partial f(\vec{x},\vec{p},\tau)}{\partial\tau}+\vec{v}\cdot\nabla f(\vec{x},\vec{p},\tau)=\Gamma(\vec{p},T(\tau))f(\vec{x},\vec{p},\tau) \tag{3.2}$$

to calculate the primordial component of p_T spectra. The dissociation rate $\Gamma(\vec{p},T(\tau))$ is still from quasifree mechanism in QGP and SU(4) meson exchange model in hadronic phase, but with p_T dependence.

The sequential regeneration of J/ψ and $\psi(2S)$ has rather dramatic consequences on their p_T spectra of their regeneration component. Following [105], we approximate the p_T spectra of the regeneration components with the standard blast-wave expression,

$$\frac{dN_{\Psi}^{\mathrm{reg}}}{p_T dp_T}=N_0(b)m_T\int_0^R rdrK_1\left(\frac{m_T\cosh\rho(r)}{T}\right)I_0\left(\frac{p_T\sinh\rho(r)}{T}\right) \tag{3.3}$$

implying thermalized charm-quark distributions. The $m_T=\sqrt{p_T^2+m^2}$ is the transverse mass.

3.2.3 Uncertainty in the Calculation

It was shown in experiments that the pp spectra for $\psi(2S)$ is harder than J/ψ pp spectra (at the LHC energy, see [139, 140]). The hardness of pp spectra can severely influence the $R_{\mathrm{AA}}(\psi(2S))$ over $R_{\mathrm{AA}}(J/\psi)$ double ratio considering the p_T cut. It becomes more pronounced for a high-p_T cut at 6.5 GeV.

We parameterize the pp spectra with

$$\frac{\mathrm{d}^2N}{d^2p_T}=\frac{N}{\left(1+\left(\frac{p_T}{D}\right)^2\right)^A}. \tag{3.4}$$

The parameters are chosen as A=6.0 (5.9), B=5.65 (6.48) for J/ψ ($\psi(2S)$, $\chi_c(1P)$) at 2.76 TeV, A=3.9 (3.7), B=4.3 (5.1) for J/ψ ($\psi(2S)$, $\chi(1P)$) at 5.02 TeV by fitting to the experimental data. To simplify the calculation, we do not include variation of pp-spectra parameters.

One essential uncertainty which significantly influence the double ratio, is the average regeneration time at which we calculate the p_T spectra at the regeneration hypersurface. We can estimate the regeneration time from time evolution of regenerated $N_\Psi^{\rm reg}(\tau)$, see Fig. 3.5. It is not so easy to extract only one regeneration time for one specie, but rather an uncertainty range. For $\psi(2S)$, there is no p_T-spectra data available, so we estimate it according to the time evolution of regeneration component. The regeneration time for J/ψ can majorly change the double ratio for the intermediate p_T cut at 3.0 GeV but not so severely for the high-p_T cut at 6.5 GeV. That is because the regenerated J/ψ are accumulated at low p_T and highly suppressed at high p_T.

The regeneration J/ψ temperature could be chosen as $\bar{T}_{\rm reg}\simeq$180 MeV (middle of mixed phase, as a baseline calculation. In order to study the influence of regeneration time to the double ratio, variation of the regeneration temperature as $\bar{T}_{\rm reg}\simeq$180 MeV, but from beginning of mixed phase to the end of mixed phase, will also be included in the calculation. As we see for the intermediate p_T cut, it can severely influence the double ratio because an intermediate p_T cut at 3.0 GeV cannot exclude all the regenerated J/ψ. The leaked tail of J/ψ spectra can influence the double ratio in the denominator.

The regeneration temperature is chosen as $\bar{T}_{\rm reg}\simeq$160-170 MeV for $\psi(2S)$. The choice of regeneration time for both J/ψ and $\psi(2S)$ are used at both 2.76 TeV and 5.02 TeV in order to make it energy independent and more consistency at different energies.

Other uncertainties included are 0-10 % shadowing in double ratio (5.02 TeV shadowing would be larger, but most of the shadowing are canceled in the double ratio), Cronin effect with broadening parameter $a_{\rm gN}$=0-0.2 $\rm GeV^2/fm$. Uncertainty in dissociation rates

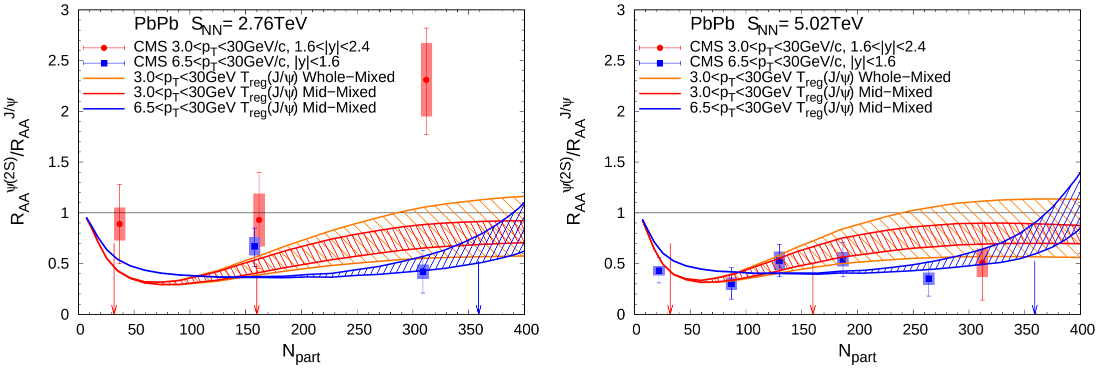

Figure 3.6: $R_{\mathrm{AA}}(\psi(2S))$ over $R_{\mathrm{AA}}(J/\psi)$ double ratio at 2.76 TeV (Left) and 5.02 TeV (Right) with the same pp spectra for J/ψ and $\psi(2S)$, compared with CMS data. The regeneration time for J/ψ is chosen as $\bar{T}_{\mathrm{reg}}{\simeq}180\,\mathrm{MeV}$, for $\psi(2S)$ is chosen as $\bar{T}_{\mathrm{reg}}{\simeq}160$-$170\,\mathrm{MeV}$. Uncertainty band is 0-10% shadowing, Cronin broadening parameter a_{gN}=0-0.2 $\mathrm{GeV}^2/\mathrm{fm}$. The red (orange) band is due to J/ψ $\bar{t}_{\mathrm{reg}}$ at middle of (from beginning to the end of) mixed phase for 3.0$<p_T<$30 GeV, The blue band is due to J/ψ $\bar{t}_{\mathrm{reg}}$ at middle of mixed phase for 6.5$<p_T<$30 GeV.

includes an additional factor of 3 for $\psi(2S)$ QGP rate and 2 for $\psi(2S)$ hadronic rate suggested by comparisons to p/d-A data [56]. A range of dissociation temperature T_{diss} (The temperature $\psi(2S)$ starts regeneration, different from regeneration temperature $T_{\mathrm{diss}}{\neq}\bar{T}_{\mathrm{reg}}$) for $\psi(2S)$ from 170 MeV to 180 MeV (end of mixed phase) is also included. The Fig. 3.5 shows the evolution for $T_{\mathrm{diss}}(\psi(2S))$=180 MeV (end of mixed phase).

To simplify the calculation, the charm cross sections $\frac{\mathrm{d}\sigma_{c\bar{c}}}{\mathrm{d}y}$ are fixed as 0.64(0.57) mb and 0.84(0.76) mb at mid-rapidity |y|<1.6 (forward rapidity 1.6<|y|<2.4) for 2.76 TeV and 5.02 TeV, guided from [109, 110] and extrapolated to the relevant energy and rapidity by FONLL [111, 112]. J/ψ cross section is roughly 0.58 % of charm cross section. The inclusive $\psi(2S)$ cross section is assumed to be 14 % of J/ψ's. The double ratio is not strongly influenced by uncertainty in the cross sections.

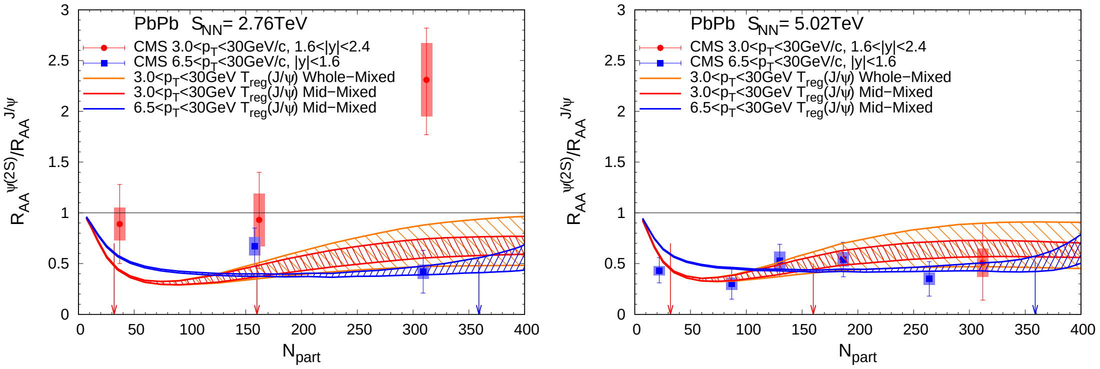

Figure 3.7: $R_{\mathrm{AA}}(\psi(2S))$ over $R_{\mathrm{AA}}(J/\psi)$ double ratio at 2.76 TeV (Left) and 5.02 TeV (Right) with different pp spectra for J/ψ and $\psi(2S)$, compare with CMS data. The regeneration time for J/ψ is chosen as $\bar{T}_{\mathrm{reg}}\simeq$180 MeV, for $\psi(2S)$ is chosen as $\bar{T}_{\mathrm{reg}}\simeq$160-170 MeV. Uncertainty band is 0-10% shadowing, Cronin broadening parameter a_{gN}=0-0.2 $\mathrm{GeV}^2/\mathrm{fm}$. The red (orange) band is due to J/ψ $\bar{t}_{\mathrm{reg}}$ at middle of (from beginning to the end of) mixed phase for 3.0<p_T<30 GeV, The blue band is due to J/ψ $\bar{t}_{\mathrm{reg}}$ at middle of mixed phase for 6.5<p_T<30 GeV.

3.2.4 Results of $\psi(2S)$ over J/ψ Double Ratio

We calculate the double ratio with uncertainties and find that regeneration time $\bar{T}_{\mathrm{reg}}$ for J/ψ gives quite big variation on double ratio.

In Fig. 3.6, the baseline at middle of the mixed phase can describe the J/ψ p_T spectra and can hardly give a double ratio greater than unity. Uncertainty on the regeneration time $\bar{T}_{\mathrm{reg}}$ for J/ψ gives great variation on double ratio. The band from the beginning to the end of mixed phase gives roughly 2-3 times thicker band than the middle of mixed phase band at central collision. The double ratio would be greater than unity with the upper limit choosing the J/ψ regeneration time at the beginning of mixed phase, where the J/ψ p_T spectra is very soft. We chose 200 MeV in our previous proceeding [57] but that is a bit extreme since the J/ψ regeneration yield at 200 MeV ($\tau\simeq$4 fm) is not yet reaching half of its final yield.

The harder pp spectra for $\psi(2S)$ brings down the double ratio, most obviously at high

p_T. For the most interesting 3.0 GeV cut, it brings down the double ratio so that even if we include a J/ψ regeneration time band within the whole mixed phase, we still can not get the double ratio larger than the unity, see FIG. 3.7. For the high-p_T region, it brings down the double ratio at central collision so that the band is within the experimental arrow.

3.3 Conclusions

We have discussed the J/ψ and $\psi(2S)$ production in A-A collisions in this section. The $R_{\rm AA}(N_{\rm part})$, $R_{\rm AA}(p_T)$, $v_2(p_T)$, $R_{\rm AA}(\sqrt{s})$ data and theoretical calculations of J/ψ show the importance of the regeneration in J/ψ production in A-A collisions.

The importance of the regeneration in the excited state $\psi(2S)$ production is further investigated. We calculate the $R_{\rm AA}(\psi(2S))$ over $R_{\rm AA}(J/\psi)$ double ratio at both 2.76 TeV and 5.02 TeV, based on the proposed "sequential regeneration" mechanism. Although, the double ratio could possibly be larger than 1 with the mechanism, it is not conclusive whether the "sequential regeneration" is supported with the current experimental measurements. In order to have better understanding of the $\psi(2S)$ production and the flow effect, one should directly measure the $R_{\rm AA}(p_T)$ of $\psi(2S)$. This will provide us direct comparison between the flow effect on J/ψ and $\psi(2S)$, and make extraction of the average regeneration time for $\psi(2S)$ available.

4. CHARMONIUM PRODUCTION IN p/d-A COLLISIONS*

In this section, we systematically study charmonium production in proton/deuteron-nucleus (p/d-A) collisions focusing on final-state effects caused by the formation of an expanding medium. We continue to use the rate equation approach within a fireball model as described in Chap. 2, adapted to the small systems in p/d-A collisions. The initial geometry of the fireball is taken from a Monte-Carlo event generator where initial anisotropies are caused by fluctuations. We calculate the centrality and transverse-momentum dependent nuclear modification factor ($R_{p/d\mathrm{A}}$) as well as elliptic flow (v_2) for both J/ψ and $\psi(2S)$ and compare them to experimental data from RHIC and the LHC.

The role of small colliding system (p-A/d-A collisions) has recently received renewed interest at RHIC and the LHC, including the quarkonium sector [120, 124, 141, 142, 143, 144, 145, 146, 122, 147, 148, 121, 149, 150, 151, 152]. A moderate J/ψ suppression (enhancement) has been found in both d-Au collisions at RHIC and forward (backward) rapidity p-Pb collisions at the LHC, largely consistent with CNM effects (most notably a nuclear anti-/shadowing of the initial parton distribution functions) [153, 154, 134, 136, 155, 156]. However, indications for a much stronger suppression of the $\psi(2S)$ have been observed in d-Au collisions at RHIC and more precisely established at the LHC, especially at backward rapidity (the nucleus-going direction) where the light-hadron multiplicity is the highest. These observations have been explained by final-state absorption on comovers [134], or, closely related, by dissociation reactions in the QGP and hadronic phase of a fireball formed in these reactions [56, 136] (both comover and thermal-suppression approaches feature comparable dissociation cross sections as well as fireball energy densities and

---

*Part of this section is reprinted with permission from “In-Medium Charmonium Production in Proton-Nucleus Collisions ” by Xiaojian Du and Ralf Rapp, 2019, Journal of High Energy Physics. 1903, 015 , Copyright 2019 by Springer.

timescales).

In the present section we expand on our earlier results for d-Au collisions [56] by extending the kinetic rate-equation framework to p-Pb collisions at the LHC, including the calculation of p_T spectra and rapidity dependencies. We construct an anisotropically expanding fireball based on initial asymmetries taken from Glauber model estimates of initial-shape fluctuations [157], which also allows us to compute charmonium elliptic flow. We recall that the rate equation approach necessarily includes regeneration contributions, which occur even in the presence of a single $c\bar{c}$ pair (sometimes referred to as "diagonal" regeneration or canonical limit). Their significance in p-Pb collisions has been suggested, *e.g.*, in Ref. [153].

The present section is organized as follows. In Sec. 4.1, we summarize the main components of the kinetic rate-equation/transport model developed for A-A collisions and describe its extension to p-A collisions, in particular the anisotropic fireball evolution. In Sec. 4.2, we discuss our theoretical results for the nuclear modification factor as a function of centrality and p_T, by first revisiting the d-Au system at RHIC, followed by 5.02 TeV and 8.16 TeV p-Pb collisions at the LHC, and compare to available experimental data from PHENIX, ALICE and LHCb. In Sec. 4.3, we discuss the v_2 results from our model in comparison to 8.16 TeV ALICE and CMS data. In Sec. 4.4, we summarize and conclude.

Our definition of backward (forward) rapidity in a p/d-A collisions follows the experimental convention of referring to the nucleus-going (proton-going) direction.

4.1 Transport Approach to Proton-Nucleus Collisions

We utilize the previously discussed transport approach and apply it to the p/d-A systems. In the kinetic rate equation Eq 2.54, the thermal relaxation time τ_c of charm quarks, has been assumed to be constant [75]) at τ_c=4.5 fm/c in A-A collisions. Langevin simulations of charm quarks in p-Pb collisions [158] have found that a significantly larger relaxation time, by a factor of 3-5, is necessary to be compatible with the observed $R_{p\mathrm{A}}$ of D-mesons; we therefore increase our previously employed relaxation time from 4 to 15 fm for small systems.

Here, we extend our previously used cylindrical volume expansion to allow for a elliptic deformation in the transverse plane,

$$V_{\mathrm{FB}} = (z_0 + v_z\tau)\,\pi R_x(\tau)R_y(\tau)\ , \tag{4.1}$$

where z_0 is the initial longitudinal size related to the formation time via $\tau_0 = z_0/\Delta y$, which we assume to be 0.8 fm, somewhat larger than in A-A collisions to account for the reduced overlap density in the smaller p-A systems. The transverse radii in x- and y-direction are parameterized as

$$\begin{aligned} R_x(\tau) &= R_0 - d + \frac{\sqrt{1+(a_x\tau)^2}-1}{a_x} && (4.2)\\ R_y(\tau) &= R_0 + d + \frac{\sqrt{1+(a_y\tau)^2}-1}{a_y}\ , && (4.3) \end{aligned}$$

with $R_0 = \frac{R_x^0+R_y^0}{2}$ and $d = \frac{R_y^0-R_x^0}{2}$. The initial radii R_x^0 and R_y^0 are estimated from the eccentricity of the initial distribution of a Monte-Carlo Glauber event generator [157],

$$e = \frac{(R_y^0)^2 - (R_x^0)^2}{(R_y^0)^2 + (R_x^0)^2} = 0.2\ , \tag{4.4}$$

with an initial transverse area $A_\perp^{p\mathrm{Pb}}$=$\pi R_x^0 R_y^0$=7.8 fm^2 [157]. The surface velocities of the fireball are computed with a relativistic acceleration ansatz

$$\begin{aligned} v_x(\tau) &= \frac{a_x\tau}{\sqrt{1+(a_x\tau)^2}} && (4.5)\\ v_y(\tau) &= \frac{a_y\tau}{\sqrt{1+(a_y\tau)^2}}\ . && (4.6) \end{aligned}$$

The parameters a_x=0.34/fm and a_y=0.13/fm are fixed in order to describe the light-hadron (pion, kaon, proton) p_T spectra and v_2 (see Fig 4.1) including their mass splitting via the anisotropic blastwave formula, Eq. (4.9), at thermal freezeout (Δa_T=$\frac{a_x-a_y}{2}$ controls the magnitude of the v_2 and a_T=$\frac{a_x+a_y}{2}$ its mass splitting). The average transverse acceleration of $a_T\sim$0.24/fm, relative to our default value of 0.1/fm in A-A collisions, reflects the larger pressure gradients in p-A collisions [159]. We have checked that our total $R_{p\mathrm{A}}$ results are rather insensitive to this value over a range of accelerations, a_T=0.1-0.4/fm. Larger accelerations slightly reduce both the suppression and regeneration (compensating each other) due to shorter fireball lifetimes (most of the hot-matter effects happen at relatively early times where longitudinal expansion dominates). Blastwave fits of light-hadron spectra [160] extract average transverse velocities of up to $\sim$0.5 which would indeed require an transverse acceleration closer to $\sim$0.4/fm in our fireball framework. However, the blastwave fits in p-Pb collisions might be more sensitive, relative to A-A collisions, to primordial hard components leaking into the fit range; thus a smaller transverse acceleration might be preferred. We therefore work with the values specified above unless otherwise stated. We also note that with the current fireball parameterization, the radii R_x and R_y cross at $\tau\sim 2\,$fm, implying a transition to an in-plane deformation, cf. Fig. 4.1. We have checked using different ansätze that this is a robust feature dictated by a rapid build-up of the v_2 while approximately recovering light-hadron v_2 data in p-A collisions. After the crossing, the in-plane acceleration should become smaller than out-of-plane. While this feature is not explicitly guaranteed by our parameterization, the chosen parameter values lead to a sign flip of the anisotropic component of the acceleration, $\Delta a(\tau) = \frac{\mathrm{d}\Delta v(\tau)}{\mathrm{d}\tau} = \frac{1}{2}\left(\frac{\mathrm{d}v_x(\tau)}{\mathrm{d}\tau} - \frac{\mathrm{d}v_y(\tau)}{\mathrm{d}\tau}\right)$, close to the crossing point of the radii at $\tau\simeq 2\,$fm. In any case, the net change in v_2 after this point is small and has very little bearing on our results.

Much like for different centralities in A-A collisions, one can expect significant vari-

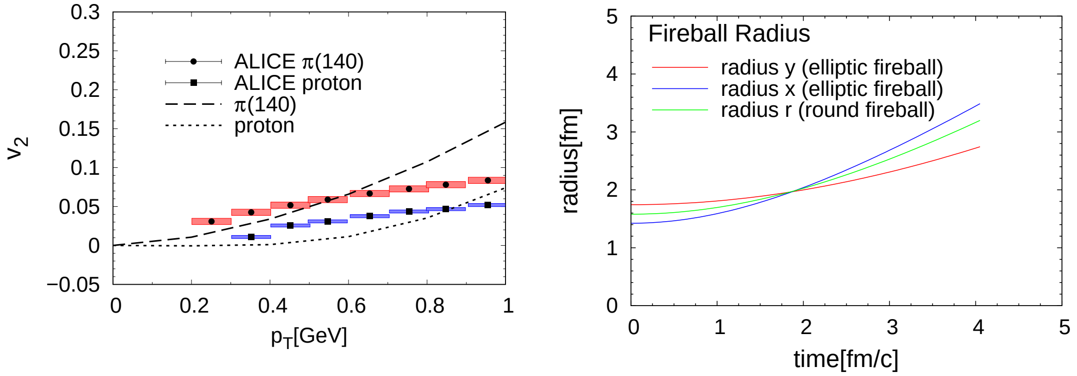

Figure 4.1: Left panel: Fit to light hadron v_2 from ALICE [161] with elliptic blastwave. Right Panel: Transverse radii for the expanding fireball in round (green line) and elliptic (red and blue lines) geometry for central p-Pb(5.02 TeV) collisions with a_T=0.24 /fm for the round fireball, and $a_{x,y}$=0.34,0.13 /fm for the elliptic fireball.

ations in the kinetic-freezeout temperature as a function of multiplicity in small systems: for a smaller total entropy the criterion that the mean-free-path is comparable to the fireball size (or inverse expansion rate) is reached at a larger particle density (or temperature). Guided by Ref. [160] we implement this effect by a centrality-dependent freezeout temperature as

$$T_{\rm fo}(N_{\rm ch}) = 145\ {\rm MeV}\left(\frac{S_{\rm tot}(N_{\rm ch})}{552}\right)^{-\frac{1}{12}} \quad . \tag{4.7}$$

The temperature evolutions following from this construction are summarized in Fig. 4.2 for 5.02 TeV and 8.16 TeV p-Pb collisions for different "centralities" (or rather, $N_{\rm ch}$) at forward and backward rapidities.

To compute p_T spectra within our approach, we decompose the rate equation into a solution for the primordial suppressed component, $N_{\rm prim}$, and the regeneration component, $N_{\rm reg}$. For the former, we solve a Boltzmann equation,

$$\frac{\partial f_{\rm prim}(\vec{x}_T,\vec{p}_T,\tau)}{\partial\tau} + \vec{v}_\Psi\cdot\frac{\partial f_{\rm prim}(\vec{x}_T,\vec{p}_T,\tau)}{\partial\vec{x}_T} = -\Gamma_\Psi(\vec{p}_T,T(\tau))f_{\rm prim}(\vec{x}_T,\vec{p}_T,\tau) \tag{4.8}$$

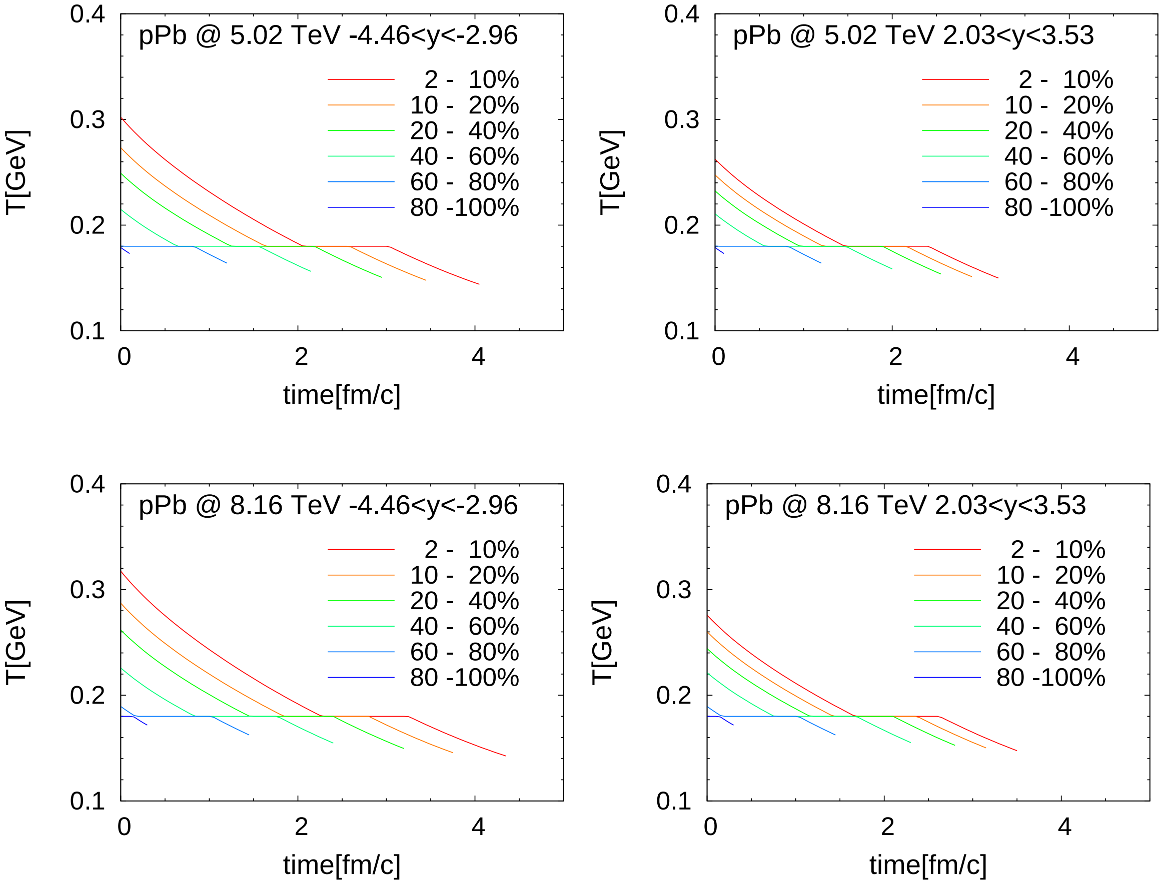

Figure 4.2: Temperature evolution from the elliptic fireball model for different centralities in p-Pb collisions at 5.02 TeV (upper panels) and 8.16 TeV (lower panels) at backward (left column) and forward (right column) rapidities.

where $\vec{v}_\Psi$ denotes the charmonium velocity in the lab frame. The 2-dimensional vectors $\vec{p}_T(p_T, \theta_p)$ and $\vec{x}_T(r, \theta_r)$ encode anisotropies in the transverse-momentum and coordinate plane, respectively, originating from different path lengths when traversing the elliptic fireball. The dissociation rate $\Gamma_\Psi(\vec{p}_T, T(\tau))$ is evaluated in the medium rest frame where temperature is defined. In principle, there is a difference between the proper time τ in the rate equation (Eq. (2.54)) and the longitudinal proper time $\tau=\sqrt{t^2 - z^2}$ in the Boltzmann equation (Eq. (4.8)). However, since we place a single fireball at the appropriate rapidity for a given experiment, we do not correct its thermal rapidity width for time dilation. We also neglect the Lorentz contraction effects in the transverse volume expansion when solving the Boltzmann equation. The maximal effect at the surface with v_T ~0.5 is less than 15%, which is well within the uncertainty range of our acceleration parameter of 0.1-0.4 /fm.

For the regeneration yield in the elliptic fireball, we use the yield obtained from the rate equation and approximate its p_T spectrum by an anisotropic blastwave description [24, 162],

$$\frac{\mathrm{d}N_{\mathrm{reg}}}{p_T \mathrm{d}p_T \mathrm{d}\theta_p} \propto m_T \int_0^{2\pi} \int_0^{R_{\max}(\theta_r)} \mathrm{d}\theta_r r \mathrm{d}r K_1(\beta)\, \mathrm{e}^{\alpha \cos(\theta_p - \theta_b)} \tag{4.9}$$

with $\alpha = \frac{p_T}{T} \sinh \rho(r, \theta_r, \tau)$, $\beta = \frac{m_T}{T} \cosh \rho(r, \theta_r, \tau)$ and transverse mass $m_T = \sqrt{p_T^2 + m_\Psi^2}$. The transverse-flow rapidity, $\rho(r, \theta_r, \tau) = \tanh^{-1}(v_\perp(r, \theta_r, \tau))$, is evaluated in terms of the fireball expansion velocity profile, $v_\perp(r, \theta_r, \tau) = (r/R_{\max}(\theta_r, \tau)) v_s(\theta_r, \tau)$, with surface velocity

$$v_s(\theta_r, \tau) = \frac{v_x(\tau) + v_y(\tau)}{2} + \frac{v_x(\tau) - v_y(\tau)}{2} \cos(2\theta_b(\theta_r, \tau)) \,. \tag{4.10}$$

Since the surface velocity on the semi-minor axis (x-direction, with θ_b=θ_r=0) is larger than on the semi-major axis (y-direction, θ_b=θ_r=π/2), it generates a positive v_2. The surface radius

$$R_{\max}(\theta_r, \tau) = \frac{1}{\sqrt{\left(\frac{\sin(\theta_r)}{R_y(\tau)}\right)^2 + \left(\frac{\cos(\theta_r)}{R_x(\tau)}\right)^2}} \tag{4.11}$$

depends on the coordinate angle θ_r and represents the boundary of the fireball, while

$$\theta_b(\theta_r, \tau) = \arctan\left(\left(\frac{R_x(\tau)}{R_y(\tau)}\right)^2 \tan(\theta_r)\right) \tag{4.12}$$

characterizes the direction of the medium flow perpendicular to the fireball boundary.

To compute the denominator of the p_T-dependent nuclear modification factor, and as an initial condition to the Boltzmann equation, we need the initial charmonium phase space distributions. We assume a factorization into transverse-momentum and coordinate space. For the p_T distribution we employ an ALICE parameterization [163, 164] of the spectra in pp collisions of the form

$$\frac{\mathrm{d}N_{pp}}{p_T\mathrm{d}p_T}(p_T) = f_{pp}(p_T) \propto \left(1+\left(\frac{p_T}{B}\right)^2\right)^{-A} , \tag{4.13}$$

with A=3.73(3.70), B=3.81(5.10) for J/ψ ($\psi(2S)$). The initial coordinate distribution is assumed to be a Gaussian,

$$f(\vec{x}(r,\theta_r)) = f_0\mathrm{exp}\left(-\frac{(r\mathrm{sin}(\theta_r))^2}{(R_y^0)^2} - \frac{(r\mathrm{cos}(\theta_r))^2}{(R_x^0)^2}\right) , \tag{4.14}$$

so that on the initial fireball boundary $f = f_0/\mathrm{e}$, and the enclosed elliptic area is equal to the initial transverse area ($\pi R_x^0 R_y^0$) within which all initial $c\bar{c}$ pairs are assumed to be produced (controlled by the normalization f_0).

The CNM effects are implemented in two steps. We first estimate the magnitude of the reduction (or enhancement) of the $c\bar{c}$ and Ψ yields from (anti-) shadowing using the EPS09-LO and EPS-NLO framework [90, 165, 166] at given rapidity and collision energy (defining an error band encoded in our final results). We then approximate the p_T dependence of the CNM effects by a Gaussian broadening to represent both the original Cronin effect as well as the p_T dependence of shadowing. See Eq. (2.122), Eq. (2.123) and Eq. (2.124) in Sec. 2.2.9.4. The path length $L(b)$ in the proton and deuteron can be neglected, $l^B(r_B, z_B) \simeq 0$; thus, only the size of nucleus A contributes to the mean path length. Treating the proton as a δ-function, $\hat{\rho}_B(r_B, z_B) = \frac{2}{\pi}\delta(r_B^2)\delta(z_B)$, and with B=1,

$\vec{r}=-\frac{\vec{b}}{2}$ and $r_A=b$, the effective path length simplifies to

$$L(b)=\frac{\int \mathrm{d}z_A l^A(b,z_A)\hat{\rho}_A(b,z_A)\mathrm{e}^{-\sigma_{\mathrm{abs}}(A-1)\int_{-\infty}^{z_A}\mathrm{d}z\hat{\rho}_A(b,z)}}{\int \mathrm{d}z_A\hat{\rho}_A(b,z_A)\mathrm{e}^{-\sigma_{\mathrm{abs}}(A-1)\int_{-\infty}^{z_A}\mathrm{d}z\hat{\rho}_A(b,z)}}\ . \tag{4.15}$$

In the limit of zero absorption, it can be further simplified as

$$L(b)=\frac{A}{\rho_0}\frac{\int_{-\infty}^{\infty}\mathrm{d}z\int_{-\infty}^{z}\mathrm{d}z'\hat{\rho}_A(b,z')\hat{\rho}_A(b,z)}{\int_{-\infty}^{\infty}\mathrm{d}z\hat{\rho}_A(b,z)} \tag{4.16}$$

which is used for the evaluation of the p_T broadening. We associate the CNM effects for the p_T dependence at the LHC with an effective broadening parameter of a_{gN}=0.1-0.2 GeV^2/fm reflecting the EPS09-LO vs. NLO uncertainty at backward rapidity, and a_{gN}=0.2-0.4 GeV^2/fm to represent the steeper trend and uncertainty from CGC calculations at forward rapidity [167, 155]. At mid-rapidity, we take an intermediate range of a_{gN}=0.1-0.3 GeV^2/fm.

The elliptic fireball allows the investigation of momentum anisotropies from final-state interactions. After obtaining the anisotropic spectra, $\mathrm{d}N_{\mathrm{AA}}/\mathrm{d}^2p_T(p_T,\theta_p)$, from the primordial and regeneration components, the elliptic flow coefficient is readily calculated as

$$v_2(p_T)=\frac{\int\limits_0^{2\pi}\frac{\mathrm{d}N_{\mathrm{AA}}}{\mathrm{d}^2p_T}(p_T,\theta_p)\cos(2\theta_p)\mathrm{d}\theta_p}{\int\limits_0^{2\pi}\frac{\mathrm{d}N_{\mathrm{AA}}}{\mathrm{d}^2p_T}(p_T,\theta_p)\mathrm{d}\theta_p}\ . \tag{4.17}$$

4.2 Nuclear Modification Factors for J/ψ and $\psi(2S)$

We are now in position to calculate the nuclear modification factors for charmonia in d-Au(0.2 TeV) collisions at RHIC (Sec. 4.2.1) and in p-Pb(5.02,8.16 TeV) collisions at the LHC (Sec. 4.2.2). The cross section inputs will be specified in the respective sections.

4.2.1 Deuteron-Gold Collisions at RHIC

Compared to our previous studies of d-Au collisions at RHIC [56], we here implement the updates as described in the previous section to ensure consistency with the new developments for p-Pb collisions. In particular, the fireball is extended to elliptic geometry, and has a smaller initial transverse area guided by the updates for p-Pb at the LHC described above; with a deuteron size approximately twice the proton size, and an inelastic NN cross section at RHIC of 2/3 of that at the LHC, we have $A_\perp^{d\mathrm{Au}} = A_\perp^{p\mathrm{Pb}} \cdot 2 \cdot 2/3$= 10.4 fm^2. As a result, the initial temperature in central d-Au now reaches $T_0 \simeq 245$ MeV. While this increases the hot-matter suppression, it slightly enhances the escape effect counter-acting the former. We also include regeneration contributions (neglected in Ref. [56]) which contribute up to ~0.05 at the $R_{d\mathrm{A}}$ level and also counter-act the increased hot-matter suppression.

The input cross sections remain unchanged, with $\frac{\mathrm{d}\sigma_{J/\psi}}{\mathrm{d}y}$=0.75 μb [168] for the J/ψ and $\frac{\mathrm{d}\sigma_{c\bar{c}}}{\mathrm{d}y}$=123 μb [169, 170] for all $c\bar{c}$ pairs. Cold-nuclear-matter effects are associated with EPS09 LO parton shadowing [90, 134] for both charmonium and open-charm production, whose centrality dependence we mimic by using a nuclear absorption cross section of σ_{abs}=0-2.4 mb, as before [56].

The model calculations are compared with PHENIX data [120] in Fig. 4.3. Fair agreement with experiment is found, very similar to our previous results [56].

4.2.2 Proton-Lead Collisions at the LHC

In addition to the information specified in Sec. 4.1, we here quote the input cross sections as determined from pp data at the LHC. For the J/ψ we use $\frac{\mathrm{d}\sigma}{\mathrm{d}y}$=3.0 and 3.6 μb at backward (-4.46<y<2.96) and forward (2.03<y<3.53) rapidity, respectively, at 5.02 TeV [106, 171], and $\frac{\mathrm{d}\sigma}{\mathrm{d}y}$=3.9(4.7) μb at backward (forward) rapidity at 8.16 TeV [150], and for $c\bar{c}$ pairs $\frac{\mathrm{d}\sigma}{\mathrm{d}y}$=0.51(0.61) mb at backward (forward) rapidity at 5.02 TeV and

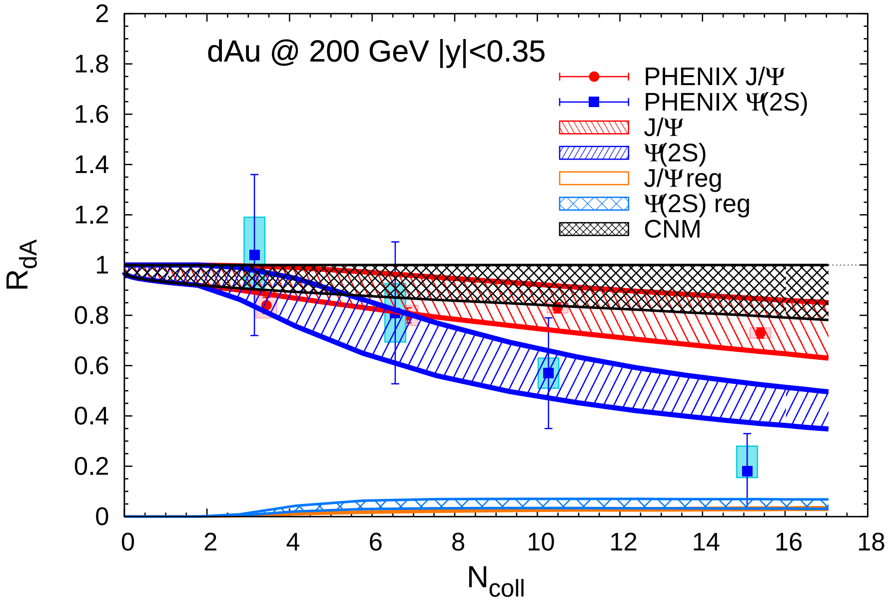

Figure 4.3: Centrality dependent $R_{d\mathrm{A}}$ for J/ψ (red bands) and $\psi(2S)$ (blue bands) in 200 GeV d-Au collision, compared with experimental data [120]. The orange (light blue) band is for the J/ψ ($\psi(2S)$) regeneration component. The CNM effect only (black band) represents the uncertainty due to shadowing (via an absorption cross section of 0-2.4 mb) and is the major source of uncertainty for the colored bands.

$\frac{\mathrm{d}\sigma}{\mathrm{d}y}$=0.66(0.80) mb at 8.16 TeV. This amounts to a fixed J/ψ over $c\bar{c}$ ratio of 0.58 % (as in our previous work [49, 56]). The charged-particle multiplicity determining the total entropy of the fireball in the respective rapidity regions is extracted from Refs. [172, 173] at 5.02 TeV and guided by Ref. [174] for 8.16 TeV. In the following, we first discuss the centrality dependence (Sec. 4.2.2.1) and then the transverse-momentum dependence (Sec. 4.2.2.2) of J/ψ and $\psi(2S)$ production in 5.02 and 8.16 TeV p-Pb collisions.

4.2.2.1 Centrality Dependence

In determining the centrality of a p-Pb collisions, we adopt the charged-particle multiplicity and relate it to the average binary collision number following Refs. [145, 172, 173, 174]. In Fig. 4.4, our J/ψ and $\psi(2S)$ calculations are compared to 5.02 TeV ALICE data.

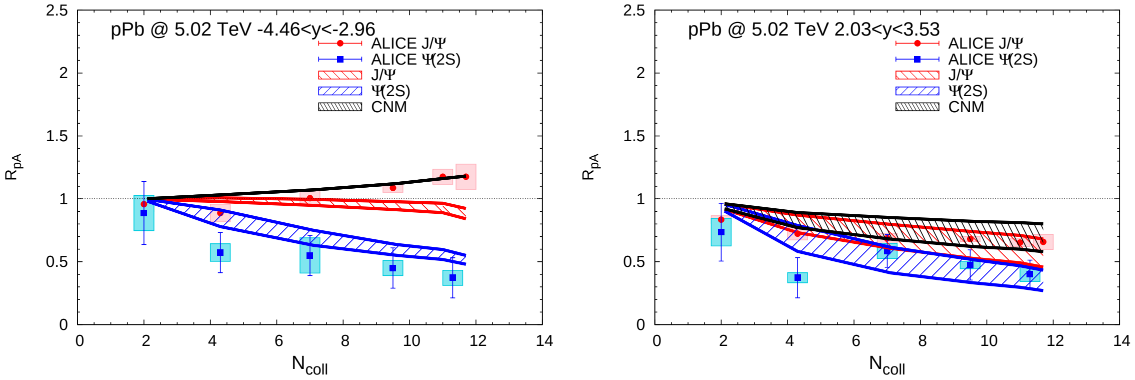

Figure 4.4: Centrality-dependent $R_{p\mathrm{A}}$ for J/ψ (red bands) and $\psi(2S)$ (blue bands) in 5.02 TeV p-Pb collisions, compared with experimental data [145, 146, 122]. The left (right) panel is for backward (forward) rapidity. The bands are due to (anti-) shadowing from EPS09 LO/NLO [165, 166] at forward (backward) rapidity, as illustrated by the black bands which do not include final-state effects.

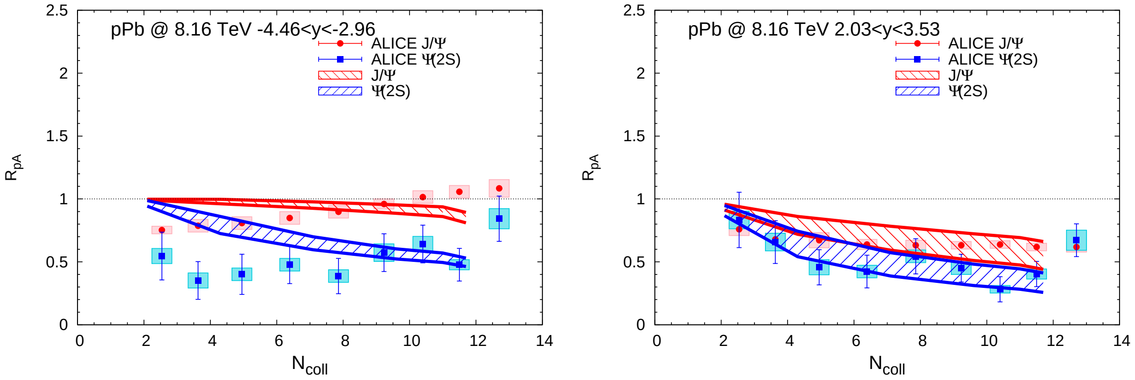

Figure 4.5: Centrality-dependent $R_{p\mathrm{A}}$ for J/ψ (red bands) and $\psi(2S)$ (blue bands) in 8.16 TeV p-Pb collisions, compared with experimental data [147]. The left (right) panel is for backward (forward) rapidity. The bands are due to anti/-shadowing from an EPS09 LO/NLO [165, 166] at forward (backward) rapidity.

The black bands show only the CNM effects, bounded by the anti-/shadowing obtained from EPS09-LO and EPS09-NLO calculations [165, 166] for both charmonia and open charm; as for the RHIC case, the centrality dependence of shadowing is mimicked by a nuclear absorption-type behavior, while for anti-shadowing we employ a parameterization of the pertinent lines shown in Fig. 3 of Ref. [134]. The CNM effects dominate the uncertainty bands at forward rapidity (charmonium formation time effects contribute $\sim$25%); the uncertainty bands at backward rapidity are entirely due to formation time effects (the same applies to Fig. 4.5). The shadowing-only bands already describe the J/ψ data quite well. A moderate hot-matter suppression of the J/ψ, together with a small regeneration contribution of about 0.05 (in units of the $R_{p\mathrm{A}}$), generate additional suppression which leads to a slight underestimation of the backward-rapidity data but is compatible with the forward-rapidity data. For the $\psi(2S)$ the much larger suppression in the hot fireball is, however, essential to approximately describe the suppression observed at both forward and backward rapidity.

In Fig. 4.5, we compare our J/ψ and $\psi(2S)$ calculations to 8.16 TeV ALICE data. There is a similar but slightly larger suppression compared to 5.02 TeV for both J/ψ and $\psi(2S)$. We see quite some discrepancy with the data for peripheral collisions at backward rapidity, but fair agreement with the data at forward rapidity.

4.2.2.2 Transverse-Momentum Dependence

Our results for the p_T dependence of charmonia, calculated as described in Sec. 4.1, are summarized in Figs. 4.6 and 4.7 for minimum-bias (MB) p-Pb collisions at 5.02 and 8.16 TeV, respectively. We recall that an additional uncertainty arises through the p_T dependence of shadowing, which is incorporated into the theoretical bands conservatively as the maximum uncertainty from all effects.

For the J/ψ, the calculated $R_{p\mathrm{A}}(p_T)$ at backward rapidities at both 5.02 and 8.16 TeV exhibits a slight depletion at low p_T followed by a mild maximum structure around $p_T \simeq 5$-6 GeV, largely caused by the nuclear p_T broadening. These trends become more pro-

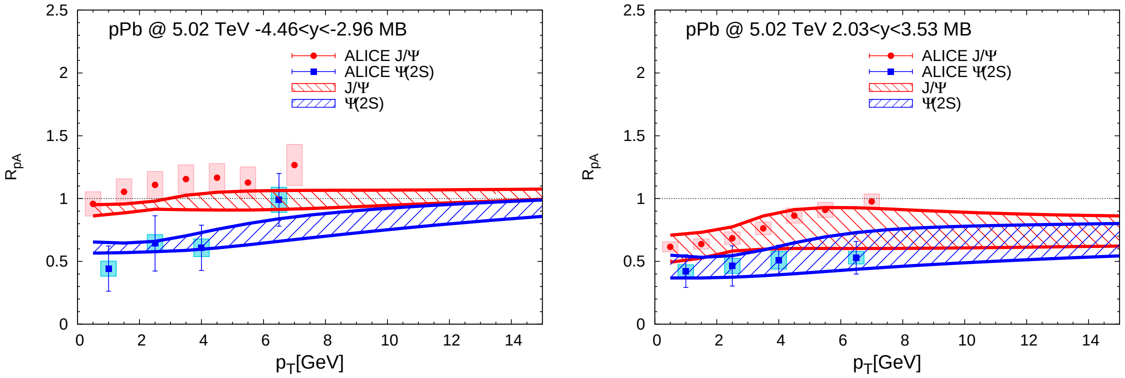

Figure 4.6: Nuclear modification factor as a function of transverse momentum for J/ψ (red bands) and $\psi(2S)$ (blue bands) in MB 5.02 TeV p-Pb collisions, compared to ALICE data [148, 121]. The left (right) panel is for backward (forward) rapidity. The uncertainty bands include variations in CNM and charmonium formation time effects.

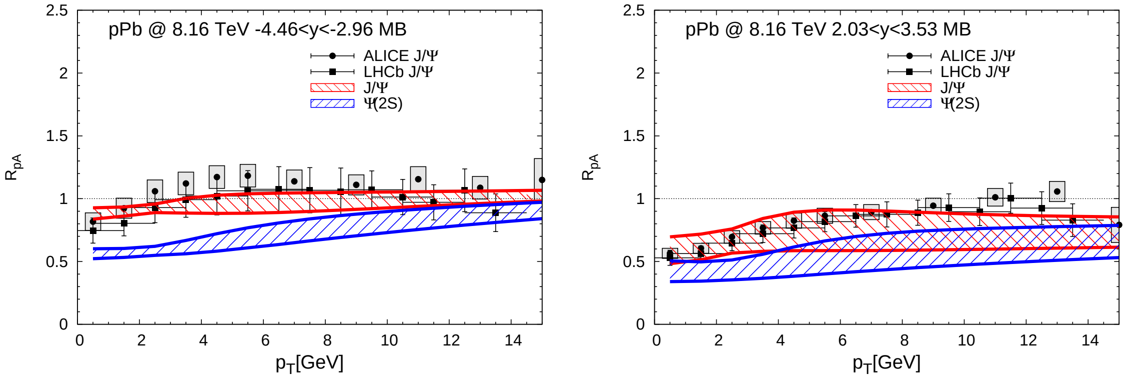

Figure 4.7: Same as Fig. 4.6 but for 8.16 TeV p-Pb collisions with ALICE and LHCb data [149, 150] at 8.16 TeV.

nounced at forward rapidity due to the generally increased strength of the CNM effects. Overall, the calculations are in agreement with ALICE and LHCb data within the theoretical and experimental uncertainties at both energies. The predictions for the $\psi(2S)$ reflect the stronger suppression already observed in the centrality dependence. Relative to the

J/ψ, most of the extra suppression is in the low-p_T region where the hot-matter effects are most pronounced while at higher p_T, formation time effects mitigate the suppression.

4.3 J/ψ and $\psi(2S)$ Elliptic Flow

We finally turn to our calculation of the charmonium elliptic flow at 8.16 TeV, where data have recently become available [151, 152]. The primordial component acquires a positive v_2 from the path length differences of the charmonium traversing the elliptic fireball, while the regeneration component acquires its v_2 from the anisotropic flow in a blastwave description. The primordial v_2 typically acquires values of 1-2%, while the v_2 of the regeneration component is much larger. However, since the latter, as mentioned above, is limited to $R_{p\mathrm{A}}$ contributions of around 0.05-0.10, its weight in the total v_2 is small. Our results shown in Fig. 4.8 predict a small v_2 of up to $\sim$2% for the J/ψ, and a larger value of up to $\sim$5% for the $\psi(2S)$, in high-multiplicity (most central) p-A collisions. We have checked tested that the maximal J/ψ v_2 generated from different versions of the fireball parameterization does not exceed 2%, essentially limited by the constraints from the initial eccentricity and the light-hadron v_2. The near-zero result for the predominantly primordial component of the J/ψ is a direct consequence of its small hot-matter suppression (and regeneration): if it does not interact significantly, it cannot sense the spatial (or momentum) anisotropies in the fireball. This is also the reason why the v_2 of the $\psi(2S)$ is much larger, since the hot medium effects on it are much larger. Since our J/ψ results clearly underestimate the experimental data, we must conclude that the observed v_2 cannot originate from final-state interactions alone. The similar v_2 at backward and forward rapidities (which have rather different multiplicities) is also in line with this conclusion. One last caveat we can think of are *elastic* interactions of the J/ψ (and $\psi(2S)$) in the expanding medium, which we have not accounted for. Very little is known about such interactions, and, in principle, one does not expect them to be large due to the parametrically smaller size of

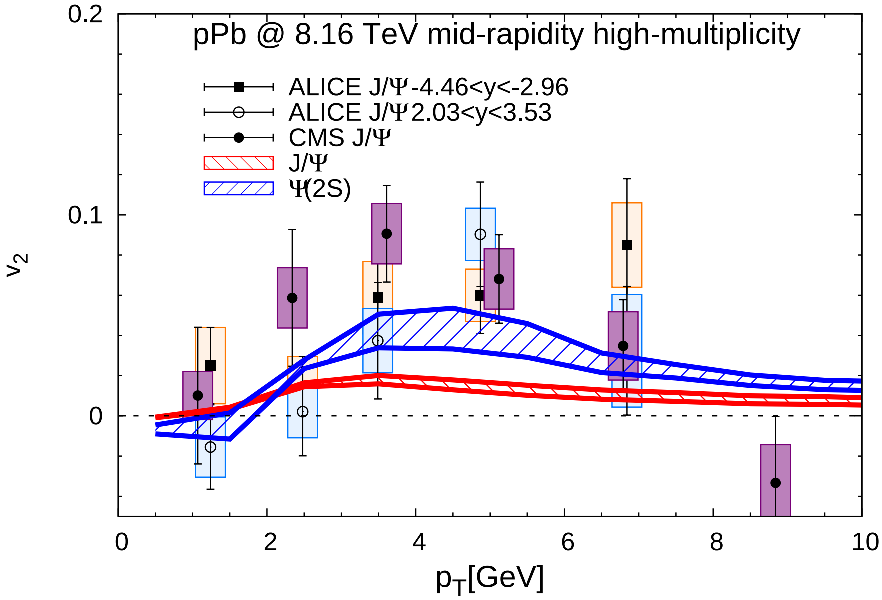

Figure 4.8: Transverse-momentum dependent v_2 for J/ψ (red band) and $\psi(2S)$ (blue band) at mid-rapidity in high-multiplicity p-Pb(8.16 TeV) collisions within the elliptic fireball model, compared to ALICE and CMS data [151, 152].

the J/ψ compared to light hadrons, while for the $\psi(2S)$, due to its small binding, almost any interaction can lead to break-up.

4.4 Conclusions

In the present section, we have extended our transport approach for in-medium quarkonia in heavy-ion collisions to calculate J/ψ and $\psi(2S)$ production in small collision systems at RHIC (d-Au) and the LHC (p-Pb). Cold-nuclear-matter effects estimated from nuclear parton distribution functions are combined with final-state effects treated within a rate-equation framework for an expanding fireball including dissociation and regeneration reactions in the QGP and hadronic phase. Our calculations provide a generally fair description of the measured centrality and transverse-momentum dependent nuclear modification factors measured in different rapidity regions, which differ in their CNM and hot-nuclear matter effects (some tension with data was found in the 8.16 TeV backward-rapidity $R_{p\mathrm{A}}(N_{\mathrm{coll}})$). This supports an interpretation where the J/ψ observables are mostly dominated by CNM effects while the loosely bound $\psi(2S)$ is subject to substantial suppression in the hot fireballs with initial temperatures of about 200-300 MeV and lifetimes of up to 4 fm. We also investigated the elliptic flow of J/ψ and $\psi(2S)$. In our setup, a nonzero v_2 results entirely from final-state interactions in the elliptic fireball. Since the final-state suppression (and regeneration) especially for the J/ψ is small, which is compatible with the small hot-matter effects on the $R_{p\mathrm{A}}$, the resulting v_2 is also small, not more than 2% (and larger, up to 5%, for the $\psi(2S)$); this disagrees with the large signal observed in the LHC data. We are therefore forced to conclude that this signal must be in large part due to initial-state (or pre-equilibrium) effects not included in our approach. This situation appears to be part of a bigger picture where the nuclear modification factor of hadrons, *e.g.*, D-mesons, shows little deviation from one while the v_2 is appreciable.

5. BOTTOMONIUM PRODUCTION IN A-A COLLISIONS[*]

The production of ground-state and excited bottomonia in ultrarelativistic heavy-ion collisions is investigated and summarized in this section within the kinetic-rate equation approach including regeneration. We augment previous calculations of our group [175] by an improved treatment of medium effects, with temperature-dependent binding energies and pertinent reaction rates, B-meson resonance states in the equilibrium limit near the hadronization temperature, and a lattice-QCD based equation of state for the bulk medium. In addition to the centrality dependence of the bottomonium yields we compute their transverse-momentum (p_T) spectra and elliptic flow with momentum-dependent reaction rates and a regeneration component based on b-quark spectra from a nonperturbative transport model of heavy-quark diffusion. The latter has noticeable consequences for the shape of the bottomonium p_T spectra. We quantify how uncertainties in the various modeling components affect the predictions for observables.

5.1 Bottomonium as a Probe of In-Medium QCD Force

Bottomonia offer a rich additional testing ground for in-medium QCD force via quarkonium transport, with stronger bind $\Upsilon(1S)$ state, and comparable bind $\Upsilon(2S)$ state to J/ψ. The role of regeneration processes for bottomonia is less obvious than it is for charmonia. In Pb-Pb($\sqrt{s}$=2.76 TeV) collisions at the LHC, the CMS Collaboration [55] reported a "sequential suppression" of bottomonia, characterized by an increasing level of suppression for $\Upsilon(1S)$, $\Upsilon(2S)$ and $\Upsilon(3S)$ states, following their ordering in vacuum binding energy. These data, along with the inclusive Υ data from the STAR and PHENIX Collaborations in Au-Au($\sqrt{s}$=0.2 TeV) and U-U($\sqrt{s}$=0.193 TeV) collisions at RHIC [52, 53, 176],

---

[*] Part of this section is reprinted with permission from "Color Screening and Regeneration of Bottomonia in High-Energy Heavy-Ion Collisions " by Xiaojian Du, Min He and Ralf Rapp, 2017, Phys.Rev. C96 no.5, 054901 , Copyright 2017 by APS.

can indeed be reasonably well described by models which do not include regeneration contributions [177, 178, 179]. This is more challenging for recent ALICE data at forward rapidity, which exhibit stronger suppression [54] than at mid-rapidity, even though a less dense medium is expected to form at forward rapidity. Cold-nuclear-matter (CNM) effects may play a role in this observation, as shadowing effects could be more pronounced at forward rapidity. Since the typical ratio of Υ relative to total $b\bar{b}$ production is only about 0.1% in elementary pp collisions (compared to $\sim$$1\%$ for charmonium to total $c\bar{c}$ production), even small regeneration yields in URHICs may give a significant contribution to the observed Υ production [180]. In Ref. [175], this was quantitatively investigated in a kinetic-rate-equation framework. On the one hand, it was found that regeneration contributions in 2.76 TeV Pb-Pb collisions are moderate for the $\Upsilon(1S)$ state, at a $\sim$$20\%$ level of the total yield in central Pb-Pb collisions (including feeddown from higher states). On the other hand, with a strong suppression of primordially produced $\Upsilon(2S)$ states [down to $\lesssim$$5\%$ in central Pb-Pb(2.76 TeV] collisions), the regeneration yield emerged as the dominant source for semi-central and central collisions. The calculated centrality dependence of the nuclear modification factors for both $\Upsilon(1S)$ and $\Upsilon(2S)$ turned out to be in approximate agreement with the CMS data, provided a so-called "vacuum binding scenario" or previously called "strong-binding scenario" (SBS) [175] was employed, where the bottomonium binding energies were assumed to be at their vacuum values. This was qualitatively motivated by theoretical scenarios with a heavy-quark (HQ) potential taken as the internal energy computed in lattice QCD (lQCD) [75]. Similar findings where also reported in other transport approaches [177, 181]. The magnitude of the regeneration contribution for the $\Upsilon(1S)$, however, does not suffice to account for the stronger suppression of the ALICE data at forward rapidity, relative to mid-rapidity. Clearly, the decomposition into primordial and regenerated components requires further studies. In the meantime, the CMS Collaboration has released p_T spectra for both $\Upsilon(1S)$ and $\Upsilon(2S)$ [182], providing an excellent opportunity for additional tests and tuning of model calculations [177].

In the present section we extend our group's previous calculations [175] of bottomonium kinetics in the fireballs of URHICs in several respects. For a more realistic treatment of the in-medium properties of bottomonia we implement in-medium binding energies as extracted from microscopic T-matrix calculations [75]. These affect both the inelastic reaction rates and the equilibrium limit of bottomonium abundances which figure in the regeneration reactions. The space-time evolution of the fireball is updated by using a lQCD-based equation of state (EoS) [85]. We compute the production yields of $\Upsilon(1S, 2S, 3S)$ states as well as their p_T spectra and the elliptic flow (v_2) based on 3-momentum dependent dissociation rates and b-quark spectra for regeneration processes which are taken from nonperturbative transport simulations (which give a fair description of open-bottom observables at the LHC [158]). In contrast to c quarks, b-quark spectra are not expected to reach near thermalization at the RHIC and the LHC, which has a significant impact on the p_T dependence of bottomonium regeneration. Since primordial Υ states are not expected to acquire a large v_2, their measured total v_2 may provide a greater sensitivity to regeneration processes than the inclusive yields or even p_T spectra. We also calculate bottomonium observables for 5.02 TeV Pb-Pb collisions as recently measured at the LHC.

The section is organized as follows. In Sec. 5.2 we briefly recall the basic ingredients of our kinetic-rate-equation approach, with emphasis on its improvements over previous work [175]. In particular, we scrutinize various mechanisms in the dissociation rates in the presence of in-medium effects on the bottomonium binding energies, improve the Υ equilibrium limits by accounting for B-meson resonance states near T_c (Sec. 5.2.1), and replace a massless-gas EoS in the fireball evolution with a parametrization from lQCD (Sec. 5.2.2); we also discuss how we calculate Y p_T spectra and their elliptic flow (Sec. 5.2.3), and the open-bottom and bottomonium input cross sections needed for phenomenology (Sec. 5.2.4). In Sec. 5.3 we start the systematic comparison of our updated results to available data with Au-Au and U-U systems at the RHIC including both centrality (Sec. 5.3.1) and p_T dependencies (Sec. 5.3.2). In Sec. 5.4 we turn to Pb-Pb(2.76 TeV) collisions at the LHC, studying centrality and rapidity dependencies for both the previously employed vacuum binding scenario (Sec. 5.4.1) and our updated approach (Sec. 5.4.2), conducting a sensitivity study of model parameters (Sec. 5.4.3), and then turning to p_T spectra (Sec. 5.4.4) and v_2 (Sec. 5.4.5). In Sec. 5.5 we provide predictions for Pb-Pb(5.02 TeV) collisions, again contrasting the previous vacuum binding scenario (Sec. 5.5.1) with the updated approach (Sec. 5.5.2), including comparisons to recently available data for $\Upsilon(1S)$, $\Upsilon(2S)$ and $\Upsilon(3S)$ states. In Sec. 5.6 we summarize our results in terms of an excitation function of the nuclear modification factor for both $\Upsilon(1S)$ and $\Upsilon(2S)$ in comparison to data from the RHIC and the LHC. In Sec. 5.7 we summarize and conclude.

5.2 Bottomonium Transport in Medium

In this section we utilize the kinetic-rate equation [84], summarized in Sec. 2.2.3 , as our simulation tool for the time evolution of bottomonium abundances in URHICs [180, 175]. We first review its basic framework and main transport parameters – reaction rate and equilibrium limit, in application to bottomonium sector – in Sec. 5.2.1, review the bulk medium evolution in Sec. 5.2.2, describe the calculation of the p_T spectra and elliptic flow of bottomonia in Sec. 5.2.3, and summarize our input cross sections to the rate equation for open bottom and bottomonia as constrained by pp data in Sec. 5.2.4.

5.2.1 Kinetic Rate Equation and Transport Coefficients for Bottomonium

The rate equation for a given Y state is characterized by loss and gain terms as is in Eq. (2.54), where the two transport coefficients are the inelastic reaction rate, Γ_Y, and the equilibrium limit, N_Y^{eq}. We include the bottomonium states $Y = \Upsilon(1S), \Upsilon(2S), \Upsilon(3S), \chi_b(1P)$ and $\chi_b(2P)$, where we combine the three states $\chi_{b0,1,2}$ into

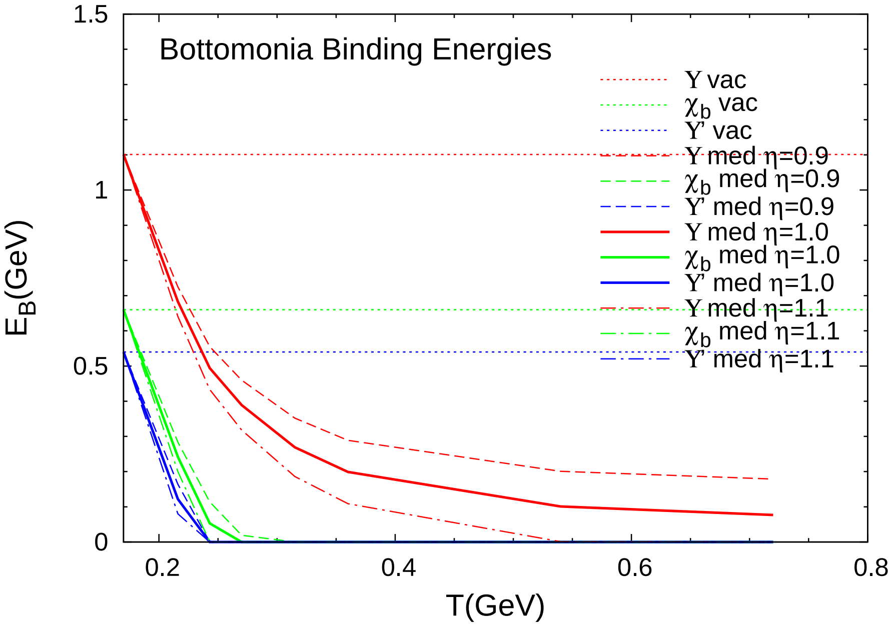

Figure 5.1: Bottomonium binding energies for the vacuum binding scenarios (dotted lines) [175] and T-matrix binding scenarios (TBS) with baseline value [75] η=1.0 (solid lines), and a 10% smaller (η=0.9, dashed lines) or larger (η=1.1, dash-dotted lines) reduction in $\Delta E_B(T)$; cf. Eq. (5.2). The red, green, and blue lines are for $\Upsilon(1S)$, χ_b, and $\Upsilon(2S)$ states, respectively.

a single one, as their vacuum mass splittings are within ∼60 MeV. Since the vacuum binding energies of most of these states, commonly defined as $E_B^Y = 2m_B - m_Y$, are significantly larger than the pseudo-critical QCD transition temperature, $T_{\rm pc}$, we neglect inelastic reactions in the hadronic phase (they may become important for $E_B^Y \lesssim T_{\rm pc}$, *i.e.*, for the $\Upsilon(3S)$, and $\chi_b(2P)$, similarly to the $\psi(2S)$ [56]) and focus on the kinetics in the quark-gluon plasma (QGP) down to a (pseudo-) critical temperature of $T_{\rm pc}$=170 MeV.

5.2.1.1 In-Medium Binding Energies and Dissociation Rates

The nature of the quarkonium dissociation rate in the QGP depends on the interplay of bound-state scales (*e.g.*, size and binding energy) and medium scales (*e.g.*, screening length (inverse Debye mass) and temperature) [47, 180, 183]. Our starting point is different scenarios for the in-medium binding energies, $E_B^\Upsilon(T)$, of the various bottomonium states. One may consider this as fundamental information that one would like to extract from the experimental data. This also includes the “melting" temperatures at which the states cease to exist, which generally do not coincide with a vanishing binding energy due to finite dissociation widths. However, the latter already affect the yields at temperatures (well) below the melting temperature, while the binding energies affect the dissociation mechanisms. In previous work [180, 175], the binding energies were bracketed by a “vacuum-binding scenario” (named “strong-binding scenario” or SBS in the previous work), where the vacuum binding was simply assumed at all temperatures, and a weak-binding scenario (WBS), which was based on a screened Cornell potential [184] with a perturbative screening mass, $m_D \sim gT$ (see Fig. 3 in Ref. [180] or Fig. 1 in Ref. [175]). These scenarios were coupled with appropriate dissociation mechanisms, *i.e.*, gluo-dissociation ($g + \Upsilon \to b + \bar{b}$) for the vacuum binding scenario and quasifree dissociation ($p + \Upsilon \to b + \bar{b} + p$ with $p = q, \bar{q}, g$) for the WBS.

In the present work we instead adopt in-medium binding energies predicted by thermodynamic T-matrix calculations [75] using internal-energy potentials, $U_{\bar{Q}Q}$, from lQCD. This choice for the underlying potential is motivated by a better agreement with quarkonium correlators and charmonium phenomenology [48] compared to more weakly coupled scenarios (such as the free energy, $F_{\bar{Q}Q}$), and also by yielding a much smaller (*i.e.*, more strongly coupled) heavy-quark diffusion coefficient which is preferred by open heavy-flavor phenomenology [158]. We denote the T-matrix binding scenario by TBS, and replot the temperature-dependent ground state binding energy by the red solid line in Fig. 5.1, as extracted from Fig. 27 left in Ref. [75]. We implement this together with the assumption of Υ bound-state masses fixed at their vacuum values. This allows us to extract the in-medium b-quark mass from the relation

$$m_{\Upsilon(1S)} = 2m_b(T) - E_B^{\Upsilon(1S)}(T) \;, \tag{5.1}$$

and subsequently use this expression to infer the binding energies, $E_B^Y(T)$, of the excited states, which are also shown in Fig. 5.1. The use of internal energies from different lQCD computations induces uncertainties of a few tens of percent in the T-matrix calculations of $E_B^{\Upsilon(1S)}(T)$. To account for this, we will also allow for two scenarios where the in-medium reduction of the $\Upsilon(1S)$ binding energy, $\Delta E_B(T) = E_B^{\text{vac}} - E_B(T)$, is decreased (increased) by 10%, $i.e.$,

$$E_B^{\eta}(T) \equiv E_B^{\text{vac}} - \eta \Delta E_B(T) \tag{5.2}$$

with η=0.9 (η=1.1). This scenario is shown by the dashed (dash-dotted) lines in Fig. 5.1. In principle, one could consider η as a parameter to be extracted from a best fit to data. It turns out that the baseline TBS (η=1.0) transitions from the vacuum binding scenario close to T_{pc} to the WBS at temperatures above $T \simeq 350$ MeV, where the binding energies of the excited states have vanished and the ground-state binding has dropped to about 200 MeV.

Next we turn to the bottomonium dissociation rates, starting with gluo-dissociation for $Y + g \to b\bar{b}$ given by [71, 72]

$$\Gamma_Y^{\text{gd}}(p_\Upsilon, T) = \int \frac{\mathrm{d}^3 p_g}{(2\pi)^3} d_g f_g(\omega_g, T) v_{\text{rel}} \sigma_{Yg\to b\bar{b}}(s) \;. \tag{5.3}$$

Here, $f_g(\omega_g, T) = (\exp\left(\frac{\omega_g}{T}\right) - 1)^{-1}$ is the Bose distribution of gluons (with degeneracy d_g=16), $s = (p^{(4)} + p_g^{(4)})^2$, and

$$v_{\text{rel}} = \frac{\sqrt{(p_1^{(4)} \cdot p_2^{(4)})^2 - m_1^2 m_2^2}}{\omega_1 \omega_2} \tag{5.4}$$

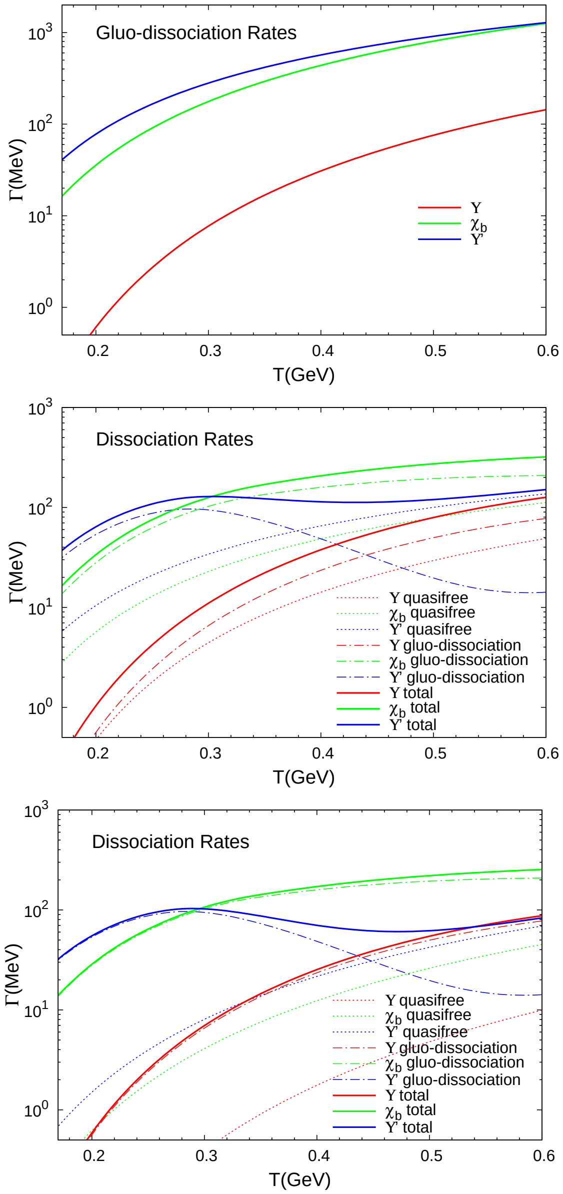

Figure 5.2: Bottomonium dissociation rates in QGP for the vacuum binding scenario using gluo-dissociation with massless (upper panel) or massive gluons (dash-dotted lines in the middle and lower panel). The middle and lower panels also show the rates from inelastic “quasifree" scattering off massive quarks and gluons (dotted lines) without (middle panel) and with (lower panel) interference corrections, and their sum with massive gluo-dissociation rates (solid lines). All rates are evaluated at zero Y 3-momentum with a strong coupling constant of g=2.0.

is the relative velocity of incoming particles. The gluo-dissociation cross sections for the different Y states are detailed in Appendix Sec. A.1. These rates have been utilized within the vacuum binding scenario in a heat bath of massless partons in Ref. [175] and are reproduced in the upper panel of Fig. 5.2. They are quite large, especially for the excited states, and were found to be compatible with the strong suppression of the $\Upsilon(2S)$ observed at the LHC. However, massless partons overestimate the EoS at given temperature, especially near $T_{\rm pc}$. Here we implement thermal gluon masses, $m_g = \sqrt{1/2(1+N_f/6)}gT$, which suppress the rates not only for low temperatures (where $m_g < E_B$), but even more so once the gluon mass becomes comparable to the binding energy, For example, at T=300 MeV, the rates for the excited states are suppressed by around a factor of 2; see the dash-dotted lines in the middle (or lower) panel of Fig. 5.2.

In addition to gluo-dissociation, next-to-leading order inelastic parton scattering, $p + Y \to b + \bar{b} + p$ with $p = q, \bar{q}, g$, can suppress (or regenerate) Y bound states. The pertinent rate reads

$$\Gamma_Y^{\rm qf}(p,T) = \sum_p \int \frac{{\rm d}^3 p_p}{(2\pi)^3} d_p f_p(\omega_p,T) v_{\rm rel} \sigma_{Yp\to b\bar{b}p}(s) \ , \tag{5.5}$$

where f_p is the Fermi or Bose distribution for p=q,$\bar{q}$ or g. In previous work we have treated inelastic parton dissociation in “quasifree" (qf) approximation, applicable for weakly bound states, where the recoil of the spectator heavy quark or antiquark is neglected while conserving 4-momentum [47]. For binding energies comparable to, or larger than, the temperature sizable corrections are expected due to interference effects between the parton scattering off the heavy quark and antiquark [185, 186]. In particular, in the limit of small bound-state size, $r \to 0$, the width vanishes since the colored medium parton does not resolve the color-neutral Y configuration anymore. These corrections amount to an interference factor $(1 - {\rm e}^{i\vec{q}\cdot\vec{r}})$ in the expression for the width, where $\vec{q}$ is the 3-momentum of the exchanged gluon. We implement the interference factor into the previously used quasifree width expression with the identification $\vec{q}^{\,2} \simeq -t$. The resulting Y widths for inelastic scattering off massive partons without and with interference correction are shown by the dotted lines in the middle and lower panels of Fig. 5.2, respectively. As expected, for the vacuum binding scenario, the interference effects give large corrections, suppressing the rates by typically a factor of around 5 (more/less at low/high temperature). The massive quasifree rates are generally well below the massive gluo-dissociation rates, except for the $Y(2S)$ for $T \gtrsim 450\,$MeV.

Our final scenario implements in-medium binding energies based on T-matrix calculations (TBS) of Ref. [75]. The reduced binding energies entail a substantial increase of the quasifree rates over the vacuum binding scenario, especially for the $\Upsilon(1S)$. Within the TBS, the latter shows significant sensitivity to the in-medium binding energy. For example, at T=350 MeV, when going from the η=1.0 baseline scenario to $\eta = 0.9$ ($\eta = 1.1$), where the binding energy varies from ∼200 MeV in the former to ∼300 MeV (∼100 MeV) in the latter, the width decreases (increases) by about 25% (50%), from 80 to 60 MeV (120 MeV), and similarly at other temperatures, see Fig. 5.3. Variations in the already small binding energy of the excited states have rather little impact on their rates. Furthermore, the gluo-dissociation mechanism in the TBS is only relevant in a small temperature window above $T_{\rm pc}$.

We note that the Bose-enhancement/Pauli-blocking factors, ($1 \pm f_p$), of the outgoing light partons in the quasifree reaction rate, Eq. (5.5), have been neglected. Their effect is an increase/decrease of the rate for outgoing gluons/quarks by less than 10%, respectively, which essentially cancel each other in the sum; see Fig. 5.4.

In Figs. 5.5, 5.6 and 5.7 we display the 3-momentum (p) dependence of the rates for the binding energy scenarios discussed above. Generically, gluo-dissociation differs from inelastic parton scattering in that the rate decreases with 3-momentum while that of the inelastic parton scattering increases. This is a direct consequence of the underlying

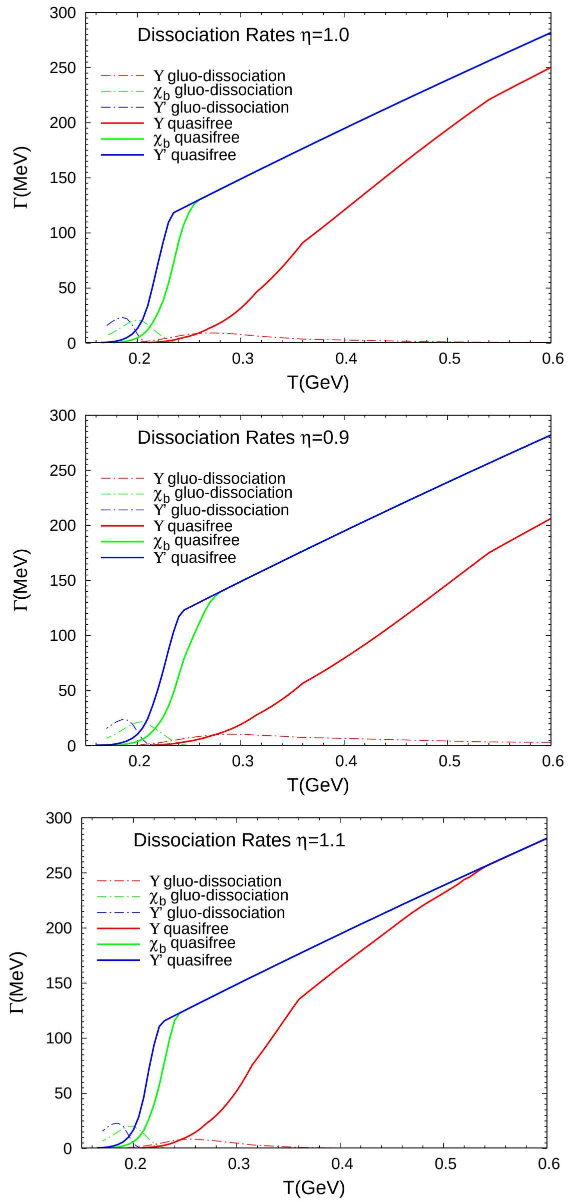

Figure 5.3: Bottomonium dissociation rates for the in-medium T-matrix binding scenario (TBS) in a massive thermal parton gas. Upper panel: baseline TBS (with η=1.0 in Fig. 5.1); middle (lower) panel: TBS with increased (decreased) binding energies η=0.9 (η=1.1); note that η=0 recovers the vacuum binding scenario. The dash-dotted and solid lines correspond to gluo-dissociation and inelastic parton scattering, respectively, while red, green, and blue colors represent $\Upsilon(1S)$, $\chi_b(1P)$ and $\Upsilon(2S)$ states, respectively. Dissociation rates are evaluated at bottomonium 3-momentum p=0. Interference corrections are included in the quasifree inelastic parton scattering.

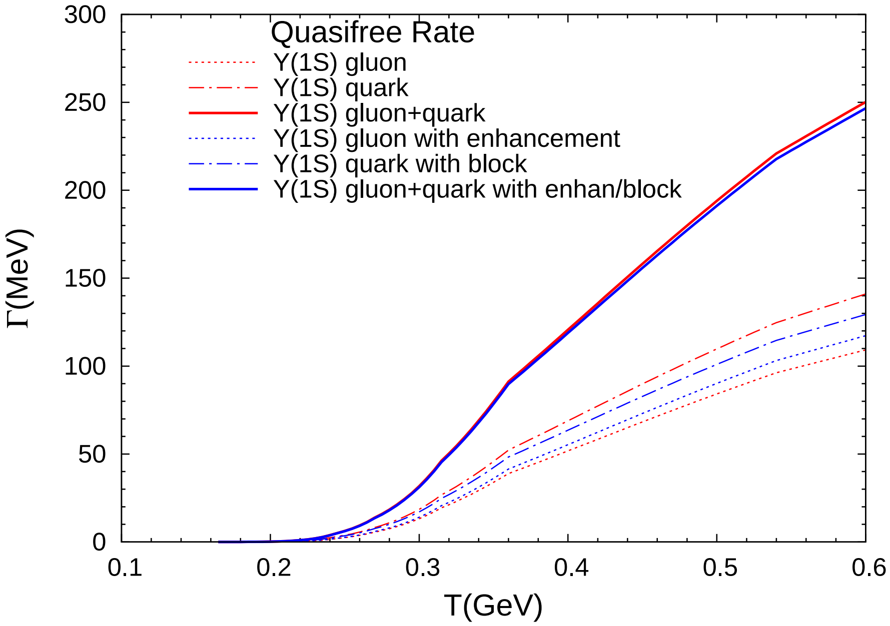

Figure 5.4: Parton-induced quasifree dissociation rates (solid lines) for the baseline in-medium T-matrix binding scenario (TBS with η=1.0) in a massive thermal parton gas with (blue lines) or without (red lines) final-state Fermi blocking and Bose enhancement factors for quarks (dash-double-dotted lines) and gluons (dotted lines), respectively. The rates are evaluated at p=0 for $\Upsilon(1S)$. Interference corrections are included.

matrix element (or cross section), which, as a function of incoming parton energy, peaks slightly above the binding energy for gluo-dissociation while it monotonically increases for inelastic parton scattering. The increase with p of the latter is more pronounced for larger binding energies, primarily due to the opening of phase space. For the vacuum binding scenario with massless partons (upper panel of Fig. 5.5) the p dependence for gluo-dissociation rate is rather flat at low T but starts to develop a decreasing trend for the excited states with increasing T. For the massive parton gas, this decreasing trend persists but is largely compensated once inelastic parton scattering is included (lower panel of Fig. 5.5).

For the TBS, the inelastic parton scattering at low T results in a marked increase of the rates with p for all Y states (upper panel of Fig. 5.6), mostly due to the phase space

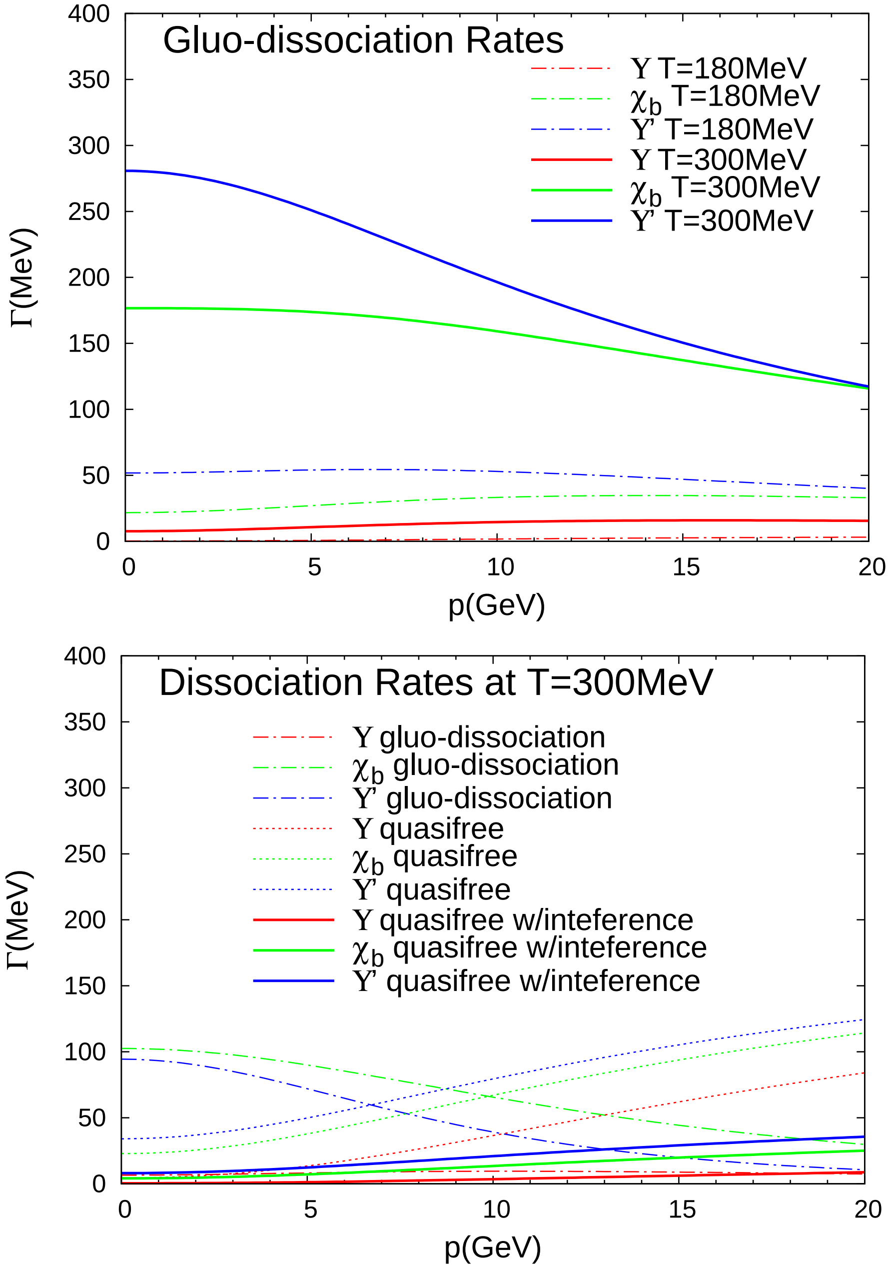

Figure 5.5: Three-momentum dependence of bottomonium dissociation rates in the vacuum binding scenario. Upper panel: gluo-dissociation with massless partons at T=180 MeV (dash-dotted lines) and T=300 MeV (solid lines). Lower panel: gluo-dissociation (dash-dotted lines) and inelastic parton scattering (solid lines) for massive partons, at a temperature of T=300 MeV. In both panels red, green and blue colors correspond to $\Upsilon(1S)$, $\chi_b(1P)$, and $\Upsilon(2S)$ states, respectively.

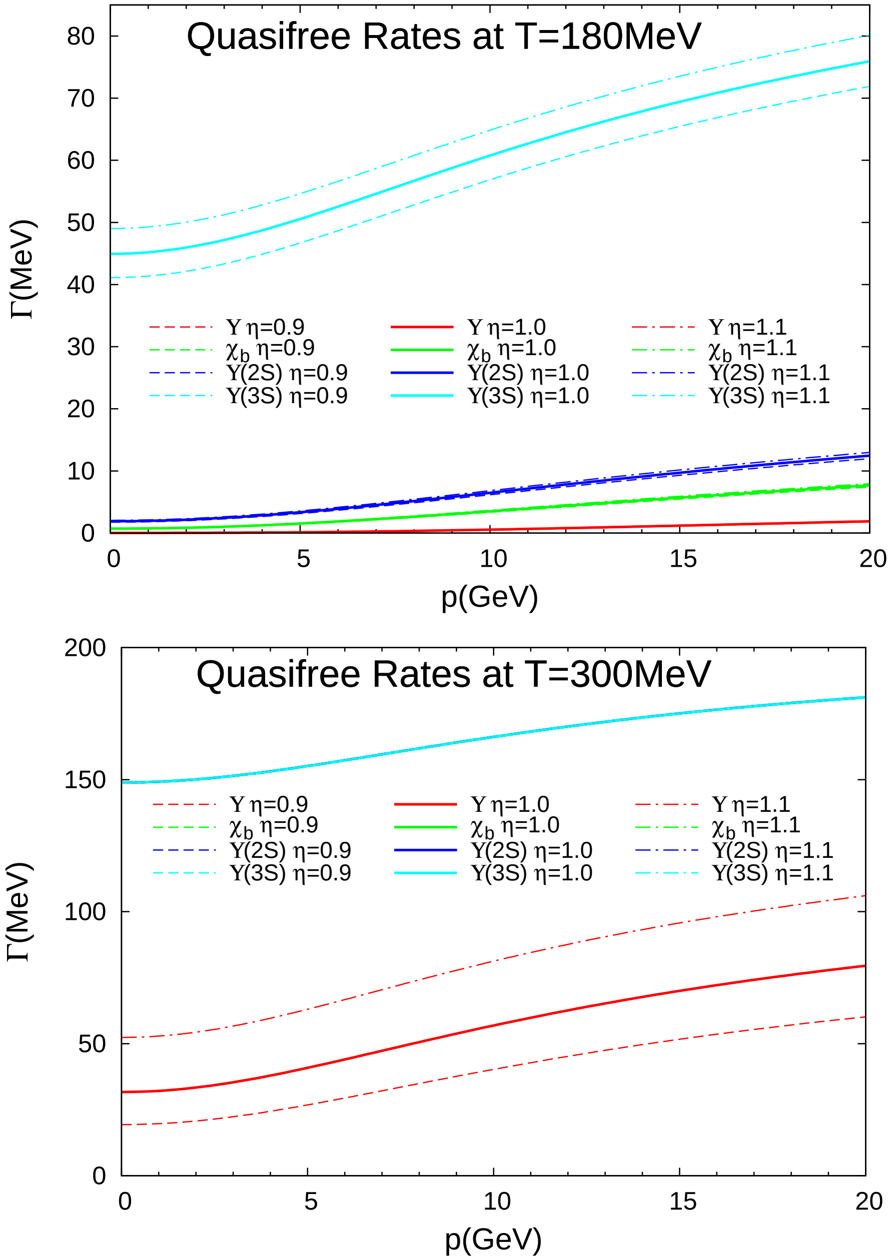

Figure 5.6: Three-momentum dependence of bottomonium dissociation rates from inelastic massive-parton scattering in the TBS for T=180 MeV (upper panel) and T=300 MeV (lower panel). The solid and dash-dotted lines correspond to the baseline TBS (η=1.0) and an increased (decreased) binding with η=0.9 (η=1.1), respectively. The red, green and blue lines correspond to the Υ, $\chi_b(1P)$, and $\Upsilon(2S)$ states, respectively.

restrictions at low p imposed by the still sizable binding energies. At higher T, where the binding is much reduced, this trend weakens (lower panel of Fig. 5.6). Note that at T=300 MeV, both $\Upsilon(2S)$ and $\chi_b(1P)$ have essentially become unbound so that the rate corresponds to twice the b-quark scattering rate. At this temperature, the $\Upsilon(1S)$ still carries a significant binding energy which induces a more pronounced p dependence (as well as sensitivity to the binding energy). The gluo-dissociation rates in the TBS are shown in Fig. 5.7. Except for the $\Upsilon(1S)$ at low T (where it is still strongly bound), they exhibit the usual decreasing trend with p. They vanish for the excited states as soon as they become unbound (for $T \lesssim 300$ MeV), while they are quite significant close to $T_{\rm pc}$ thus counter-balancing the increasing trend of the quasifree rate. This also applies to the $\Upsilon(1S)$ as long as its binding energy is larger than the temperature, *i.e.*, for $T \lesssim 300$ MeV.

5.2.1.2 Equilibrium Limit

Detailed balance between dissociation and formation reactions implies that the long-time limit of the rate equation recovers the equilibrium abundances of quarkonia, $N_Y^{\rm eq}$ in Eq. (2.54). Assuming that the total number of $b\bar{b}$ pairs is conserved throughout the fireball expansion, a pertinent conservation law is formulated with Eq. (2.90), where the sum of thermal densities of open ($n_{\rm op}$) and hidden ($n_{\rm hid}$) bottom states in the system is matched to $N_{b\bar{b}}$ via a temperature-dependent fugacity factor, γ_b, for each centrality of an A-A collision at given energy. The bottom densities are evaluated at each temperature according to the phase of the fireball at volume $V_{\rm FB}$, *i.e.*, with bottom quarks in the QGP for $T > T_{\rm pc}$, with bottom hadrons in the hadronic phase for $T < T_{\rm pc}$, and via a standard mixed-phase partitioning for $T = T_{\rm c}$ (if applicable, see Sec. 5.2.2 for a discussion on the mixed phase). The number of $b\bar{b}$ pairs at given impact parameter is determined by the production cross section $\sigma_{pp\to b\bar{b}}$, as $N_{b\bar{b}} = (\sigma_{pp\to b\bar{b}}/\sigma_{pp}^{\rm inel})N_{\rm coll}S_{\rm CNM}$, where $N_{\rm coll}$ denotes the number of primordial NN collisions upon first impact of the incoming nuclei and

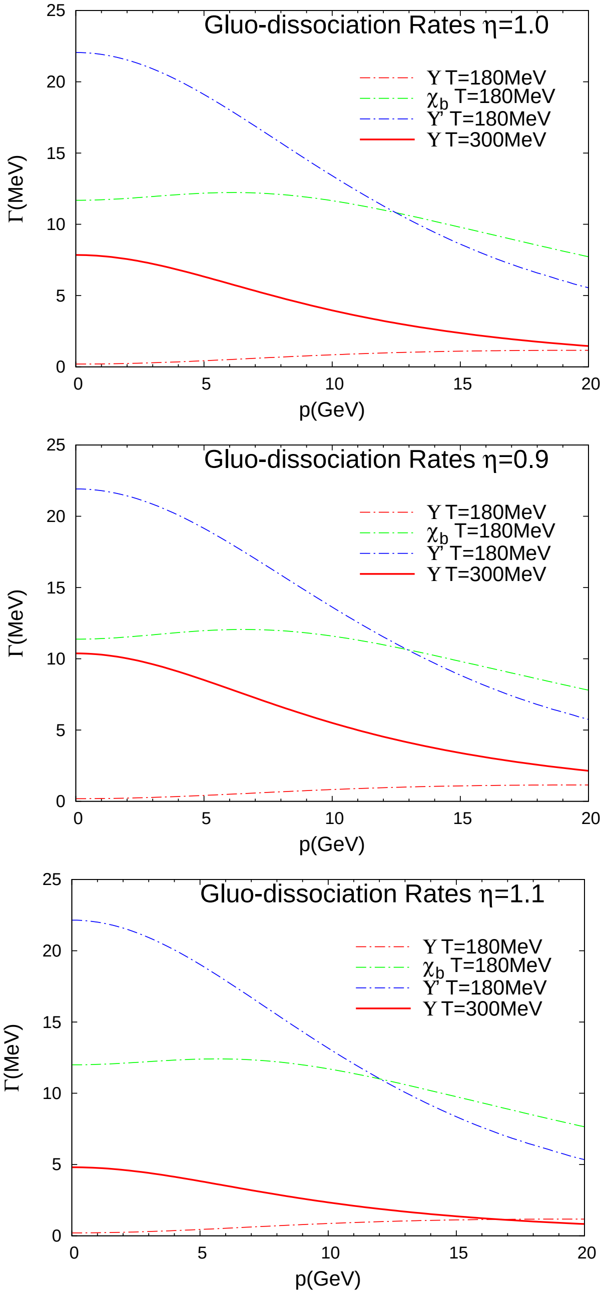

Figure 5.7: Three-momentum dependence of bottomonium rates from gluo-dissociation in the TBS for the baseline scenario (η=1.0, upper panel) and increased (decreased) binding η=0.9, middle panel (η=1.1, lower panel) at T=180 MeV (dash-dotted lines) and T=300 MeV (solid lines). The red, green and blue lines correspond to the Υ, $\chi_b(1P)$, and $\Upsilon(2S)$ states, respectively.

S_{CNM} is a shadowing correction. The thermal equilibrium value of a bottomonium state then follows Eq. (2.91).

Three corrections to the equilibrium limit are in order for a more realistic implementation in URHICs, two due to chemistry and one due to kinetics (sensitivity checks of the parameters associated with these corrections will be elaborated in Sec. 5.4.3).

The first correction concerns a finite correlation volume, V_{corr}, which accounts for the finite distance by which a single $b\bar{b}$ can separate after essentially point-like production [83]. This limits the available phase space, which we model following our previous treatment of charmonia [84]. The correlation volume V_{corr} in Eq. (2.94) is parameterized following the form of Eq. (2.92), so that for bottomonia: the initial radius of the correlation volume, $r_0 \simeq$0.8-1.2 fm, and the recoil velocity, $\langle v_b \rangle$=0.6-0.7, is estimated from B-meson p_T spectra (we use the central values unless otherwise noted). For an increasing number of $b\bar{b}$ pairs, the individual correlation volumes may overlap, eventually merging into a single one to be used in the canonical suppression factor.

The second correction, further following our previous treatment of charmonia [48], concerns the emergence of open-bottom hadronic degrees of freedom as T_{pc} is approached from above (this has recently been supported in an analysis of charm susceptibilities computed in lQCD [187]). Specifically, we allow for the existence of ground-state (S-wave) open-bottom mesons B, B^*, B_s, and B_s^* with their respective spin-isospin degeneracies. The presence of such states reduces the b-quark fugacity factor and thus the equilibrium limit of the bottomonium states in the rate equation. Going up in temperature from T_{pc}, we continuously phase out the resonance states around a switching temperature of T=220 MeV to obtain a smooth connection to b-quark only degrees of freedom, cf. Fig. 5.8. We will elaborate on the impact of this effect on the regeneration contribution to the Y R_{AA}'s in nuclear collisions in Sec. 5.4.3.

The third correction to the equilibrium limit arises from an incomplete kinetic equili-

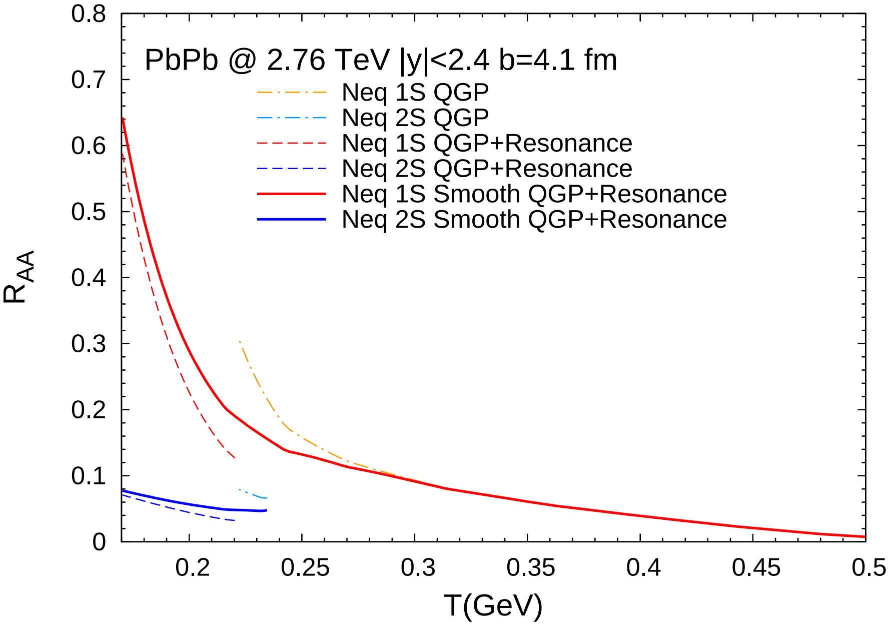

Figure 5.8: Equilibrium limits of Y states with (dashed lines) and without (dash-dotted lines) B-meson resonance degrees of freedom, and their smooth interpolation (solid lines) around a switching temperature of T=220 MeV. The red (blue) and yellow (light blue) curves are for b-quark only (b-quark plus resonance) degrees of freedom for $\Upsilon(1S)$ and $\Upsilon(2S)$, respectively. The default TBS parameter η=1.0 is used.

bration of b quarks in URHICs, which affects the gain term in the rate equation (Eq. (2.54)). In particular, harder b-quark spectra than the thermalized limit imply a reduced phase space overlap for bound-state formation. Following Ref. [74], we model this by implementing a thermal relaxation factor into the Y equilibrium limits, utilizing the form of Eq. (2.58) with a b-quark relaxation time of $\tau_{\rm b} \simeq 11\,{\rm fm}/c$ [75] at $\sim 2\,T_{\rm c}$, slowly increasing with decreasing temperature. This approximation has been supported by the studies in Ref. [188].

5.2.2 Bulk Medium Evolution and Solutions of the Rate Equation

To solve the rate equation, the space-time evolution of the medium is needed. We assume the conservation of total entropy in a cylindrical isotropic fireball expansion of volume following Eq. (2.97) and Eq. (2.105) with a relativistic transverse acceleration and initial transverse radius R_0 estimated from the Glauber model. The total entropy, in

Eq. (2.96), is determined from the final-state hadron multiplicities for a collision of given energy and centrality [*e.g.*, $S_{\rm tot}$=22000 for Pb-Pb(2.76TeV) covering Δy=1.8 units in rapidity]. For the QGP entropy density, $s_{\rm QGP}(T)$, we update our previous massless quasiparticle EoS with a fit to lQCD data [85] for the TBS calculation. The initial longitudinal length in the Bjorken limit is the product of the rapidity coverage of the fireball, Δy=1.8 and the QGP formation time, τ_0 [for which we use 0.2(0.6) fm at LHC (RHIC) energies], $z_0 = \Delta y \tau_0$. The relative longitudinal velocity of the two fireball fronts for Δy=1.8 corresponds to v_z=1.4, and the relativistic transverse acceleration is taken as a_T=0.1/fm. For the case of the quasiparticle EoS, we follow Eq. (2.106). with T_c=180 MeV (as used previously). The resulting time evolutions of temperature for central Pb-Pb(2.76 TeV) collisions for the massless quasiparticle EoS and the updated lQCD EoS are compared in Fig. 5.9. The nonperturbative effects lead to slightly higher (lower) temperatures in the transition (high-temperature) region, as well as the absence of a mixed phase. The lifetimes at the end of the QGP/mixed phase are within $\sim$10%.

We now have all ingredients to solve the rate equation. For later purposes, we will decompose it into two parts. The suppression-only (or primordial) part is obtained from

$$\frac{\mathrm{d}N_Y^{\rm prim}(\tau)}{\mathrm{d}\tau} = -\Gamma_Y(\tau) N_Y^{\rm prim}(\tau)\ , \tag{5.6}$$

which has the solution

$$N_Y^{\rm prim}(\tau) = N_Y^{\rm prim}(\tau_0)\, \exp\left(-\int\limits_{\tau_0}^{\tau} \Gamma_Y(\tau')\mathrm{d}\tau'\right)\ , \tag{5.7}$$

characterizing the primordially produced bottomonia which survive the fireball evolution. On the other hand, subtracting the rate equation of the primordial component from the

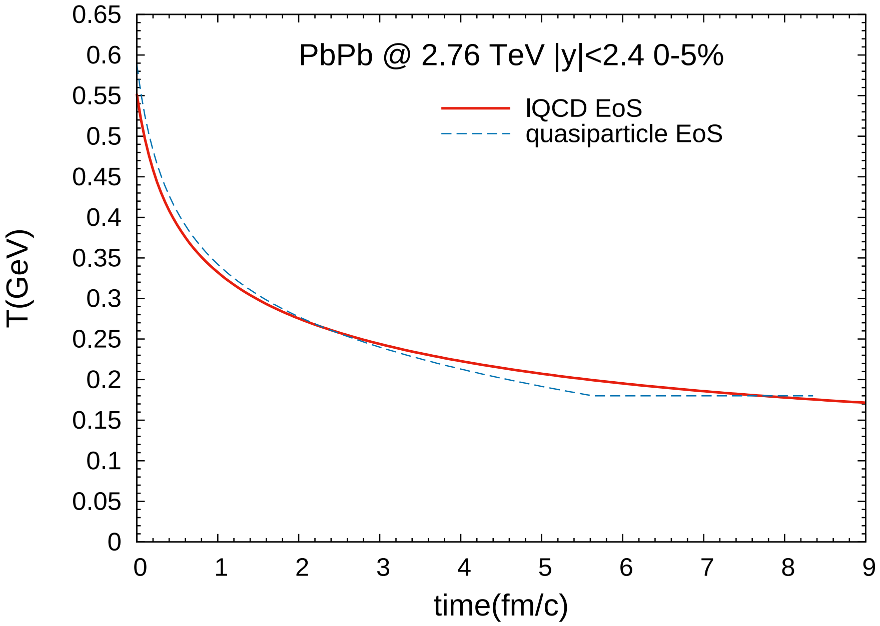

Figure 5.9: Temperature evolution of the expanding firecylinder for central Pb-Pb(2.76 TeV) collisions using a lattice EoS with T_{pc}=170 MeV (red solid line), compared to a massless quasiparticle EoS with mixed phase at T_{c}=180 MeV (blue dashed line).

total one yields an equation for the regenerated component,

$$\frac{\mathrm{d}N_Y^{\mathrm{reg}}(\tau)}{\mathrm{d}\tau} = -\Gamma_Y(\tau)\left[N_Y^{\mathrm{reg}}(\tau) - N_Y^{\mathrm{eq}}(\tau)\right], \tag{5.8}$$

whose solution can also be written in a closed form as

$$\begin{aligned} N_Y^{\mathrm{reg}}(\tau) &= \frac{\int\limits_{\tau_{\mathrm{diss}}}^{\tau} \Gamma_Y(\tau')N_Y^{\mathrm{eq}}(\tau')\exp\left(\int\limits_{\tau_{\mathrm{diss}}}^{\tau'} \Gamma_Y(\tau'')\mathrm{d}\tau''\right)\mathrm{d}\tau'}{\exp\left(\int\limits_{\tau_{\mathrm{diss}}}^{\tau} \Gamma_Y(\tau'')\mathrm{d}\tau''\right)} \\ &= \int\limits_{\tau_{\mathrm{diss}}}^{\tau} \Gamma_Y(\tau')N_Y^{\mathrm{eq}}(\tau')\mathrm{e}^{-\int\limits_{\tau'}^{\tau}\Gamma_Y(\tau'')\mathrm{d}\tau''}\mathrm{d}\tau' \end{aligned} \tag{5.9}$$

where the total lifetime of the fireball, τ=τ_{f}, is given by the end of the QGP/mixed phase. The exponential factor $\mathrm{e}^{-\int_{\tau'}^{\tau}\Gamma_Y(\tau'')\mathrm{d}\tau''}$ in the last line represents the in-medium suppression of the regenerated quarkonia. The lower integration bound $\tau_{\rm diss}$ characterizes the time in the fireball evolution where the temperature has dropped to the dissociation temperature of a given Y state, below which regeneration becomes operative. For the TBS, we have $T_{\rm diss}{\simeq}260$ MeV, 240 MeV and 190 MeV for $\chi_b(1P)$, $\Upsilon(2S)$ and $\Upsilon(3S)$, respectively. The initial condition, $N_Y^{\rm prim}(\tau_0) = N_{\rm coll}\frac{\sigma^{\rm tot}_{pp\to Y}}{\sigma^{\rm inel}_{pp}} S^Y_{\rm CNM}$ for the Y numbers includes CNM effects, in particular nuclear shadowing, calculated from the Glauber model (nuclear absorption is included at the RHIC but neglected at the LHC due to the short nuclear passage time).

5.2.3 Transverse-Momentum Spectra and Elliptic Flow

The rate equation approach above provides the 3-momentum inclusive yields of the produced bottomonia. The explicit 3-momentum dependence of the yields can be recovered in an approximate way by utilizing the decomposition into primordial and regenerated components discussed above, following Ref. [105]. For the primordial component, one straightforwardly solves the space-time dependent Boltzmann equation for the bottomonium phase space distribution function while for the regeneration component a coalescence model is employed. This is elaborated in more detail in the respective Secs. 5.2.3.1 and 5.2.3.2, while Sec. 5.2.3.3 discusses our evaluation of the bottomonium elliptic flow.

5.2.3.1 Transverse-Momentum Spectra of Surviving Primordial Bottomonia

Without a gain term (and without a mean field), the Boltzmann transport equation for the bottomonium phase space distribution, f_Y, reads

$$\frac{\partial f_Y(\vec{x},\vec{p},\tau)}{\partial\tau} + \vec{v}\cdot\frac{\partial f_Y(\vec{x},\vec{p},\tau)}{\partial\vec{x}} = -\Gamma_Y(\vec{p},T(\tau))f_Y(\vec{x},\vec{p},\tau) \tag{5.10}$$

where $\vec{v} = \vec{p}/E_p$ denotes the bottomonium velocity ($E_p^2 = m_Y^2 + p^2$) and $\Gamma_Y(p,T)$ the 3-momentum dependent dissociation rate (as displayed in Figs. 5.5, 5.6, and 5.7). Its solution can be cast in the form

$$f_Y(\vec{x},\vec{p},\tau) = f_Y(\vec{x}-\vec{v}(\tau-\tau_0),\vec{p},\tau_0)\mathrm{e}^{-\int\limits_{\tau_0}^{\tau}\Gamma_Y(\vec{p},T(\tau'))\mathrm{d}\tau'} , \tag{5.11}$$

from which p_T spectra can be extracted assuming boost invariance as

$$\frac{\mathrm{d}^2N_Y(p_T,\phi)}{\mathrm{d}^2p_T} = \int f_Y(\vec{x}_T,\vec{p}_T,\tau)d^2x_T\ . \tag{5.12}$$

The initial phase-space distribution, $f_Y(\vec{x},\vec{p}_T,\tau_0) = f_Y^{\mathrm{Glb}}(\vec{x})f_Y^{\mathrm{AA}}(\vec{p}_T)$, is factorized into p_T spectra taken from experimental data in pp collisions and a Glauber model for the spatial distribution,

$$f_Y^{\mathrm{Glb}}(\vec{x}_T) = \int \rho_A(\vec{x}_T+\vec{b}/2,z)\rho_A(\vec{x}_T-\vec{b}/2,z')\mathrm{d}z\mathrm{d}z' \tag{5.13}$$

for an A-A collision at impact parameter b.

We furthermore include formation time effects [98, 97, 99] to account for the finite time for the bound state to develop from the primordially produced $b\bar{b}$ wave package. This evolution tends to reduce the suppression rate, intuitively associated with a geometric expansion of the wave package from its near point-like production to the bound-state size [189]. Accordingly, we assume the formation time τ_{form} to depend on the vacuum binding energy, and correct the dissociation rate for $\tau \leq \tau_{\mathrm{form}}\gamma$ as

$$\alpha_Y(\vec{p},T(\tau)) \equiv \Gamma_Y(\vec{p},T(\tau))\frac{\tau}{\tau_{\mathrm{form}}}\frac{m_Y}{\sqrt{p^2+m_Y^2}}\ . \tag{5.14}$$

in the (early) evolution of the primordial p_T spectra. The explicit formation time values for $\Upsilon(1S)$, $\Upsilon(2S)$ and $\Upsilon(3S)$ are chosen as 0.5, 1.0 and 1.5 fm, respectively. The latter two are close to typical values used for the J/ψ and χ_c, as they have comparable binding energies [$E_B(J/\psi)\simeq$640 MeV vs. $E_B(\Upsilon(2S))\simeq$540 MeV, and $E_B(\chi_c)\simeq$230 MeV vs. $E_B(\Upsilon(3S))\simeq$200 MeV]. The inverse Lorentz-γ factor, $\gamma^{-1} = \frac{m_Y}{\sqrt{p^2+m_Y^2}}$, suppresses the high-$p_T$ reaction rates especially for excited states which have larger formation times. The reduced primordial suppression at high p_T counterbalances the p_T dependence in the thermal dissociation rates.

5.2.3.2 Transverse-Momentum Spectra from Regeneration

The momentum spectra of regenerated quarkonia carry the imprint of the momentum distributions of the recombining heavy quarks (or mesons). For charmonia, the regeneration typically occurs several fm/c into the evolution of the fireball, where charm-quark spectra, with a thermal relaxation rate of a few fm/c, are probably not far from their equilibrium distribution. Thus, the regenerated charmonia can be rather well approximated by a blast-wave description close to $T_{\rm pc}$, which is supported by the momentum spectra measured at the LHC [118]. The situation changes for bottom(onium), primarily because the $\sim$3 times larger b-quark mass, relative to c quarks, implies a factor 3 longer thermal relaxation times, and, to a lesser extent, because bottomonia are formed earlier in the fireball evolution, due to their larger binding energies. Therefore, approximating regenerated bottomonia with a thermal blast-wave expression cannot be expected to be accurate. Instead, we here resort to an instantaneous coalescence model [190], which allows us to use more realistic non-equilibrium transverse-momentum spectra of b quarks as input. We take these spectra from relativistic Langevin simulations of heavy quarks [158] in a hydrodynamic background medium (akin to the fireball evolution used for the rate equation) with nonperturbative heavy-quark transport coefficients which are computed from the same underlying T-matrix interactions [75] as the bottomonium binding energies discussed in Sec. 5.2.1.1.

The expression for the 2-differential p_T spectra of an Y meson formed through instantaneous coalescence from bottom quark and antiquarks with p_T distributions, $\mathrm{d}^2N_{b,\bar{b}}/\mathrm{d}^2p_T$

(or $\mathrm{d}^2N_Y^{\mathrm{coal}}/\mathrm{d}^2p_T$), is given by [190]

$$\begin{aligned}
\frac{\mathrm{d}^2N_Y^{\mathrm{coal}}(p_T,\phi)}{\mathrm{d}^2p_T} &= C_{\mathrm{reg}}\int \mathrm{d}^2p_{1t}\mathrm{d}^2p_{2t}\frac{\mathrm{d}^2N_b}{\mathrm{d}^2p_{1t}}\frac{\mathrm{d}^2N_{\bar{b}}}{\mathrm{d}^2p_{2t}} \\
&\times \delta^{(2)}(\vec{p}_T-\vec{p}_{1t}-\vec{p}_{2t}) \\
&\times \Theta\left[\Delta_p^2-\frac{(\vec{p}_{1t}-\vec{p}_{2t})^2}{4}+\frac{(m_{1t}-m_{2t})^2}{4}\right].
\end{aligned} \tag{5.15}$$

Here, C_{reg} denotes a normalization constant which is matched to the regeneration yield obtained from the rate equation, and $m_t=\sqrt{p_t^2+m_b^2}$ is the transverse mass of the b quarks. The Θ function characterizes the momentum space wave function of the formed Y, suppressing high relative momenta of the coalescing b quarks. The covariant momentum space radius, Δ_p, is inversely proportional to the coordinate-space radius via the uncertainty relation, $\Delta_p\Delta_x\simeq 1$. We use $\Delta_x\simeq r_{\Upsilon[\Upsilon(2S),\chi_b(1P)]}=0.2[0.5]$ fm. The p_T spectra are obtained by integrating the 2-differential spectrum in Eq. (5.15) over the azimuthal angle,

$$\frac{\mathrm{d}N_Y^{\mathrm{coal}}(p_T)}{\mathrm{d}p_T}=\int_0^{2\pi}\frac{\mathrm{d}^2N_Y^{\mathrm{coal}}(p_T,\phi)}{\mathrm{d}^2p_T}p_T\mathrm{d}\phi\,. \tag{5.16}$$

As an estimate of the uncertainty in the regeneration time, we will adopt snapshots of the evolving b-quark distributions from the Langevin simulations at different local temperatures with pertinent flow velocities in the underlying hydro evolution of Ref. [158].

Finally, to account for the p_T dependence of the formation rate, which is not captured by the instantaneous coalescence approximation, we weight the coalescence spectrum, Eq. (5.16), by the p_T dependence of the inelastic reaction rate,

$$\frac{dN_Y^{\mathrm{reg}}}{dp_T}=\hat{\Gamma}_Y(p_T,\bar{T}_{\mathrm{reg}})\frac{\mathrm{d}N_Y^{\mathrm{coal}}}{\mathrm{d}p_T} \tag{5.17}$$

where $\hat{\Gamma}_Y(p_T,\bar{T}_{\mathrm{reg}})\equiv\Gamma_Y(p_T,\bar{T}_{\mathrm{reg}})/\bar{\Gamma}_Y(\bar{T}_{\mathrm{reg}})$ includes a normalization $\bar{\Gamma}_Y$ such that the norm of the regeneration component as obtained from the rate equation is preserved.

5.2.3.3 Elliptic Flow

Another observable with a potential to disentangle primordially produced and regenerated quarkonia is their elliptic flow. It is quantified by the second coefficient, $v_2(p_T)$, in the the Fourier expansion of their azimuthal-angle differential distribution,

$$\frac{\mathrm{d}^2 N}{\mathrm{d}^2 p_T} = \frac{1}{2\pi} \frac{\mathrm{d}N(p_T)}{p_T \mathrm{d}p_T} [1 + 2v_2(p_T) \cos(2\phi) + \dots], \tag{5.18}$$

where ϕ is defined relative to the x axis, which lies in the reaction plane aligned with the impact parameter. At mid-rapidity, odd harmonics are suppressed, while higher even harmonics ($v_4, v_6, \dots$) for bulk hadron production are typically much smaller than v_2. From the above expansion one projects out the second coefficient via

$$v_2(p_T) = \frac{\frac{1}{2\pi} \int\limits_0^{2\pi} \frac{\mathrm{d}^2 N(p_T,\phi)}{p_T \mathrm{d}p_T \mathrm{d}\phi} \cos(2\phi) \mathrm{d}\phi}{\frac{1}{2\pi} \int\limits_0^{2\pi} \frac{\mathrm{d}^2 N(p_T,\phi)}{p_T \mathrm{d}p_T \mathrm{d}\phi} \mathrm{d}\phi} . \tag{5.19}$$

For the primordial component, we explicitly track the bottomonium paths through an elliptically expanding fireball; the pertinent v_2^{prim} is generated entirely due to path length differences and usually rather small in magnitude [191] (contributions from elastic scatterings are not accounted for; little is known about such processes). For the regeneration component, the coalescence expression, Eq. (5.15), incorporates the v_2 information through the convolution of the underlying b- and $\bar{b}$-quark flows. The total elliptic flow follows as the weighted sum of the two contributions,

$$v_2(p_T) = \frac{R_{\mathrm{AA}}^{\mathrm{prim}}(p_T) v_2^{\mathrm{prim}}(p_T) + R_{\mathrm{AA}}^{\mathrm{coal}}(p_T) v_2^{\mathrm{coal}}(p_T)}{R_{\mathrm{AA}}^{\mathrm{prim}}(p_T) + R_{\mathrm{AA}}^{\mathrm{coal}}(p_T)} . \tag{5.20}$$

p_T[GeV]	$\chi_b(1P)$[%]	$\chi_b(2P)$[%]	$\chi_b(3P)$[%]	total $\chi_b(nP)$[%]
6∼8	14.8	3.3		18.1
8∼10	17.2	5.2		22.4
10∼14	21.3	4.0	1.7	27.0
14∼18	24.4	5.2	1.8	31.4
18∼22	27.2	5.5	1.9	34.6
22∼40	29.2	6.0	2.9	38.1

Table 5.1: Feeddown fractions from $\chi_b(nP)$ states to $\Upsilon(1S)$ from LHCb [192].

5.2.4 Open-Bottom and Bottomonium Input Cross Sections

The basic quantity to compute below is the nuclear modification factor, defined as the ratio of yields in an A-A collision at a given centrality divided by the $N_{\rm coll}$-scaled yield in pp,

$$R_{\rm AA} = \frac{N_Y^{\rm AA}}{N_{\rm coll}\frac{\sigma_{pp\to Y}}{\sigma_{pp}^{\rm inel}}} \ . \tag{5.21}$$

This has been measured as a function of several variables, *i.e.*, nucleon participant number ($N_{\rm part}$) as a measure of centrality (which we estimate from the optical Glauber model), transverse momentum (p_T), rapidity (y), and collision energy ($\sqrt{s}$). The numerator in Eq. (5.21) contains the primordial component, which is also proportional to the product of $N_{\rm coll}\sigma_{pp\to Y}$ (times a suppression factor), and the regeneration component, which is largely controlled by the open-bottom cross section, $\sigma_{pp\to b\bar{b}}$, independent of the denominator (although in practice we will assume a proportionality between open- and hidden-bottom cross sections).

Feeddowns from higher excited states contribute to the inclusive production of an observed meson. A detailed summary of feeddown fractions can be found in Appendix Sec. A.2. For the p_T-dependent $R_{\rm AA}$'s at both RHIC and LHC energies, we include the p_T dependence of the feeddown in our calculations. By using harder p_T spectra for excited states, but with the same branching fraction as at low p_T, we automatically obtain a larger feeddown at high p_T which is essentially consistent with LHCb Collaboration data [192];

cf. Table 5.1.

We slightly update several input cross sections for the TBS calculations relative to Ref. [175], as summarized in Table 5.2, but keep the ratio $\frac{\sigma_Y}{\sigma_{b\bar{b}}} \simeq 0.176\,\%$ as in our previous work which is within the uncertainty of measured values. This ratio only affects the regeneration component of $R_{\rm AA}$. In general, the small pp cross sections for $b\bar{b}$ pairs render their number less than 1 even in A-A collisions at the LHC. Therefore, the corresponding Y equilibrium limits are in the canonical limit, so that $R_{\rm AA}^{\rm reg}$ is essentially linear in $\frac{\sigma_Y}{\sigma_{b\bar{b}}}$, and thus approximately constant for not too peripheral collisions (for the latter, the small QGP lifetime implies that the relaxation time approximation for b-quark diffusion will lead to a noticeable suppression). Overall, our results for the $R_{\rm AA}$'s will be influenced insignificantly by the update of the input pp cross sections.

For the bottomonium input cross sections at $\sqrt{s}$=200 GeV we adopt the STAR measurement [193] of $\Upsilon(1S+2S+3S)$, $\frac{{\rm d}\sigma}{{\rm d}y}\cdot Br(\mu\bar{\mu}) = 81\pm5\pm8\,pb$. We reconstruct σ_{1S}^{tot} using the di-muon branching ratios $Br(1S\to\mu\bar{\mu}) = 2.48\,\%$, $Br(2S\to\mu\bar{\mu}) = 1.93\,\%$, and $Br(3S\to\mu\bar{\mu}) = 2.18\,\%$ with cross sections $\sigma_{2S} = 0.33\sigma_{1S}^{tot}$ and $\sigma_{3S} = 0.15\sigma_{1S}^{tot}$ (see Appendix Sec. A.2), so that $\frac{{\rm d}\sigma_{1S}^{tot}}{{\rm d}y} = \frac{81\,pb}{1\cdot2.48\,\%+0.33\cdot1.93\,\%+0.15\cdot2.18\,\%} \simeq 2.35\,nb$. We use the same values for open-bottom cross section as in previous work [175], *i.e.*, $\sigma_{pp\to b\bar{b}}$=3.2 μb, with a factor of 0.52 to obtain $\sigma_{pp\to b\bar{b}}$=1.67μb in one fireball (Δy=1.8), or $\frac{{\rm d}\sigma_{pp\to b\bar{b}}}{{\rm d}y}$=0.92 μb. This is consistent with the most recent PHENIX results [194]. For simplicity, we use the same input values for uranium-uranium (U-U) collisions at 193 GeV.

For pp collisions at 2.76 TeV, we use the the inclusive $\Upsilon(1S)$ cross section of $\frac{{\rm d}\sigma_{pp\to\Upsilon(1S)}}{{\rm d}y}$=30.3 nb for $|y|$<2.4 based on CMS pp data [182], which is $\sim$25% smaller than in Ref. [175]. With $\frac{\sigma_{\Upsilon(1S)}}{\sigma_{b\bar{b}}} \simeq 0.176\,\%$ this gives $\frac{{\rm d}\sigma_{pp\to b\bar{b}}}{{\rm d}y}$=17.2 μb at 2.76 TeV for $|y|$<2.4 which is consistent with the upper range of FONLL calculations [195], 15±6.2 μb. We estimate a 10 % reduction from $|y|$<0.9 to $|y|$<2.4. From a comparison of 7 TeV ALICE [196] and CMS [197] data, we estimate the forward-rapidity (2.5<$|y|$<4.0) cross sec-

Differential cross section $\frac{\mathrm{d}\sigma}{\mathrm{d}y}$	0.20 TeV	2.76 TeV	5.02 TeV
pp$\to$ $\Upsilon(1S)$($\lvert y\rvert < 0.5$)[nb]	2.35	-	-
pp$\to$ $\Upsilon(1S)$($\lvert y\rvert < 2.4$)[nb]	-	30.3	57.6
pp$\to$ $\Upsilon(1S)$($2.5 < y < 4.0$)[nb]	-	15.1	28.8
pp$\to$ $\Upsilon(2S)$($\lvert y\rvert < 0.5$)[nb]	0.77	-	-
pp$\to$ $\Upsilon(2S)$($\lvert y\rvert < 2.4$)[nb]	-	10.0	19.0
pp$\to$ $\Upsilon(2S)$($2.5 < y < 4.0$)[nb]	-	5.0	9.5
pp$\to$ $b\bar{b}$($\lvert y\rvert < 0.5$)[μb]	0.92	-	-
pp$\to$ $b\bar{b}$($\lvert y\rvert < 2.4$)[μb]	-	17.2	32.7
pp$\to$ $b\bar{b}$($2.5 < y < 4.0$)[μb]	-	8.6	16.4

Table 5.2: Summary of input cross sections extracted from pp collisions used in our calculations. The $\frac{\mathrm{d}\sigma_{pp\to Y}}{\mathrm{d}y}$ values at 200 GeV are based on STAR data [193]. The value for $\frac{\mathrm{d}\sigma_{pp\to b\bar{b}}}{\mathrm{d}y}$ is adopted from previous work [175] which is consistent with PHENIX results [194]. The $\frac{\mathrm{d}\sigma_{pp\to Y}}{\mathrm{d}y}$ values at 2.76 and 5.02 TeV for $|y| < 2.4$ are based on CMS data [182, 198, 199], with a fixed $\frac{\sigma_{pp\to Y}}{\sigma_{pp\to b\bar{b}}}$ ratio of 0.176 %, as in previous work [175]. A 50 % reduction in the cross sections is assumed when going from mid-rapidity ($|y| < 2.4$) to forward rapidity ($2.5 < y < 4.0$) [196, 197].

tion at about 45 % of the mid-rapidity ($|y|$<0.9) value, or 50 % of the ($|y|$<2.4) value. The $\Upsilon(2S)$ cross section is about 33 % of inclusive $\Upsilon(1S)$ as discussed in Appendix Sec. A.2.

At 5.02 TeV, we adopt for the inclusive $\Upsilon(1S)$ cross section the recent CMS pp reference [198, 199], $\frac{\mathrm{d}\sigma_{pp\to Y}}{\mathrm{d}y}$=64.0 nb (57.6 nb) for $|y| < 0.9$ ($|y| < 2.4$), together with the $\Upsilon(1S)$ over open-bottom ratio of 0.176 % and the same reduction of 55 % (50 %) from mid-rapidity $|y| < 0.9$ ($|y| < 2.4$) to forward rapidity $2.5 < y < 4.0$.

The absolute input cross sections at different energies for different states for the TBS calculations are summarized in Table. 5.2.

5.3 Bottomonium Production at RHIC

We are now in position to present our numerical results for bottomonium observables in comparison to experimental data, starting with RHIC energies. Before presenting and discussing the results for the centrality and p_T dependencies in Secs. 5.3.1 and 5.3.2, let us briefly outline our implementation of CNM effects, which we estimate from d-Au collisions. We assume no shadowing on open-bottom and bottomonium production and interpret the STAR measurement of $R_{\rm dAu}(1S) = 0.83{\pm}0.15({\rm dAu}_{\rm stat}){\pm}0.1(pp_{\rm stat}){\pm}$ 0.03 (sys) [52] as being due to nuclear absorption with a YN absorption cross section in a range of $\sigma_Y^{\rm abs}$=0-3 mb (identical for all bottomonia).

5.3.1 Centrality Dependence with In-Medium Binding Energies

Our results for the $R_{\rm AA}(N_{\rm part})$ for inclusive $\Upsilon(1S)$ and $\Upsilon(1S+2S+3S)$ states in Au-Au and U-U collisions are shown in Figs. 5.10 and 5.11, respectively, in comparison to RHIC data. We focus on the T-matrix binding scenario (TBS) with baseline binding strength, η=1.0. The suppression of the inclusive $\Upsilon(1S)$ yield (upper panels) is mostly due to the excited states (as well as nuclear absorption), which manifests itself as a stronger suppression in the combined $R_{\rm AA}$ of $\Upsilon(1S+2S+3S)$ [middle (lower) panel in Fig. 5.10 (5.11)]. Primordial production dominates but regeneration, in the canonical limit with $N_{b\bar{b}} < 1$ even in central collisions, is non-zero. Our results for U-U show slightly more suppression than for Au-Au, and both are generally consistent with the data.

5.3.2 Transverse-Momentum Dependence with In-Medium Binding Energies

We proceed to compute Y p_T spectra by utilizing their $R_{\rm AA}$'s for primordial and regenerated components as obtained in the previous section to form the weighted sum

$$R_{\rm AA}(p_T) \;=\; \frac{\frac{dN_Y^{\rm prim}}{p_T{\rm d}p_T}+\frac{dN_Y^{\rm reg}}{p_T{\rm d}p_T}}{N_{\rm coll}\frac{dN_Y^{pp}}{p_T{\rm d}p_T}} = R_{\rm AA}^{\rm prim}\frac{\frac{d\hat{N}_Y^{\rm prim}}{p_T{\rm d}p_T}}{\frac{d\hat{N}_Y^{pp}}{p_T{\rm d}p_T}} + R_{\rm AA}^{\rm reg}\frac{\frac{d\hat{N}_Y^{\rm reg}}{p_T{\rm d}p_T}}{\frac{d\hat{N}_Y^{pp}}{p_T{\rm d}p_T}} \tag{5.22}$$

where the “hat" indicates a normalized distribution,

$$\int\limits_0^\infty p_T{\rm d}p_T\frac{{\rm d}\hat{N}(p_T)}{p_T{\rm d}p_T} = 1\ , \tag{5.23}$$

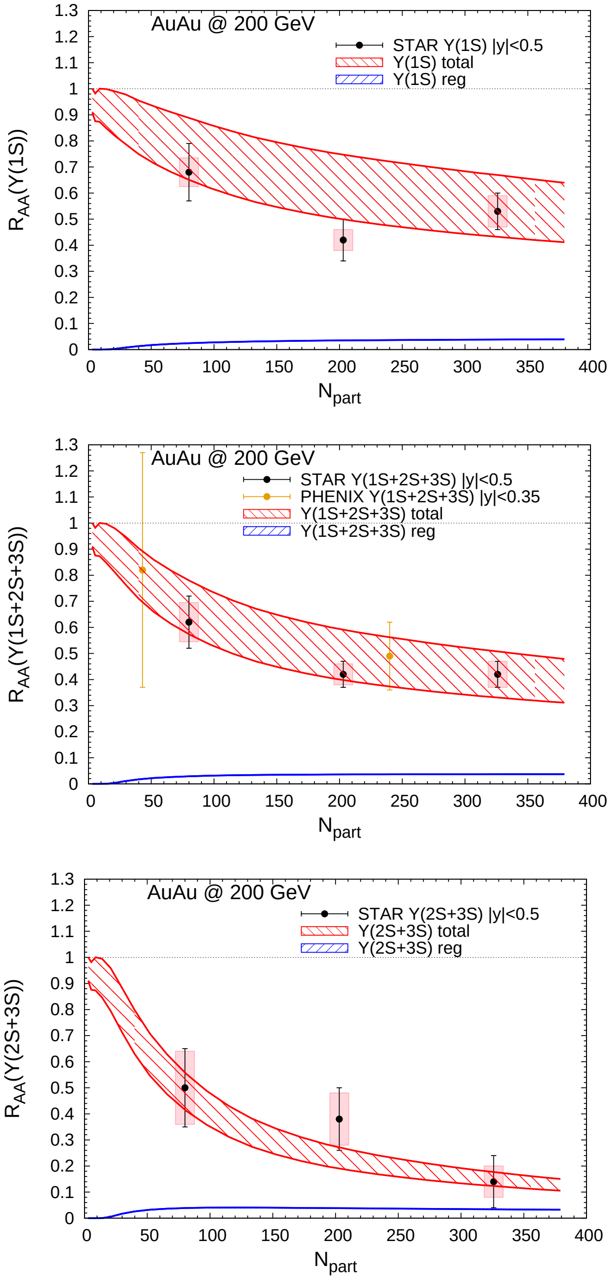

Figure 5.10: Centrality dependence of bottomonium yields in Au-Au(200 GeV) collisions using the baseline TBS ($\eta = 1.0$) with updated feeddowns. The total (red band) and regenerated (blue lines) contributions are shown for inclusive $\Upsilon(1S)$ (upper panel), $\Upsilon(1S + 2S + 3S)$ (middle panel), and $\Upsilon(2S + 3S)$ (lower panel) production at mid-rapidity ($|y|$<0.5) and compared to STAR [193] and PHENIX [53] data. The band width of the total yields is due to CNM effects with $\sigma_Y^{\rm abs}$=0-3 mb [52].

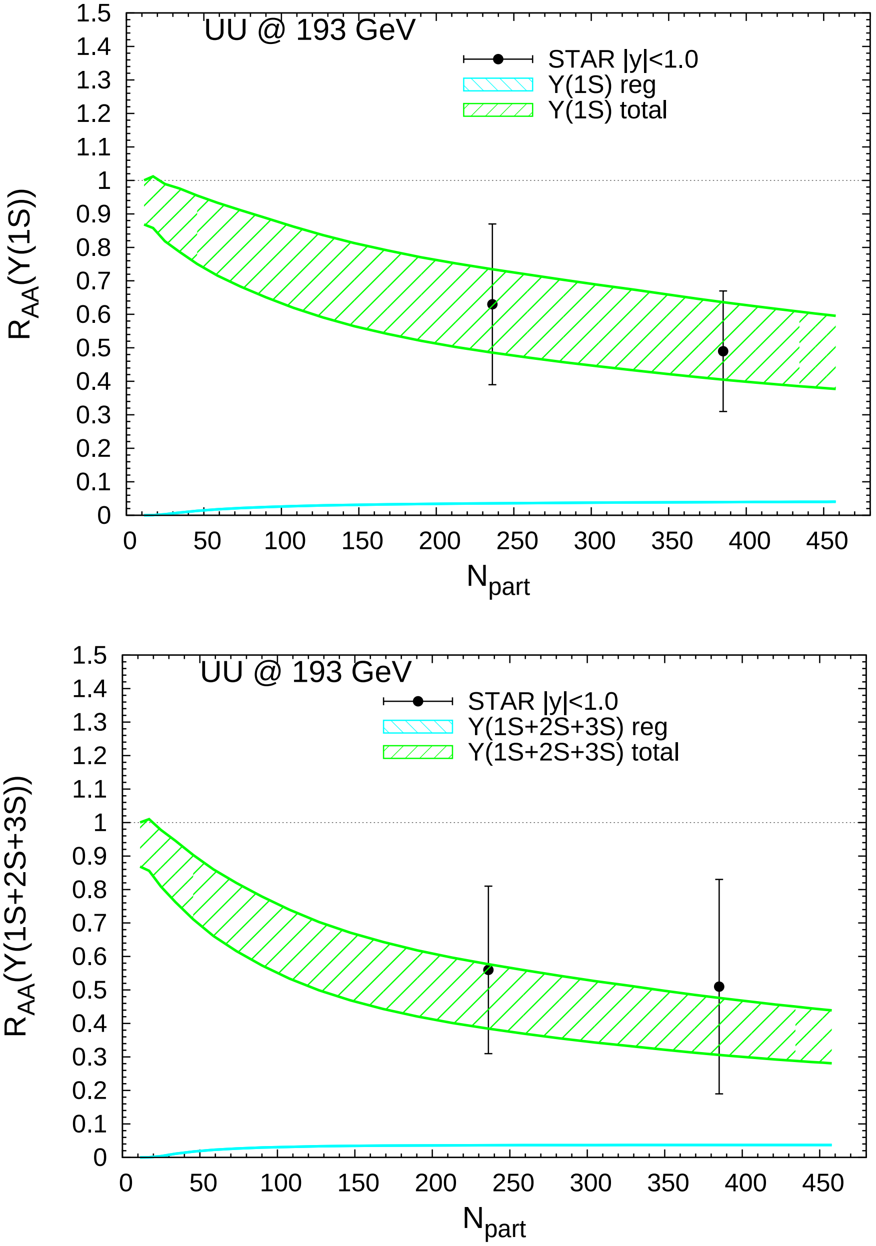

Figure 5.11: Centrality dependence of bottomonium yields in U-U(193 GeV) collisions using the baseline TBS with updated feeddowns. The total (green band) and regenerated (light-blue line) contributions are shown for inclusive $\Upsilon(1S)$ (upper panel) and $\Upsilon(1S + 2S + 3S)$ (lower panel) at mid-rapidity ($|y|$<1.0) and compared to STAR data [176]. The band width of the total yields is due to CNM effects with $\sigma_{\Upsilon}^{\rm abs}$=0-3 mb [52].

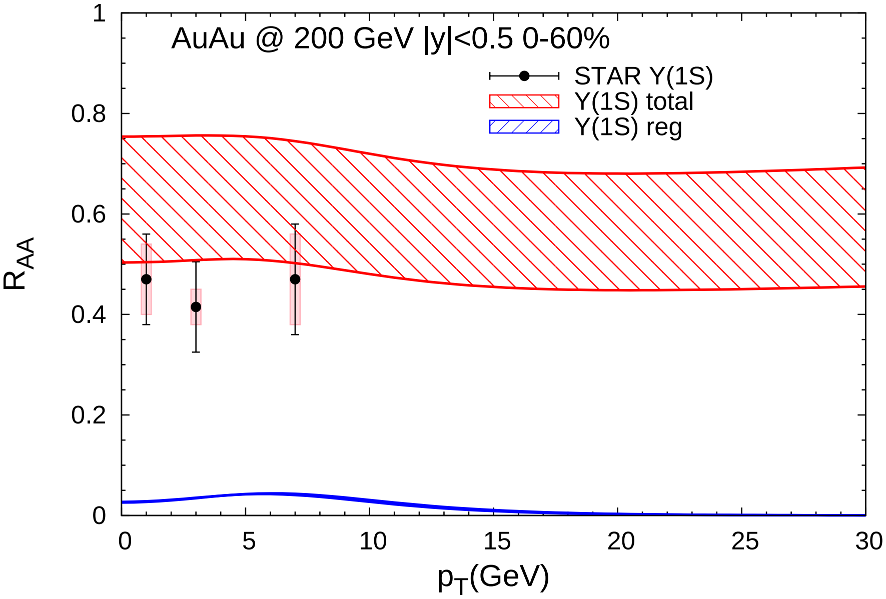

Figure 5.12: The p_T-dependent $R_{\rm AA}$ for inclusive $\Upsilon(1S)$ in 0-60 % Au-Au(200 GeV) collisions within the baseline TBS, compared to STAR data [193]. The red (blue) band is for the total (regeneration) yield, where the band width of the former is due to CNM effects with $\sigma_Y^{\rm abs}$=0-3 mb [52].

and the $R_{\rm AA}$ coefficients represent a given centrality class, *e.g.*, 0-60 %. For the normalized pp spectra, we employ an empirical parametrization,

$$\frac{{\rm d}^2\hat{N}_{pp}(p_T)}{{\rm d}^2p_T}=\frac{N}{\left(1+\left(\frac{p_T}{D}\right)^2\right)^A} \tag{5.24}$$

with fit parameters A=3.0 and D=5.3 GeV estimated from m_T scaling from charmonium p_T spectra [48] as baseline. The p_T-dependent $R_{\rm AA}$ for 0-60% Au-Au(200 GeV) is shown in Fig. 5.12. It tends to slightly overestimate the STAR data, although the lower end of the band (with maximal nuclear absorption) is close to the data, a trend which is also reflected in the centrality-dependent $R_{\rm AA}$ (recall the upper panel of Fig. 5.10)

5.4 Bottomonium Production in 2.76 TeV Pb-Pb Collisions at the LHC

Turning to Pb-Pb collisions at the LHC, we first focus on $\sqrt{s}$=2.76 TeV. To make contact with the earlier employed vacuum binding scenario [175], we start by revisiting the inclusive R_{AA}'s for $\Upsilon(1S)$ and $\Upsilon(2S)$ within the vacuum binding scenario approach (with massless gluo-dissociation rates and a quasiparticle EoS, and input cross sections as used in Ref. [175] with an up to 25% shadowing in central collisions for both open bottom and bottomonia), but with updated feeddown fractions [albeit neglecting explicit feeddown from $\Upsilon(3S)$ and $\chi_b(2P)$ states]. We then turn to the TBS calculation with all updates included, also treating $\Upsilon(3S)$ and $\chi_b(2P)$ and their feeddown contributions explicitly.

5.4.1 Centrality Dependence with Vacuum Binding Energies

We compare the feeddown-updated vacuum binding scenario to the recent CMS data [182] in Fig. 5.13; we find fair agreement with the strong $\Upsilon(2S)$ suppression while the $\Upsilon(1S)$ yields tend to be somewhat overestimated, essentially due to the now smaller feeddown. The stronger suppression exhibited by the forward-rapidity ALICE data [54] cannot be reproduced, as before. The $b\bar{b}$ production cross sections do not vary strongly enough with rapidity to generate the extra suppression. In particular, the regeneration contribution at this energy does not provide a quadratic dependence on the open-bottom cross section since the bottom yields are in the canonical limit, *i.e.*, with no more than one $b\bar{b}$ pair in the fireball.

5.4.2 Centrality Dependence with In-Medium Binding Energies

Next we turn to the results of our updated approach based on the TBS. Aside from the cross section inputs, CNM effects are implemented via a shadowing suppression of both open bottom and bottomonia of up to 15 % at mid-rapidity, estimated from EPS09 NLO calculations [90] and ATLAS p-Pb data for $\Upsilon(1S)$ [200], and up to 30 % at forward/backward rapidity from p-Pb data from LHCb [201] and ALICE [202].

The baseline TBS (with η=1.0) provides a fair description of the recent CMS data [182] for both $\Upsilon(1S)$ and $\Upsilon(2S)$ data; cf. upper panel of Fig. 5.14. Compared to the (feeddown-updated) vacuum binding scenario shown in the previous figure, the additional $\Upsilon(1S)$ suppression appears to be less than one might have expected given the much reduced binding energies. The main reason for this is the now massive thermal quasiparticles in the dissociation rates (as dictated by a more realistic EoS), which render gluo-dissociation ineffectively. The addition of the quasifree rates within the TBS leads to an overall increase of the rates compared to the vacuum binding scenario, but not by much. The inclusion of correlation volume effects leads to an increase of the regeneration component, while the B-meson resonance states close to $T_{\rm pc}$ reduce it. Regeneration is relatively small for the ground state, but amounts to about $\sim$50% of the $\Upsilon(2S)$ yield in central collisions. This is somewhat smaller than in the vacuum binding scenario where it is the dominant contribution, which improves the description of the semi-central and central CMS data [we will elaborate on the quantitative role of the B-meson resonance states in the $\Upsilon(2S)$ regeneration contribution in the next section]. The enhanced suppression of the $\Upsilon(1S)$, relative to the vacuum binding scenario, is welcome in comparison to the forward-rapidity ALICE data (lower panel of Fig. 5.14), although the latter are still significantly overpredicted.

To test the sensitivity of our results to a key in-medium property of the bottomonia, *i.e.*, their temperature-dependent binding energy as a measure of color screening, we additionally display in the upper panel of Fig. 5.14 the results of calculations where the baseline TBS binding energies are less (further) reduced, by decreasing (increasing) the in-medium reduction of E_B relative to the vacuum by 10 %; recall Eq. (5.2). This is implemented by changing the parameter η=1.0 to η=0.9 (η=1.1), displayed by the solid vs. dashed (dash-dotted) lines in Fig. 5.1 (recall that η=0 recovers the vacuum binding scenario). One finds a significant increase (decrease) of the inclusive $\Upsilon(1S)$ $R_{\rm AA}$, while the $\Upsilon(2S)$ $R_{\rm AA}$ is little affected [since $E_B(T)$ is already small]. Thus the inclusive $\Upsilon(1S)$ can in principle serve as a measure of color screening, provided other modeling uncertainties can be sufficiently controlled, as originally envisaged in Ref. [180]. In the following section, we will therefore scrutinize several of these uncertainties quantitatively. Since η=1.0 provides a compromise between the CMS and ALICE data, we adopt this value from hereon as our default (unless otherwise noted).

5.4.3 Sensitivity to Model Parameters with In-Medium Binding Energies

This section is dedicated to quantify model dependencies unrelated to the in-medium binding energies of the bottomonium states. Specifically, we will quantify uncertainties in the implementation of the following components: (i) B-meson resonance formation, (ii) correlation volume, (iii) bottomonium formation time, (iv) QGP formation time, (v) fireball expansion, and (vi) b-quark relaxation time. We will discuss all these effects relative to our baseline TBS results (without shadowing), mostly focusing on (but not limited to) the centrality dependence of the $\Upsilon(1S)$ $R_{\rm AA}$ at mid-rapidity in Pb-Pb (2.76 TeV) collisions, with selected results also for the $\Upsilon(2S)$ and $\Upsilon(3S)$.

In the upper panel of Fig. 5.15 we display the comparison of total and regenerated contributions when switching off the presence of the B-meson resonance states in the calculation of the Y equilibrium limits near $T_{\rm pc}$ (recall Fig. 5.8). Without the resonance states, the b-quark fugacity factor is significantly larger in this temperature range, leading to an increase in the regeneration (while the primordial contribution is unaffected). The impact is most significant for the $\Upsilon(2S)$, where the regeneration contribution increases by close to a factor of 3 in central collisions. The effect is much less for the $\Upsilon(1S)$ (at $\sim$50%, translating into less than 20% for the total), since in the temperature range where the enhancement of the fugacity factor is active, the inelastic reaction rate of the $\Upsilon(1S)$ is already rather small, *e.g.*, $\Gamma_{\Upsilon(1S)} \lesssim 10$ MeV at T=220 MeV. For the $\Upsilon(3S)$ the increase of the regeneration component is also close to a factor of 3, but the absolute value of the regeneration contribution in the $R_{\rm AA}$ is smaller than for the $\Upsilon(2S)$ due to its larger mass (*i.e.*, smaller equilibrium limit). The relative enhancement of the regeneration components when neglecting B-meson resonance states is comparable at RHIC energy (not shown here), but overall less significant due to the generally larger primordial components compared to 2.76 TeV.

We note that the calculations published in our recent papers [203, 35] did not yet include the B-meson resonance effects, which indeed led to problems with overestimating the $\Upsilon(2S)$ yields measured by CMS in semi-central and central Pb-Pb collisions at both 2.76 and 5.02 TeV. This problem is now largely resolved upon inclusion of this effect, which, as we mentioned above, is consistent with recent analysis of lQCD results for c-quark susceptibilities [187], and was predicted by T-matrix calculations with the U potential in Refs. [204, 75]. Thus, the qualitative feature of heavy-light resonances above $T_{\rm pc}$ is by now well established, but one still needs to further check its implementation. Toward this end we show in the lower panel of Fig. 5.15 the sensitivity of the $\Upsilon(1S)$ $R_{\rm AA}$ to the onset temperature assumed for the B-meson formation; it turns out to be small.

Second, we test the sensitivity to the modeling of the b-quark correlation volume, Eq. (2.92), by varying the mean speed, $\langle v_b \rangle$, with which the b and $\bar{b}$ quark expand the radius of the volume within which canonical (or "diagonal") regeneration can occur. A larger speed leads to a larger correlation volume which increases the available phase space for b quarks and thus decreases the b-quark fugacity, γ_b, and the pertinent regeneration yield. This model component creates a small uncertainty in the $\Upsilon(1S)$ $R_{\rm AA}$; cf. Fig. 5.16.

Third, we test the sensitivity to the formation times, $\tau_{\rm form}$, of the Y states, by varying the default values of 0.5, 1.0 and 1.5 fm for $\Upsilon(1S)$, $\Upsilon(2S)$, and $\Upsilon(3S)$, respectively, by $\pm 20\,\%$. Larger formation times reduce the dissociation rates in the early stages thus resulting in less suppression of the primordial component. This is mostly relevant for the $\Upsilon(1S)$ whose suppression has the largest sensitivity to the earliest phases. However, the pertinent variation of its total $R_{\rm AA}$ is below 5%; cf. Fig. 5.17.

Fourth, we test the sensitivity to the initial QGP formation time, τ_0, which controls the initial temperature, T_0. Varying τ_0 by ± 0.1 fm around the default value of 0.2 fm, which implies a formidable range of initial temperatures of $T_0 \simeq$520-750 MeV, produces relatively small modifications in the $\Upsilon(1S)$ $R_{\rm AA}$; cf. Fig. 5.18. One of the reasons for this is that the $\Upsilon(1S)$ formation times "protect" it from large dissociation rates in the earliest phase of the medium evolution. Another reason is that, despite the large range in temperature, the variation in the absolute time duration is actually rather small (since the default value is already quite small), so that even rather large widths do not have a strong impact. This further implies that pre-equilibrium evolution also has a small effect on the Y production yields.

Fifth, we have checked the sensitivity to the fireball expansion parametrization, in Eq. (2.97) and Eq. (2.105). When increasing the transverse acceleration by 20%, from a_T=0.1/fm to 0.12/fm, both the regeneration contribution and the total $\Upsilon(1S)$ $R_{\rm AA}$ change by no more than within the typical line thickness of the baseline curves; cf. Fig. 5.19.

Sixth, we vary the thermal relaxation time of b quarks, τ_b, which controls the time scale for approaching the Y equilibrium limits. Larger relaxation times cause the equilibrium limits to be recovered slower which reduces the regeneration contributions; recall Eq. (2.58) for the explicit expression of this implementation. The thermal relaxation time of heavy quarks is one of the key transport parameters in URHICs, being proportional to the spatial heavy-quark diffusion coefficient via $\mathcal{D}_s = \tau_Q(T/m_Q)$. Intense efforts are ongoing to extract this quantity from open heavy-flavor observables, *i.e.*, from D-meson $R_{\rm AA}$'s and v_2's, or, in the future, and more directly related to the present context, from B-meson observables. Our default choice of τ_b=11 fm at a "pivot point" of $2\,T_{\rm c}$, with a mild temperature dependence, approximately reflects our current knowledge of this quantity (cf. Ref. [205] for a recent review). Not unexpectedly, the regeneration contribution to the $\Upsilon(1S)$ $R_{\rm AA}$ varies by almost $\pm 20\%$ when varying this parameter by $\pm 20\%$; see Fig. 5.20. However, the relative variation in the total $\Upsilon(1S)$ $R_{\rm AA}$ is much smaller, within $\pm 5\%$. Future analysis of open-bottom observables to extract the temperature-dependent bottom diffusion coefficient in the QGP will help to reduce this uncertainty.

5.4.4 Transverse-Momentum Dependence with In-Medium Binding Energies

For the pp baseline spectra, which figure into the denominator of the $R_{\rm AA}(p_T)$, we use the same expression, Eq. (5.24), as given in Sec. 5.3.2, but with parameters A=3.0 (3.0), D=5.8 (6.6) GeV refitted to $\Upsilon(1S)$ ($\Upsilon(2S)$) spectra at 2.76 TeV, as well as A=2.3 (2.3) and D=4.9 (5.9) GeV at 5.02 TeV [206, 207, 208, 209, 210].

To compute the coalescence component, a temperature range for the hydro hypersurface has to be specified to evaluate the b-quark spectra from the Langevin simulations in the hydrodynamic background. This range represents the window over which most of the regeneration of the corresponding bottomonium state occurs. Inspection of the time (temperature) evolution of the regeneration yields reveals that the relevant temperature windows are $\bar{T}_{\rm reg}$=220-278 MeV for the $\Upsilon(1S)$, $\bar{T}_{\rm reg}$=183-201 MeV for the $\Upsilon(2S)$ and $\bar{T}_{\rm reg}$=189-212 MeV for the χ_b states in minimum-bias (MB) Pb-Pb (2.76 TeV) collisions. We use the upper and lower limits of these windows to define the uncertainty band for the p_T spectra of the regenerated bottomonia.

The resulting $R_{\rm AA}(p_T)$'s for $\Upsilon(1S)$ and $\Upsilon(2S)$ are displayed in Fig. 5.21 for the TBS with η=1.0. The interplay of primordial suppression and coalescence processes results in a total $\Upsilon(1S)$ $R_{\rm AA}$'s with a mild maximum structure around $p_T \simeq m_{\Upsilon(1S)}$, caused by the regeneration contribution, in approximate agreement with CMS data [182]. For the $\Upsilon(2S)$, we find an over-prediction at low p_T, which is not really apparent in the centrality-dependent $R_{\rm AA}(N_{\rm part})$ in Fig. 5.14. However, when instead replacing the regeneration contribution with a thermal blast-wave expression (corresponding to thermally equilibrated b-quark distributions), the low-p_T maximum structure in the $R_{\rm AA}(p_T)$ becomes more pronounced and leads to larger deviations from the CMS data, see Fig. 5.22. It thus appears that kinetically not equilibrated b-quark spectra are an important ingredient to properly interpret the bottomonium p_T spectra.

5.4.5 Elliptic Flow with In-Medium Binding Energies

Based on the bottomonium p_T spectra discussed in the previous section, we provide world first predictions [59] † for their elliptic flow within the framework laid out in Sec. 5.2.3.3; see Fig. 5.23. The same sources of uncertainties apply as encoded in the bands for the p_T spectra. The resulting $\Upsilon(1S)$ v_2 turns out to be a factor of 2-3 smaller than the one of the $\Upsilon(2S)$. However, this is not due to the larger relative contribution of the coalescence yields, since the latter affects the total weighted v_2 for both particles very little: for the $\Upsilon(1S)$ the coalescence contribution has almost no effect on the total v_2, while for the $\Upsilon(2S)$ it increases the total relative to the primordial by up to a maximum of 1$\%$ at low $p_T \simeq 5$ GeV, where, however, the total v_2 signal is not even at 2$\%$. Thus, at our predicted level of coalescence contributions, and due to their concentration at low p_T where the absolute signal is small, we conclude that it will be very challenging at best to discern them from the primordial contributions. On the other hand, the significantly larger *total* v_2 of the $\Upsilon(2S)$ compared to the $\Upsilon(1S)$ is a more robust signal; it is due to the fact that the $\Upsilon(1S)$ suppression occurs earlier in the fireball evolution, where path length differences in the suppression cannot be sensed as much as they can for the $\Upsilon(2S)$ where the suppression mechanism is active to lower temperatures, *i.e.*, later in the fireball evolution. In other words, a temperature-sequential suppression, which is widely believed to be at

---

†It is also calculated by other groups [211, 212] later.

the origin of the difference of the $\Upsilon(1S)$ and $\Upsilon(2S)$ yields, should also manifest itself as a difference in their v_2, irrespective of regeneration.

5.5 Bottomonium Production in 5.02 TeV Pb-Pb collisions at the LHC

We now turn to Pb-Pb collisions at 5.02 TeV which were recently conducted at the LHC. Several new bottomonium data from this run have already become available over the course the present work, and we include those in our discussion. For the fireball evolution, we have assumed the charged-particle rapidity density, $\frac{\mathrm{d}N_{ch}}{\mathrm{d}y}$, to increase by about 22.5 %, from 2.76 to 5.02 TeV, *e.g.*, from 1750 to 2150 in 0-5% central collisions [213]. This corresponds to an increase of the total entropy in the fireball from 22000 to almost 27000. With an entropy density of $s \sim T^3$ in the early hot phases, the initial temperature increases by about 7%. For the charged-particle rapidity density we implement a reduction of 20 % from mid-rapidity, $|y| < 2.4$, to forward rapidity, $2.5 < y < 4.0$ [214], as previously done at 2.76 TeV. We will start our discussion again by recalling the results from the earlier used vacuum binding scenario in Sec. 5.5.1, and then turn to the centrality, p_T, and azimuthal-angle dependencies for the default TBS in Sec. 5.5.2.

5.5.1 Centrality Dependence with Vacuum Binding Energies

We first display our 5.02 TeV results for Y production in the previously used vacuum binding scenario [175] with updated feeddown fractions (but without explicit treatment of the $3S$ or $2P$ states), at both mid- and forward rapidities, cf. Figs. 5.24 and 5.25, respectively. Compared to the vacuum binding scenario results at 2.76 TeV, the $\Upsilon(1S)$ suppression slightly increases by up to ~5% in central collisions, due to stronger color screening with increased rates at higher temperature. On the other hand, the $\Upsilon(2S)$ suppression becomes slightly less in central collisions at 5.02 TeV due to a small increase in regeneration, while a stronger suppression is found for peripheral collisions ($N_{\mathrm{part}} \lesssim 50$), where the suppressed primordial contribution dominates (again for both rapidity regions). This feature is reminiscent of the J/ψ case.

5.5.2 Centrality and Transverse-Momentum Dependence with In-Medium Binding Energies

Next, we turn to the TBS at 5.02 TeV, encoding our theoretical improvements in the Y transport approach over the previously used vacuum binding scenario. The centrality dependence of the $R_{\rm AA}$ for $\Upsilon(1S)$ and $\Upsilon(2S)$ at mid-rapidity is shown in the upper panel of Fig. 5.26, and for the $\Upsilon(1S)$ at forward rapidity in the lower panel of Fig. 5.26. They are compared to CMS data [198, 199] at mid-rapidity and to ALICE data [215, 216] at forward rapidity, respectively. The in-medium effects lead to a significantly stronger suppression of the $\Upsilon(1S)$ relative to the vacuum binding scenario discussed in the previous section. At the same time, the $\Upsilon(1S)$ suppression within the TBS is only slightly increased relative to the 2.76 TeV results (recall Fig. 5.14). The $\Upsilon(2S)$ $R_{\rm AA}$ also shows a small increase in suppression by about 15%, amounting, however, to only a ∼0.01 change at the absolute level in the $R_{\rm AA}$ in central collisions. For the latter, the $\Upsilon(3S)$ is suppressed by another factor of ∼2. At forward rapidity, the comparison to recent ALICE data [215, 216], shown in the lower panel of Fig. 5.26, is more favorable than it was at 2.76 TeV.

Next, we compare our calculations for the $\Upsilon(2S)$-over-$\Upsilon(1S)$ double ratio at 5.02 TeV to CMS data [217] in Fig. 5.27; as to be expected from the agreement with the individual $R_{\rm AA}$'s, the calculated double ratio also agrees fairly well with the observed centrality dependence.

Finally, we extract transverse-momentum dependent observables from our calculations, starting with the p_T dependence of the $R_{\rm AA}$ for $\Upsilon(1S)$ and $\Upsilon(2S)$ at mid- and forward rapidities; cf. Fig. 5.28. Similar to what we found at 2.76 TeV, the $\Upsilon(1S)$ $R_{\rm AA}(p_T)$ exhibits a mild maximum structure due to the regeneration contribution computed with non-thermalized b-quark spectra (taken from Langevin transport calculations at 5.02 TeV), at both mid- and forward rapidities. The calculations approximately agree with both CMS data at mid-rapidity (upper panel of Fig. 5.28) and ALICE data at forward rapidity (middle panel of Fig. 5.28). The $\Upsilon(2S)$ $R_{\rm AA}(p_T)$ is also similar to 2.76 TeV, with a moderate monotonous rise with p_T. The absolute magnitude of the calculated p_T spectra agrees better with the CMS data than at 2.76 TeV. We also plot the p_T-dependent double ratio at mid-rapidity in the lower panel of Fig. 5.28; again, based on the agreement with the individual $R_{\rm AA}(p_T)$'s in the upper panel, no surprises are found.

The p_T dependence of the elliptic flow for $\Upsilon(1S)$ and $\Upsilon(2S)$ in mid-central Pb-Pb collisions at mid-rapidity is displayed in Fig. 5.29. The v_2 for both the primordial and regenerated $\Upsilon(1S)$ are small, below 2%, since both processes occur early in the fireball evolution – essentially within the first 2fm/c – during which both path length differences and collective-flow anisotropies are limited. The v_2 is more than doubled for the $\Upsilon(2S)$ in both components, which, after an initial rise, levels off at about 4%. As was the case at 2.76 TeV, the v_2 does not show a very promising sensitivity to the regeneration component, since the latter is rather small and concentrated at low p_T, where the mass effect suppresses the signal. However, the difference between $\Upsilon(1S)$ and $\Upsilon(2S)$ v_2's is appreciable; about a factor of $\sim$2. We note that we did not include initial geometry fluctuations nor elastic rescattering of the Y states in the medium (once they are reasonably tightly bound), which may play a role in generating a larger v_2 of the primordial component at high p_T or the total yields at small and moderate p_T, respectively.

5.6 Excitation Function from RHIC to the LHC

We now return to the question of the excitation function discussed in Sec. 3.1.2 for J/ψ, and here for $\Upsilon(1S)$ and $\Upsilon(2S)$. In an attempt to combine the information attained within our updated TBS approach to Y production from RHIC to top LHC energy, we compare our results for the collision energy dependence of the minimum-bias (MB) $R_{\rm AA}$'s for $\Upsilon(1S)$ and $\Upsilon(2S)$ to STAR and CMS data at mid-rapidity in Fig. 5.30. We find a gradual increase in the suppression for both states, with a stronger absolute suppression of the $\Upsilon(2S)$ than the $\Upsilon(1S)$ especially at the LHC. These features support a sequential suppression scenario, rather directly reflected in both calculations and data due to relatively small regeneration contributions. The latter is due to a combination of the small $b\bar{b}$ cross section (which at current energies does not produce more than 1 pair per fireball) and the role played by B-meson resonance formation near $T_{\rm pc}$. The possibly most significant indication for the regeneration contribution is a hint for a flattening of the $\Upsilon(2S)$ $R_{\rm AA}(\sqrt{s})$ when going from 2.76 to 5.02 TeV, in both data and calculations. The slight increase in the $\Upsilon(1S)$ regeneration, which is subleading at current energies, is expected to become more significant at collision energies beyond $\sim$10 TeV.

As pointed out in Ref. [35], the decreasing Y excitation functions are markedly different from their J/ψ counter-parts in Sec. 3.1.2, despite the comparable [or even larger] binding energy of the $\Upsilon(2S)$ [$\Upsilon(1S)$]. This lends considerable support to the overall picture of quarkonium kinetics developed over the last decade. The relatively large uncertainty in the CNM effects at RHIC clearly calls for an improved measurement in p-A d-A collisions at these energies (interesting effects have also been observed in p-Pb at the LHC [218, 202, 200, 219, 201]). At face value, the $\Upsilon(1S)$ suppression measured by STAR in Au-Au ($\sqrt{s}$=0.2 TeV), which is very similar to the LHC datum at 2.76 TeV, is not easily understood from hot-medium effects alone, while a larger CNM absorption at RHIC could offer a natural explanation for this observation. An analogous situation is present for the J/ψ, where the larger CNM suppression at the lower SPS energies ($\sqrt{s}$=0.017 TeV), relative to RHIC, is an important ingredient to interpret the energy dependence of the hot-medium effects [35]. In addition, a more precise measurement of the Y excited states at RHIC would go a long way in improving estimates of the $\Upsilon(2S)$ and $\Upsilon(3S)$ dissociation energies.

5.6.1 Comparison Between Charmonium and Bottomonium

Let us analyze the difference with the excitation functions of J/ψ and $\Upsilon(2S)$ in more detail. Despite the similar binding energies, their $R_{\rm AA}$s at the LHC are very different. However, when excluding the cold nuclear matter effects, their primordial suppression from final state interactions turn out to be rather comparable, see Fig. 5.31. Therefore the difference in the total $R_{\rm AA}$ can only be explained by their different regeneration yields in pp collisions. There is about one (primordial) J/ψ for every two hundred produced $c\bar{c}$ pairs, while only one (primordial) $\Upsilon(2S)$ for every two thousand $b\bar{b}$ pairs. Thus a naïve expectation would be that the bottomonium has larger regeneration at the $R_{\rm AA}$ level. However, the bottomonium regeneration is brought down due to several reasons. First, the $b\bar{b}$ pair production cross section is rather small compared with $c\bar{c}$ pairs. There is only one or two $b\bar{b}$ pair at the LHC energies, essentially rendering the statistical production in the canonical limit, and consequently a flat centrality dependence of the regeneration component. Second, the off-thermalized bottom quarks are less easy to recombine and form bottomonium, limiting the regeneration rate due to a longer heavy-quark thermal relaxation time compared with charm quarks, see discussion in Sec. 2.2.3. Third, the larger bottom quark mass (we will see below) also brings down the relative regeneration yield.

In the following, we will present a more quantitative estimate to illustrate the arguments above. We can neglect the hidden sector in the heavy-quark conservation equation due to its tiny portion compared with the open sector. Because the produced $b\bar{b}$ pairs are in the canonical limit and the produced $c\bar{c}$ pairs are in the grand-canonical limit, the heavy-quark conservation equation reads

$$N_{Q\bar{Q}} = \gamma_Q n_Q V_{\rm FB} \frac{I_1(\gamma_Q n_Q V_{\rm FB})}{I_0(\gamma_Q n_Q V_{\rm FB})} \simeq \begin{cases} \gamma_b^2 n_b^2 V_{\rm FB}^2 = N_{b\bar{b}} & \text{for } b\bar{b} \\ \gamma_c n_c V_{\rm FB} = N_{c\bar{c}} & \text{for } c\bar{c} \end{cases} \tag{5.25}$$

with $N_{Q\bar{Q}}$ the total $Q\bar{Q}$ pair number, γ_Q the fugacity factor, n_Q the heavy-quark density, $V_{\rm FB}$ the fireball volume. Consequently, their equilibrium limits are

$$\begin{cases} N^{\rm eq}_{\Upsilon(2S)} = \gamma_b^2 n_{\Upsilon(2S)} V_{\rm FB} \simeq N_{b\bar{b}} \left(\frac{n_{\Upsilon(2S)}}{n_b^2} \frac{1}{V_{\rm FB}}\right) & \text{for } \Upsilon(2S) \\ N^{\rm eq}_{J/\psi} = \gamma_c^2 n_{J/\psi} V_{\rm FB} \simeq N^2_{c\bar{c}} \left(\frac{n_{J/\psi}}{n_c^2} \frac{1}{V_{\rm FB}}\right) & \text{for } J/\psi \end{cases} \tag{5.26}$$

where the density of particle i (i=$\Upsilon(2S)$, J/ψ, b, c) is

$$n_i \simeq d_i \int \frac{{\rm d}^3 p}{(2\pi)^3} e^{-\frac{\sqrt{p^2+m^2}}{T}} = \frac{d}{2\pi^2} m_i^2 T K_2\left(\frac{m_i}{T}\right), \tag{5.27}$$

with d_i the degeneracy factor, m_i the particle mass, T the temperature, and $K_2(x)$ the second order modified Bessel function of the second kind.

At the $R_{\rm AA}$ level, we have roughly

$$R^{\rm reg}_{\rm AA} = \begin{cases} \frac{N^{\rm reg}_{\Upsilon(2S)}}{N_{\rm coll} N^{pp}_{\Upsilon(2S)}} = \frac{N^{\rm reg}_{\Upsilon(2S)}}{N_{\Upsilon(2S)}} \propto \frac{N^{\rm eq}_{\Upsilon(2S)} \mathcal{R}_{\Upsilon(2S)}}{N_{\Upsilon(2S)}} \simeq \left(\frac{N_{b\bar{b}}}{N_{\Upsilon(2S)}}\right) \left(\mathcal{R}_{\Upsilon(2S)}\right) \left(\frac{n_{\Upsilon(2S)}}{n_b^2}\right) \left(\frac{1}{V_{\rm FB}}\right) \\ \frac{N^{\rm reg}_{J/\psi}}{N_{\rm coll} N^{pp}_{J/\psi}} = \frac{N^{\rm reg}_{J/\psi}}{N_{J/\psi}} \propto \frac{N^{\rm eq}_{J/\psi} \mathcal{R}_{J/\psi}}{N_{J/\psi}} \simeq \left(\frac{N^2_{c\bar{c}}}{N_{J/\psi}}\right) \left(\mathcal{R}_{J/\psi}\right) \left(\frac{n_{J/\psi}}{n_c^2}\right) \left(\frac{1}{V_{\rm FB}}\right) \end{cases} \tag{5.28}$$

There are four brackets, except for the last bracket $\frac{1}{V_{\rm FB}}$ which is the same for $\Upsilon(2S)$ and J/ψ, the first, second and the third brackets (Denoted by B_1, B_2, B_3) are responsible for the three differences mentioned above.

Take 5.02 TeV mid-rapidity 0-20% centrality for example, we have $\frac{{\rm d}\sigma_{\Upsilon(2S)}}{{\rm d}y}$=0.019 μb,

$\frac{d\sigma_{b\bar{b}}}{dy}$=32.8 μb, $\frac{d\sigma_{J/\psi}}{dy}$=5 μb, $\frac{d\sigma_{c\bar{c}}}{dy}$=850 μb, $\sigma_{\rm inel}$=65000 μb, and

$$N_i = \left(\Delta y \frac{\mathrm{d}\sigma_i}{\mathrm{d}y}\right) \frac{N_{\rm coll}}{\sigma_{\rm inel}} \simeq \left(1.8 \frac{\mathrm{d}\sigma_i}{\mathrm{d}y}\right) \frac{1350}{67000\mu b} = 0.036\mu b^{-1} \left(\frac{\mathrm{d}\sigma_i}{\mathrm{d}y}\right). \tag{5.29}$$

So there are roughly $N_{c\bar{c}}$≈31 $c\bar{c}$ pairs. Thus

$$\frac{B_1(J/\psi)}{B_1(\Upsilon(2S))} = \frac{\left(\frac{N^2_{c\bar{c}}}{N_{J/\psi}}\right)}{\left(\frac{N_{b\bar{b}}}{N_{\Upsilon(2S)}}\right)} = \frac{\left(\frac{N_{c\bar{c}}}{N_{J/\psi}}\right)}{\left(\frac{N_{b\bar{b}}}{N_{\Upsilon(2S)}}\right)} N_{c\bar{c}} = \frac{\left(\frac{850}{5}\right)}{\left(\frac{32.8}{0.019}\right)} 31 \approx 3.05. \tag{5.30}$$

At a specific average regeneration temperature T=200 MeV, the fireball lifetime is roughly τ=5 fm (according to temperature evolution). We have

$$\frac{B_2(J/\psi)}{B_2(\Upsilon(2S))} = \frac{\mathcal{R}_{J/\psi}}{\mathcal{R}_{\Upsilon(2S)}} = \frac{1-\exp\left(-\frac{\tau}{\tau_c}\right)}{1-\exp\left(-\frac{\tau}{\tau_b}\right)} = \frac{1-\exp\left(-\frac{5.5}{4.5}\right)}{1-\exp\left(-\frac{5.5}{11}\right)} \approx 1.8 \tag{5.31}$$

and

$$\frac{B_3(J/\psi)}{B_3(\Upsilon(2S))} = \frac{\left(\frac{n_{J/\psi}}{n_c^2}\right)}{\left(\frac{n_{\Upsilon(2S)}}{n_b^2}\right)} = \frac{\left(\frac{m_{J/\psi}}{m_c^2}\right)}{\left(\frac{m_{\Upsilon(2S)}}{m_b^2}\right)} \frac{K_2\left(\frac{m_{J/\psi}}{T}\right)/K_2^2\left(\frac{m_c}{T}\right)}{K_2\left(\frac{m_{\Upsilon(2S)}}{T}\right)/K_2^2\left(\frac{m_b}{T}\right)} \approx 3.8 \tag{5.32}$$

.

We have in total an enhancement factor of $\frac{B_1(J/\psi)}{B_1(\Upsilon(2S))}\frac{B_2(J/\psi)}{B_2(\Upsilon(2S))}\frac{B_3(J/\psi)}{B_3(\Upsilon(2S))}$=20.9. This factor illustrates the large J/ψ regeneration compared with the $\Upsilon(2S)$ regeneration at the $R_{\rm AA}$ level.

Of course the real calculations involve nontrivial convolutions of temperature dependent rates and equilibrium limits, over a time evolution. The above estimates might not be very accurate, but they illustrate the effects that enhance the regeneration of J/ψ compared with $\Upsilon(2S)$.

5.7 Conclusions

In the current section we have refined our previous Boltzmann/rate-equation approach to bottomonium transport in heavy-ion collisions. The improvements include the use of in-medium binding energies and their consequences for dissociation mechanisms and pertinent rates, a lQCD-based equation of state for the fireball evolution, correlation volume effects for regeneration reactions, and B-meson resonance states appearing close to T_{pc} affecting the regeneration transport parameter. In this way, the approach has been brought to the same level as employed before for charmonia, and thus enables interpretations of bottomonium data on an equal footing. In particular, the role of regeneration contributions, which are essential for charmonia at the LHC, is a priori less obvious for bottomonia. In an attempt to augment possible signatures of those, we extended our calculations of the centrality dependence of inclusive bottomonium yields to transverse-momentum spectra and elliptic flow.

Overall, our improved approach allows for a fair description of existing $\Upsilon(1S)$, $\Upsilon(2S)$ and $\Upsilon(3S)$ observables at RHIC and the LHC, including new data released from both facilities very recently. We have found that the suppression level of the $\Upsilon(1S)$ R_{AA} at the LHC has a significant sensitivity to the in-medium binding energy used in the calculations and thus can, in principle, serve as a quantitative measure of the screening of the heavy-quark potential in the QGP. A similar sensitivity at RHIC energies requires a better control over the CNM effects. At this point, the LHC data suggest a rather strong heavy-quark potential which supports $\Upsilon(1S)$ states out to temperatures of $T{\simeq}500\,\mathrm{MeV}$. Inelastic reaction rates can, of course, break up $\Upsilon(1S)$ states at temperatures well below that. The strong suppression of the $\Upsilon(2S)$, on the other hand, suggests its melting at much lower temperatures, around $T{\simeq}240\,\mathrm{MeV}$, implying strong screening effects on the linear ("confining") part of the heavy-quark potential in this regime. We also found that the emergence of B-mesons near $T_{\rm pc}$, which lowers the equilibrium limit of the Y states, reduces the regeneration of the $\Upsilon(2S)$, which helps in quantitatively describing the pertinent CMS data at both 2.76 and 5.02 TeV. Some tension persists between our results and the forward-rapidity $\Upsilon(1S)$ ALICE data in Pb-Pb(2.76 TeV) collisions, which show a stronger suppression than obtained from our calculations. The regeneration contributions for both $\Upsilon(1S)$ and $\Upsilon(2S)$ come out at a rather generic level of around $R_{\rm AA}\simeq$ 0.05-0.1 [smaller for the $\Upsilon(3S)$], across centrality (for $N_{\rm part}\gtrsim 100$), rapidity and collision energy (even down to RHIC energies). This is mostly a consequence of the canonical limit, *i.e.*, small open-bottom cross sections which limit the number of $b\bar{b}$ pairs to either zero or one in a given fireball. In the calculations of transverse-momentum spectra, the 3-momentum dependence of the dissociation rates tends to produce a decrease of the primordial $R_{\rm AA}(p_T)$, which, however, is counter-balanced by formation time effects at high p_T. For the regeneration component, the inclusion of realistic b-quark spectra, taken from Langevin transport simulations which do not kinetically equilibrate, turns out to be significant. Even though the coalescence contribution is not large, a thermal blast-wave approximation for regenerated bottomonia produces a low-p_T enhancement in the $R_{\rm AA}(p_T)$ which is disfavored by the CMS data (in contrast to the J/ψ case, where a marked low-p_T enhancement is observed). On the other hand, using the transport b-quark spectra, the regeneration component generates a mild maximum structure in the $\Upsilon(1S)$ $R_{\rm AA}(p_T)$ around $p_T \lesssim 10\,$GeV, which is consistent with experiment. Our predictions for Y elliptic flow do not exhibit significant discrimination power between primordial and regeneration mechanisms. However, we predict a factor of $\sim$2 larger total v_2 for the $\Upsilon(2S)$ than for the $\Upsilon(1S)$, since the inelastic reactions for the former remain active to lower temperatures. This should be helpful in either refuting or corroborating the sequential melting and regeneration, as opposed to, *e.g.*, statistical production of both particles at the same temperature.

Future work should focus on improving the precision of the approach on several fronts.

Our initial checks of various model components (pertaining to the bulk evolution, correlation volume, Y formation time and b-quark thermalization) indicate a promising robustness of our results, in particular with regards to connecting the observed level of $\Upsilon(1S)$ suppression to the screening of the fundamental QCD force in the QGP. However, the interplay of the early bulk medium evolution with quantum effects in the $b\bar{b}$ wave package deserves further studies [220, 221, 222, 223]. This also applies to nonperturbative interactions in the Y dissociation mechanisms (*e.g.*, by using explicit T-matrix interactions), which, after all, play a central role in understanding the strong coupling of individual heavy quarks diffusing through the QGP. These developments will improve our understanding of the systematic errors in the present results and enable a more controlled assessment of the modifications of the fundamental QCD force in the QGP.

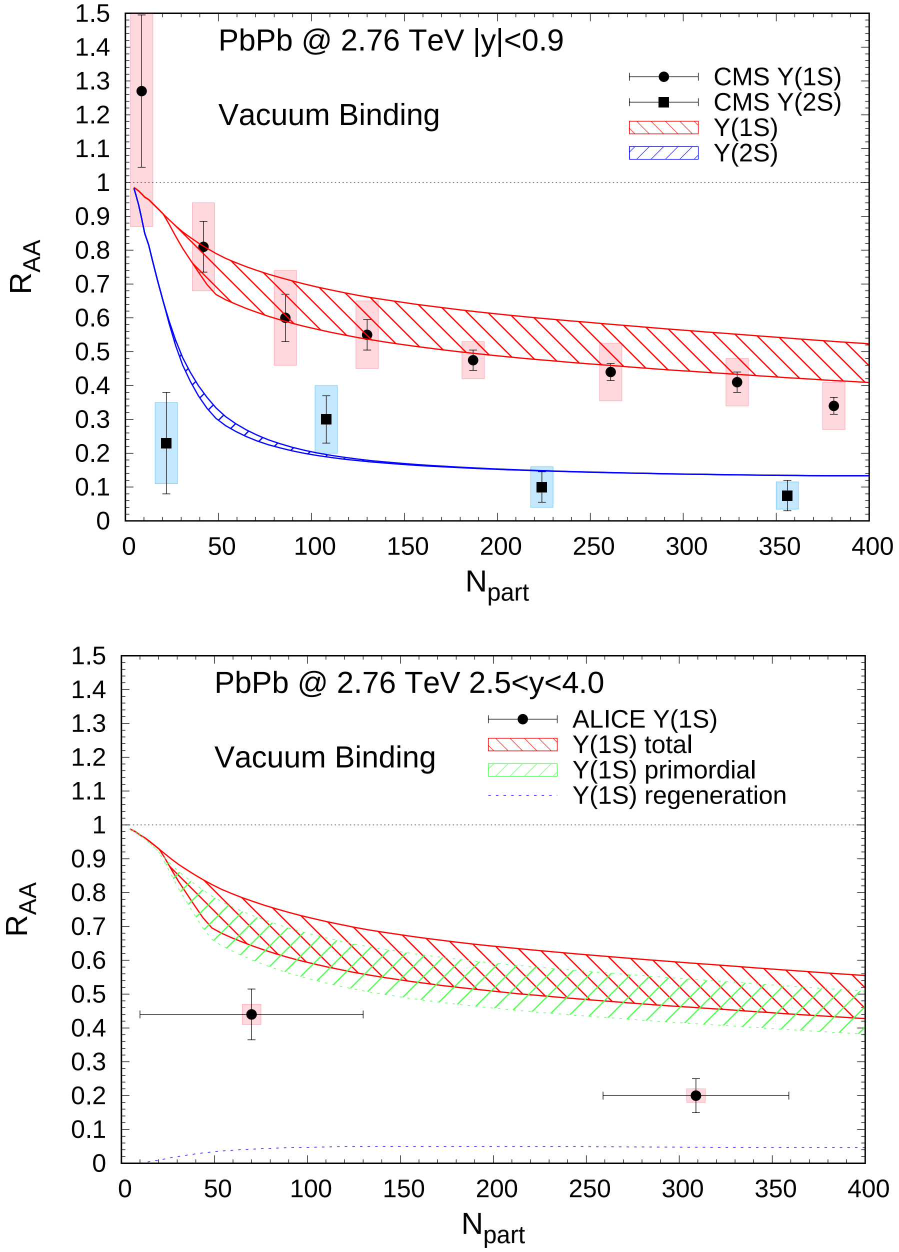

Figure 5.13: Centrality dependence of bottomonium production in Pb-Pb(2.76 TeV) collisions within the vacuum binding scenario [175] with updated feeddowns. Upper panel: $\Upsilon(1S)$ (red band) and $\Upsilon(2S)$ (blue band) at mid-rapidity compared to CMS data [182]. Lower panel: $\Upsilon(1S)$ at forward rapidity compared to ALICE data [54], where we also show the regeneration contribution (dotted line). The band widths of the totals in both panels are due to a 0-25% variation in the shadowing suppression of the initial bottomonium yields.

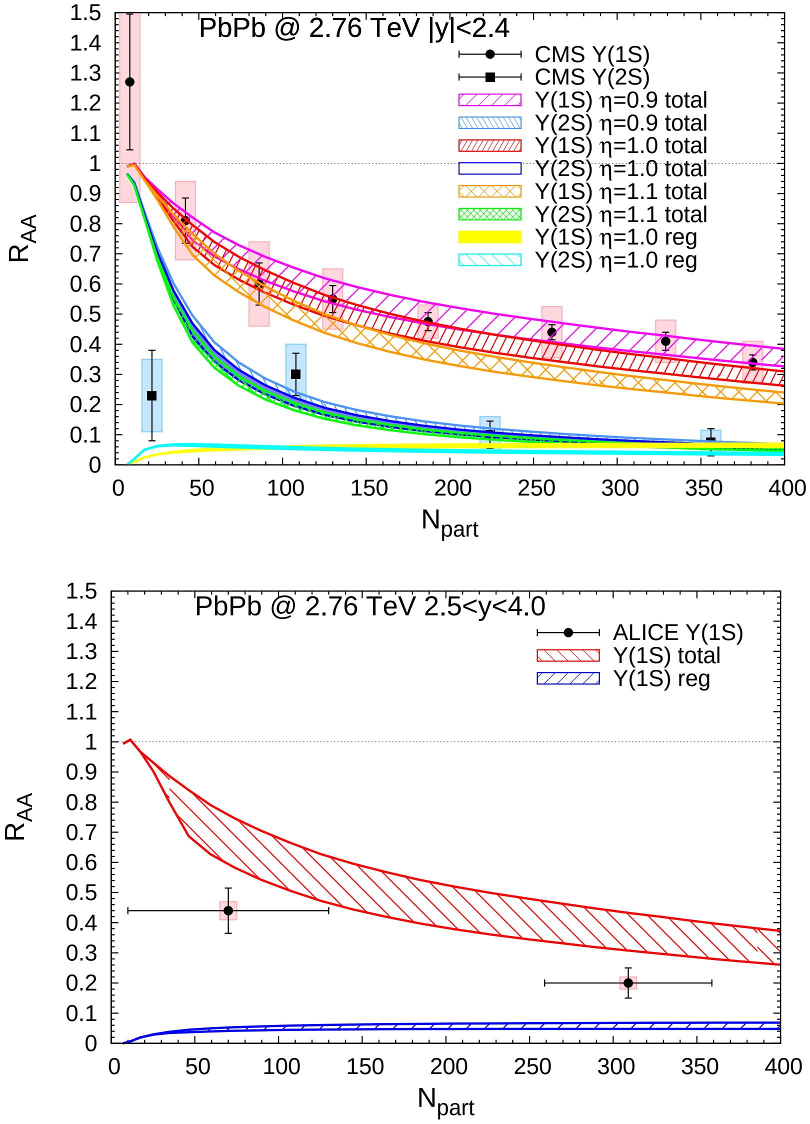

Figure 5.14: Centrality dependence of $\Upsilon(1S)$ and $\Upsilon(2S)$ production in Pb-Pb(2.76 TeV) collisions within the TBS. Upper panel: inclusive $\Upsilon(1S)$ and $\Upsilon(2S)$ results at mid-rapidity for η=0.9, η=1.0 and η=1.1 scenarios compared to CMS data [182]. The red (blue) band is the total $\Upsilon(1S)$ ($\Upsilon(2S)$) R_{AA} for baseline η =1.0, the pink (light blue) band is the total $\Upsilon(1S)$ ($\Upsilon(2S)$) R_{AA} for η=0.9, the orange (green) band is the total $\Upsilon(1S)$ ($\Upsilon(2S)$) R_{AA} for η=1.1, and the yellow (cyan) band is the $\Upsilon(1S)$ ($\Upsilon(2S)$) regeneration contribution with η=1.0. The regeneration components for different scenarios have tiny differences. The bands reflect the uncertainty due to shadowing between 0-15%. Lower panel: inclusive $\Upsilon(1S)$ (red band) and regenerated component (blue band) at forward rapidity for η=1.0, compared to ALICE data [54]; the bands reflect the uncertainty due to a shadowing reduction between 0-30%.

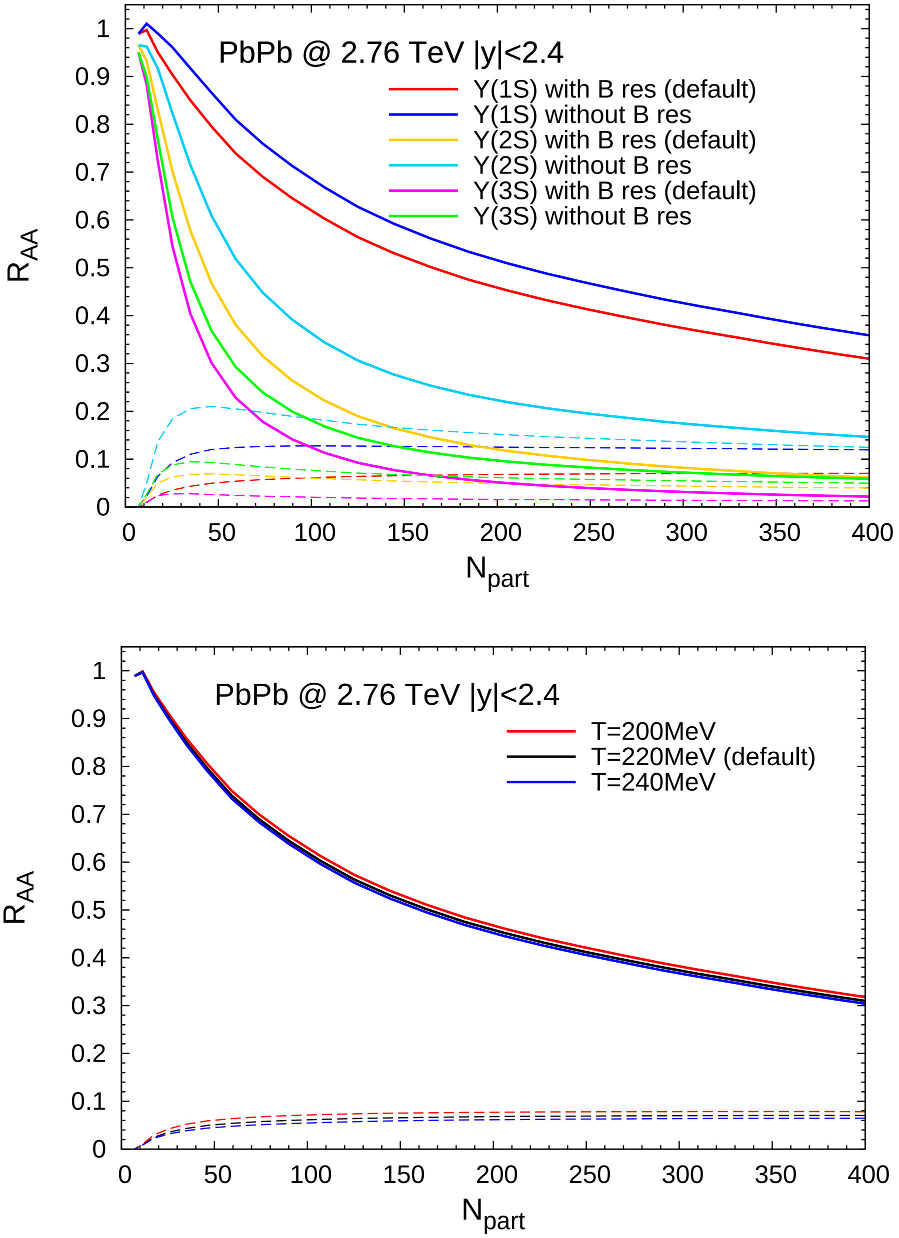

Figure 5.15: Upper panel: comparison of $\Upsilon(1S)$, $\Upsilon(2S)$, and $\Upsilon(3S)$ $R_{\rm AA}$'s (solid lines: total; dashed lines: regeneration contribution) for the TBS with and without B-meson resonance states near $T_{\rm pc}$, assuming the default switching temperature of T=220 MeV. The red/blue curves are with/out resonances for $\Upsilon(1S)$, the cyan/yellow curve are with/out resonances for $\Upsilon(2S)$, and the magenta/green curves are with/out resonances for $\Upsilon(3S)$. Lower panel: sensitivity of the default scenario to the switching temperature.

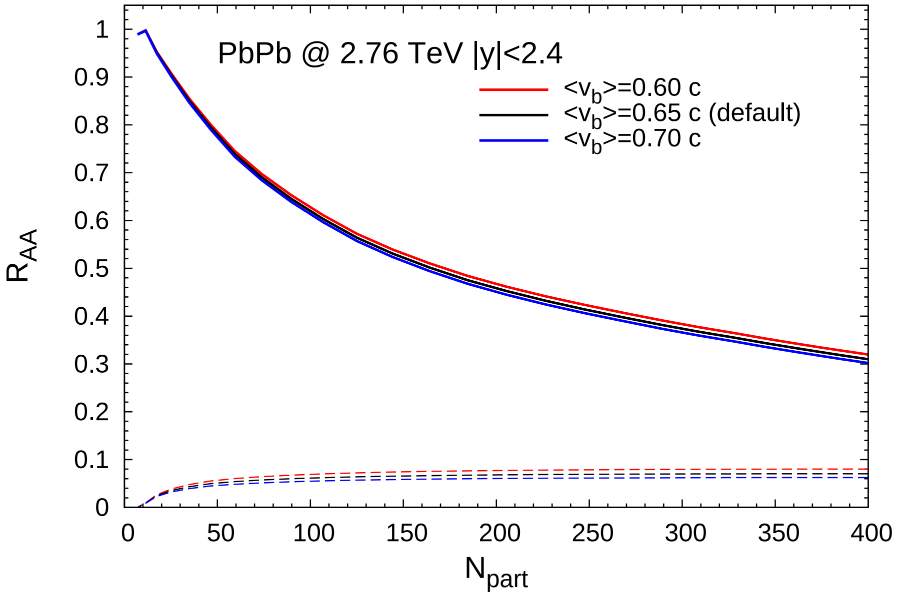

Figure 5.16: Sensitivity of $\Upsilon(1S)$ production to the mean b-quark speed, $\langle v_b \rangle$, by which the correlation volume expands (red, black and blue lines are for $\langle v_b \rangle$=0.6c, 0.65c, and 0.7c, respectively). Solid (dashed) lines are for the total (regeneration component of the) $\Upsilon(1S)$ $R_{\rm AA}$ regeneration component

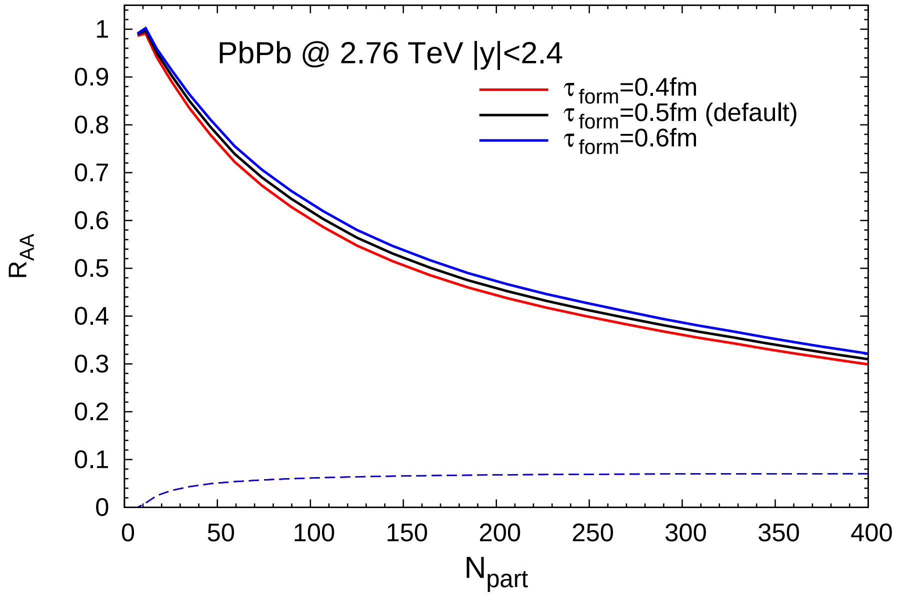

Figure 5.17: Sensitivity of $\Upsilon(1S)$ production to a variation of the Y formation times by $\pm 20\,\%$.

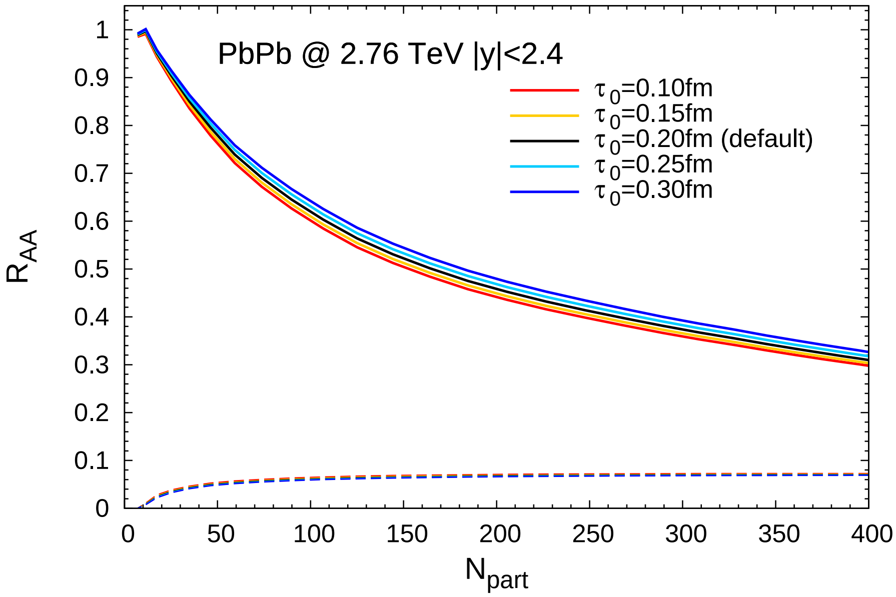

Figure 5.18: Sensitivity of $\Upsilon(1S)$ production to a variation of the QGP formation time over the range τ_0=0.1-0.3 fm/c. The regeneration component (dashed lines) is virtually unaffected.

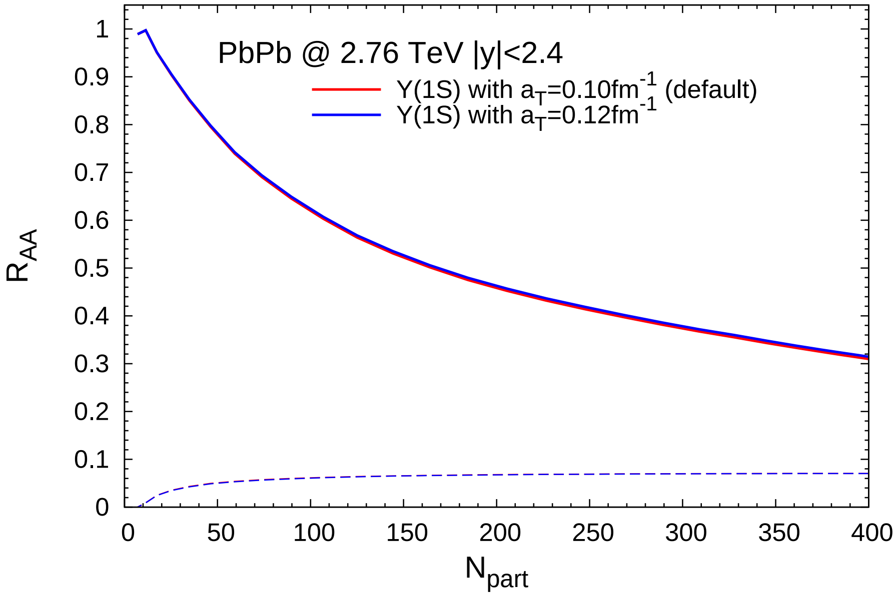

Figure 5.19: Sensitivity of $\Upsilon(1S)$ production to a variation of the fireball expansion acceleration over the range a_{T}=0.10-0.12 /fm.

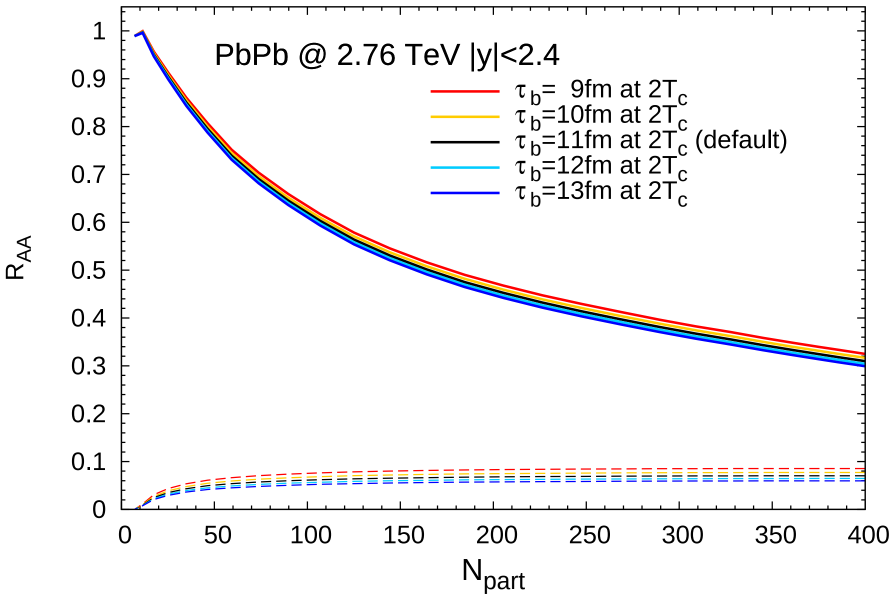

Figure 5.20: Sensitivity of $\Upsilon(1S)$ production to the b-quark thermalization time, τ_b, over the range τ_b=8-12 fm at $2T_{\rm pc}$. Dashed lines are for the regeneration component.

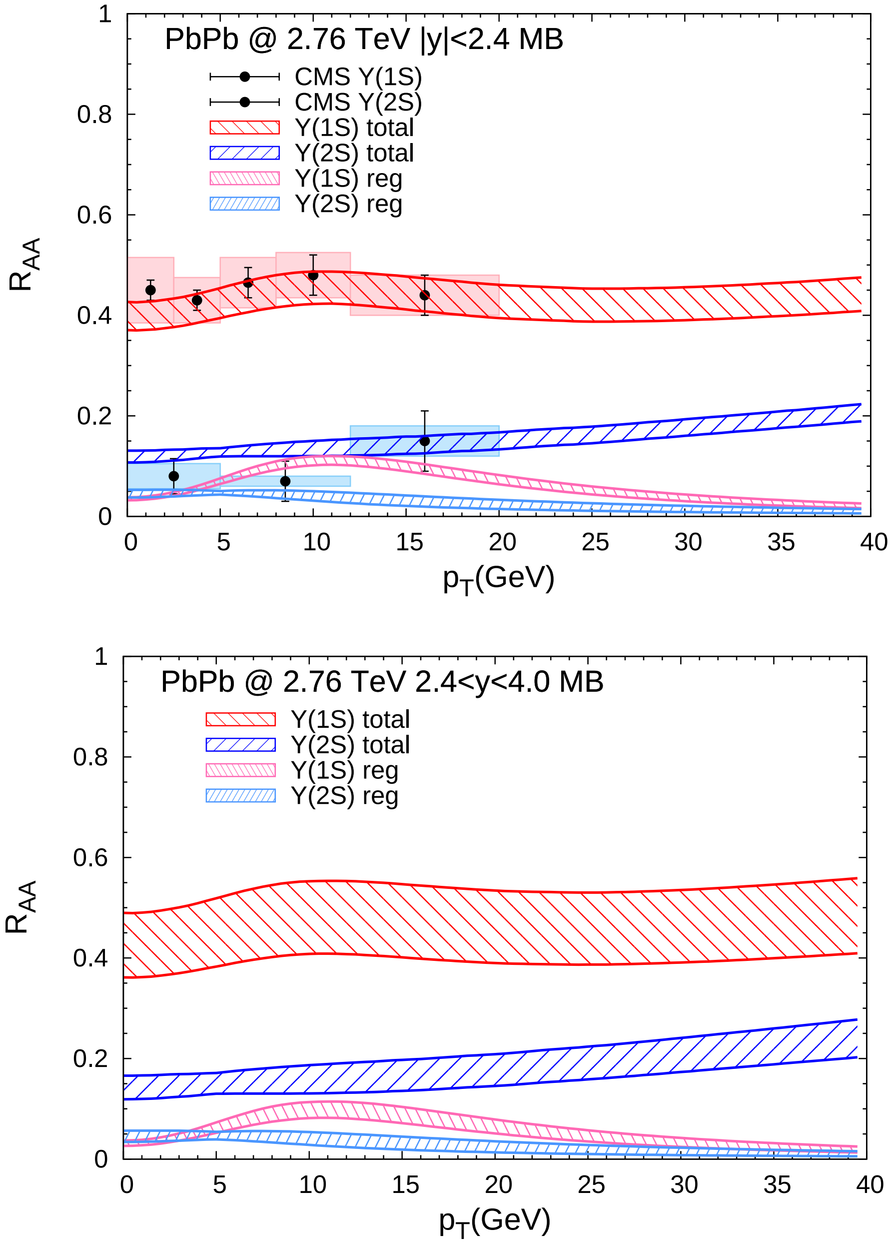

Figure 5.21: Transverse-momentum dependent $R_{\rm AA}$ for inclusive $\Upsilon(1S)$ (red band) and $\Upsilon(2S)$ (blue band) production and their regeneration component (pink and light blue bands, respectively) in minimum-bias Pb-Pb(2.76 TeV) collisions within the TBS for η=1.0 at mid- and forward rapidity (upper and lower panel, respectively), compared to CMS data [182]. The width of the total bands includes a 0-15% (0-30%) shadowing suppression for $|y| < 2.4$ ($2.5 < y < 4.0$), the variation in the temperature window for the regeneration component (also shown separately) and the uncertainty in the pp baseline spectra.

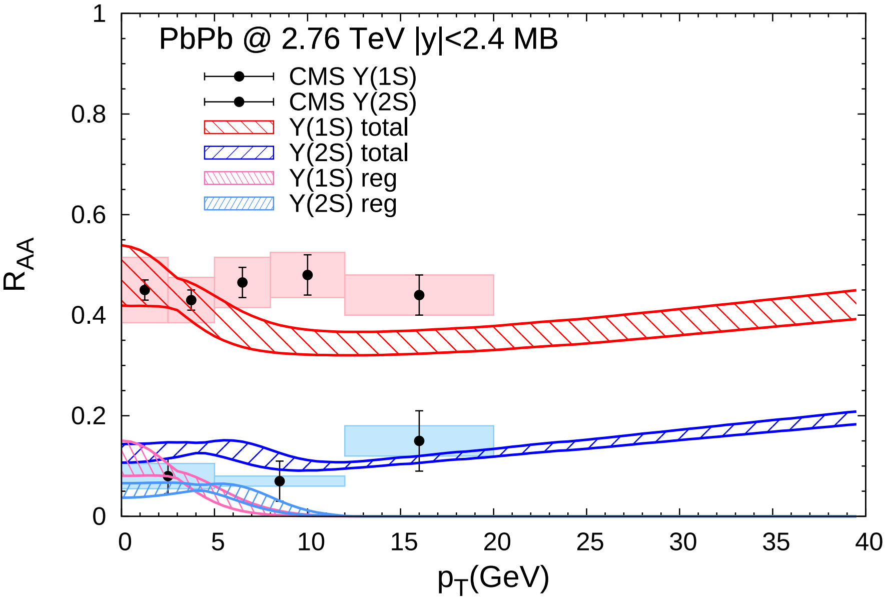

Figure 5.22: Same as upper panel in Fig. 5.21 but with the regeneration component evaluated by a thermal blast-wave approximation for the respective Y states.

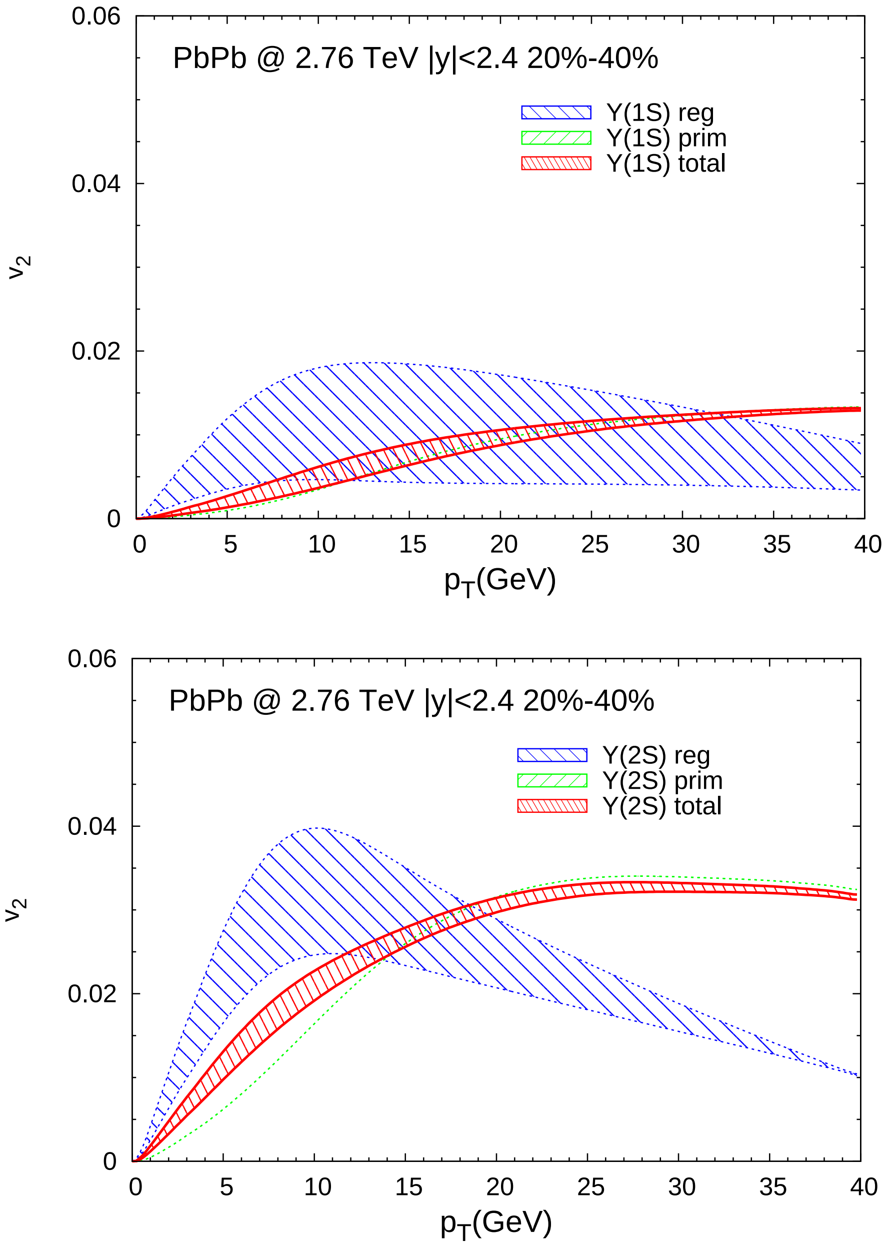

Figure 5.23: The p_T dependence of elliptic flow of $\Upsilon(1S)$ (upper panel) and $\Upsilon(2S)$ (lower panel) in semi-central Pb-Pb(2.76 TeV) at mid-rapidity within the TBS (η=1.0). In both panels the blue, green, and red curves are for the regeneration component, primordial component and their weighted sum, respectively, where the band widths reflect uncertainties from varying the average regeneration temperatures.

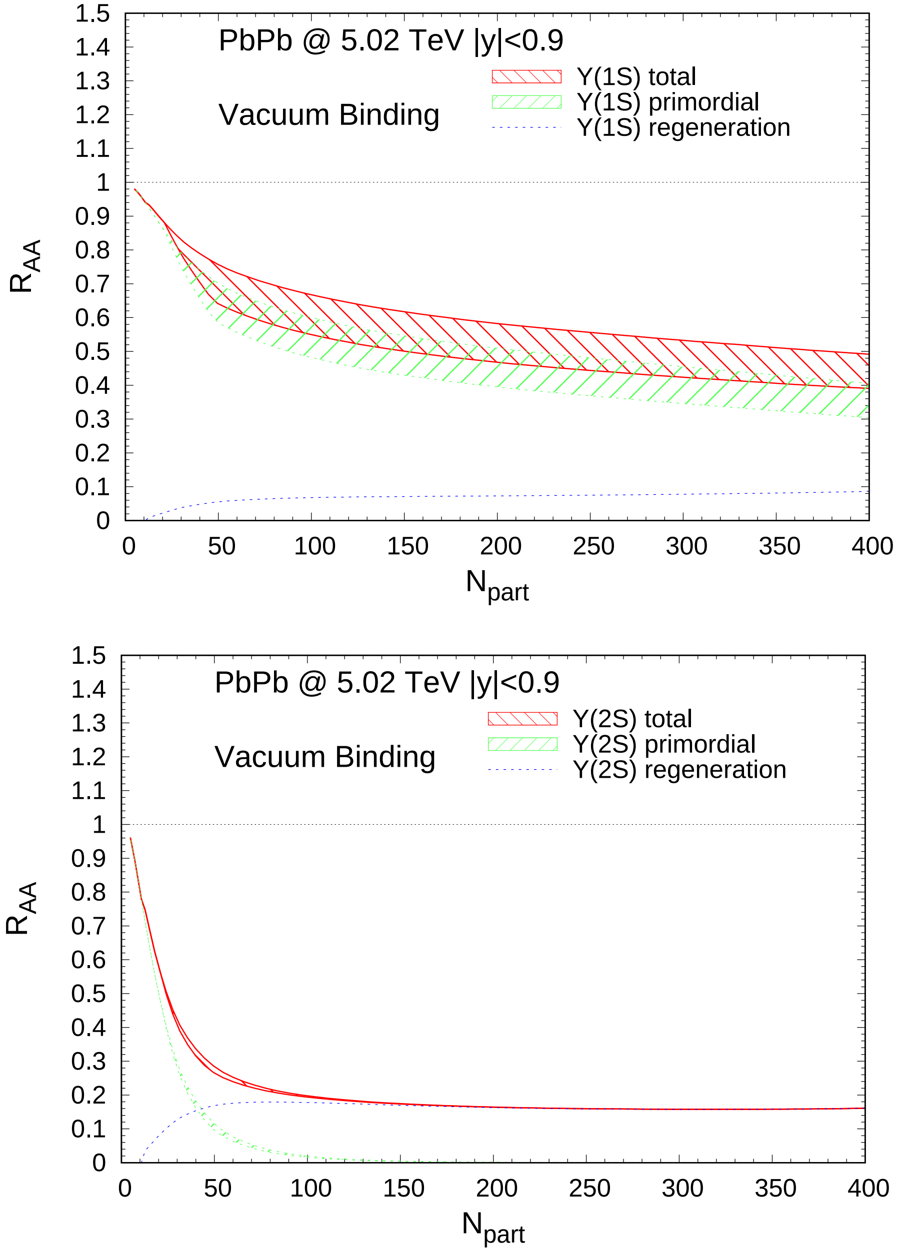

Figure 5.24: Centrality dependence of $R_{\rm AA}$ for $\Upsilon(1S)$ (upper panel) and $\Upsilon(2S)$ (lower panel) within the vacuum binding scenario in Pb-Pb(5.02 TeV) collisions at mid-rapidity. Red, green and blue lines represent the total, primordial and regeneration contributions, where the bands reflect a 0-25% shadowing effect.

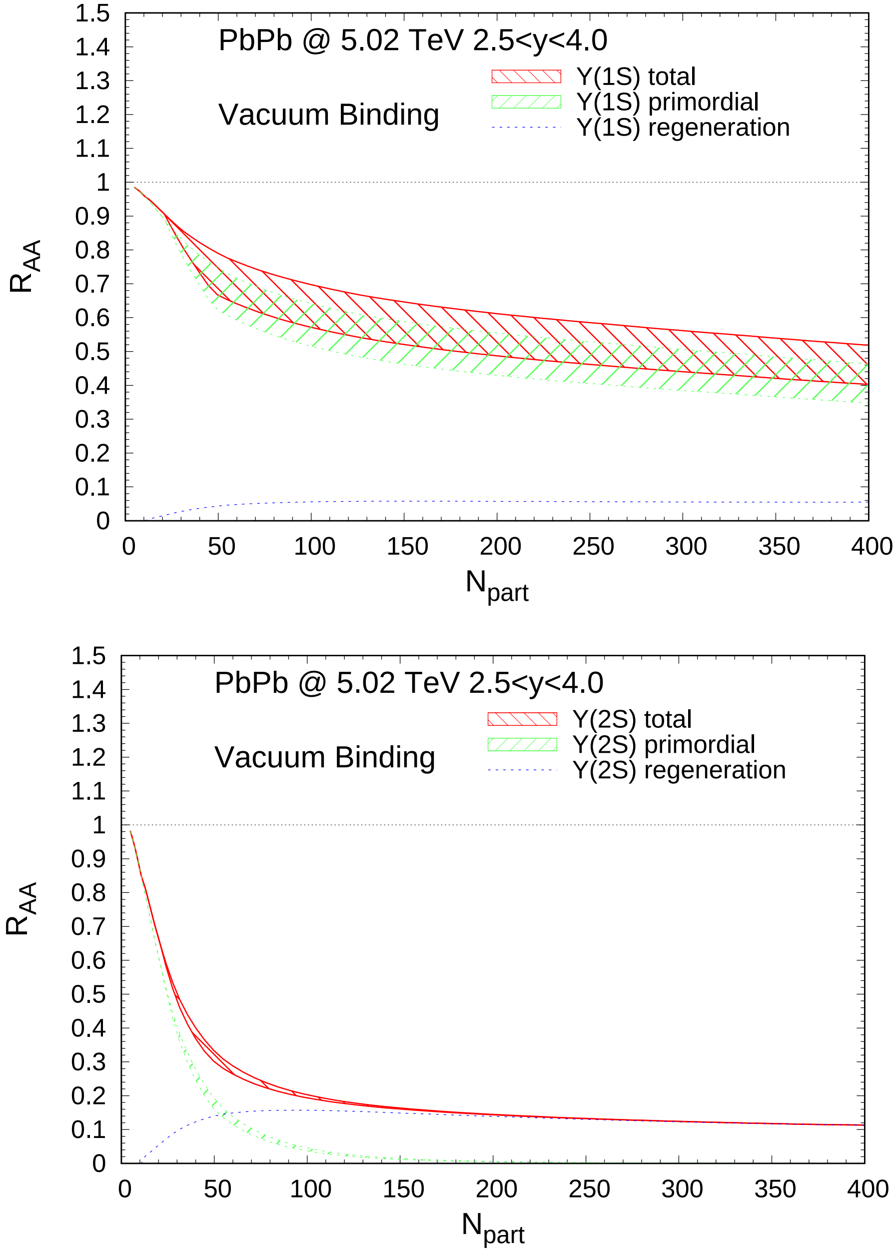

Figure 5.25: Same as Fig. 5.24 but at forward rapidity.

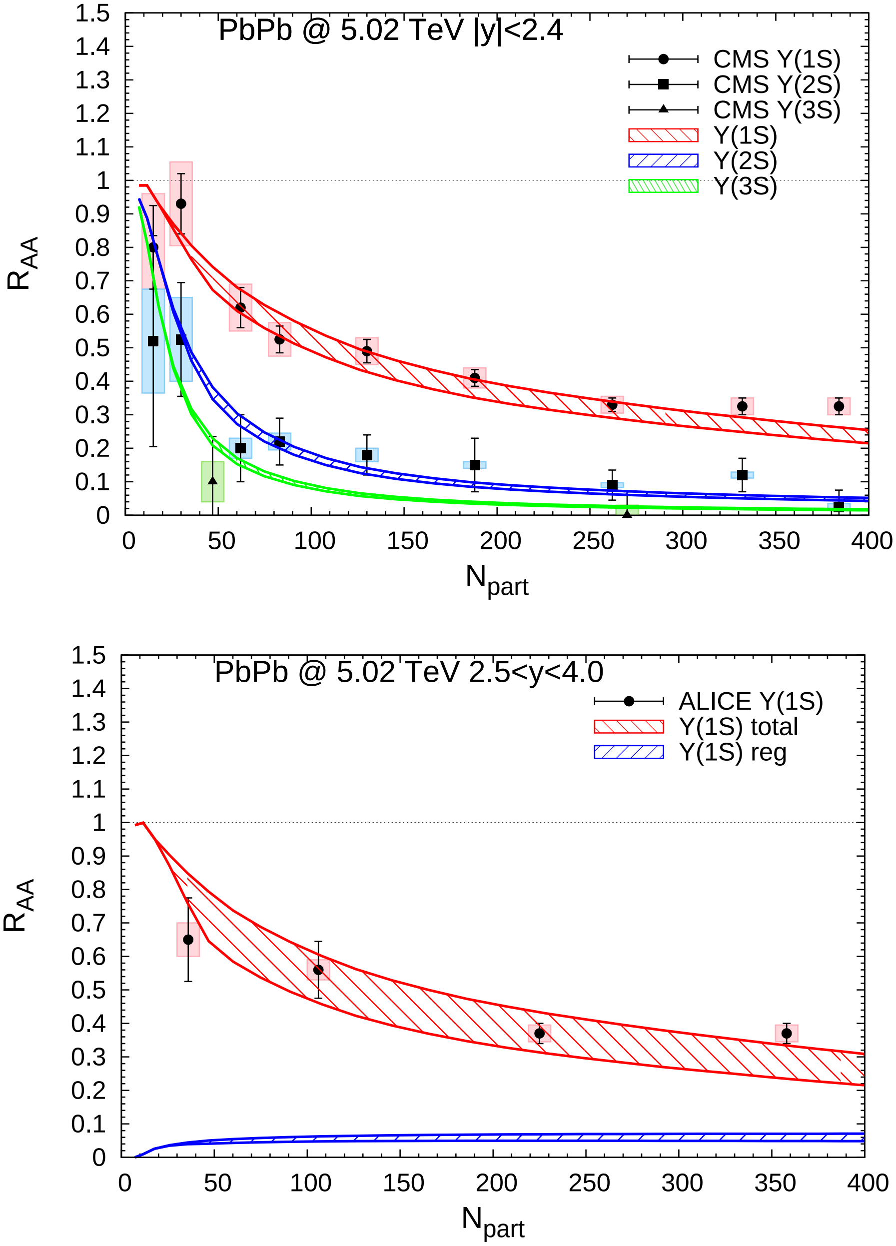

Figure 5.26: Centrality dependence of bottomonium $R_{\rm AA}$'s in Pb-Pb(5.02 TeV) collisions within the TBS (η=1.0). Upper panel: mid-rapidity $\Upsilon(1S)$, $\Upsilon(2S)$ and $\Upsilon(3S)$ (red, blue and green bands, respectively) compared to CMS data [198, 199]; the bands are due to a 0-15% shadowing suppression. Lower panel: forward rapidity $\Upsilon(1S)$ compared to ALICE data [215, 216]; the bands are due to a 0-30% shadowing suppression.

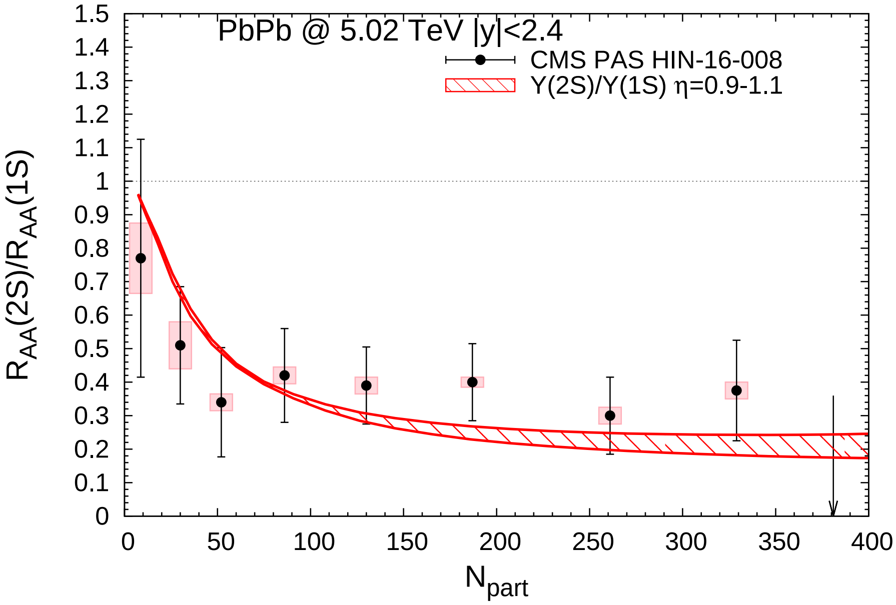

Figure 5.27: Centrality dependence of the $\Upsilon(2S)/\Upsilon(1S)$ R_{AA} double ratio in 5.02 TeV Pb-Pb collisions at mid-rapidity within the TBS (with an uncertainty band from in-medium binding energies for η=0.9-1.1), compared to CMS data [217].

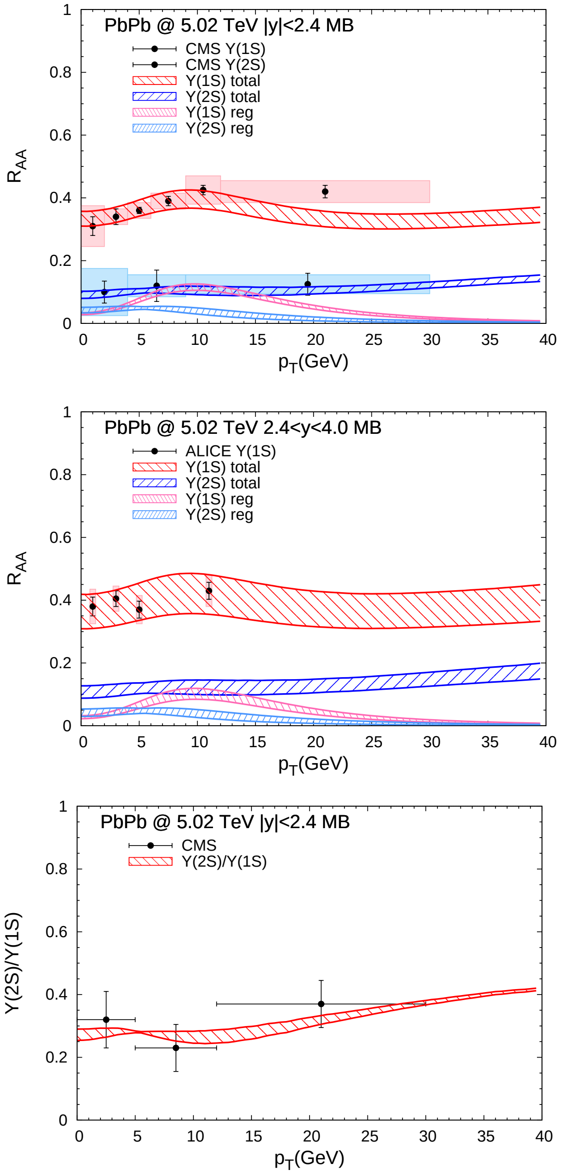

Figure 5.28: The p_T dependence of $\Upsilon(1S)$ and $\Upsilon(2S)$ yields in MB Pb-Pb(5.02 TeV) collisions at mid and forward rapidities within the TBS (η=1.0). Upper panel: mid-rapidity $\Upsilon(1S)$ and $\Upsilon(2S)$ $R_{\rm AA}$ for total (red and blue curves, respectively) and regeneration components (pink and light-blue curves, respectively), compared to CMS data [198, 199]; the bands reflect variations due to a 0-15% shadowing suppression and the average regeneration temperatures ($\bar{T}_{\rm reg}$) of the two states. Middle panel: same as upper panel but at forward rapidity with a 0-30% shadowing range, compared to ALICE data [216]. Lower panel: $\Upsilon(2S)/\Upsilon(1S)$ $R_{\rm AA}$ double ratio compared to CMS data [217]; the band reflects variations in the $\bar{T}_{\rm reg}$'s.

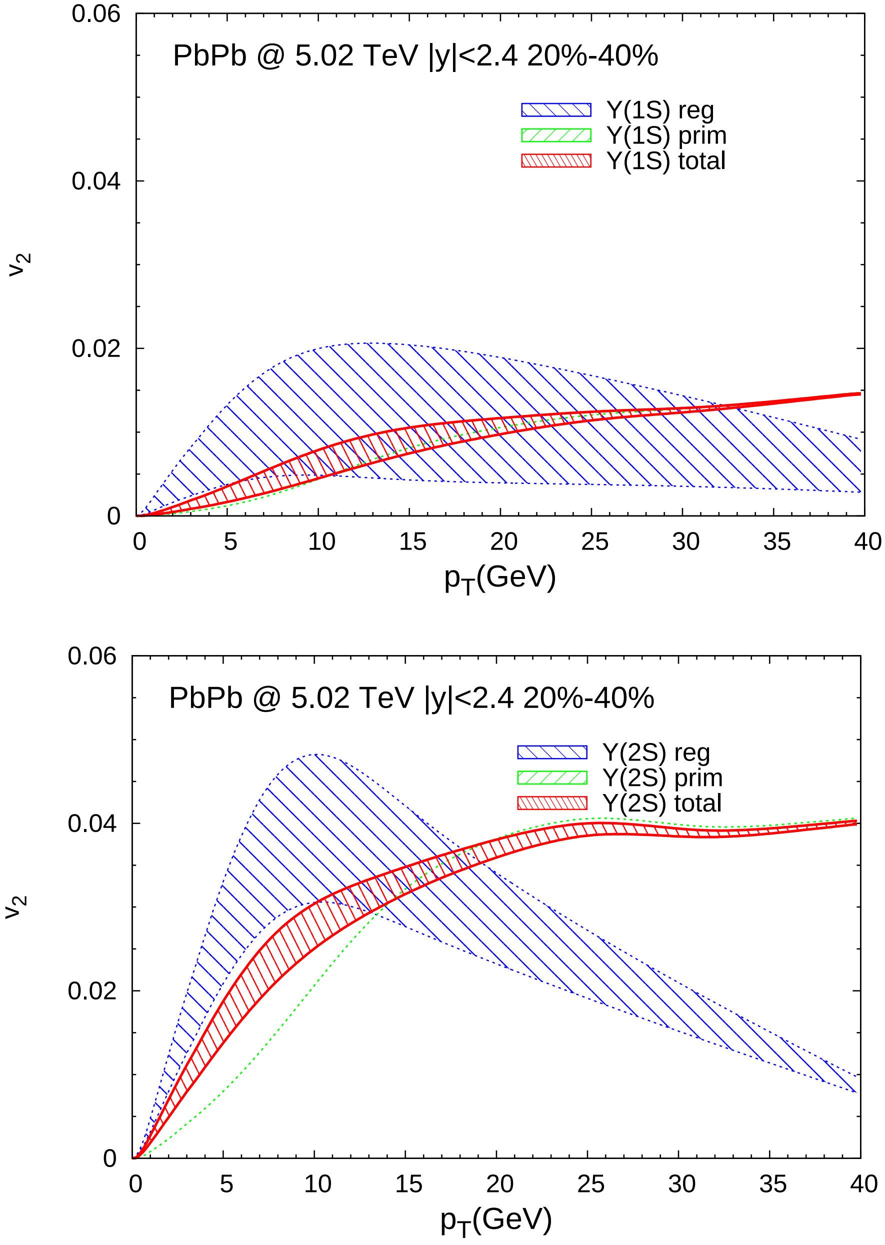

Figure 5.29: The p_T dependence of elliptic flow of $\Upsilon(1S)$ (upper panel) and $\Upsilon(2S)$ (lower panel) in semi-central Pb-Pb(5.02 TeV) at mid-rapidity within the TBS (η=1.0). In both panels the blue, green, and red curves are for the regeneration component, primordial component, and their weighted sum, respectively, where the band widths reflect uncertainties from varying the average regeneration temperatures.

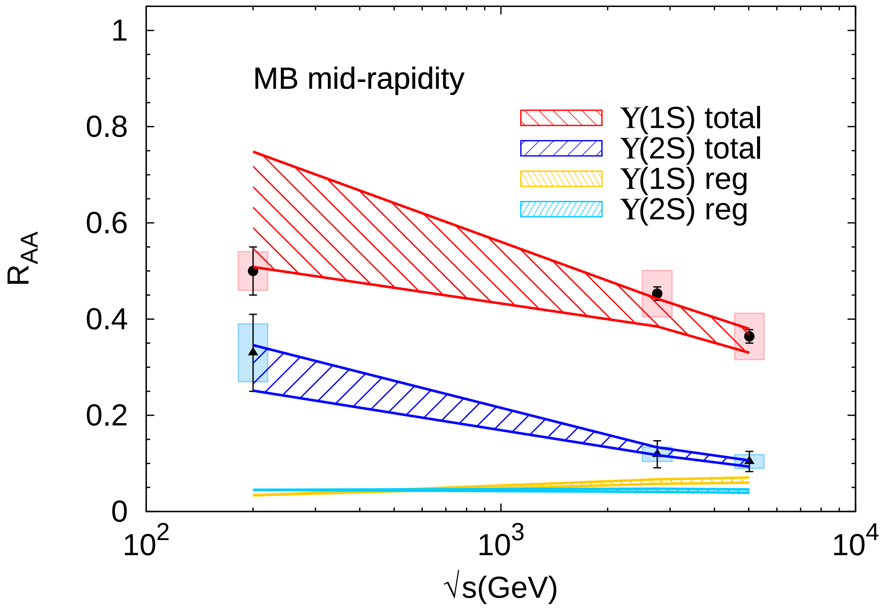

Figure 5.30: Excitation function the MB R_{AA} of $\Upsilon(1S)$ and $\Upsilon(2S)$ with TBS compared to STAR [193] and CMS [182, 198, 199] data at mid-rapidity.

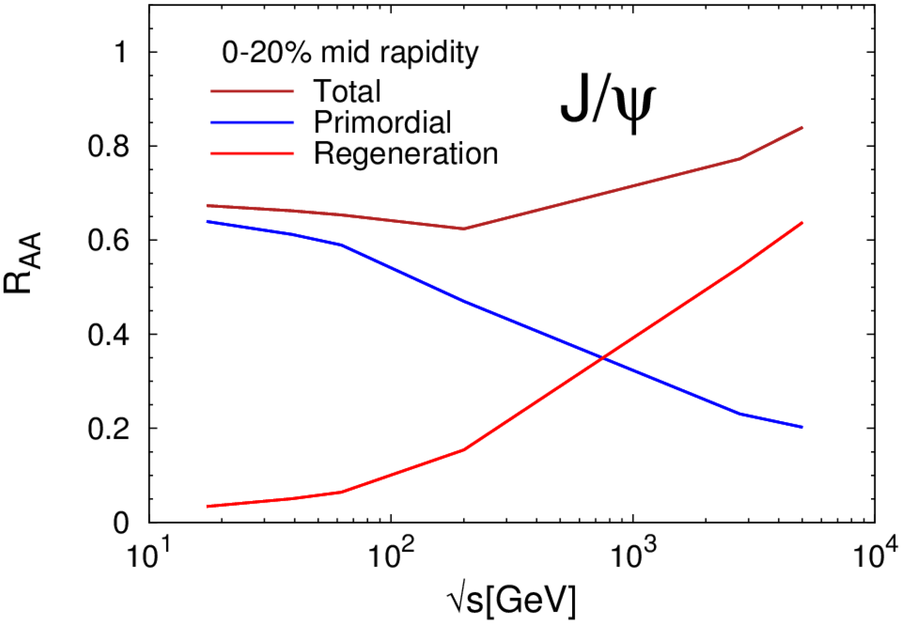

Figure 5.31: Excitation function R_{AA} of J/ψ with hot medium effects only. The primordial part is comparable with $\Upsilon(2S)$ excitation function shown in Fig. 5.30. Figure is from [35].

6. STATISTICAL EXTRACTION OF THE HEAVY-QUARK POTENTIAL*

The in-medium color potential is a fundamental quantity for understanding the properties of the strongly coupled quark-gluon plasma (sQGP). Open and hidden heavy-flavor (HF) production in URHICs has been found to be a sensitive probe of this potential [227, 59]. Here we utilize the well developed and tested quarkonium transport approach in combination with insights from open HF diffusion to extract the color-singlet potential from experimental results on Υ production in URHICs. Starting from a parameterized trial potential, we evaluate the Υ transport parameters and conduct systematic fits to available data for the centrality dependence of ground and excited states at RHIC and the LHC. The best fits and their statistical significance are converted into a temperature dependent potential.

6.1 Feasibility of Extracting the Potential

The confining force of QCD plays a central role in the quantitative description of the bound-state spectra of charmonia and bottomonia in vacuum [9], characterized by a linear term in color-singlet potential between a color charge and its anti-charge. It has also been applied rather successfully for light hadrons [228, 229] (with caveats in the chiral sector). Thus, the in-medium properties of quarkonia have long been recognized as promising probe for the formation of the QGP in URHICs [37, 100, 101, 42, 230, 35]. In addition, the consequences of in-medium potentials on heavy-quark (HQ) diffusion [204, 75, 231] and QGP structure [232, 233, 234, 235, 236, 237] have been studied, where remnants of the confining force above the pseudo-critical temperature, T_{pc}, were found to be essential in explaining the properties of the sQGP. Recent efforts to define the potential [185, 238,

---

*Part of this section is reprinted with permission from “Extraction of the Heavy-Quark Potential from Bottomonium Observables in Heavy-Ion Collisions” by Du, Xiaojian and Liu, Shuai Y. F. and Rapp, Ralf, ArXiv:1904.00113, Copyright 2019 by ArXiv.

183] and relate it to quantities computed in lQCD, such as the free energy or quarkonium correlators, made progress in extracting this potential [239, 240, 241]. In these approaches the HQ free and internal energies, previously used as potential proxies, are rather outputs of suitably defined interaction kernels. However, the present results are not unique, ranging from a weak potential [240, 237] close to the free energy to a stronger one [242, 241, 237] close to the vacuum potential at moderate QGP temperatures.

Transport analyses of open and hidden heavy-flavor (HF) production in URHICs require relatively strong coupling strength/potentials for heavy-light [75, 231, 227] and heavy-heavy interactions, respectively. For example, quarkonium observables in URHICs [48, 243, 175, 244, 181] tend to favor the U-potential over the F-potential proxy, albeit systematic constraints have not been evaluated yet. Bottomonium observables are particularly promising to achieve that as shown in the previous section.

In the present section, we conduct a statistical analysis of the centrality dependence of available bottomonium data at RHIC and the LHC, with the goal of constraining the HQ potential at finite temperature. Toward this end, we employ our previously developed semi-classical Boltzmann/rate equation approach which has been extensively tested by a wide variety of quarkonium observables from SPS via RHIC to LHC energies for both charmonia and bottomonia [84, 48, 49, 59]. Its results are largely consistent with other semi-classical approaches [243, 244, 245, 181, 179, 246, 247, 248], although quantitative cross comparisons under controlled conditions remain to be carried out [35]. Furthermore, the effects of explicit quantum evolution equations for quarkonia are receiving increased attention [249, 221, 222, 250, 251]. However, it has not yet been scrutinized in how far quantum effects affect the extraction of transport parameters, and most of the pertinent calculations do not yet employ realistic potentials including the string term, which plays a critical role even for bottomonia. The implications for the systematic uncertainty of semi-classical approaches will have to be elaborated in future work.

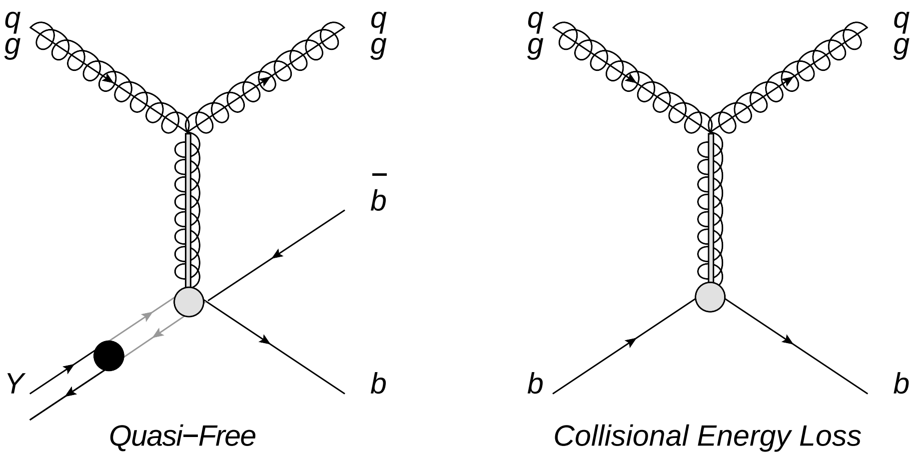

Figure 6.1: Relation between the single HQ interaction in the QGP and the “quasifree" dissociation process of quarkonia. The vertical line represents the in-medium potential between incoming thermal partons quarkonium.

The key connection between the in-medium potential and quarkonium transport is the inelastic reaction rate which increases as the potential weakens. In practice, inelastic parton ($i = q, \bar{q}, g$) scattering of the type $i + Y \rightarrow i + b + \bar{b}$ has been identified as the leading contribution to the dissociation rate in the relevant regime of temperatures where the binding energies are relatively small (also referred to as an imaginary part of the HQ potential [185, 238, 183], or “quasifree dissociation" [47]). Since the basic diagrams essentially correspond to heavy-light scattering, $i + b \rightarrow i + b$, they are closely related to HQ diffusion, cf. Fig. 6.1. From HF phenomenology it is now well established that HQ transport coefficients require a large enhancement over perturbative results [227, 231]. Reliable extractions of the in-medium HQ potential in quarkonium transport have to account for this. See the flow chart of the whole machinery in Fig. 6.2.

6.2 Bottomonium Transport and In-Medium Potential

The quarkonium transport framework employed in this work utilizes the rate equation (see Eq. (2.54) in Chap. 2, developed in [84, 48, 59]) for different bottomonium states,

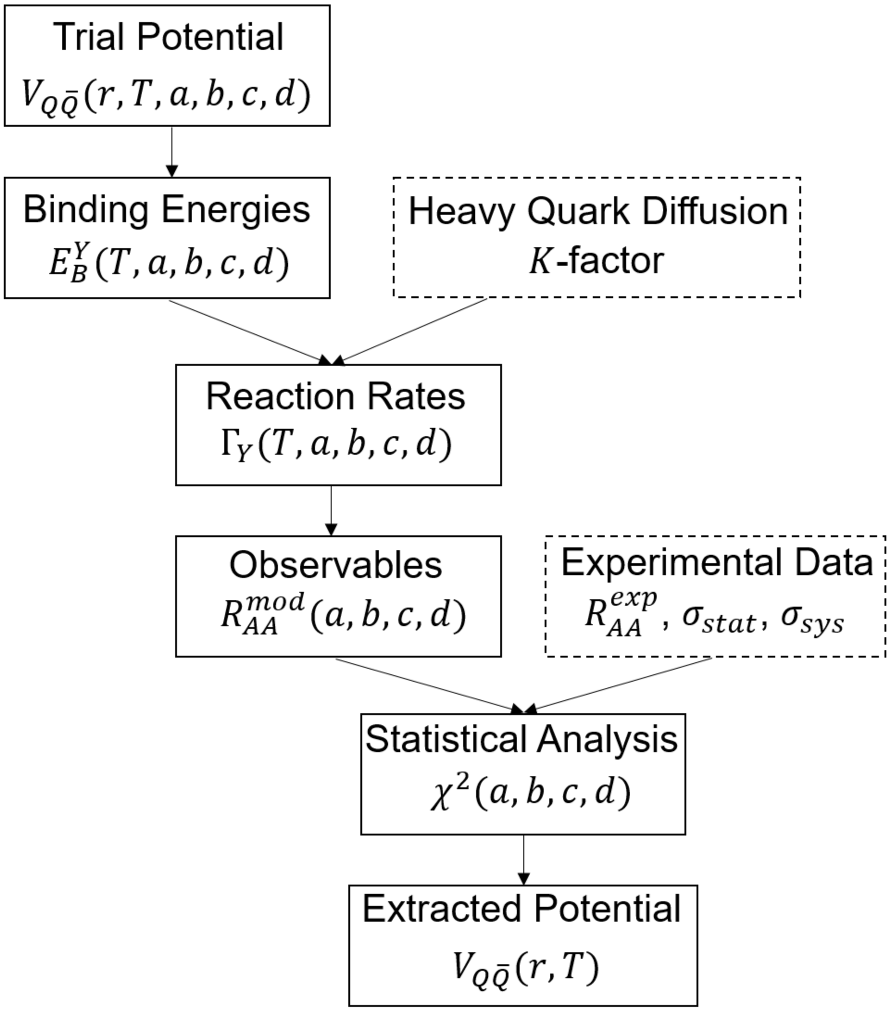

Figure 6.2: Flow chart of the statistical extraction of potential. a,b,c,d are fit parameters.

Y=$\Upsilon(1S)$, $\Upsilon(2S)$, $\Upsilon(3S)$, $\chi_b(1P)$. The bottomonium equilibrium limit, $N^{\rm eq}(T(\tau))$, governs regeneration processes and is obtained from the thermal model with experimental input for open-bottom cross sections (we also include a relaxation time correction for incomplete b-quark thermalization and correlation volume effects in the canonical ensemble). However, the regeneration contribution to bottomonia is relatively small, and $N^{\rm eq}(T)$ depends only weakly on the potential through the b and Y masses.

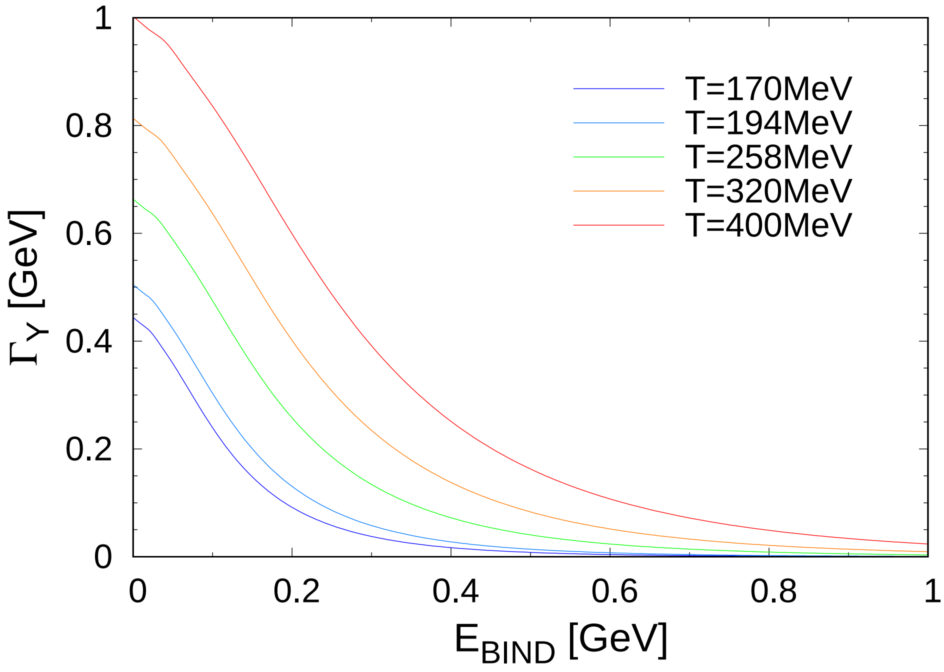

Figure 6.3: Binding-energy dependence of the quasifree dissociation width (K=5) for fixed Υ mass of 9.46 GeV at different temperatures.

The central quantity is the inelastic reaction rate, $\Gamma(T(\tau))$, which depends on temperature through the thermal-parton density and the Υ binding energy which controls the final-state phase space of the dissociation process, cf. Fig. 6.3. The main contribution to the rate stems from quasifree dissociation [73, 47] for which we include interference effects causing a r-dependent reduction of the widths increasing with the binding energy of the bound state [59]. The much smaller contributions to the rate from gluo-dissociation [71, 72] are also accounted for. A significant extension over our previous work [59] is the implementation of constraints from open HF phenomenology, which require HQ scattering rates in the QGP well beyond perturbative estimates. This is done by introducing a K factor in the quasifree reaction rate, which for simplicity we assume to be temperature- and momentum-averaged. In the presence of large dissociation widths, the issue of the onset temperature for regeneration reactions needs to be revisited, *i.e.*, at what temperature in the cooling of the fireball bound-state formation commences. In our previous work, where the quasifree rates were relatively small, the default assumption was to use the vanishing of the binding energy, $E_B^Y(T_{\rm reg})$=0, to define the temperature, $T_{\rm reg}$, below which regeneration sets in. However, for binding energies much smaller than the width (for a large K factor), the formation time of the bound state becomes longer than its lifetime. Therefore, we amend the criterion for $T_{\rm reg}$ by defining it as the temperature where the binding energy becomes comparable to the reaction rate, $E_B^Y(T_{\rm reg})$=$\Gamma_Y(T_{\rm reg})$ (as it turns out, both criteria lead to virtually identical results for the extracted potentials, with some difference in the composition of primordial and regeneration components for excited states). Above $T_{\rm reg}$ the dissociation of would-be quarkonia (*i.e.*, primordially produced $b\bar{b}$ quarks that in a pp collision would evolve into a quarkonium bound state) is still operative at a rate of twice the collision rate of a single b quark. A more rigorous treatment of these issues requires a quantum evolution approach which we defer to future work.

The key quantity to calculate the in-medium binding energies is the in-medium potential $V(r,T)$ for which we adopt a screened Cornell-type potential. For an efficient use in the statistical analysis discussed below, we utilize a 2-parameter ansatz for the T-dependence of the potential (akin to that in Ref. [252]), with a Debye screened color-Coulomb term and a confining term whose screening is controlled by a string breaking distance, $R_{\rm SB}$,

$$V_{Q\bar{Q}}(r) = \begin{cases} -\frac{4}{3}\alpha_s\, \mathrm{e}^{-m_D r}/r + \sigma r & , r < R_{\rm SB} \\ -\frac{4}{3}\alpha_s\, \mathrm{e}^{-m_D r}/r + \sigma R_{\rm SB} & , r > R_{\rm SB}\ . \end{cases} \tag{6.1}$$

Here, m_D and $m_S \equiv 1/R_{\rm SB}$ are the pertinent screening masses. We have checked that the sharp-cutoff version of the string term closely resembles the results for binding energies

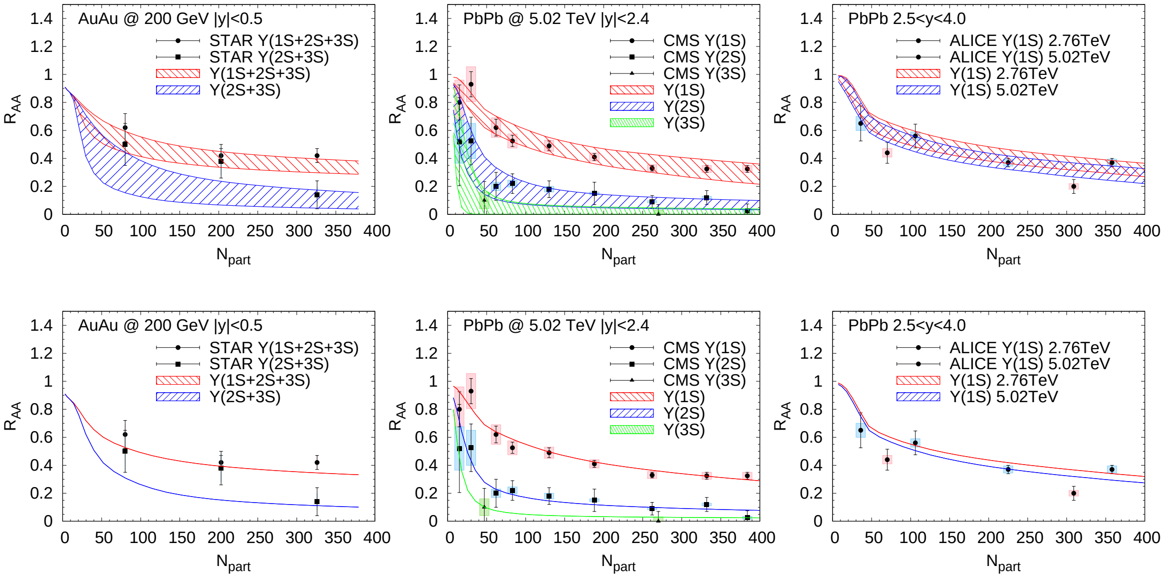

Figure 6.4: Bands of 95% confidence level (upper panels) and best-fit results (lower panels) for the Y $R_{\rm AA}$'s in the K=5 scenario, compared to: $\Upsilon(1S+2S+3S)$ and $\Upsilon(2S+3S)$ STAR data in Au-Au(0.2 TeV) collisions (left panels), $\Upsilon(1S,2S,3S)$ CMS data at mid-rapidity in PbPb(5.02 TeV) collisions (middle panels), and $\Upsilon(1S)$ ALICE data at forward rapidity in Pb-Pb(2.76,5.02 TeV) collisions (right panels).

from more elaborate smooth versions as used, *e.g.*, in Refs. [75, 237]. Its advantages are an analytical evaluation of its partial-wave expansion (which can be done analytically) and the dependence on a single parameters (whose temperature dependence, however, turns out to be more involved). For a given potential the binding energies are obtained from a T-matrix equation and subsequently serve as input into the reaction rate. In the spirit of the semi-classical Boltzmann approach, they are computed in the narrow-width approximation, while the width effects (including interference) are represented by the reaction rates.

6.3 Statistical Approach

To implement the in-medium potential into a statistical analysis of bottomonium data within our transport framework, we parameterize the temperature dependence of the screening masses. Guided by previous studies of the potential model within the T-matrix approach, we utilize a constant strong-coupling constant, α_s, and string tension, σ, together with a Debye mass linear in temperature, while the screening of the string term requires more flexibility. We make the ansätze

$$m_D = aT_o\tilde{T}, \tag{6.2}$$

$$m_S = m_S^{\text{vac}} + T_o\left[c\tilde{T} - (c-b)\left(\sqrt{\tilde{T}^2+d^2} - d\right)\right], \tag{6.3}$$

where $m_S^{\text{vac}}\simeq$1/fm is the inverse string-breaking distance in vacuum and $\tilde{T} = \frac{T}{T_o} - 1$ is the "reduced" temperature relative to the onset temperature of screening. The four dimensionless fit parameters characterize the slope of m_D (a), the high-T and low-T slopes of m_S (b and c, respectively), and the transition between the two (d); *e.g.*, for d=0, the low-T slope drops out. The in-medium b-quark mass includes a self energy from the potential [75, 237], $m_b = m_b^0 + \frac{1}{2}\left(-\frac{4}{3}\alpha_s m_D + \frac{\sigma}{m_S}\right)$, where m_b^0 is the bare mass. With m_b^0=4.719 GeV, α_s=0.298, σ=0.220 GeV^2 and m_S^{vac}=0.194 GeV a good fit to the vacuum masses of $\Upsilon(1S)$, $\Upsilon(2S)$, $\chi_b(1P)$ and $\chi_b(2P)$ is obtained. For the onset temperature of screening, our default value is T_o=0.15 GeV, slightly below the QCD pseudo-critical temperature. Guided by lQCD data [253] for the infinite-distance limit of the HQ free energy below T_{pc}, we have also checked a smaller value of T_o=0.13 GeV, but did not find significant differences in the final results for the extracted in-medium potential (as we will see below, the screening of the string term turns out to be small up to $T\simeq$0.2 GeV).

For a given set of parameters, (a, b, c, d), the binding energies of the different bottomonium states are calculated as a function of temperature, $E_Y(T; a, b, c, d)$, and the corresponding Y masses (figuring in the equilibrium limit, N_Y^{eq}) follow as

$$m_Y(T) = 2m_b(T) - E_Y(T)\ . \tag{6.4}$$

With those inputs, we generate the reaction rates and evolve the Y numbers through the rate equation to compute a full set of Y nuclear modification factors,

$$R_{\rm AA}^{Y} = \frac{N_{\rm AA}^{Y}(N_{\rm part})}{N_{\rm coll}(N_{\rm part})N_{pp}^{Y}} \ , \tag{6.5}$$

as a function of centrality (characterized by the number of nucleon participants, $N_{\rm part}$) at RHIC ($\sqrt{s}$=$0.193, 0.2\,$TeV) and the LHC ($\sqrt{s}$=$2.76, 5.02\,$TeV, at both forward and mid-rapidity); $N_{\rm AA}^{Y}(N_{\rm part})$ denotes the final Y yield in an A-A collision, which is normalized to its binary-collision number-scaled yield in pp collisions, $N_{\rm coll}N_{pp}^{Y}$. As in our previous work [59] we utilize an entropy-conserving thermal fireball expansion (with a lQCD/hadron-resonance-gas equation of state) at each impact parameter and collision energy (which determine the total entropy via the observed charged-particle multiplicity). The initial Y numbers, $N_Y(\tau = 0)$, in the rate equation (and the total $b\bar{b}$ number needed for the equilibrium limit, $N_Y^{\rm eq}$) are determined from measured cross sections in pp collisions, plus additional “cold-nuclear matter" (CNM) effects. Specifically, we employ baseline values for EPS09 nuclear shadowing [90] at the LHC of up to 15% and 30% in central collisions at mid and forward rapidity, respectively, and a nuclear absorption cross section of 3 mb at RHIC to account for the observed Y suppression in p-Au collisions. We have checked that upon reducing the CNM effects by a factor of 2, the overall fit quality worsens, with a thinner 95 % confidence level region and a slightly weaker extracted potential. Without CNM effects essentially no solutions were found within a 95 % confidence level.

For each parameter set, (a, b, c, d), we evaluate the chi-squared as

$$\chi^2 = \sum_{i=1}^{N} \left(\frac{R_{\rm AA}^{\rm mod}(a,b,c,d) - R_{\rm AA}^{\rm exp}}{\sigma_{\rm exp}} \right)^2 \ , \tag{6.6}$$

summed over N=53 experimental data points, $R_{\rm AA}^{\rm exp}$ (cf. Tab. 6.1), and pertinent model

Experiment	Rapidity	Data (R_{AA})	Reference
193 GeV U-U	$\lvert y\rvert < 1.0$	1S, 1S+2S+3S	STAR [176]
200 GeV Au-Au	$\lvert y\rvert < 0.5$	1S, 2S+3S, 1S+2S+3S	STAR [193]
2.76 TeV Pb-Pb	$\lvert y\rvert < 2.4$	1S, 2S	CMS [182]
2.76 TeV Pb-Pb	$2.5 < y < 4.0$	1S	ALICE [54]
5.02 TeV Pb-Pb	$\lvert y\rvert < 2.4$	1S, 2S, 3S	CMS [254]
5.02 TeV Pb-Pb	$2.5 < y < 4.0$	1S	ALICE [255]

Table 6.1: Summary of RHIC [176, 193] and LHC [182, 54, 254, 255] data utilized in our analysis.

Parameter	Range	Meaning
a	1.0-4.0	T slope of m_D
b	0.0-2.0	high-T slope of m_S
c	0.0-8.0	low-T slope of m_S
d	0.0-0.9	c-to-b transition region

Table 6.2: Summary of the n=4 fit parameters.

values, $R_{\mathrm{AA}}^{\mathrm{mod}}$; σ_{exp} denotes the quadratically combined 1-σ statistical and systematic experimental error,

$$\sigma_{\mathrm{exp}} = \sqrt{\sigma_{\mathrm{stat}}^2 + \sigma_{\mathrm{sys}}^2}\ . \tag{6.7}$$

Assuming that a given model result represents the true values, and that the data are normal-distributed around these, the distribution of χ^2 values for given ν=$N-n$, $\chi^2(\nu)$, is universal (and normalized) and can be used to define a confidence level. We employ a 95% confidence level which for ν=53-4=49 implies χ^2 values below χ^2(49)=66.3; this corresponds to an α-value of 0.05, *i.e.*, the integration of the χ^2 distribution above 66.3 yields 0.05, or: if the model is correct, there is only a 5% chance that the χ^2-value is above 66.3.

The χ^2 values are computed over a grid of parameters (a, b, c, d) (cf. Tab. 6.2) which encompasses the minimum χ^2_{min} representing the "best fit" and the 95 % confidence hypersurface defined by the maximal $\chi^2_{\rm max}$=66.3. In between the grid points the results are emulated using a 4-dimensional quadratic interpolation mapped onto the $R_{\rm AA}$ values.

Open HF phenomenology in URHICs, especially the large elliptic flow observed for low-momentum D-mesons at both RHIC and the LHC, requires a large enhancement of the HQ thermalization rates over those obtained from pQCD Born diagrams [227]. Therefore, in addition to the baseline pQCD quasifree rate, we evaluate 2 scenarios with a K factor of 5 and 10 in our statistical analysis.

6.4 Potential Extraction

In Fig. 6.4 we summarize our Y $R_{\rm AA}$ fit results for a selection of ALICE, CMS and STAR data for K=5; the bands agree well with the data. A very similar fit quality is achieved for K=1 and 10. In all cases the "best fit" results have $\chi^2_{\rm min}$≈46. As in our previous work [59], we encounter a discrepancies with the 2.76 TeV Pb-Pb forward-rapidity data; when arbitrarily excluding them from the fit, the $\chi^2_{\rm min}$ drops from ∼46 to ∼35.

Inspection of the parameter space in the (a, b) plane (Fig. 6.5) reveals a substantial shrinking of the 95 % confidence region of the T-dependence of the confining force (parameter b) as the heavy-light interaction strength (K factor) is increased. At moderate temperatures, the increase in the width caused by the K factor is compensated by a reduced screening to increase the binding and lower the final-state phase space. On the other hand, the screening of the color-Coulomb potential is not strongly constrained, characterized by a large range of values of the temperature slope, a, of the Debye mass along a valley of $\chi^2/\nu \lesssim 1$. This finding highlights the sensitivity of bottomonium observables to the confining potential, which is also tightly connected to the strength of the heavy-light interaction. Without knowledge of the latter, it is difficult to draw definite conclusions.

The main transport parameter, the reaction rate, is shown in Fig. 6.6. The most relevant temperature region for phenomenology at RHIC and the LHC is $T \lesssim 400\,$MeV since

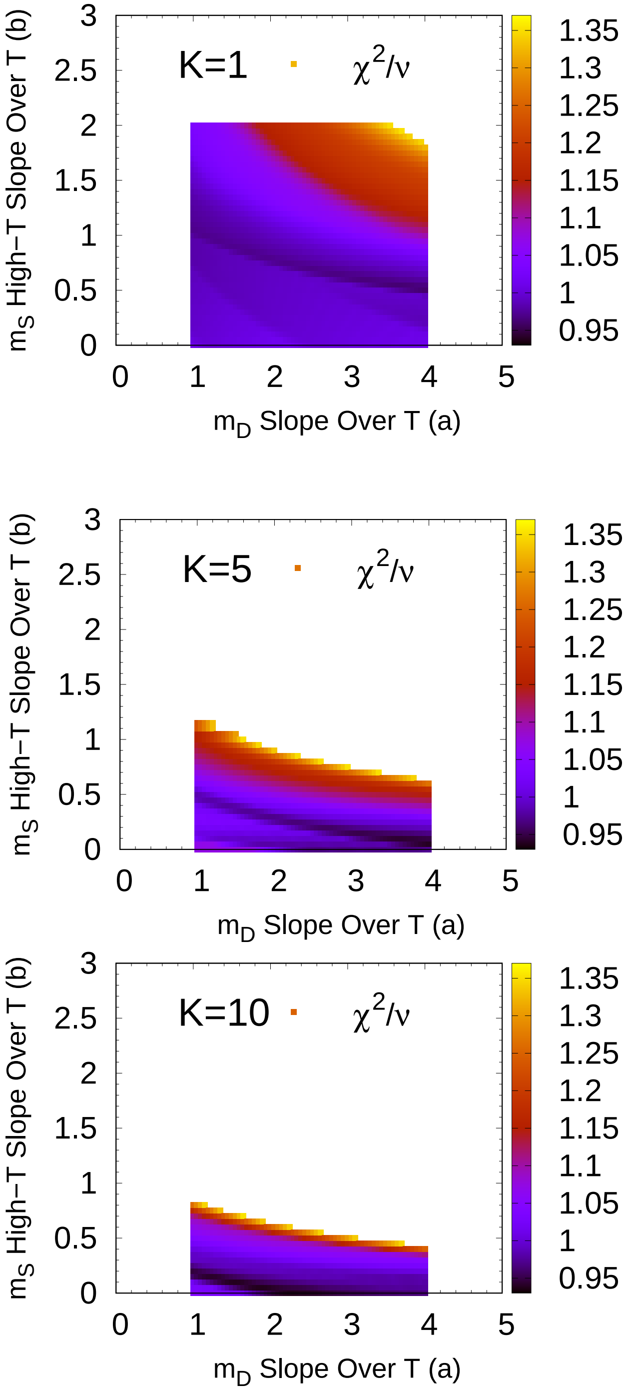

Figure 6.5: Color-coded χ^2/ν contours in the (a, b) parameter space (temperature slopes of string and Debye screening masses), projected to the minimum values in the associated (c, d) space, for K=1 (upper), 5 (middle) and 10 (lower).

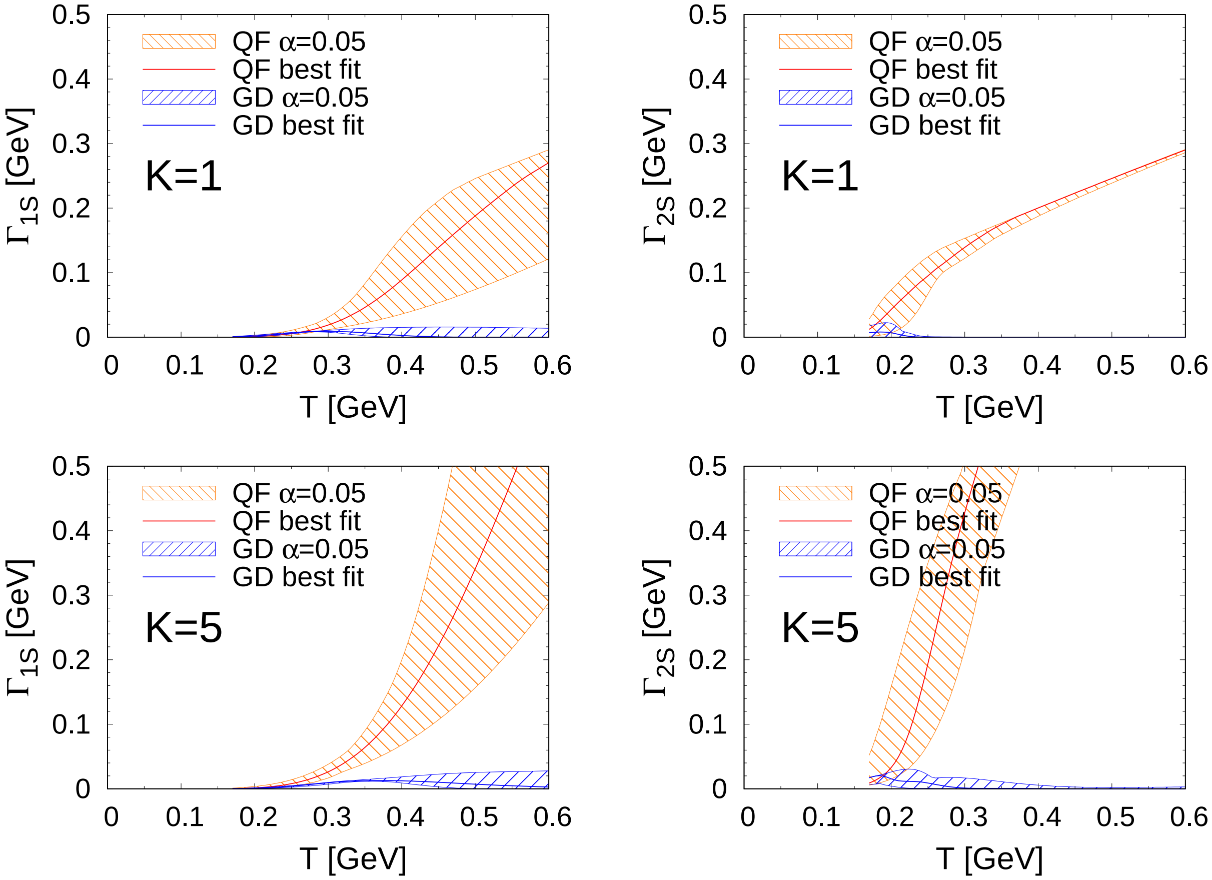

Figure 6.6: 95% confidence bands and best fits (lines) for quasifree (red) and gluo-dissociation (blue) rates for $\Upsilon(1S)$ (left panels) and $\Upsilon(2S)$ (right panels) for K=1 (upper panels) and K=5 (lower panels).

the fireball lifetime at higher temperature is (well) below 0.5fm/c (based on our previous finding [59] that the Y $R_{\rm AA}$'s are rather insensitive against variations in the initial QGP formation time, which controls the initial temperature; this is in part due to finite Y formation times). In this temperature range, the resulting $\Upsilon(1S)$ widths are very similar for K=1 and K=5; they also agree with the microscopic calculations in the T-matrix approach [237]. At higher temperature, the 95 % confidence bands become broad, but still have overlap until $T \simeq$ 600 MeV. The case could be made that this region can be probed rather sensitively in a future circular collider in the tens of TeV regime. On the other hand, the $\Upsilon(2S)$ rates differ largely beyond $T{\simeq}300\,\text{MeV}$ (reached after roughly 1 fm/c in central Pb-Pb collisions at the LHC), due to the different K factors at (near) vanishing binding. Again, this is somewhat mitigated by its finite formation time, but in any case, the $\Upsilon(2S)$ is highly suppressed in semi/central collisions (by 90% or more at the LHC) with a good fraction of the final yield due to regeneration which starts at $T \lesssim 250\,\text{MeV}$, with then comparable rates for K=1 and K=5.

In Fig. 6.7 we display our main result, *i.e.*, the extracted in-medium HQ potentials at different temperatures for K=1 and 5. At low T, the potentials are close to the vacuum one in both scenarios, but for K=5 the potential remains substantially stronger at higher temperatures. Since the K=1 potential is incompatible with open HF phenomenology [231], the K=5 potential should be considered a much more realistic solution. Remarkably, the latter closely coincides with the “strong-binding scenario" in the microscopic T-matrix calculations of Ref. [237] which were only constrained by lQCD data (equation of state, quarkonium correlators and free energy), not by URHIC phenomenology.

6.5 Conclusions

Utilizing a well-tested quarkonium transport approach, we have conducted a statistical analysis to constrain the in-medium heavy-quark potential via bottomonium observables in heavy-ion collisions. The potential determines the in-medium Y binding energies, which in turn govern the reaction rate as the main transport coefficient. Guided by theoretical analyses of lQCD data on the HQ free energy, we have employed a 4-parameter ansatz to capture essential temperature effects on the color-Coulomb and confining force components. As an important additional ingredient, we have allowed for a nonperturbative enhancement in the bottomonium reaction rates. We have then constructed 95 % confidence regions of fits to R_{AA} data at RHIC and the LHC to extract the in-medium potential for 3 different K factors in the heavy-light interaction. The resulting reaction rates essentially coincide in the relevant temperature region, as dictated by the transport fit to the data, but larger K factors lead to significantly stronger extracted potentials in the QGP. The stronger potentials, in turn, are required to obtain HQ transport coefficients that are viable for open HF phenomenology at RHIC and the LHC. Our approach thus highlights the importance of combined analyses of open and hidden HF probes in a microscopic approach, and supports earlier independent findings that remnants of the confining force above T_c are instrumental for the strong-coupling features of the QGP. Several improvements of our work are envisaged. Our previous checks of systematic uncertainties in the transport approach (including the bulk medium evolution, Y formation times and the impact of b-quark diffusion), should be revisited, together with explicit calculations of nonperturbative effects in the reaction rate [237, 231]. This may require the use of a quantum transport framework as currently being developed from several angles [249, 221, 222, 250, 251], as well as more advanced statistical tools to cope with an enlarged parameter space [256]. Extensions to the charmonium sector, where a rich data set is available, should also be pursued, posing additional challenges due to large regeneration contributions and the smaller charm-quark mass.

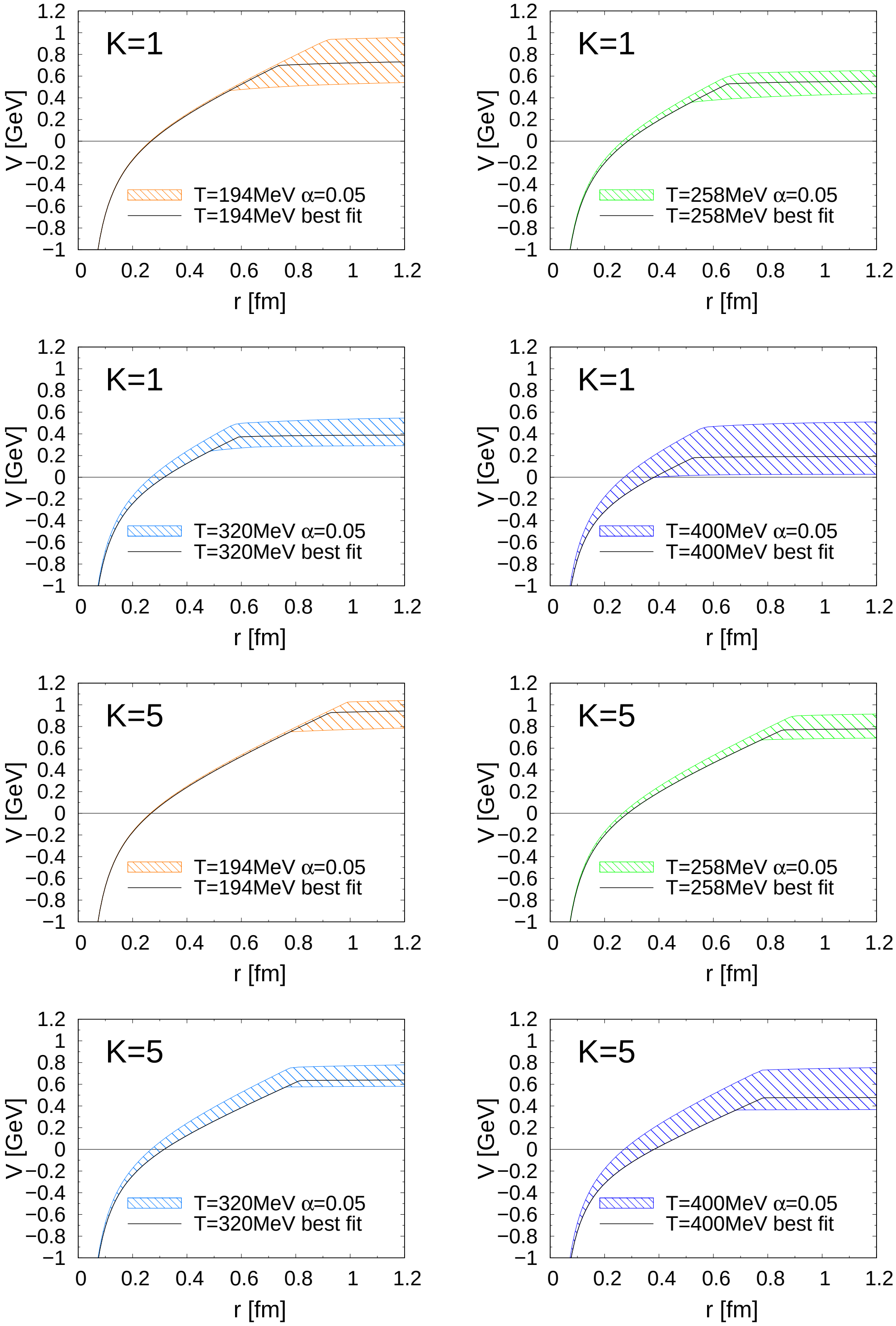

Figure 6.7: 95% confidence level bands for the extracted potential, $V(r) = V_{Q\bar{Q}}(r) - \frac{4}{3}\alpha_s m_D$, and the “best fits" (lines) at different temperatures for the K=1 (upper 2 rows) and K=5 (lower 2 rows) scenarios.

7. CONCLUSIONS AND OUTLOOK

Physics in the nonperturbative regime of Quantum Chromodynamics (QCD) is difficult to study, but it is crucial to understand fundamental strong-interaction phenomena. One important nonperturbative effect is confinement, that quarks and gluons are bound into color-neutral hadrons. An empirically parameterized potential with a perturbative Coulomb term and a nonperturbative confining term can successfully describe hadron spectroscopy. Lattice QCD (lQCD) studies show a noticeable energy density increase around a critical temperature $T_c \simeq 155\,\mathrm{MeV}$, indicating deconfinement and the existence of a new phase of matter: quark-gluon plasma (QGP) consisting of strongly interacting but freely moving quarks and gluons. Ultrarelativistic heavy-ion collisions (URHICs) are capable of reproducing a QGP creating extreme conditions of temperature and enabling the study of thermal properties of QCD, including the medium modification of the heavy quark-antiquark strong potential. Heavy quarkonia are promising probes to investigate the in-medium potential since they are directly bound by the potential, and the diversity of quarkonium species serves the purpose of probing different parts of the potential.

In order to systematically study quarkonium production in URHICs, we adopt a previously established transport approach, based on rate and Boltzmann equations, and further develop it. The machinery is refined and extended in several aspects and applied to study the quarkonium production in URHICs over a wide range of energies and collision systems.

We first utilize the transport approach to study J/ψ production in A-A collisions at LHC energies and compare the theoretical calculations with experimental data including Pb-Pb collisions and recently measured Xe-Xe collisions. The leveling off of the centrality dependent nuclear modification factor, $R_{\mathrm{AA}}(N_{\mathrm{part}})$ at N_{part}>200 is explained by the interplay of two different contributions: a suppression of primordial production and a enhancement through regeneration of J/ψ. The importance of the regeneration contribution is further verified by the $R_{\mathrm{AA}}(p_T)$. Analyzing the excitation function, it becomes even more apparent that the increasing trend of $R_{\mathrm{AA}}(\sqrt{s})$ is provided by the larger regeneration contribution at higher collisions energies. The large J/ψ v_2 measured in experiments also indicates a large regeneration contribution. It is also recognized that the thermally produced J/ψ p_T spectra are slightly softer than the experimental data, indicating non-thermalized charm-quark spectra during the recombination into J/ψ.

Next, we investigate the exited charmonium $\psi(2S)$ within the transport framework. Due to the smaller binding energy of $\psi(2S)$ compared to that of J/ψ, the $\psi(2S)$ reaction rate in the QGP medium is much larger than it is for J/ψ, leading to a significantly larger suppression, consistent with the sequential suppression picture. Inspired by this, we propose the so called "sequential regeneration" mechanism for A-A collisions, stating a serial recombination of J/ψ and $\psi(2S)$. This is because the $\psi(2S)$ with a smaller binding energy can only survive, and therefore recombine from charm quarks, at a lower temperature than the J/ψ, corresponding to later times. The later-coalescencing charm quarks carry more flow from the evolving medium and push the $\psi(2S)$ into harder p_T spectra. With a specific cut at low p_T, the sequential regeneration provides the possibility to generate a large $\psi(2S)$ over J/ψ R_{AA} double ratio in PbPb collisions. At the LHC, current data are not fully conclusive, and future $\psi(2S)$ measurements would be helpful to understand the $\psi(2S)$ production in URHICs.

Small system collisions, $i.e.$ *p*/*d*-A collisions, have become a rather hot topic in the heavy-ion community. Its anisotropies from initial-state fluctuations are worth studying. An extension of our transport model in A-A collisions to *p*/*d*-A collisions is carried out by constructing an elliptic fireball background, with fireball parameters constrained from spectra and elliptic flow from light hadrons. It turns out that the hadronic interaction could also be important in the small systems at RHIC energy, where the typical fireball temperature is close to T_c. This prompts us to revisit the hadronic reaction rates utilized in the transport model with more hadronic resonances interacting with charmonia, and apply the new rates in the d-Au collision at RHIC. The final-state interaction in p/d-A collisions indeed favors a larger suppression for $\psi(2S)$ than for J/ψ. In p-Pb collisions at 5.02 TeV, this is more extreme in the Pb-going direction with higher charged-particle multiplicity than in the p-going direction with smaller charged-particle multiplicity. These findings are also exhibited by experimental data, indicating the existence of QGP formation in p/d-A collisions. It is also found that the portion of regeneration in p/d-A is quite small. We further calculated the elliptic flow, v_2, of J/ψ and $\psi(2S)$, caused by a leakage effect for the primordial component and by flow effects from regeneration. The anisotropic suppression inside the fireball with the leakage leads to anisotropies of the primordial suppression. The small J/ψ suppression, which is confirmed both by model calculations and the experimental data, should therefore lead to small anisotropies of J/ψ with final-state interactions. Consequently, our model calculation with final-state interactions gives a small J/ψ v_2, which however does not agree with the large values in the experimental data. This discrepancy indicates the possibility that the J/ψ v_2 could be built up by initial-state effects, $e.g.$ collective gluon fields [257].

We also study bottomonium production in URHICs with the transport model framework, establishing a Boltzmann evolution of bottomonium in phase space, augmented with Langevin-simulated non-thermal bottom quarks via coalescence. The T-matrix calculated in-medium binding energies, instead of vacuum binding energies, are implemented in the calculation. The bottomonium transport model thus reaches the same level of sophistication as for charmonium. Both model calculations and experimental data show significantly more suppression for the excited $\Upsilon(2S)$ and $\Upsilon(3S)$ states than for the ground state $\Upsilon(1S)$. The regeneration contribution is found to be small but not negligible for $\Upsilon(2S)$. We check and demonstrate the advantages of utilizing bottomonia, especially $\Upsilon(1S)$, to probe the in-medium quark-antiquark potential: the $R_{\rm AA}$ is found to be rather sensitive to the in-medium binding energy and relatively insensitive to auxiliary effects of the model. The calculation of bottomonium p_T spectra from coalescence of non-thermalized but transported b-quark spectra agrees well with CMS data, supporting the pressure of moderate regeneration contributions at small p_T. The bottomonium v_2s for both $\Upsilon(1S)$ and $\Upsilon(2S)$ are also predicted within our extended framework with an elliptic fireball and coalescence model.

Despite their similar binding energies, the $\Upsilon(2S)$ and J/ψ have very different excitation functions. These different phenomena, demonstrated by both experimental data and theoretical predictions, are a strong confirmation of the regeneration mechanism. Although the production of $\Upsilon(2S)$ per $b\bar{b}$ pair is ten times smaller than the J/ψ per $c\bar{c}$ pair in pp collisions, leading to a naïve expectation of larger $\Upsilon(2S)$ regeneration than for J/ψ, it is a priori not obvious why regeneration of the Υ states in URHICs should be small. The production cross section of $b\bar{b}$ is much smaller than for $c\bar{c}$ and the number of produced $b\bar{b}$ is in the canonical limit for, while in grand-canonical limit for $c\bar{c}$. Thus an additional enhancement factor of $N_{c\bar{c}}$ for J/ψ regeneration is present. Second, the longer thermal relaxation time for bottom quarks also severely reduces the bottomonium regeneration. Third, the larger bottom quark mass further augments the difference that J/ψ regeneration is larger than $\Upsilon(2S)$.

Inspired by our study of the bottomonium observables indicating the sensitivity to their in-medium binding energies, we further utilize the bottomonium transport approach to probe the in-medium QCD force in a more quantitative manner. A numerically intensive and powerful statistical machinery based on a chi-square test is developed and integrated into the transport model. A T-matrix approach is employed to convert a parameterized trial quark-antiquark potential to bottomonium binding energies, relying on the color screening of the Coulomb and string terms of the potential. The binding energies are key inputs into to transport coefficients, and they are mapped into R_{AA} observables via the transport model. Because of the intensive numerical calculations, an emulator is also developed to simulate R_{AA} in a more dense parameter space. A large K-factor is implemented into the reaction rates to mimic the findings in research of heavy-quark diffusion, stimulated from the strong connection of "quasifree" dissociation in the quarkonium sector and collisional diffusion in the heavy-quark sector. Next, a chi-square test comparing the model-calculated R_{AA}s with the experimental R_{AA}s is performed within the parameter space. An extracted potential is then quantified with a statistical confidence level and a minimal chi-squared value (best-fit). The statistical extractions favor a rather strong potential with large K-factors. The extracted potential features a strong component of the remnants of the the confining part, which have previously been found to render the quark-gluon plasma to be strongly coupled. This is also the first extraction of the fundamental QCD force directly from experimental data.

Our comprehensive quarkonium transport model with its extensions for p/d-A collisions, bottomonium sectors, and statistical analysis can well describe the overall experimental data in URHICs and give a quantitative extraction of the quark-antiquark potential. However, several future developments of the model are worth pursuing. First (1), a hydrodynamic background with spatial temperature dependence and more realistic flow fields should be utilized to replace the simple fireball model. Second (2), the initial formation of quarkonium is nonperturbative, requiring a more rigorous study via quantum evolution of the heavy-quark pairs. Third (3), we have shown the importance of a joint study of the open and the hidden heavy-flavor sectors in the following aspects: (a) realistically simulated heavy-quark spectra provide reasonable quarkonium regeneration spectra especially for bottomonium; (b) Simulations of heavy quarks in coordinate space provide an explicit evaluation of the correlation volume effect; (c) the identical scattering amplitudes in the reduced 2→2 quarkonium "quasifree" process and the 2→2 heavy-quark collisional energy loss enable the application of insights from the open sector into the hidden sector and vice versa. Thus, it would be interesting to integrate the transport of open/hidden heavy flavors, within a combined framework. It can be done classically with a Langevin simulation of heavy-quark diffusion and a Boltzmann evolution of heavy quarkonium, connected by an explicit regeneration and a consistent reaction width in both simulations.

A recent trend of quarkonium studies aims at an integrated framework with an open quantum system, via a Lindblad formalism [249]. This is one way of solving the problems of items (2) and (3) mentioned above, together. All these developments will help us to further advance our understanding of quarkonium transport in QGP and ultimately unravel the physical mechanisms of the fundamental QCD force and its color screening.

REFERENCES

[1] C.-N. Yang and R. L. Mills, Phys. Rev. **96**, 191 (1954), [,150(1954)].

[2] H. Fritzsch, M. Gell-Mann, and H. Leutwyler, Phys. Lett. **47B**, 365 (1973).

[3] D. J. Gross and F. Wilczek, Phys. Rev. Lett. **30**, 1343 (1973).

[4] H. D. Politzer, Phys. Rev. Lett. **30**, 1346 (1973).

[5] S. Bethke, Prog. Part. Nucl. Phys. **58**, 351 (2007).

[6] E. D. Bloom *et al.*, Phys. Rev. Lett. **23**, 930 (1969).

[7] M. Breidenbach *et al.*, Phys. Rev. Lett. **23**, 935 (1969).

[8] K. G. Wilson, Phys. Rev. D **10**, 2445 (1974).

[9] E. Eichten *et al.*, Phys. Rev. Lett. **34**, 369 (1975).

[10] G. S. Bali and K. Schilling, Phys. Rev. **D46**, 2636 (1992).

[11] O. Kaczmarek and F. Zantow, Phys. Rev. D **71**, 114510 (2005).

[12] Y. Nambu, Int. J. Mod. Phys. **A23**, 4063 (2008).

[13] R. Hagedorn, Nuovo Cim. Suppl. **3**, 147 (1965).

[14] Wuppertal-Budapest, S. Borsanyi *et al.*, JHEP **09**, 073 (2010).

[15] A. Bazavov *et al.*, Phys. Rev. D **85**, 054503 (2012).

[16] P. Petreczky, Nucl. Phys. **A830**, 11C (2009).

[17] R. Rapp, T. Schäfer, E. V. Shuryak, and M. Velkovsky, Phys. Rev. Lett. **81**, 53 (1998).

[18] M. G. Alford, K. Rajagopal, and F. Wilczek, Phys. Lett. **B422**, 247 (1998).

[19] R. Rapp and H. van Hees, (2008), arXiv:0803.0901.

[20] U. Heinz and R. Snellings, Ann. Rev. Nucl. Part. Sci. **63**, 123 (2013).

[21] M. Luzum and P. Romatschke, Phys. Rev. **C78**, 034915 (2008), [Erratum: Phys. Rev.C79,039903(2009)].

[22] H. Song, S. A. Bass, U. Heinz, T. Hirano, and C. Shen, Phys. Rev. Lett. **106**, 192301 (2011), [Erratum: Phys. Rev. Lett.109,139904(2012)].

[23] A. Andronic, P. Braun-Munzinger, K. Redlich, and J. Stachel, Nature **561**, 321 (2018).

[24] P. Huovinen, P. F. Kolb, U. W. Heinz, P. V. Ruuskanen, and S. A. Voloshin, Phys. Lett. **B503**, 58 (2001).

[25] ALICE Collaboration, K. Aamodt *et al.*, Phys. Rev. Lett. **105**, 252302 (2010).

[26] STAR Collaboration, J. Adams *et al.*, Nucl. Phys. **A757**, 102 (2005).

[27] PHENIX Collaboration, K. Adcox *et al.*, Nucl. Phys. **A757**, 184 (2005).

[28] M. Gyulassy and M. Plumer, Phys. Lett. **B243**, 432 (1990).

[29] X.-N. Wang and M. Gyulassy, Phys. Rev. Lett. **68**, 1480 (1992).

[30] PHENIX Collaboration, S. S. Adler *et al.*, Phys. Rev. Lett. **91**, 072301 (2003).

[31] S. Wicks, W. Horowitz, M. Djordjevic, and M. Gyulassy, Nucl. Phys. **A784**, 426 (2007).

[32] Particle Data Group, M. Tanabashi *et al.*, Phys. Rev. **D98**, 030001 (2018).

[33] E598 Collaboration, J. J. Aubert *et al.*, Phys. Rev. Lett. **33**, 1404 (1974).

[34] SLAC-SP-017, J. E. Augustin *et al.*, Phys. Rev. Lett. **33**, 1406 (1974), [Adv. Exp. Phys.5,141(1976)].

[35] R. Rapp and X. Du, Nucl. Phys. **A967**, 216 (2017).

[36] P. Petreczky and K. Petrov, Phys. Rev. D **70**, 054503 (2004).

[37] T. Matsui and H. Satz, Phys. Lett. **B178**, 416 (1986).

[38] S. Digal, P. Petreczky, and H. Satz, Phys. Rev. **D64**, 094015 (2001).

[39] NA38 Collaboration, C. Baglin *et al.*, Phys. Lett. **B220**, 471 (1989).

[40] NA50 Collaboration, M. C. Abreu *et al.*, Phys. Lett. **B410**, 337 (1997).

[41] J.-P. Blaizot and J.-Y. Ollitrault, Phys. Rev. Lett. **77**, 1703 (1996).

[42] R. Rapp, D. Blaschke, and P. Crochet, Prog. Part. Nucl. Phys. **65**, 209 (2010).

[43] PHENIX Collaboration, S. S. Adler *et al.*, Phys. Rev. **C69**, 014901 (2004).

[44] P. Braun-Munzinger and J. Stachel, Phys. Lett. **B490**, 196 (2000).

[45] R. L. Thews, M. Schroedter, and J. Rafelski, Phys. Rev. **C63**, 054905 (2001).

[46] M. I. Gorenstein, A. Kostyuk, H. Stoecker, and W. Greiner, Phys. Lett. **B509**, 277 (2001).

[47] L. Grandchamp and R. Rapp, Phys. Lett. **B523**, 60 (2001).

[48] X. Zhao and R. Rapp, Phys. Rev. **C82**, 064905 (2010).

[49] X. Zhao and R. Rapp, Nucl. Phys. **A859**, 114 (2011).

[50] CMS Collaboration, S. Chatrchyan *et al.*, JHEP **1205**, 063 (2012).

[51] ALICE Collaboration, B. Abelev *et al.*, Phys. Rev. Lett. **109**, 072301 (2012).

[52] STAR Collaboration, L. Adamczyk *et al.*, Phys. Lett. B **735**, 127 (2014), [Erratum: Phys. Lett.B743,537(2015)].

[53] PHENIX Collaboration, A. Adare *et al.*, Phys. Rev. C **91**, 024913 (2015).

[54] ALICE Collaboration, B. B. Abelev *et al.*, Phys. Lett. B **738**, 361 (2014).

[55] CMS Collaboration, S. Chatrchyan *et al.*, Phys. Rev. Lett. **109**, 222301 (2012), [Erratum: Phys. Rev. Lett.120,no.19,199903(2018)].

[56] X. Du and R. Rapp, Nucl. Phys. **A943**, 147 (2015).

[57] X. Du and R. Rapp, J. Phys. Conf. Ser. **779**, 012042 (2017).

[58] X. Du and R. Rapp, JHEP **03**, 015 (2019).

[59] X. Du, R. Rapp, and M. He, Phys. Rev. C **96**, 054901 (2017).

[60] X. Du, S. Y. F. Liu, and R. Rapp, (2019), arXiv:1904.00113.

[61] J. Doob, *Stochastic processes* (Wiley, New York, 1953).

[62] S. Ross, *Introduction to probability models* (Academic Press, San Diego, CA, 2003).

[63] G. F. Lawler, *Introduction to stochastic processes* (Chapman and Hall/CRC, 2006).

[64] K. Itô, Proc. Imp. Acad. **20**, 519 (1944).

[65] A. Kolmogoroff, Mathematische Annalen **104**, 415 (1931).

[66] D. S. Lemons and A. Gythiel, American Journal of Physics **65**, 1079 (1997).

[67] A. D. Fokker, Annalen der Physik **348**, 810 (1914).

[68] A. Einstein, Annalen der Physik **322**, 549 (1905).

[69] D. B. Walton and J. Rafelski, Phys. Rev. Lett. **84**, 31 (2000).

[70] L. Yan, P. Zhuang, and N. Xu, Phys. Rev. Lett. **97**, 232301 (2006).

[71] M. E. Peskin, Nucl. Phys. B **156**, 365 (1979).

[72] G. Bhanot and M. E. Peskin, Nucl. Phys. B **156**, 391 (1979).

[73] B. L. Combridge, Nucl. Phys. B **151**, 429 (1979).

[74] L. Grandchamp and R. Rapp, Nucl. Phys. **A709**, 415 (2002).

[75] F. Riek and R. Rapp, Phys. Rev. **C82**, 035201 (2010).

[76] N. Brambilla, A. Pineda, J. Soto, and A. Vairo, Rev. Mod. Phys. **77**, 1423 (2005).

[77] S. Chen and M. He, Phys. Rev. C **96**, 034901 (2017).

[78] S. Chen and M. He, Phys. Lett. **B786**, 260 (2018).

[79] Z.-w. Lin and C. Ko, Phys. Rev. **C62**, 034903 (2000).

[80] K. L. Haglin and C. Gale, Phys. Rev. **C63**, 065201 (2001).

[81] T. Barnes, E. Swanson, C. Wong, and X. Xu, Phys. Rev. **C68**, 014903 (2003).

[82] R. Rapp, Phys. Rev. **C66**, 017901 (2002).

[83] S. Hamieh, K. Redlich, and A. Tounsi, Phys. Lett. **B486**, 61 (2000).

[84] L. Grandchamp, R. Rapp, and G. E. Brown, Phys. Rev. Lett. **92**, 212301 (2004).

[85] M. He, R. J. Fries, and R. Rapp, Phys. Rev. C **85**, 044911 (2012).

[86] R. Rapp, Adv. High Energy Phys. **2013**, 148253 (2013).

[87] H. Fritzsch, Phys. Lett. **67B**, 217 (1977).

[88] C.-H. Chang, Nucl. Phys. **B172**, 425 (1980).

[89] G. T. Bodwin, E. Braaten, and G. P. Lepage, Phys. Rev. **D51**, 1125 (1995), [Erratum: Phys. Rev.D55,5853(1997)].

[90] K. J. Eskola, H. Paukkunen, and C. A. Salgado, JHEP **04**, 065 (2009).

[91] C. Gerschel and J. Hufner, Phys. Lett. **B207**, 253 (1988).

[92] M. L. Miller, K. Reygers, S. J. Sanders, and P. Steinberg, Ann. Rev. Nucl. Part. Sci. **57**, 205 (2007).

[93] S. Gavin and M. Gyulassy, Phys. Lett. **B214**, 241 (1988).

[94] J. Hufner, Y. Kurihara, and H. J. Pirner, Phys. Lett. **B215**, 218 (1988), [Acta Phys. Slov.39,281(1989)].

[95] J. Hufner and P.-f. Zhuang, Phys. Lett. **B515**, 115 (2001).

[96] A. Andronic *et al.*, Eur. Phys. J. **C76**, 107 (2016).

[97] F. Karsch and R. Petronzio, Z. Phys. **C37**, 627 (1988).

[98] J. P. Blaizot and J.-Y. Ollitrault, Phys. Rev. **D39**, 232 (1989).

[99] S. Gavin and R. Vogt, Nucl. Phys. **B345**, 104 (1990).

[100] L. Kluberg and H. Satz, Color Deconfinement and Charmonium Production in Nuclear Collisions, in *Relativistic Heavy Ion Physics*, edited by R. Stock, 2010.

[101] P. Braun-Munzinger and J. Stachel, Landolt-Bornstein **23**, 424 (2010).

[102] K. Zhou, N. Xu, Z. Xu, and P. Zhuang, Phys. Rev. **C89**, 054911 (2014).

[103] T. Song, K. C. Han, and C. M. Ko, Phys. Rev. C **84**, 034907 (2011).

[104] A. Andronic, P. Braun-Munzinger, K. Redlich, and J. Stachel, J. Phys. **G37**, 094014 (2010).

[105] X. Zhao and R. Rapp, Phys. Lett. **B664**, 253 (2008).

[106] ALICE Collaboration, J. Adam *et al.*, Phys. Lett. **B766**, 212 (2017).

[107] ALICE Collaboration, S. Acharya *et al.*, Phys. Lett. **B785**, 419 (2018).

[108] ALICE Collaboration, S. Acharya *et al.*, Phys. Rev. Lett. **119**, 242301 (2017).

[109] ALICE Collaboration, S. Acharya *et al.*, Eur. Phys. J. **C77**, 550 (2017).

[110] LHCb Collaboration, R. Aaij *et al.*, JHEP **06**, 147 (2017).

[111] M. Cacciari, M. Greco, and P. Nason, JHEP **05**, 007 (1998).

[112] M. Cacciari, S. Frixione, and P. Nason, JHEP **03**, 006 (2001).

[113] ALICE Collaboration, S. Acharya *et al.*, Eur. Phys. J. **C79**, 388 (2019).

[114] NA50 Collaboration, M. C. Abreu *et al.*, Phys. Lett. **B477**, 28 (2000).

[115] PHENIX Collaboration, A. Adare *et al.*, Phys. Rev. Lett. **98**, 232301 (2007).

[116] STAR Collaboration, L. Adamczyk *et al.*, Phys. Rev. **C90**, 024906 (2014).

[117] STAR Collaboration, L. Adamczyk *et al.*, Phys. Lett. **B771**, 13 (2017).

[118] ALICE Collaboration, B. B. Abelev *et al.*, Phys. Lett. **B734**, 314 (2014).

[119] ALICE Collaboration, R. T. Jiménez Bustamante, Nucl. Phys. **A967**, 576 (2017).

[120] PHENIX Collaboration, A. Adare *et al.*, Phys. Rev. Lett. **111**, 202301 (2013).

[121] ALICE Collaboration, B. B. Abelev *et al.*, JHEP **1412**, 073 (2014).

[122] ALICE Collaboration, J. Adam *et al.*, JHEP **06**, 050 (2016).

[123] LHCb Collaboration, R. Aaij *et al.*, JHEP **03**, 133 (2016).

[124] PHENIX Collaboration, A. Adare *et al.*, Phys. Rev. **C95**, 034904 (2017).

[125] PHENIX Collaboration, A. Drees, Nucl. Part. Phys. Proc. **289-290**, 417 (2017).

[126] STAR Collaboration, T. Todoroki, Nucl. Phys. **A967**, 572 (2017).

[127] CMS Collaboration, C. Collaboration, CMS-PAS-HIN-16-015 (2017).

[128] NA50 Collaboration, B. Alessandro *et al.*, Eur. Phys. J. **C49**, 559 (2007).

[129] CMS Collaboration, V. Khachatryan *et al.*, Phys. Rev. Lett. **113**, 262301 (2014).

[130] CMS Collaboration, A. M. Sirunyan *et al.*, Phys. Rev. Lett. **118**, 162301 (2017).

[131] ALICE Collaboration, J. Adam *et al.*, JHEP **05**, 179 (2016).

[132] ALICE Collaboration, R. Arnaldi, Nucl. Phys. **A904-905**, 595c (2013).

[133] B. Chen, Y. Liu, K. Zhou, and P. Zhuang, Phys. Lett. **B726**, 725 (2013).

[134] E. G. Ferreiro, Phys. Lett. **B749**, 98 (2015).

[135] L. S. Kisslinger, Int. J. Theor. Phys. **55**, 1847 (2016).

[136] B. Chen, T. Guo, Y. Liu, and P. Zhuang, Phys. Lett. **B765**, 323 (2017).

[137] B. Chen, X. Du, and R. Rapp, Nucl. Part. Phys. Proc. **289-290**, 475 (2017).

[138] Y.-Q. Ma, R. Venugopalan, K. Watanabe, and H.-F. Zhang, Phys. Rev. **C97**, 014909 (2018).

[139] LHCb Collaboration, R. Aaij *et al.*, Eur. Phys. J. **C72**, 2100 (2012).

[140] ALICE Collaboration, B. Paul, PoS **ICPAQGP2015**, 043 (2017).

[141] CMS Collaboration, A. M. Sirunyan *et al.*, Eur. Phys. J. **C77**, 269 (2017).

[142] ATLAS Collaboration, M. Aaboud *et al.*, Eur. Phys. J. **C78**, 171 (2018).

[143] CMS Collaboration, A. M. Sirunyan *et al.*, Phys. Lett. **B790**, 509 (2019).

[144] ATLAS Collaboration, M. Aaboud *et al.*, Eur. Phys. J. **C78**, 762 (2018).

[145] ALICE Collaboration, J. Adam *et al.*, JHEP **11**, 127 (2015).

[146] ALICE Collaboration, M. Leoncino, Nucl. Phys. **A956**, 689 (2016).

[147] ALICE Collaboration, ALICE-PUBLIC-2017-007 (2017).

[148] ALICE Collaboration, J. Adam *et al.*, JHEP **06**, 055 (2015).

[149] ALICE Collaboration, S. Acharya *et al.*, JHEP **07**, 160 (2018).

[150] LHCb Collaboration, R. Aaij *et al.*, Phys. Lett. **B774**, 159 (2017).

[151] ALICE Collaboration, S. Acharya *et al.*, Phys. Lett. **B780**, 7 (2018).

[152] CMS Collaboration, CMS-PAS-HIN-18-010 (2018).

[153] Y. Liu, C. M. Ko, and T. Song, Phys. Lett. **B728**, 437 (2014).

[154] F. Arleo and S. Peigné, JHEP **10**, 073 (2014).

[155] B. Ducloué, T. Lappi, and H. Mäntysaari, Phys. Rev. **D94**, 074031 (2016).

[156] J. L. Albacete *et al.*, Nucl. Phys. **A972**, 18 (2018).

[157] J. Nagle, private communication (2018).

[158] M. He, R. J. Fries, and R. Rapp, Phys. Lett. B **735**, 445 (2014).

[159] T. Kalaydzhyan and E. Shuryak, Nucl. Phys. **A931**, 899 (2014).

[160] ALICE Collaboration, O. Vázquez, New results on collectivity with ALICE, in *5th Large Hadron Collider Physics Conference (LHCP 2017) Shanghai, China, May 15-20, 2017*, 2017.

[161] ALICE Collaboration, V. Pacík, Nucl. Phys. **A982**, 451 (2019).

[162] F. Retiere and M. A. Lisa, Phys. Rev. **C70**, 044907 (2004).

[163] F. Bossu *et al.*, (2011), arXiv:1103.2394.

[164] J. Book, *Phenomenological interpolation of the inclusive J/psi cross section to proton-proton collisions at 2.76 TeV and 5.5 TeV* (University of Frankfurt, 2015).

[165] R. Vogt, Phys. Rev. **C81**, 044903 (2010).

[166] R. Vogt, Phys. Rev. **C92**, 034909 (2015).

[167] B. Ducloué, T. Lappi, and H. Mäntysaari, Phys. Rev. **D91**, 114005 (2015).

[168] PHENIX Collaboration, A. Adare *et al.*, Phys. Rev. **D85**, 092004 (2012).

[169] PHENIX Collaboration, A. Adare *et al.*, Phys. Rev. **C84**, 044905 (2011).

[170] STAR Collaboration, L. Adamczyk *et al.*, Phys. Rev. **D86**, 072013 (2012).

[171] ALICE Collaboration, S. Acharya *et al.*, Eur. Phys. J. **C77**, 392 (2017).

[172] ALICE Collaboration, J. Adam *et al.*, Phys. Rev. **C91**, 064905 (2015).

[173] ATLAS Collaboration, M. Spousta, Nucl. Phys. **A932**, 404 (2014).

[174] CMS Collaboration, A. M. Sirunyan *et al.*, JHEP **01**, 045 (2018).

[175] A. Emerick, X. Zhao, and R. Rapp, Eur. Phys. J. **A48**, 72 (2012).

[176] STAR Collaboration, L. Adamczyk *et al.*, Phys. Rev. C **94**, 064904 (2016).

[177] B. Krouppa, R. Ryblewski, and M. Strickland, Phys. Rev. C **92**, 061901 (2015).

[178] B. Krouppa and M. Strickland, Universe **2**, 16 (2016).

[179] J. Hoelck, F. Nendzig, and G. Wolschin, Phys. Rev. C **95**, 024905 (2017).

[180] L. Grandchamp, S. Lumpkins, D. Sun, H. van Hees, and R. Rapp, Phys. Rev. C **73**, 064906 (2006).

[181] K. Zhou, N. Xu, and P. Zhuang, Nucl. Phys. A **931**, 654 (2014).

[182] CMS Collaboration, V. Khachatryan *et al.*, Phys. Lett. B **770**, 357 (2017).

[183] N. Brambilla, J. Ghiglieri, A. Vairo, and P. Petreczky, Phys. Rev. D **78**, 014017 (2008).

[184] F. Karsch, M. T. Mehr, and H. Satz, Z. Phys. C **37**, 617 (1988).

[185] M. Laine, O. Philipsen, P. Romatschke, and M. Tassler, JHEP **0703**, 054 (2007).

[186] Y. Park, K.-I. Kim, T. Song, S. H. Lee, and C.-Y. Wong, Phys. Rev. **C76**, 044907 (2007).

[187] S. Mukherjee, P. Petreczky, and S. Sharma, Phys. Rev. **D93**, 014502 (2016).

[188] T. Song, K. C. Han, and C. M. Ko, Phys. Rev. **C85**, 054905 (2012).

[189] L. Gerland, L. Frankfurt, M. Strikman, and H. Stoecker, Phys. Rev. **C69**, 014904 (2004).

[190] V. Greco, C. M. Ko, and P. Levai, Phys. Rev. **C68**, 034904 (2003).

[191] X.-N. Wang and F. Yuan, Phys. Lett. **B540**, 62 (2002).

[192] LHCb Collaboration, R. Aaij *et al.*, Eur. Phys. J. **C74**, 3092 (2014).

[193] STAR Collaboration, Z. Ye, Nucl. Phys. A **967**, 600 (2017).

[194] PHENIX Collaboration, A. Adare *et al.*, Phys. Rev. **C96**, 024907 (2017).

[195] M. Cacciari *et al.*, JHEP **10**, 137 (2012).

[196] ALICE Collaboration, B. B. Abelev *et al.*, Eur. Phys. J. **C74**, 2974 (2014).

[197] CMS Collaboration, S. Chatrchyan *et al.*, Phys. Lett. **B727**, 101 (2013).

[198] CMS Collaboration, C. Flores, talk at Quark Matter (2017).

[199] CMS Collaboration, CMS-PAS-HIN-16-023 (2017).

[200] ATLAS Collaboration, ATLAS-CONF-2015-050 (2015).

[201] LHCb Collaboration, R. Aaij *et al.*, JHEP **07**, 094 (2014).

[202] ALICE Collaboration, B. B. Abelev *et al.*, Phys. Lett. **B740**, 105 (2015).

[203] X. Du, M. He, and R. Rapp, Nucl. Phys. **A967**, 904 (2017).

[204] H. van Hees, M. Mannarelli, V. Greco, and R. Rapp, Phys. Rev. Lett. **100**, 192301 (2008).

[205] F. Prino and R. Rapp, J. Phys. G **43**, 093002 (2016).

[206] CDF Collaboration, D. Acosta *et al.*, Phys. Rev. Lett. **88**, 161802 (2002).

[207] ATLAS Collaboration, G. Aad *et al.*, Phys. Rev. **D87**, 052004 (2013).

[208] CMS Collaboration, V. Khachatryan *et al.*, Phys. Rev. **D83**, 112004 (2011).

[209] LHCb Collaboration, R. Aaij *et al.*, Eur. Phys. J. **C72**, 2025 (2012).

[210] LHCb Collaboration, R. Aaij *et al.*, Eur. Phys. J. **C74**, 2835 (2014).

[211] P. P. Bhaduri, N. Borghini, A. Jaiswal, and M. Strickland, (2018), 1809.06235.

[212] D. Das and N. Dutta, Int. J. Mod. Phys. **A33**, 1850092 (2018).

[213] H. Niemi, K. J. Eskola, R. Paatelainen, and K. Tuominen, Phys. Rev. **C93**, 014912 (2016).

[214] ALICE Collaboration, E. Abbas *et al.*, Phys. Lett. **B726**, 610 (2013).

[215] ALICE Collaboration, G. G. Fronzé, Nucl. Part. Phys. Proc. **289-290**, 397 (2017).

[216] ALICE Collaboration, A. L. I. Das, talk at Quark Matter (2017).

[217] CMS Collaboration, A. M. Sirunyan *et al.*, Phys. Rev. Lett. **120**, 142301 (2018).

[218] E. Scomparin, Nucl. Phys. **A967**, 208 (2017).

[219] CMS Collaboration, S. Chatrchyan *et al.*, JHEP **04**, 103 (2014).

[220] J.-P. Blaizot, D. De Boni, P. Faccioli, and G. Garberoglio, Nucl. Phys. A **946**, 49 (2016).

[221] R. Katz and P. B. Gossiaux, Annals Phys. **368**, 267 (2016).

[222] N. Brambilla, M. A. Escobedo, J. Soto, and A. Vairo, Phys. Rev. D **96**, 034021 (2017).

[223] S. Kajimoto, Y. Akamatsu, M. Asakawa, and A. Rothkopf, Phys. Rev. **D97**, 014003 (2018).

[224] LHCb Collaboration, R. Aaij *et al.*, JHEP **06**, 064 (2013).

[225] ALICE Collaboration, J. Adam *et al.*, Eur. Phys. J. **C76**, 184 (2016).

[226] CMS Collaboration, V. Khachatryan *et al.*, Phys. Lett. **B743**, 383 (2015).

[227] A. Beraudo *et al.*, Nucl. Phys. **A979**, 21 (2018).

[228] S. Godfrey and N. Isgur, Phys. Rev. D **32**, 189 (1985).

[229] W. Lucha, F. F. Schoberl, and D. Gromes, Phys. Rept. **200**, 127 (1991).

[230] A. Mocsy, P. Petreczky, and M. Strickland, Int. J. Mod. Phys. A **28**, 1340012 (2013).

[231] S. Y. F. Liu, M. He, and R. Rapp, Phys. Rev. **C99**, 055201 (2019).

[232] G. E. Brown, C.-H. Lee, M. Rho, and E. Shuryak, Nucl. Phys. A **740**, 171 (2004).

[233] E. V. Shuryak and I. Zahed, Phys. Rev. D **70**, 054507 (2004).

[234] M. Mannarelli and R. Rapp, Phys. Rev. C **72**, 064905 (2005).

[235] J. Liao and E. Shuryak, Phys. Rev. D **82**, 094007 (2010).

[236] S. Y. F. Liu and R. Rapp, (2016), arXiv:1612.09138.

[237] S. Y. F. Liu and R. Rapp, Phys. Rev. C **97**, 034918 (2018).

[238] A. Beraudo, J.-P. Blaizot, and C. Ratti, Nucl. Phys. A **806**, 312 (2008).

[239] A. Rothkopf, T. Hatsuda, and S. Sasaki, Phys. Rev. Lett. **108**, 162001 (2012).

[240] Y. Burnier, O. Kaczmarek, and A. Rothkopf, Phys. Rev. Lett. **114**, 082001 (2015).

[241] S. Y. F. Liu and R. Rapp, Nucl. Phys. A **941**, 179 (2015).

[242] A. Bazavov, Y. Burnier, and P. Petreczky, Nucl. Phys. A **932**, 117 (2014).

[243] Y. Liu, B. Chen, N. Xu, and P. Zhuang, Phys. Lett. B **697**, 32 (2011).

[244] M. Strickland and D. Bazow, Nucl. Phys. A **879**, 25 (2012).

[245] E. G. Ferreiro, Phys. Lett. **B731**, 57 (2014).

[246] B. Krouppa, A. Rothkopf, and M. Strickland, Phys. Rev. D **97**, 016017 (2018).

[247] S. Aronson, E. Borras, B. Odegard, R. Sharma, and I. Vitev, Phys. Lett. B **778**, 384 (2018).

[248] E. G. Ferreiro and J.-P. Lansberg, JHEP **10**, 094 (2018).

[249] Y. Akamatsu, Phys. Rev. D **91**, 056002 (2015).

[250] J.-P. Blaizot and M. A. Escobedo, Phys. Rev. **D98**, 074007 (2018).

[251] X. Yao and T. Mehen, Phys. Rev. **D99**, 096028 (2019).

[252] A. Mocsy and P. Petreczky, Phys. Rev. Lett. **99**, 211602 (2007).

[253] A. Bazavov and P. Petreczky, Phys. Rev. **D87**, 094505 (2013).

[254] CMS Collaboration, A. M. Sirunyan *et al.*, Phys. Lett. **B790**, 270 (2019).

[255] ALICE Collaboration, S. Acharya *et al.*, Phys. Lett. **B790**, 89 (2019).

[256] J. E. Bernhard, J. S. Moreland, S. A. Bass, J. Liu, and U. Heinz, Phys. Rev. C **94**, 024907 (2016).

[257] C. Zhang, C. Marquet, G.-Y. Qin, S.-Y. Wei, and B.-W. Xiao, Phys. Rev. Lett. **122**, 172302 (2019).

[258] Z. Citron *et al.*, Future physics opportunities for high-density QCD at the LHC with heavy-ion and proton beams, in *HL/HE-LHC Workshop: Workshop on the Physics of HL-LHC, and Perspectives at HE-LHC Geneva, Switzerland, June 18-20, 2018*, 2018, 1812.06772.

APPENDIX A

BOTTOMONIUM RATES AND FEEDDOWNS IN SEC. 5*

A.1 Inelastic Bottomonium Cross Sections

In this appendix section we briefly recollect the expressions used for the cross sections for the inelastic bottomonium reactions with quarks and gluons.

For gluo-dissociation, $g + Y \to b + \bar{b}$, we employ the cross sections derived from the operator product expansion for a Coulombic bound state by Bhanot and Peskin [71, 72],

$$\sigma_{Yg\to b\bar{b}} = \frac{r_0}{m_b} g_Y(x) \tag{A.1}$$

where r_0 is the ground-state radius and

$$g_Y(x) = \begin{cases} \frac{2}{3}\pi\left(\frac{32}{3}\right)^2 \frac{(x-1)^{\frac{3}{2}}}{x^5} & \text{for } \Upsilon(1S) \\ \frac{2}{3}\pi\left(\frac{32}{3}\right)^2 \frac{16(x-1)^{\frac{3}{2}}(x-3)^2}{x^7} & \text{for } \Upsilon(2S) \\ \frac{2}{3}\pi\left(\frac{32}{3}\right)^2 \frac{4(x-1)^{\frac{1}{2}}\left(9x^2-20x+12\right)}{x^7} & \text{for } \chi(1P) \end{cases} \tag{A.2}$$

where $x = k_0/E_B$ and $k_0 = \frac{s-m_Y^2-m_g^2}{2m_Y}$ is the incident gluon energy in the quarkonium for a center-of-mass energy squared:

$$s = (p_Y^{(4)} + p_g^{(4)})^2 = m_Y^2 + m_g^2 + 2\omega_Y\omega_g - 2\vec{p}_Y \cdot \vec{p}_g \; ; \tag{A.3}$$

---

[*] Part of this appendix is reprinted with permission from “Color Screening and Regeneration of Bottomonia in High-Energy Heavy-Ion Collisions ” by Xiaojian Du, Min He and Ralf Rapp, 2017, Phys.Rev. C96 no.5, 054901 , Copyright 2017 by APS.

$p_Y^{(4)} = (\omega_Y, \vec{p}_Y)$ and $p_g^{(4)} = (\omega_g, \vec{p}_g)$ denote the 4-momenta of the incoming bottomonium and outgoing gluon, respectively. The color-Coulomb binding energy and radius follow the hydrogen form,

$$
\begin{aligned}
E_0 &= \left(\frac{N^2-1}{2N}\alpha_s\right)^2 \frac{m_b}{4} = \left(\frac{2\alpha_s}{3}\right)^2 m_b && \text{(A.4)} \\
r_0 &= \frac{2}{m_b\alpha_s}\left(\frac{2N}{N^2-1}\right) = \frac{3}{2m_b\alpha_s} && \text{(A.5)}
\end{aligned}
$$

which slightly differs from the large-N_c limit expressions

$$
\begin{aligned}
E_0 &= \left(\frac{N}{2}\alpha_s\right)^2 \frac{m_b}{4} = \left(\frac{3\alpha_s}{4}\right)^2 m_b && \text{(A.6)} \\
r_0 &= \frac{2}{m_b\alpha_s}\left(\frac{2}{N}\right) = \frac{4}{3m_b\alpha_s} && \text{(A.7)}
\end{aligned}
$$

underlying the coefficients in Eq. (A.2).

In previous work [175], the binding energies in the vacuum binding scenario were taken at the vacuum values defined by $E_B = 2m_B - m_Y = 1.1[0.54]\,\text{GeV}$ for the $\Upsilon(1S)$ [$\Upsilon(2S)$] with the coupling constant fixed via the ground-state expression, Eq. (A.4). We here adopt an alternative treatment, which we believe to be more realistic, by eliminating the r_0 dependence and rewriting the cross section as the first power in α_s times a factor involving the binding energies using the relation of the bottomonium radius to their binding energies from the hydrogen model expression. With $\sigma \sim \frac{r_0}{m_b} \sim \alpha_s \cdot r_0^2 \sim \frac{\alpha_s}{m_b E_B}$, the cross sections become

$$
\sigma_{Yg\to b\bar{b}} = \frac{2\alpha_s}{3m_b E_0} g_Y(x) \tag{A.8}
$$

Since the in-medium binding energies of the Y states are not necessarily small compared to the temperature, we also include a phenomenological treatment of interference effects for the quasifree reaction rates. Starting from the original expression for the quasifree cross section, schematically given by $\sigma_{\Upsilon p\to b\bar{b}p}(s)\simeq\int\frac{\mathrm{d}\sigma_{\Upsilon p\to b\bar{b}p}(s,t,u)}{\mathrm{d}t}\mathrm{d}t$, (which includes the t-channel from both quark and gluon as partons, s- and u-channels from gluon as parton, and their mixed terms) the interference correction is implemented as

$$\sigma_{\Upsilon p\to b\bar{b}p}(s)\simeq\int\mathrm{d}t\left(\frac{\mathrm{d}\sigma_{\Upsilon p\to b\bar{b}p}(s,t,u)}{\mathrm{d}t}\right)\times\left(1-\frac{\sin(\sqrt{-t}r)}{\sqrt{-t}r}\right)\tag{A.9}$$

(which also influences the p_T dependence). To relate the dependence on the coordinate r to the in-medium binding energy, E_B, we utilize the Coulomb relations for the two scales $p\sim m_b\alpha_s\sim\frac{1}{r}$ and $E_B\sim m_b\alpha_s^2$. One can then either re-express the mass or coupling constant leading to $E_B\sim\frac{\alpha_s}{r}$ or $E_B\sim\frac{1}{m_b r^2}$, respectively. To check which relation is more realistic, especially in the presence of the nonperturbative string term, we determine the numerical coefficients for each option from the vacuum binding energy and radius of the $\Upsilon(1S)$ and then inspect the pertinent prediction for the $\Upsilon(2S)$. With $\alpha_s\simeq0.3$, $m_b\simeq5$ GeV and a vacuum binding and radius of $E_B(\Upsilon(1S))\simeq1$ GeV and $r(\Upsilon(1S))\simeq0.2$ fm, we find $E_B\simeq3.3\frac{\alpha_s}{r}$ or $E_B\simeq5\frac{1}{m_b r^2}$ for the two options above. Using $r(\Upsilon(2S))\simeq0.5$ fm then gives $E_B(2S)\simeq3.3\frac{\alpha_s}{r}\simeq0.4$ GeV or $E_B(2S)\simeq5\frac{1}{m_b r^2}\simeq0.16$ GeV. Since the first replacement is closer to the empirical $\Upsilon(2S)$ binding of ~0.54 GeV, we will adopt it in our calculations.

A.2 Feeddowns and pp Baseline Cross Sections for Excited States

In this appendix section we detail our implementation for updated feeddown fractions. Starting from Ref. [96], the direct $\Upsilon(1S)$ cross section is 70 %(50 %) at low (high) p_T, on average 67 %. The feeddowns to the $1S$ state are approximately 17 % from $1P$, 9 % from $2S$, 1 % from $3S$ and 6 % from $2P$ and $3S$ together. The main change from the previous work of Ref. [175] is from the $\chi_b(nP)$ states which now contribute less at low p_T [192]; cf. Table. 5.1. Because of the newly included explicit treatment of the $\Upsilon(3S)$ state, we implement detailed feeddown fractions discussed below for the TBS calculation. For the vacuum binding scenario calculation, we only include $\Upsilon(1S)$, $\Upsilon(2S)$ and $\chi_b(1P)$ states. A correction from explicitly including $\Upsilon(3S)$ and $\chi_b(2P)$ states in the vacuum binding scenario calculation would result in ca. $\sim$10 % more regeneration for the $\Upsilon(2S)$ and a negligible contribution to the $\Upsilon(1S)$.

From several experimental data [208, 207, 197, 209, 224, 225, 210], we conclude $\sigma_{2S} \simeq 0.33\sigma_{1S}^{\rm tot}$ and $\sigma_{3S} \simeq 0.15\sigma_{1S}^{\rm tot}$. With the branching ratios $Br(2S \to 1S) = 26.7\,\%$ and $Br(3S \to 1S) = 6.6\,\%$, we obtain feeddown fractions of $Fd(2S \to 1S)$=$0.33 \cdot 26.7\,\% = 8.8\,\%$ and $Fd(3S \to 1S)$=$0.15 \cdot 6.6\,\% = 0.99\,\%$, which are consistent with Ref. [96].

The cross section ratio of $\frac{\sigma(\chi_{b2}(1P))}{\sigma(\chi_{b1}(1P))} = 0.85$ from Ref. [226] indicates a smaller production of the heavier $1P$ state. An assumption for the lighter $\chi_{b0}(1P)$ with a ratio $\frac{\sigma(\chi_{b0}(1P))}{\sigma(\chi_{b1}(1P))} \simeq 1.5$ gives an approximate branching ratio for the $1P$ state of

$$\begin{aligned} Br(1P \to 1S) &\simeq \frac{Br(\chi_{b0}(1P) \to 1S) \cdot 1.5}{3.35} \\ &\quad + \frac{Br(\chi_{b1}(1P) \to 1S) \cdot 1.0}{3.35} \\ &\quad + \frac{Br(\chi_{b2}(1P) \to 1S) \cdot 0.85}{3.35} \\ &= \frac{1.8 \cdot 1.5 + 33.9 \cdot 1.0 + 19.1 \cdot 0.85}{3.35}\,\% \\ &= 15.8\,\%\,. \end{aligned} \tag{A.10}$$

We estimate a $1P$ cross section of $\frac{17\,\%}{15.8\,\%} \simeq 1.08$ of the inclusive $1S$ cross section, $\sigma_{1P} \simeq 1.08\sigma_{1S}^{tot}$. We estimate the fraction $\frac{\sigma_{2P}}{\sigma_{1P}} \simeq 0.8$ from Ref. [165] so that $\sigma_{2P} \simeq 0.864\sigma_{1S}^{tot}$.

Assuming the same ratio between different χ_b states for the $2P$ multiplet, we estimate

$$\begin{aligned} Br(2P \to 1S) &\simeq \frac{Br(\chi_{b0}(2P) \to 1S) \cdot 1.5}{3.35} \\ &\quad + \frac{Br(\chi_{b1}(2P) \to 1S) \cdot 1.0}{3.35} \\ &\quad + \frac{Br(\chi_{b2}(2P) \to 1S) \cdot 0.85}{3.35} \\ &= \frac{0.9 \cdot 1.5 + 10.8 \cdot 1.0 + 8.1 \cdot 0.85}{3.35} \% \\ &= 5.7\,\%. \end{aligned} \tag{A.11}$$

and

$$\begin{aligned} Br(2P \to 2S) &\simeq \frac{Br(\chi_{b0}(2P) \to 2S) \cdot 1.5}{3.35} \\ &\quad + \frac{Br(\chi_{b1}(2P) \to 2S) \cdot 1.0}{3.35} \\ &\quad + \frac{Br(\chi_{b2}(2P) \to 2S) \cdot 0.85}{3.35} \\ &= \frac{4.6 \cdot 1.5 + 19.9 \cdot 1.0 + 10.6 \cdot 0.85}{3.35} \% \\ &= 10.7\,\% \,. \end{aligned} \tag{A.12}$$

The latter is almost the same as $Br(3S \to 2S) = 10.6\,\%$. These estimates result in feeddown fractions

$$\begin{aligned} Fd(2P \to 1S) &= \frac{\sigma_{2P} Br(2P \to 1S)}{\sigma_{1S}^{tot}} = 0.864 \cdot 5.7\,\% \\ &= 4.9\,\% \end{aligned} \tag{A.13}$$

and

$$Fd(2P \to 2S) = \frac{\sigma_{2P} Br(2P \to 2S)}{\sigma_{2S}} = \frac{0.864 \cdot 10.7\,\%}{0.33} = 28\,\%\,, \tag{A.14}$$

consistent with Ref. [96].

The above estimate furthermore leads to a total cross section for the higher excited $3S$ and $2P$ states of about $1.014\sigma_{1S}^{\rm tot}$. With $Br(3S \to 1S) = 6.6\,\%$ and $Br(2P \to 1S) = 5.7$, we have

$$\begin{aligned} &Fd(3S + 2P \to 1S) \\ &= \frac{\sigma_{3S} Br(3S \to 1S) + \sigma_{2P} Br(2P \to 1S)}{\sigma_{1S}^{tot}} \\ &= 0.15 \cdot 6.6\,\% + 0.864 \cdot 5.7\,\% = 5.9\,\% \end{aligned} \tag{A.15}$$

and, with $Br(3S \to 2S) = 10.6\,\%$ and $Br(2P \to 2S) = 10.7$,

$$\begin{aligned} &Fd(3S + 2P \to 2S) \\ &= \frac{\sigma_{3S} Br(3S \to 2S) + \sigma_{2P} Br(2P \to 2S)}{\sigma_{2S}} \\ &= \frac{0.15 \cdot 10.6\,\% + 0.864 \cdot 10.7\,\%}{0.33} = 33\,\%\,, \end{aligned} \tag{A.16}$$

consistent with Ref. [96].

Since the branching ratios from $3S$ or $2S$ to $1P$ are all smaller than $1\,\%$, we neglect these feeddown channels.